Imperial College London

Improved Rainfall Downscaling for Real-Time Urban Pluvial Flood Forecasting

By

Li-Pen Wang

A thesis submitted in fulfilment of the requirements for the degree of PhD and the Diploma of Imperial College London

Department of Civil and Environmental Engineering

2012

Abstract

Traditionally, hydrologists had a relatively minor role in rainfall data processing; they usually simply took data from meteorologists. However, meteorological organisations usually provide weather service over a larger area and scale (i.e. country level); the applicability of this large-scale information to urban hydrological applications is therefore questionable. This work tries to provide a local view on rainfall processing, aiming to improve the suitability (in terms of accuracy and resolution) of operational rainfall data for urban hydrological uses.

This work explores advanced downscaling and adjustment techniques to address the identified issues in urban hydrology: accuracy and resolution. On the basis of a a review and the testing of state of the art techniques, the Bayesian-based adjustment technique and the newly-developed cascade-based downscaling techniques are found to be suitable tools to improve respectively the accuracy, and the resolution of operational radar (and raingauge) rainfall estimates. In addition, a combined application of these two techniques is tested; the results suggested that, although extra uncertainty may appear, this combination demonstrates a clear potential for providing accurate and high-resolution (street-scale and 5-min) rainfall estimates.

Acknowledgments

I would like to sincerely thank the full scholarship provided by the Ministry of Education of Taiwan. Without this 3-year support, I could not have completed my PhD programme.
I would like to thank my supervisors Čedo Maksimović and Christian Onof for the confidence they have had in my work, allowing me to conduct the research freely. Particularly, I would like to thank Cedo for giving me the chance to take part in a number of interesting national and international research projects and related conferences and meetings; this made my PhD a much more enriching experience. I also owe special thanks to Christian for his mentoring and friendship; I really appreciate the hours we spent together, discussing the details of my work, deriving equations and talking about tennis.
I would also like to thank the examiners of my PhD thesis, Dr. Neil McIntyre and Dr. Patrick Willems. Their valuable comments made me feel more confident about the contribution of my work and also provided me with useful insights about its weak points..
I am also grateful for the technical support of Dr. Cinzia Mazzetti (Project manager at PROGEA Srl, Bologna, Italy), who was always very patient with my questions.
I was very lucky to be able to work with many nice people, especially "the Team" (Nuno Simões and Susana Ochoa), Juan Pablo Rodriguez Sanchez and Supattra Visessri (Art); I thank them for making my PhD life rewarding and fun. During this time I also had the pleasure of sharing the day-to-day with my colleagues Tingting Zhang, Jennifer Jian, Otuawe Moro, Duan Juan and Suzan Sharifan. They were always happy to share their thoughts and experiences with me. In addition, I would like to thank my "Londoner" friends, Chih-Yu Lee, Maureen Coat, Suna Srisamai, Angélica Anglés and Anthuanette Hidalgo. They have always supported me and have made my life in London colourful. I am also very grateful to my friends in Taiwan, especially Gloria Chang and Patrick Hsieh, who have always tried their best to support me and encourage me.
My strongest thanks are for my parents, Wen-Pei Fan and Chung-Yun Wang, for these thirty-one years of unreserved support and encouragement. I would also like to thank my sister, Li-Yun Wang, and her husband, Peter Lai, for their support and for taking care of my family during this time. Finally, I want to thank the strong support of my girl friend, Cherry, and her family, Pacho, Mónica, Alejo and especially Nora. Their encouragement for completing the last part of this PhD was very important for me

Contents

List of Figures **8**

List of Tables **20**

1 Introduction **23**

1.1 Background 23
1.2 Research problems 27
1.3 Research Objectives and Methodology 31
1.4 Thesis outline 32

2 Experimental Site And Data Set **35**

2.1 Cranbrook catchment 35
2.1.1 Environmental setting 35
2.1.2 Monitoring network 37
In-situ rain gauge and level gauge sites 37
Weather radar sites 37
2.2 Hydraulic models of the Cranbrook catchment 39
2.2.1 Overland network modelling 40
2.2.2 Sewer network modelling 41
2.2.3 Dual-drainage modelling 42
2.3 Rainfall data sets 45
2.3.1 In-Situ Raingauge data 45
2.3.2 Radar data 46
2.3.3 Other data sources 48
2.4 Rainfall Events for Case Studies 49
2.5 Summary 52

3 Urban Rainfall Estimation **54**
3.1 Raingauge measurements . . . 54
3.2 Radar rainfall estimates . . . 56
3.2.1 $Z - R$ conversion . . . 57
3.2.2 Gauge-based adjustment . . . 59
3.3 Applications of gauge-based adjustment to urban rainfall processing . . . 64
3.3.1 Mean bias adjustment . . . 64
3.3.2 Bayesian-based adjustment . . . 66
3.3.3 Comparison of adjustment techniques . . . 77
3.4 Summary . . . 81

4 Rainfall Downscaling **90**
4.1 Reviews of downscaling techniques for hydrological applications . . . 90
4.1.1 Generalised Linear Models . . . 90
4.1.2 Poisson cluster models . . . 92
4.1.3 Cascade-based models . . . 93
4.2 Theory of Multifractals . . . 98
4.2.1 Euclidean Dimension . . . 98
4.2.2 Monofractals . . . 99
4.2.3 Multifractals . . . 100
4.2.4 Self-similar and Left-sided Multifractals . . . 103
4.2.5 The Generating Equation . . . 106
4.2.6 Applications of multifractals to rainfall downscaling . . . 110
4.2.7 Summary . . . 111
4.3 Semi-deterministic cascade model . . . 113
4.3.1 Quad-nomial cascade model . . . 115
4.3.2 Temporal downscaling . . . 116
4.3.3 Spatial downscaling . . . 121
4.4 Fully-empirical cascade model . . . 128
4.4.1 Derivation of fragmentation ratios . . . 130
4.4.2 Relative positions of rainfall volumes . . . 131
4.4.3 Causality . . . 133
4.4.4 Applications of the FE model to temporal rainfall downscaling . . . 134
4.5 Applications of cascade-based downscaling to urban hydrology . . . 139
4.5.1 Temporal downscaling of raingauge measurements . . . 139

4.5.2 Spatial downscaling of radar images 147
4.6 Summary 156

5 Combined Applications of Downscaling and Adjustment Techniques 158
5.1 Measurement of impact 159
5.2 Applications of downscaled rainfall estimates 162
5.3 Applications of downscaled and adjusted rainfall estimates 173
5.4 Summary 176

6 Conclusions and Perspectives for further Research 194

Bibliography 198

A Urban Flood Forecasting in the Cranbrook Catchment 210

B Estimation of Empirical $\tau(q)$ Curves 217

C Discrete-in-Scale Random Cascade Models 219
C.1 Random Cascade processes and $\tau(q)$ curve 219
C.2 Relation of $\tau(q)$ and $K(q)$ curves 221
C.3 β Model 222
C.4 α Model 223
C.5 Log-Poisson Model 224

D Statistical Moments of a Semi-Deterministic Cascade Process 227

E Results: Adjusted Radar Rainfall and Hydraulic Outputs 231

List of Figures

1.1 The conceptual scheme of the idea that integrates rainfall/weather models over multiple spatial and temporal scales 27
1.2 Performance of the radar-based forecasts versus lead time at different spatial and temporal scales for the 23/08/2010 event [source: Wang et al. (2011)] . 29
1.3 Performance of hydraulic outputs resulting from the STEPS rainfall nowcasts at different spatial and temporal scales for 23/08/2010 event [source: Wang et al. (2011)] 30

2.1 Location of the Cranbrook catchment in relation to the River Roding catchment 36
2.2 Geographical deployment of in-situ raingauge sites and the photos of the monitoring network installed in the Cranbrook catchment [source: Ochoa et al. (2011b)] 38
2.3 Two meteorological radars (Chenies and Thurnham) which are operated by the UK Met Office and coverage of the Cranbrook catchment [source: Ochoa et al. (2011b)] 39
2.4 2D (upper) and 1D (lower) model of the overland network of the Cranbrook catchment: entire catchment (left) and details (right) [source: Ochoa et al. (2011b)] 43
2.5 Sewer network of the Cranbrook catchment [source: Ochoa et al. (2011b)] . 44
2.6 The 1D-1D dual drainage network of the Cranbrook catchment [source: Wang et al. (2011)] 45
2.7 Rainfall information measured by the local in-situ raingauges for the selected events: rainfall totals (the upper) and maximum rainfall rates (the lower). 51

3.1 Schematic of the Bayesian-based adjustment proposed by Todini (2001b) . 71

3.2 Images of radar, Block-Kriged and Bayesian-based adjusted radar rainfall fields (from left to right) between time steps 00:20 and 00:35 (from top to bottom) for the 23/08/2010 event 72
3.3 Images of radar, Block-Kriged and Bayesian-based adjusted radar rainfall fields (from left to right) between time steps 15:10 and 15:25 (from top to bottom) for the 26/05/2011 event 73
3.4 Images of radar, Block-Kriged and Bayesian-based adjusted radar rainfall fields (from left to right) between time steps 17:05 and 17:20 (from top to bottom) on 05/06/2011 for the 05-06/06/2011 event 74
3.5 Images of radar, Block-Kriged and Bayesian-based adjusted radar rainfall fields (from left to right) between time steps 11:50 and 12:05 (from top to bottom) for the 03/01/2012 event 75
3.6 Images of radar, Block-Kriged and Bayesian-based adjusted radar rainfall fields (from left to right) at time steps where peaks were observed for four selected events on (a) 23/08/2012, (b) 26/05/2011, (c) 05-06/06/2011 and (d) 03/01/2012 76
3.7 The comparison of raingauge observations, the coincidental radar and merged radar estimates in the rainfall event taking place on 23/08/2010 in the Cranbrook catchment, London 78
3.8 The quantile comparison of the raingauge observations and the various radar rainfall estimates (each point represents the instantaneous rainfall depth in 5-min time intervals. The original radar data: triangular markers; the mean-field bias corrected radar estimates: round markers; the Bayesian-based adjusted radar estimates: filled round markers) over the Cranbrook catchment for the four selected events 79

4.1 The sketch for the two-stage Generalised Linear Models: Occurrence and Amounts models 93
4.2 The sketch for the Bartlett-Lewis rectangular pulse model (Koutsoyiannis and Onof, 2001) 93
4.3 The diagram for a multiplicative cascade process 97
4.4 The multifractal spectrum $f(\alpha)$ estimated from a typical self-similar measure (Falconer, 2003) 107
4.5 The associated Legendre transform ($\tau(q)$) of the multifractal spectrum in Figure 4.4 107

4.6 The solid line denotes the first scenario where $w_i = 0.1$ for all i; the dashed line represents the second scenario where $w_i = 0.111$ for all i, except one equal to 0.001; and the dotted line is where $w_i = 0.07$ for all i, except one equal to 0.37 (Harte, 2001). 111
4.7 General schematic of the construction of cascade models 112
4.8 Schematic of the multinomial multiplicative cascade process 115
4.9 Application of the quad-nomial cascade to rainfall time series downscaling 118
4.10 The q-th moment $\chi(q, \epsilon)$ as a function of time scale ϵ over the range from 5 min to 1 month (left) and the range from 5 min to 1 day (right) for $0 \leq q \leq 5$ from Greenwich raingauge data. A scaling break can be observed around $\epsilon = 1$ day and a well straight-line behaviour can be characterised over 5 min to 1 day scales. 119
4.11 Empirical and theoretical $\tau(q)$ curves from Greenwich raingauge data over the time scales 5 min to 1 day; the round markers are empirical $\tau(q)$ curves, whilst the solid and dashed lines are theoretical $\tau(q)$ curves derived respectively from SD and LP models 120
4.12 Application of the quad-nomial cascade to rainfall field downscaling 123
4.13 Evolution of $\tau(q)$ curves in the 20090209 10:00-17:00 event over 64×64 km^2 Greater London area; the dashed lines are empirical $\tau(q)$ curves and the solid lines are theoretical $\tau(q)$ curves estimated by solving the generating equation 124
4.14 Empirical and theoretical $\tau(q)$ curves at time steps 14:55 and 15:25 in the 20090209 10:00-17:00 event over 64×64 km^2 Greater London area; the round (15:25) and square (14:55) markers are empirical$\tau(q)$ curves, whilst the solid (15:25) and dashed (14:55) lines are theoretical $\tau(q)$ curves derived respectively from SD and LP models 125
4.15 Mean and spatial variation (Std, standard deviation) of rainrates in the 20090209 10:00-17:00 event. The dark solid lines were estimated from 1-km Nimrod data over 64×64 km^2 Greater London area; the gray solid lines and the gray areas with gray dashed border lines were estimated from the downscaled rainfall fields (8 km to 1 km) in the coincidental area, respectively generated by the SD and LP models 126

4.16 Mean and spatial variation (Std, standard deviation) of rainrates in the 20090209 10:00-17:00 event. The dark solid lines were estimated from 1-km Nimrod data over 5×6 km^2 Cranbrook catchment; the gray areas with gray solid border lines and with gray dashed border lines were estimated from the downscaled rainfall fields (8 km to 1 km) in the coincidental area, respectively generated by the SD and LP models 127
4.17 Schematic of the binomial fully empirical multiplicative cascade process . . 130
4.18 Schematic of estimation of fragmentation ratios between two successive cascade levels 131
4.19 Probability of the occurrence of three cascading states (i.e. $P(0/1)$, $P(1/0)$ and $P(x/x)$) according to different positions: "starting" and "isolated" . . 132
4.20 Schematic of causality between two pairs of temporally consecutive fragmentation ratios (top-right), and their variations according to different cascading states and timescale ranges 134
4.21 Weight distributions of fragmentation ratios between two successive cascade levels for all states (1/0, 0/1 and x/x) over timescales ranging from 80 min to 5 min 137
4.22 Weight distributions of non-zero fragmentation ratios between two successive cascade levels (i.e. x/x state) over timescales ranging from 80 min to 5 min 138
4.23 Comparison of monthly statistics of 5-min rainfall observations and synthetic time series generated respectively by SD, FE and LP models 139
4.24 Comparison of 5-min rainfall observations and synthetic time series of two selected events generated by FE and LP models 144
4.25 Comparison of flow rates (in m^3/s) resulting from observed 5-min rainfall observations (round markers) and the stochastically downscaled 5-min time series for event A using the FE (the area with dark dashed border) and LP (the area with gray solid border) models 145
4.26 Comparison of flows (in m^3/s) resulting from observed 5-min rainfall observations (round markers) and the stochastically downscaled 5-min time series for event B using the FE (the area with dark dashed border) and LP (the area with gray solid border) models 146

4.27 Mean (upper) and Standard deviation (lower) profiles of the original (gray solid line), stochastically downscaled (gray area with solid boundary) and ensemble (dark dashed line) radar rainfall estimates (from 8 km to 1 km scale) in the Cranbrook catchment for the event 23/08/2010 148
4.28 Mean (upper) and Standard deviation (lower) profiles of the original (gray solid line), stochastically downscaled (gray area with solid boundary) and ensemble (dark dashed line) radar rainfall estimates (from 8 km to 1 km scale) in the Cranbrook catchment for the event 26/05/2011 149
4.29 Mean (upper) and Standard deviation (lower) profiles of the original (gray solid line), stochastically downscaled (gray area with solid boundary) and ensemble (dark dashed line) radar rainfall estimates (from 8 km to 1 km scale) in the Cranbrook catchment for the event 05-06/06/2011 150
4.30 Mean (upper) and Standard deviation (lower) profiles of the original (gray solid line), stochastically downscaled (gray area with solid boundary) and ensemble (dark dashed line) radar rainfall estimates (from 8 km to 1 km scale) in the Cranbrook catchment for the event 03/01/2012 151
4.31 The comparison of the estimated flow depths at three selected pipes (from upper to lower figures: 1455.1 up-stream; 463.1 mid-stream; 307.1 down-stream) in the Cranbrook catchment for the event 23/08/2010. The estimated flow depths were obtained respectively using the original radar rainfall (gray dashed lines) and the stochastically downscaled (8 km to 1 km) radar rainfall estimates (enveloped by the dark solid lines) and their ensemble estimates (dark dashed-dotted lines) as inputs 152
4.32 The comparison of the estimated flow depths at three selected pipes (from upper to lower figures: 1455.1 up-stream; 463.1 mid-stream; 307.1 down-stream) in the Cranbrook catchment for the event 26/05/2011. The estimated flow depths were obtained respectively using the original radar rainfall (gray dashed lines) and the stochastically downscaled (8 km to 1 km) radar rainfall estimates (enveloped by the dark solid lines) and their ensemble estimates (dark dashed-dotted lines) as inputs 153

4.33 The comparison of the estimated flow depths at three selected pipes (from upper to lower figures: 1455.1 up-stream; 463.1 mid-stream; 307.1 down-stream) in the Cranbrook catchment for the event 05-06/06/2011. The estimated flow depths were obtained respectively using the original radar rainfall (gray dashed lines) and the stochastically downscaled (8 km to 1 km) radar rainfall estimates (enveloped by the dark solid lines) and their ensemble estimates (dark dashed-dotted lines) as inputs 154
4.34 The comparison of the estimated flow depths at three selected pipes (from upper to lower figures: 1455.1 up-stream; 463.1 mid-stream; 307.1 down-stream) in the Cranbrook catchment for the event 03/01/2012. The estimated flow depths were obtained respectively using the original radar rainfall (gray dashed lines) and the stochastically downscaled (8 km to 1 km) radar rainfall estimates (enveloped by the dark solid lines) and their ensemble estimates (dark dashed-dotted lines) as inputs 155

5.1 The comparison of the estimated flow depths at three selected pipes (from upper to lower figures: 1455.1 up-stream; 463.1 mid-stream; 307.1 down-stream) in the Cranbrook catchment for the event 23/08/2010. The estimated flow depths were obtained by using the original radar rainfall (gray dashed lines) and the stochastically downscaled (1 km to 500 m) radar rainfall estimates (enveloped by the dark solid lines) and their ensemble estimates (dark dashed-dotted lines) as inputs 165
5.2 The comparison of the estimated flow depths at three selected pipes (from upper to lower figures: 1455.1 up-stream; 463.1 mid-stream; 307.1 down-stream) in the Cranbrook catchment for the event 26/05/2011. The estimated flow depths were obtained by using the original radar rainfall (gray dashed lines) and the stochastically downscaled (1 km to 500 m) radar rainfall estimates (enveloped by the dark solid lines) and their ensemble estimates (dark dashed-dotted lines) as inputs 166

5.3 The comparison of the estimated flow depths at three selected pipes (from upper to lower figures: 1455.1 up-stream; 463.1 mid-stream; 307.1 down-stream) in the Cranbrook catchment for the event 05-06/06/2011. The estimated flow depths were obtained by using the original radar rainfall (gray dashed lines) and the stochastically downscaled (1 km to 500 m) radar rainfall estimates (enveloped by the dark solid lines) and their ensemble estimates (dark dashed-dotted lines) as inputs 167
5.4 The comparison of the estimated flow depths at three selected pipes (from upper to lower figures: 1455.1 up-stream; 463.1 mid-stream; 307.1 down-stream) in the Cranbrook catchment for the event 03/01/2012. The estimated flow depths were obtained by using the original radar rainfall (gray dashed lines) and the stochastically downscaled (1 km to 500 m) radar rainfall estimates (enveloped by the dark solid lines) and their ensemble estimates (dark dashed-dotted lines) as inputs 168
5.5 Variation of uncertainty range profiles at three selected pipes (from upper to lower figures: 1455.1 up-stream; 463.1 mid-stream; 307.1 down-stream) in the Cranbrook catchment for the event 23/08/2010. The estimated ranges were obtained by using the rainfall estimates, downscaled from the **original** 1 km radar rainfall to 500 (gray dashed lines), 250 (gray solid lines) and 125 (dark solid lines) m, as inputs 169
5.6 Variation of uncertainty range profiles at three selected pipes (from upper to lower figures: 1455.1 up-stream; 463.1 mid-stream; 307.1 down-stream) in the Cranbrook catchment for the event 26/05/2011. The estimated ranges were obtained by using the rainfall estimates, downscaled from the **original** 1 km radar rainfall to 500 (gray dashed lines), 250 (gray solid lines) and 125 (dark solid lines) m, as inputs 170
5.7 Variation of uncertainty range profiles at three selected pipes (from upper to lower figures: 1455.1 up-stream; 463.1 mid-stream; 307.1 down-stream) in the Cranbrook catchment for the event 05-06/06/2011. The estimated ranges were obtained by using the rainfall estimates, downscaled from the **original** 1 km radar rainfall to 500 (gray dashed lines), 250 (gray solid lines) and 125 (dark solid lines) m, as inputs 171

5.8 Variation of uncertainty range profiles at three selected pipes (from upper to lower figures: 1455.1 up-stream; 463.1 mid-stream; 307.1 down-stream) in the Cranbrook catchment for the event 03/01/2012. The estimated ranges were obtained by using the rainfall estimates, downscaled from the **original** 1 km radar rainfall to 500 (gray dashed lines), 250 (gray solid lines) and 125 (dark solid lines) m, as inputs 172
5.9 Variation of standard deviation profiles of the radar rainfall rates, downscaled from 1 km to 500 (gray dashed lines), 250 (yellow solid lines) and 125 (red solid lines) m in the Cranbrook catchment for the event 23/08/2010. The gray dashed lines are from the original radar data, and the dark dashed line is from the adjusted radar estimates 178
5.10 Variation of standard deviation profiles of the radar rainfall rates, downscaled from 1 km to 500 (gray dashed lines), 250 (yellow solid lines) and 125 (red solid lines) m in the Cranbrook catchment for the event 26/05/2011. The gray dashed lines are from the original radar data, and the dark dashed line is from the adjusted radar estimates 179
5.11 Variation of standard deviation profiles of the radar rainfall rates, downscaled from 1 km to 500 (gray dashed lines), 250 (yellow solid lines) and 125 (red solid lines) m in the Cranbrook catchment for the event 05-06/06/2011. The gray dashed lines are from the original radar data, and the dark dashed line is from the adjusted radar estimates 180
5.12 Variation of standard deviation profiles of the radar rainfall rates, downscaled from 1 km to 500 (gray dashed lines), 250 (yellow solid lines) and 125 (red solid lines) m in the Cranbrook catchment for the event 03/01/2012. The gray dashed lines are from the original radar data, and the dark dashed line is from the adjusted radar estimates 181
5.13 The comparison of the estimated flow depths at three selected pipes (from upper to lower figures: 1455.1 up-stream; 463.1 mid-stream; 307.1 down-stream) in the Cranbrook catchment for the event 23/08/2010. The estimated flow depths were obtained by using the original radar rainfall (gray dashed lines), the adjusted radar rainfall (gray solid lines) and the stochastically downscaled (1 km to 500 m) adjusted radar rainfall estimates (enveloped by the dark solid lines) and their ensemble estimates (dark dashed-dotted lines) as inputs 182

5.14 Standard deviation profiles of the original (gray solid lines) and adjusted (dark solid lines) radar rainfall rates at various downscaling scales in the Cranbrook catchment for the event 23/08/2010 (from upper to lower): from 1 km to 500, 250 and 125 m. The gray dashed lines are downscaled from the original radar data, while the dark dashed lines are from the adjusted radar estimates 183
5.15 Standard deviation profiles of the original (gray solid lines) and adjusted (dark solid lines) radar rainfall rates at various downscaling scales in the Cranbrook catchment for the event 26/05/2011 (from upper to lower): from 1 km to 500, 250 and 125 m. The gray dashed lines are downscaled from the original radar data, while the dark dashed lines are from the adjusted radar estimates 184
5.16 Standard deviation profiles of the original (gray solid lines) and adjusted (dark solid lines) radar rainfall rates at various downscaling scales in the Cranbrook catchment for the event 05-06/06/2011 (from upper to lower): from 1 km to 500, 250 and 125 m. The gray dashed lines are downscaled from the original radar data, while the dark dashed lines are from the adjusted radar estimates 185
5.17 Standard deviation profiles of the original (gray solid lines) and adjusted (dark solid lines) radar rainfall rates at various downscaling scales in the Cranbrook catchment for the event 03/01/2012 (from upper to lower): from 1 km to 500, 250 and 125 m. The gray dashed lines are downscaled from the original radar data, while the dark dashed lines are from the adjusted radar estimates 186
5.18 The comparison of the estimated flow depths at three selected pipes (from upper to lower figures: 1455.1 up-stream; 463.1 mid-stream; 307.1 down-stream) in the Cranbrook catchment for the event 26/05/2011. The estimated flow depths were obtained by using the original radar rainfall (gray dashed lines), the adjusted radar rainfall (gray solid lines) and the stochastically downscaled (1 km to 500 m) adjusted radar rainfall estimates (enveloped by the dark solid lines) and their ensemble estimates (dark dashed-dotted lines) as inputs 187

5.19 The comparison of the estimated flow depths at three selected pipes (from upper to lower figures: 1455.1 up-stream; 463.1 mid-stream; 307.1 down-stream) in the Cranbrook catchment for the event 05-06/06/2011. The estimated flow depths were obtained by using the original radar rainfall (gray dashed lines), the adjusted radar rainfall (gray solid lines) and the stochastically downscaled (1 km to 500 m) adjusted radar rainfall estimates (enveloped by the dark solid lines) and their ensemble estimates (dark dashed-dotted lines) as inputs 188
5.20 The comparison of the estimated flow depths at three selected pipes (from upper to lower figures: 1455.1 up-stream; 463.1 mid-stream; 307.1 down-stream) in the Cranbrook catchment for the event 03/01/2012. The estimated flow depths were obtained by using the original radar rainfall (gray dashed lines), the adjusted radar rainfall (gray solid lines) and the stochastically downscaled (1 km to 500 m) adjusted radar rainfall estimates (enveloped by the dark solid lines) and their ensemble estimates (dark dashed-dotted lines) as inputs 189
5.21 Variation of uncertainty range profiles at three selected pipes (from upper to lower figures: 1455.1 up-stream; 463.1 mid-stream; 307.1 down-stream) in the Cranbrook catchment for the event 23/08/2010. The estimated ranges were obtained by using the rainfall estimates, downscaled from the **adjusted** 1 km radar rainfall to 500 (gray dashed lines), 250 (gray solid lines) and 125 (dark solid lines) m, as inputs 190
5.22 Variation of uncertainty ranges (in mm) at three selected pipes (from upper to lower figures: 1455.1 up-stream; 463.1 mid-stream; 307.1 down-stream) in the Cranbrook catchment for the event 26/05/2011. The estimated ranges were obtained by using the rainfall estimates, downscaled from the **adjusted** 1 km radar rainfall to 500 (gray dashed lines), 250 (gray solid lines) and 125 (dark solid lines) m, as inputs 191
5.23 Variation of uncertainty range profiles at three selected pipes (from upper to lower figures: 1455.1 up-stream; 463.1 mid-stream; 307.1 down-stream) in the Cranbrook catchment for the event 05-06/06/2011. The estimated ranges were obtained by using the rainfall estimates, downscaled from the **adjusted** 1 km radar rainfall to 500 (gray dashed lines), 250 (gray solid lines) and 125 (dark solid lines) m, as inputs 192

5.24 Variation of uncertainty range profiles at three selected pipes (from upper to lower figures: 1455.1 up-stream; 463.1 mid-stream; 307.1 down-stream) in the Cranbrook catchment for the event 03/01/2012. The estimated ranges were obtained by using the rainfall estimates, downscaled from the **adjusted** 1 km radar rainfall to 500 (gray dashed lines), 250 (gray solid lines) and 125 (dark solid lines) m, as inputs 193

E.1 The comparison of mean raingauge observations (the brown bars or markers) and the coincidental radar estimates (the gray solid line: the original radar rainfall; the gray dashed line: the mean-field adjusted radar rainfall; the dark line: the Bayesian adjusted radar rainfall) for the 23/08/2010 event crossing the Cranbrook catchment (from upper to bottom): variations of rainfall rates, standard deviations and accumulations 232

E.2 The comparison of mean raingauge observations (the brown bars or markers) and the coincidental radar estimates (the gray solid line: the original radar rainfall; the gray dashed line: the mean-field adjusted radar rainfall; the dark line: the Bayesian adjusted radar rainfall) for the 26/05/2011 event crossing the Cranbrook catchment (from upper to bottom): variations of rainfall rates, standard deviations and accumulations 233

E.3 The comparison of mean raingauge observations (the brown bars or markers) and the coincidental radar estimates (the gray solid line: the original radar rainfall; the gray dashed line: the mean-field adjusted radar rainfall; the dark line: the Bayesian adjusted radar rainfall) for the 05-06/06/2011 event crossing the Cranbrook catchment (from upper to bottom): variations of rainfall rates, standard deviations and accumulations 234

E.4 The comparison of mean raingauge observations (the brown bars or markers) and the coincidental radar estimates (the gray solid line: the original radar rainfall; the gray dashed line: the mean-field adjusted radar rainfall; the dark line: the Bayesian adjusted radar rainfall) for the 03/01/2012 event crossing the Cranbrook catchment (from upper to bottom): variations of rainfall rates, standard deviations and accumulations 235

E.5 The comparison of the observed (the round markers) with the estimated flow depths at three selected pipes (1455.1: up-stream; 463.1: mid-stream; 307.1: down-stream) in the Cranbrook catchment for the event 23/08/2010. The estimated flow depths were obtained by using mean raingauge observations (the dark solid line) and the coincidental radar estimates (the gray dashed line: the original radar rainfall; the gray solid line: the mean-field adjusted radar rainfall; the dashed-dotted line: the Bayesian adjusted radar rainfall) as inputs 236
E.6 The comparison of the observed (the round markers) with the estimated flow depths at three selected pipes (1455.1: up-stream; 463.1: mid-stream; 307.1: down-stream) in the Cranbrook catchment for the event 26/05/2011. The estimated flow depths were obtained by using mean raingauge observations (the dark solid line) and the coincidental radar estimates (the gray dashed line: the original radar rainfall; the gray solid line: the mean-field adjusted radar rainfall; the dashed-dotted line: the Bayesian adjusted radar rainfall) as inputs 237
E.7 The comparison of the observed (the round markers) with the estimated flow depths at three selected pipes (1455.1: up-stream; 463.1: mid-stream; 307.1: down-stream) in the Cranbrook catchment for the event 05-06/06/2011. The estimated flow depths were obtained by using mean raingauge observations (the dark solid line) and the coincidental radar estimates (the gray dashed line: the original radar rainfall; the gray solid line: the mean-field adjusted radar rainfall; the dashed-dotted line: the Bayesian adjusted radar rainfall) as inputs 238
E.8 The comparison of the flow depths obtained by using mean raingauge observations (the dark solid line) and the coincidental radar estimates (the gray dashed line: the original radar rainfall; the gray solid line: the mean-field adjusted radar rainfall; the dashed-dotted line: the Bayesian adjusted radar rainfall) as inputs at three selected pipes (1455.1: up-stream; 463.1: mid-stream; 307.1: down-stream) in the Cranbrook catchment for the event 03/01/2012 239

List of Tables

2.1 Summary of geometric information of the data sets used in this thesis (LL: lower left; TR: top right; RG: raingauge; RD: radar/Nimrod) 48

2.2 Summary statistics of 5-min and daily rainfall data recorded in the Greenwich raingauge (CV: coefficient of variation; r_i : lag-i autocorrelation coefficient; dry period %: proportion of dry periods) 49

2.3 Summary information of the four selected storms over the Cranbrook catchment during the monitoring period from August 2010 to January 2012, including storm date, duration, storm total rainfall (mean of raingauge observations; in mm), maximum individual raingauge accumulation over the catchment, maximum catchment-averaged rainfall rate (in mmh^{-1}), maximum individually-observed rainfall rate (in mmh^{-1}), flow level peaks observed at the Valentine Park sewer (in meter). 52

3.1 Summary of raingauge and the coincidental radar accumulations and the sample bias for the selected events, where RG Total is the mean raingauge accumulations $\sum_{j=1}^{m} RG_{ij}/m$, Radar@RG Total is the co-located mean radar rainfall accumulation $\sum_{j=1}^{m} R_i(T_i, x_j)/m$ and Radar Total is the mean radar accumulation over the whole Cranbrook catchment 65

3.2 Summary statistics of the raingauge observations and the coincidental radar estimates for the 23/08/2010 event at the locations of local raingauges and over the Cranbrook Catchment (R^2: coefficient of determination; β: the regression coefficient; rmse: root mean squared error) 83

3.3 Summary statistics of the raingauge observations and the coincidental radar estimates for the 26/05/2011 event at the locations of local raingauges and over the Cranbrook Catchment (R^2: coefficient of determination; β: the regression coefficient; rmse: root mean squared error) 84

3.4 Summary statistics of the raingauge observations and the coincidental radar estimates for the 05-06/06/2011 event at the locations of local raingauges and over the Cranbrook Catchment (R^2: coefficient of determination; β: the regression coefficient; rmse: root mean squared error) 85
3.5 Summary statistics of the raingauge observations and the coincidental radar estimates for the 03/01/2012 event at the locations of local raingauges and over the Cranbrook Catchment (R^2: coefficient of determination; β: the regression coefficient; rmse: root mean squared error) 86
3.6 Summary of the observed (Obs) and estimated (RG, Radar 1km, Corrected Radar 1km and Bayesian Radar 1km) peak water levels at the Valentine Park sewer (pipe 463.1 in the hydraulic model) for each event and the relative differences with the observed data 86
3.7 Summary of the estimated (RG, Radar 1km, Corrected Radar 1km and Bayesian Radar 1km) peak water levels at three selected pipes (pipe 1455.1, 463.1 and 307.1, respectively located at the up-, mid- and down- streams of the Cranbrook catchment) for each event and the relative differences (%)with the peak water levels obtained by using raingauge data as inputs . 87
3.8 Summary statistics of the estimated (RG, Radar 1km, Corrected Radar 1km and Bayesian Radar 1km) water levels at the three selected pipes (pipe 1455.1, 463.1 and 307.1, respectively located at the up-, mid- and down-streams of the Cranbrook catchment) compared to the water levels obtained by using raingauge data as inputs 88

4.1 Summary statistics of the observed and estimated rainfall estimates for events A and B in the Greenwich gauge (STD: standard deviation in mm/hr; r_i : lag-i autocorrelation coefficient in the 5-min temporal resolution) . . . 141
4.2 Summary statistics of the flow rates resulting from observed and estimated rainfall time series for events A (STD: standard deviation in m^3/s; r_i : lag-i autocorrelation coefficient in the 5-min temporal resolution) 142
4.3 Summary statistics of the flows resulting from observed and estimated rainfall time series for events B (STD: standard deviation in m^3/s; r_i : lag-i autocorrelation coefficient in the 5-min temporal resolution) 143

5.1 Summary statistics of uncertainty ranges U_s resulting from rainfall estimates, downscaled from 1-km to 500/250/125 m, at three selected pipes (pipe 1455.1, 463.1 and 307.1, respectively located at the up-, mid- and down- streams of the Cranbrook catchment) for four selected events 164
5.2 Summary statistics of uncertainty ranges U_s resulting from adjusted rainfall estimates, downscaled from 1-km to 500/250/125 m, at three selected pipes (pipe 1455.1, 463.1 and 307.1, respectively located at the up-, mid- and down- streams of the Cranbrook catchment) for four selected events 175
5.3 Summary statistics of uncertainty reduction resulting from the radar rainfall adjustment process at three selected pipes (pipe 1455.1, 463.1 and 307.1, respectively located at the up-, mid- and down- streams of the Cranbrook catchment) for four selected events 175
5.4 Summary of the proportion of the contributions from downscaling and adjustment processes to uncertainty in flood modelling, i.e., $U_s/U_{adjusted}$, at three selected pipes (pipe 1455.1, 463.1 and 307.1, respectively located at the up-, mid- and down- streams of the Cranbrook catchment) for four selected events 176

Chapter 1

Introduction

In this chapter, the current development of urban pluvial (surface water) modelling/forecasting in the UK is firstly reviewed to provide the background and further to define the aim of this research. Then, a brief review of the state-of-the-art rainfall modelling/forecasting and an example of its applications to urban pluvial flood forecasting are given. Based upon this, the targeted problems and the objectives of this work are presented. Finally, the structure of this dissertation is summarised to provide a clear overview of this research.

1.1 Background

In recent years, many cities in the United Kingdom and other countries suffered from serious damages caused by floods; in the summer of 2007, for example, over 55,000 homes and businesses in the UK were flooded due to the fact that urban drains, river channels, and flood defences were unable to cope with the extreme quantities of water resulting from pluvial, fluvial and coastal causes (EA, 2007). According to the post-flood study of 2007 summer floods conducted by the Environment Agency, around two-thirds of flooded properties were affected by pluvial (also known as surface water) floods, which are mainly induced by intense rainfall. Compared to coastal and fluvial flooding (which are induced respectively by the surge of sea and river water), pluvial flooding was given much less attention in the past and the associated forecasting and warning systems did not exist in the UK[1] (Parker et al., 2011). Some follow-up studies further emphasised the importance of appropriately tackling pluvial floods as the associated statistics show that over 4 million

[1]There were Environment Agency Flood Warnings, which however cover coastal and fluvial floods at risky areas only (FFC, 2010).

properties in the UK are currently at risk from this type of flooding (EA, 2009) and approximately 2 million people in the urban areas are at an annual pluvial risk of 0.5 % or greater (i.e. 200-year return period; see Houston et al. (2011) and Pitt (2008)).

Pluvial (Surface water) floods caused serious disasters and massive losses particularly in urban areas because these areas are in general highly-populated and filled with businesses; in addition, these areas are usually small and a large percentage of surface is covered by impervious pavement and therefore the concentration time is short and the available response time to flooding is much less. This type of flooding usually happens quickly and locally and therefore advanced and reliable warning is difficult. To tackle this type of flooding, the Pitt Review called for Integrated Urban Flood Management, which addressed both technical and socio-economical issues (Pitt, 2008).

To respond to the recommendations of the Pitt Review, in its socio-economic aspects, for example, a large-scale emergency flood exercise across England and Wales, named Exercise Watermark, has been launched. This activity was organised by Defra (Department for Environment, Food and Rural Affairs) and Welsh Assembly Government in synergy with the Environment Agency; the aim of it is to bring together government bodies, big business, and local communities to trial responses to a range of scenarios which could occur during a flood emergency. For the technical issues, there are mainly two aspects that have been addressed in order to obtain accurate pluvial flood forecasts over urban areas. The first lies in the development of reliable and efficient hydraulic models so that they are able to effectively and timely reflect hydraulic behaviours of floods in urban areas in real time. The second lies in the generation of high-resolution rainfall forecasts, which will be used as inputs for the corresponding hydraulic modelling. Since the hydraulic modelling aspect is not the focus of this work, further discussion is not detailed here; for the readers who are interested in this aspect, a brief review is carried out and further references are suggested in Section 2.2. A further discussion of the rainfall forecasting aspects is as follows.

It has been widely recognised that the uncertainty of rainfall forecasts propagates the overall hydrological processes and dominates the accuracy of urban pluvial flood modelling (Singh, 1997; Collier, 2009; Golding, 2009b). Rainfall forecasting techniques therefore play key role in obtaining reliable pluvial flood forecasts, and many related works have been carried out to provide better rainfall forecasts. Among these works, one of the most important achievements is the "Extreme Rainfall Alerts (ERAs)" service. This service was jointly initiated by the Environment Agency and the Met Office in July 2008, focusing on pluvial (surface water) flood warnings, and it is currently operated by the Flood Forecasting

Centre (FFC). The idea is to indicate the probability of extreme rainfall that could lead to pluvial flooding in specific urban areas (Golding, 2009a; FFC, 2010)[2]. Based upon the weather forecasts conducted by the MetUM[3], once there is more than a 20 % chance of extreme rainfall, the ERAs will be launched. The reliability of this service therefore largely relies on the predictability of the MetUM.

The MetUM is a type of Numerical Weather Prediction (NWP) models, which are in general implemented by solving a set of equations of fluid dynamics and thermodynamics to estimate the future state of the atmosphere. The modelling scales mainly range from synoptic scale ($\geq$ 1000 km grid) to mesoscale ($\sim$ 5 km to several hundred km grid). The major advantage of NWP models lies in their enabling longer lead-time forecasting (up to 3 days, depending on the required spatial and temporal resolutions), and with the increasing computational power, the achievable resolution is now in the kilometre scale. For example, the operational MetUM currently runs on 1.5/4 km grids[4] over the UK area and provides weather forecasts with up to 36 hr lead time. However, due to the chaotic (non-linear) nature of atmospheric processes, the NWP models can only produce the general character and information of storms in specific areas. This means that NWP models can forecast the possibility of having heavy rainfall in the coming afternoon in London; however they cannot accurately predict the microphysics (such as the detailed location, timing and evolution) of every storm. In addition, with increasing simulation time (i.e. forecasting lead time), the reliability of NWP models decreases. The impact of this decrease will be particularly magnified at small spatial and temporal scales. The outputs of NWP models are therefore very fluctuant/noisy over urban scales, which substantially increases the difficulty in providing satisfactorily accurate rainfall forecasts for urban hydrological applications. Rico-Ramirez et al. (2009), for example, applied high-resolution NWP precipitation ensemble forecasts (the smallest spatial resolution is the $\approx$ 1km^2 grid) to flood modelling over a small urban area in Yorkshire, UK; the predicted precipitation, however, is of insufficient accuracy compared to that obtained from ground raingauge stations. This result suggested that it is inappropriate to use merely the NWP forecasts as input for quantitative rainfall and flood prediction over urban areas. However, they can be useful in indicating that "something

[2]This service of pluvial flood warnings is in a country-level, which provides merely the possibility that serious pluvial floods could happen or not rather than high-resolution flood forecast details for small urban areas. A system that can predict flood details does not exist in the UK yet.

[3] The MetUK stands for Unified Model, the Numerical Weather Prediction model developed by the Met Office.

[4]The MetUM 1.5 km, also termed UKV model, covers the whole UK area. This model was developed to gradually replace the original MetUM 4 km (also termed UK 4km model) in order to have a better description of small-scale weather systems, such as thunderstorm, and winter snow (Lean et al., 2011).

serious" might be forthcoming.

In order to obtain reliable rainfall forecasts that are more suitable for urban hydrological and hydraulic uses, alternative methods that are able to predict more accurate rainfall details should be employed. There is however an inevitable trade-off between forecasting resolution and lead time. The conventional short-term high-resolution rainfall forecasting techniques that simply rely on the extrapolation of current rainfall fields provide up to 30-45 min lead time forecasts (Sokol and Pešice, 2009). This lead time is however insufficient for the corresponding urban hydraulic modelling to accurately estimate the distribution of surface floods. It is therefore a challenging issue to retain the sufficient lead time for high-resolution rainfall forecasting.

The operational Met Office STEPS model[5] undertakes 1-2 km and 5/15 min rainfall nowcasting with 3/6 hr lead time by merging high-resolution (4 km) MetUM forecasts with extrapolated radar rainfall estimates in real time (Pierce, 2009). The concept behind the STEPS indicates the approach to high-resolution rainfall forecasting with the sufficient lead time, that is, the integration of rainfall forecasting/modelling over multiple spatial/temporal scales (shown as Figure 1.1). However, this achievement (up to 1 km/5 min/3hr lead time nowcasting) may not always satisfy the requirements for urban-scale pluvial flood modelling, since the required spatial- and temporal-resolutions for rainfall estimates/forecasts are highly correlated to the concentration time (or the size) of the catchment (Berne et al., 2004) and in some cases of very small areas the suggested resolutions could be 1-5 min and 100-500 m (Fabry et al., 1994). Therefore, for urban areas, very likely the operational STEPS system is unable to provide rainfall nowcasts with sufficient accuracy and resolution.

This research therefore focuses on improving the suitability of the operational rainfall estimates, aiming to generate higher-resolution and reliable rainfall estimates that are more suitable for urban flood modelling/forecasting uses. In order to have a further understanding of the operational STEPS system and its deficiency for urban flood forecasting, a study was undertaken during this PhD programme by applying high-resolution STEPS nowcasts to an urban catchment in London (Wang et al., 2011). A summary of this work will be given in the following section to report the associated findings and to help identify the targeted research problems of this work.

[5]The STEPS stands for Short Term Ensemble Prediction System, a very short-range rainfall nowcasting technique jointly developed by the Met Office and the Australian Bureau of Meteorology.

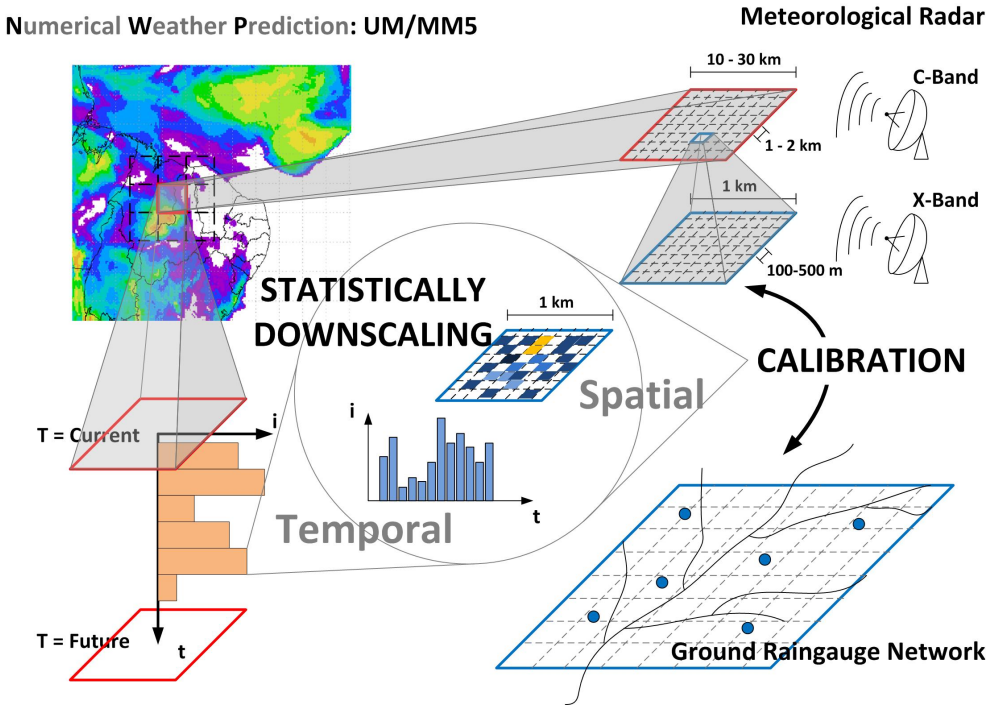


Figure 1.1: The conceptual scheme of the idea that integrates rainfall/weather models over multiple spatial and temporal scales

1.2 Research problems

A study that evaluated the applicability of different high-resolution (1/2 km and 5/10/15 min) STEPS nowcasts to urban flood forecasting over the Cranbrook catchment[6] was conducted by Wang et al. (2011). This work is summarised in the following; for the complete paper, the reader is referred to Appendix A.

In this application, the deterministic nowcasting system of STEPS was employed to produce short-term rainfall forecasts (Bowler et al., 2006). This system in STEPS was developed based upon the spectral decomposition proposed by (Seed, 2003) with the incorporation of the optical flow equation proposed by Bowler et al. (2004). For details of the STEPS, the readers are referred to Bowler et al. (2006) and Pierce (2009). The nowcasting model has been set up to run at 1/2 km spatial resolutions and 5/10/15 min temporal resolutions. The domain size was fixed to 500 km X 500 km covering the window with lower left coordinates of 200 km (easting)and -100 km (northing), and top right coordinates of

[6]The Cranbrook catchment is also the study site through this PhD programme. A detailed introduction of it and the hydraulic models used to simulate its hydraulic behaviours are given in Chapter 2.

700 km (easting) and 400 km (northing). The nowcasting model was set up to produce 3 hr lead-time forecasts initialised every 10 min for all the events. In order to evaluate the reliability of STEPS nowcasts, the operational 1-km and 5-min Nimrod radar data and their corresponding hydraulic outputs were used here as references.

Three rainfall events crossing the Cranbrook catchment in the period of August 2010 - February 2011 were studied. Figure 1.2 shows the skill (in terms of correlation between STEPS nowcasts and the associated Nimrod estimates) of all rainfall forecasts for the 23/08/2010 event against the lead time at different spatial and temporal scales over Greater London. The results indicate that the performance of the precipitation forecast depends on the spatial scale, with lower skill obtained at small scales but higher skill at larger scales. This suggests that there is higher uncertainty in small-scale rainfall nowcasting. However, the associated results of hydraulic analyses (shown in Figure 1.3) depicts that the flood forecasts obtained with 1 km resolution rainfall forecast are in general better than those obtained with 2 km resolution rainfall forecast for lead times shorter than 120 min. This suggests that although 2-km nowcasts have higher correlation with radar data over a larger area (i.e. 100 km X 100 km Greater London area), it does not mean that 2-km nowcasting will definitely perform better than 1-km nowcasting over a small and local area (i.e. 5 km X 6 km Cranbrook catchment) because of the spatial variability of rainfall fields. In this case the 1-km nowcasts, which exhibit higher spatial variability, are better inputs for the hydraulic model with lead times up to 120 minutes. In terms of temporal resolution, the results show that for the lead time up to 90 minutes the rainfall forecast at 5 min resolution generates the best flood forecast. After 90 minutes lead time, the performance of the 5 min resolution rainfall forecast significantly decreases and better flood forecasts are achieved with 10 min and 15 min rainfall forecast. These results indicate the complex behaviour of rainfall over various spatial and temporal scales and different size of areas and suggest the necessity to conduct full-scale flood modelling over a specific urban area.

In addition to Wang et al. (2011), an application of STEPS nowcasts to urban flood prediction was carried out by Liguori et al. (2011). The probabilistic radar rainfall nowcasts in synergy with the NWP forecasts were combined by STEPS to provide 1-km and 15-min rainfall forecasts with 6 h lead time. Results showed that as compared to the radar (Nimrod) rainfall measurements and the resulting hydraulic outputs, the operational STEPS system provides quite reliable results with up to 120 min lead time; however, as compared to the in-situ rainfall and flow observations, significant underestimations and faulty timing were commonly seen. One of the major reasons lies in the deficient accuracy or suitability

of radar inputs for urban applications. Therefore, the consequent STEPS nowcasts may not be able to provide quantitatively accurate results for urban flood forecasting purposes.

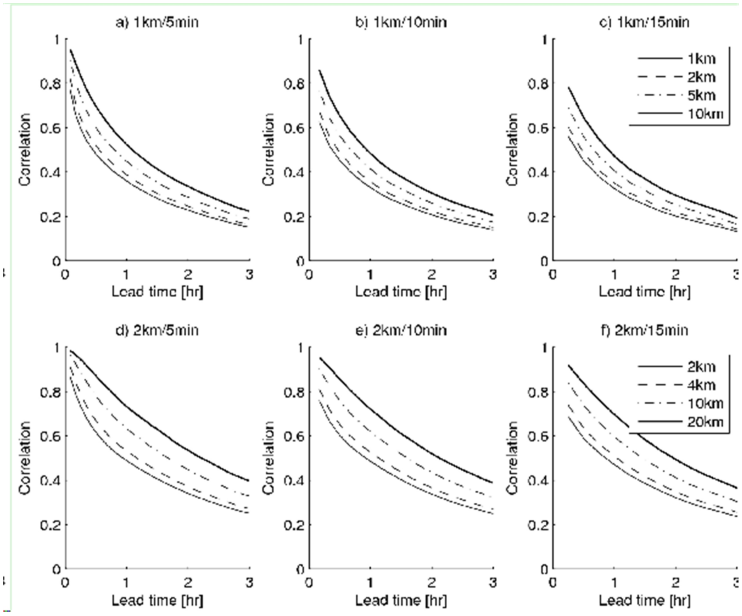


Figure 1.2: Performance of the radar-based forecasts versus lead time at different spatial and temporal scales for the 23/08/2010 event [source: Wang et al. (2011)]

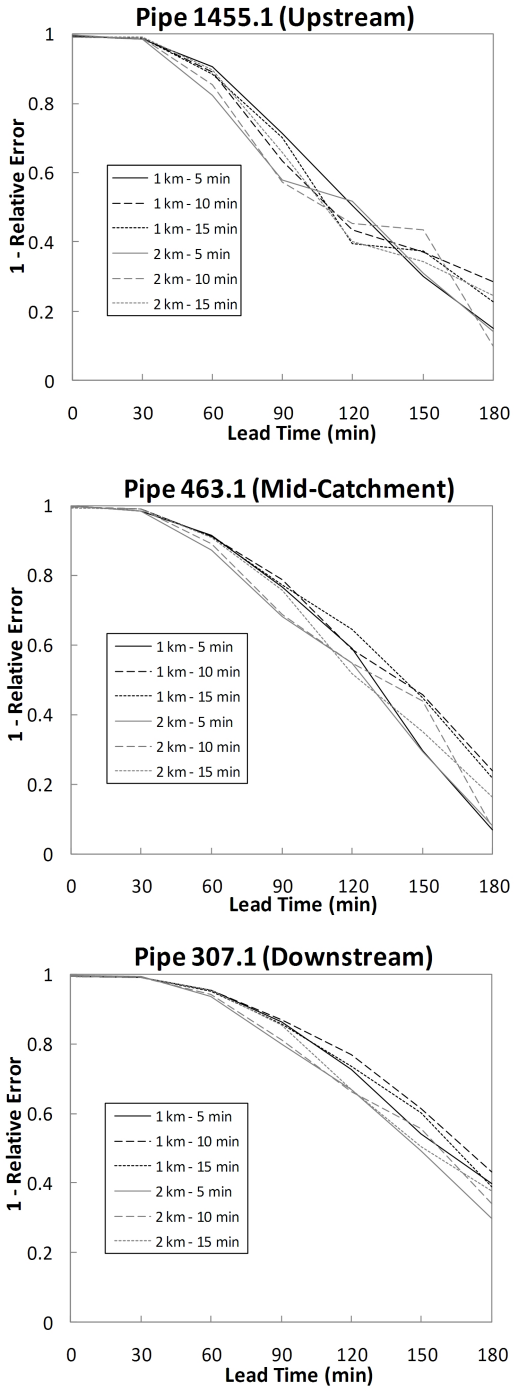


Figure 1.3: Performance of hydraulic outputs resulting from the STEPS rainfall nowcasts at different spatial and temporal scales for 23/08/2010 event [source: Wang et al. (2011)]

1.3 Research Objectives and Methodology

Based upon the findings mentioned above, the main problems of the operational short-term rainfall forecasting technique can be identified as insufficient accuracy (reliability) and spatio-temporal resolution. The main objective of this work is therefore to enhance the suitability (in terms of accuracy and resolution) of the operational rainfall estimates for urban flood forecasting/modelling uses using advanced statistical techniques. This leads to the detailed objectives of this research:

1. Develop a new rainfall processing procedure that improves the accuracy and resolution of the operational rainfall estimates.

2. Evaluate the impact of this new procedure on urban pluvial flood modelling/forecasting.

3. Analyse the propagation of uncertainty caused by the proposed rainfall processing procedure through urban pluvial flood modelling.

In order to fulfill these objectives, the methodology of this research is proposed as follows:

1. Accuracy improvement: Review and test existing gauge-based radar rainfall adjustment techniques and choose the most suitable technique for urban hydrological uses.

2. Resolution improvement: Develop and test new rainfall downscaling techniques, based upon the scale-invariant properties of rainfall, that enable the generation of street-scale (smaller than 1 km gridlength in space) and sub-hourly rainfall estimates.

3. Applicability evaluation: Apply the processed rainfall estimates, respectively based upon the adjustment and downscaling techniques, to the case study (i.e. a small urban catchment in London), to evaluate their individual applicability (in terms of accuracy and resolution) to urban hydrological simulation.

4. Combined application: Combine adjustment and downscaling techniques to implement a new rainfall processing procedure particularly for urban hydrology.

5. Uncertainty analysis: Analyse the associated impact of these techniques on the subsequent hydraulic outputs obtained by this combination.

6. Recommendation: Provide comments on the proposed research and suggest future work.

1.4 Thesis outline

In this chapter, the background of and the motivation for this research have been given, and the associated research problems and objectives have been identified through investigating the current development of urban pluvial flood modelling/forecasting in the UK. The proposed methodology has also been outlined. Based upon this methodology, the following thesis structure is designed to implement each proposed item.

In Chapter 2, the study catchment used throughout this PhD programme is described, including its environmental setting and hydraulic models. In addition, the data sets and case study used in this work to help testing and developing methodologies are illustrated in this Chapter. This chapter provides the catchment and dataset information that are used in the following chapters.

Chapters 3 and 4 are the main contributions of this work. The topic of improving the reliability (in terms of accuracy and resolution) of the operational rainfall estimates for urban flood forecasting is studied. Because, in the literature, the techniques that have been developed to deal with the subjects of accuracy and resolution are very different, the review of their current developments is therefore conducted individually in each chapter rather than in one chapter.

Chapter 3 focuses on the enhancement of the accuracy of radar rainfall. This includes the introduction of two most widely-used rainfall sensors (i.e. raingauge and weather radar) in urban areas and a brief review of their applications to urban hydrology. Then, a detailed review of gauge-based radar rainfall adjustment techniques, which are keys to merge the rainfall information from multiple sensors to obtain more accurate and useful rainfall estimates. Two adjustment techniques, based upon different adjustment paradigms, are implemented to understand their impacts on urban flood modelling and therefore choose the most suitable technique.

Chapter 4 develops new downscaling techniques based upon the theory of Multifractals and multiplicative cascade models. This involves a brief of downscaling techniques and a detailed review of the theory of Multifractals and its link with the cascade models. Based upon these reviews, two new downscaling models are developed. One of them can be used for both spatial and temporal downscaling, whilst the other is only for temporal downscaling. These new developments are further applied to real raingauge and radar rainfall data over the London area to assess their potential and their impact on urban hydrological and hydraulic modelling.

In Chapter 5, the proposed spatial downscaling model is further used to generate street-

scale rainfall estimates, which are then applied to the case study to understand the impact of high-resolution rainfall inputs on urban flood modelling. In addition, a combination of adjustment and downscaling techniques is implemented to further assess the associated benefit and uncertainty.

Finally, a summary and conclusions of this work are given in Chapter 6 to provide an overview of the developments. Some possible future directions based upon this research will be also suggested.

Chapter 2

Experimental Site And Data Set

In this chapter, a description of the experimental site used to carry out the full-scale testing of the proposed work is firstly given. The construction of the hydraulic models of the experimental site is then detailed. The data sets covering the study region are then listed and explained, including the local raingauge network and radar-derived rainfall measurements and forecasts. In addition, some other archived data sets, which were not directly related to the study area but were used to preliminarily evaluate the proposed techniques, are also listed here. Finally, the use of these data sets, whether for the intermediate assessments of the developed techniques or for the full-scale testing, is summarised.

2.1 Cranbrook catchment

2.1.1 Environmental setting

The Cranbrook catchment is located within the London Borough of Redbridge (situated on the northeast of the Greater London) and is run through by the River Roding (Figure 2.1). The River Roding starts at Molehill Green surrounded by the Stansted Airport at West and Great Dunmow at East. The river runs through the Essex districts of Epping and Uttlesford and the London Boroughs of Redbridge, Newham and Barking, before discharging into the Thames at Barking Creek (Environment Agency, 2006). The River Roding has several tributaries entering it, and two of them are the Cran Brook and Seven Kings.

According to EA (2006), the River Roding has a rapid response to rainfall, which is typical of densely-urbanised catchments overlying London clay. Flood events have been

recorded in the Roding catchment since 1926, with the most recent event being in October 2000 and February 2009, when several properties were flooded.

The drainage area of this catchment is approximately 910 hectares ($\sim 9km^2$). The main watercourse is approximately 5.75 km long, of which 5.69 km is culverted. The catchment is predominantly urban with several parks, playing fields and a golf course. This area has a history of local flooding and the major types of flooding are pluvial and fluvial flooding. Although the study area is subject to these two types of flooding, more attention has been given to fluvial flooding in the past and the associated models, forecasting and warning systems have been well established. In contrast, little attention has been given to pluvial flooding in this area. For this reason, the focus of this case study was on pluvial flood modelling and flooding.

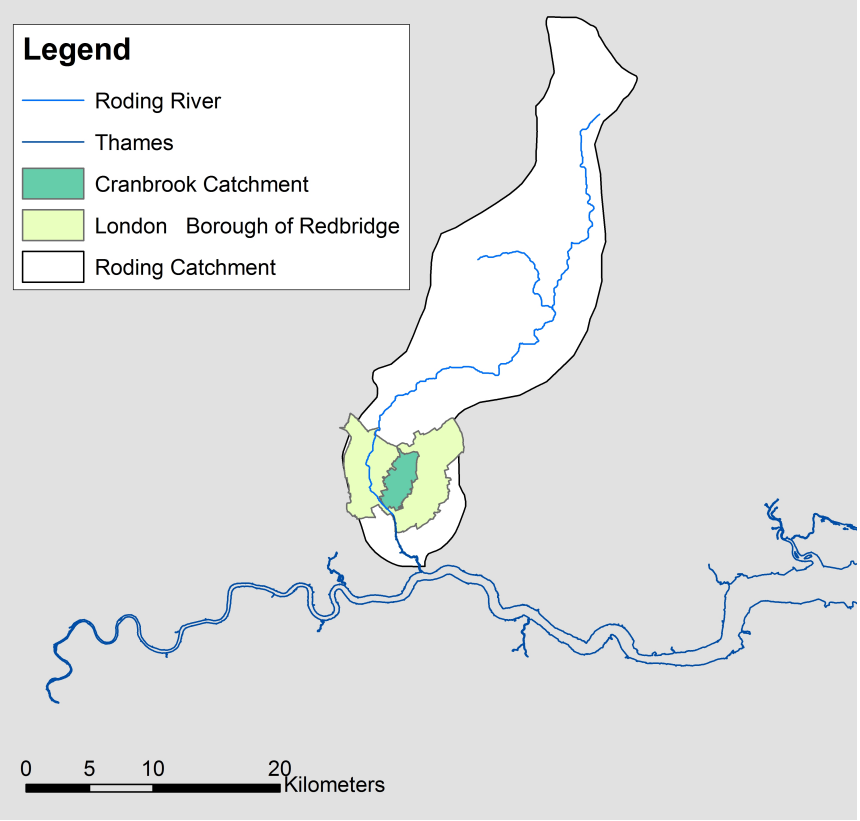


Figure 2.1: Location of the Cranbrook catchment in relation to the River Roding catchment

2.1.2 Monitoring network

In-situ rain gauge and level gauge sites

In order to monitor the Cranbrook catchment and gather real time data that can be used for calibration, validation and real time operation, a real-time accessible monitoring network has been installed and operated in the Cranbrook catchment since April 2010 (see photos in Figure 2.2). The sensors that have been installed are as follows:

- Three tipping bucket rain gauges, with 1-2 min data sampling frequency. These rain gauges are installed in the roof tops of 3 high schools of Redbridge (Beal High School, Chadwell Heath Foundation School and Ursuline High School). Their locations in relation to the Cranbrook catchment are shown as the round markers in Figure 2.2;

- Two sensors for water depth measurement in sewers with 1-15 min data sampling frequency[1]; One of the sensors is installed in a sewer located in Cranbrook road and the other one in a sewer inside Valentines Park (the square markers in Figure 2.2);

- One sensor for water depth measurement in open channel (downstream boundary condition) with sampling frequency 1-15 min; This sensor is installed in the open channel that flows through Valentines Park (the triangular marker in Figure 2.2);

- One pressure sensor for Roding River level monitoring with 5-15 min sampling frequency (the cross marker in Figure 2.2).

All of the sensors are equipped with data acquisition and real-time access wireless communication units, which allow for measurements to be accessed in real-time.

Weather radar sites

The Cranbrook catchment is within the coverage of two weather radars operated by the UK Met Office: the Chenies radar (single-polarisation) and the Thurnham radar (dual-polarisation). The prior is located at Flauden near Amersham, UK; The latter is near Maidstone, Kent in England; Their locations in relation to the Cranbrook catchment and the River Roding are shown in Figure 2.3. Both of them are C-band radars, operating

[1]The water depth measurements are dynamically sampled. When the water depths are lower than a given level, they are recorded every 15 min; when higher than the level, they are sampled in 1 min time interval.

on a wavelength of 4-8 cm and a frequency of 4-8 GHz (for details of weather radars, the readers are referred to Collier (1996)).

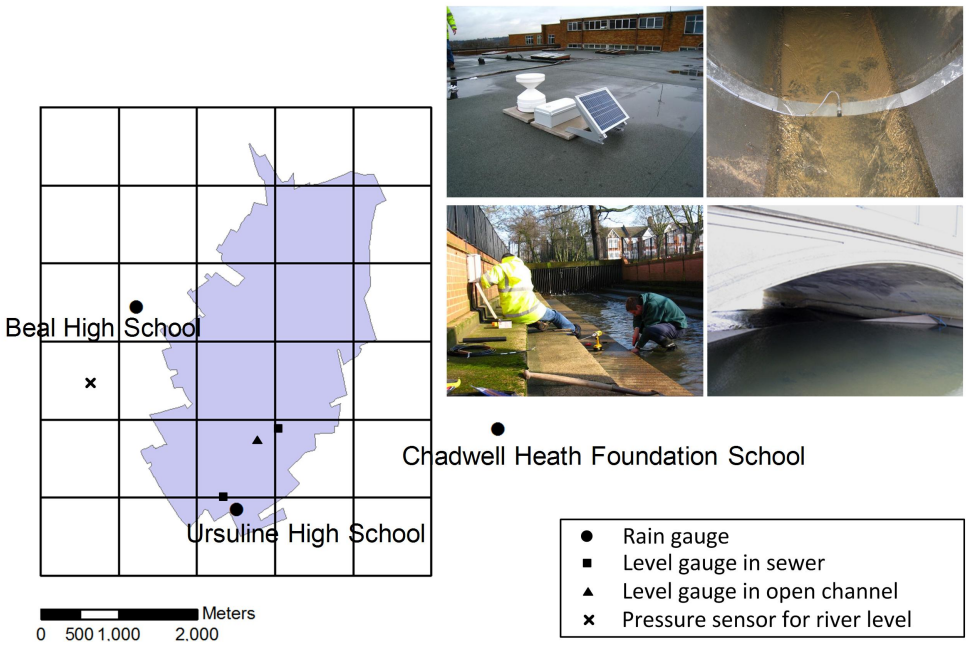


Figure 2.2: Geographical deployment of in-situ raingauge sites and the photos of the monitoring network installed in the Cranbrook catchment [source: Ochoa et al. (2011b)]

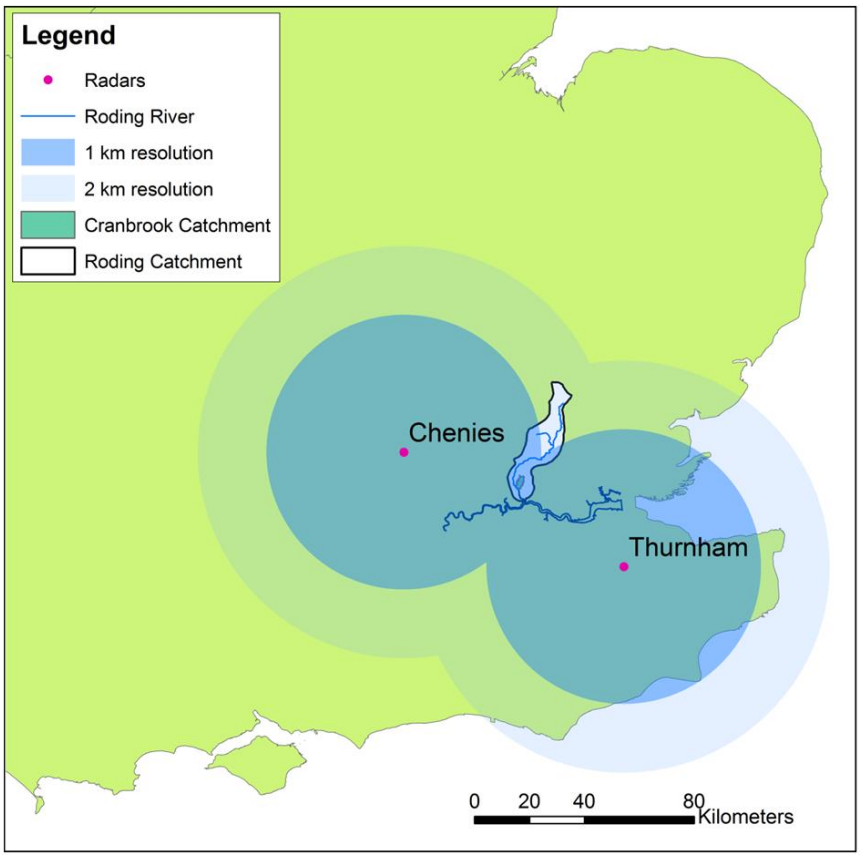


Figure 2.3: Two meteorological radars (Chenies and Thurnham) which are operated by the UK Met Office and coverage of the Cranbrook catchment [source: Ochoa et al. (2011b)]

2.2 Hydraulic models of the Cranbrook catchment

This work targets modelling/forecasting pluvial flooding, which is caused by intense rainfall whose volume and/or flows exceed the capacity of the urban drainage system. This type of flooding is typically localised and happens in a very short time period; it therefore requires detailed yet efficient modelling (Ochoa et al., 2011b).

In order to realistically represent the details of the local topography and the interactions between the overland and sewer networks, as well as the boundary conditions that determine the performance of the system, the dual-drainage concept is employed here (Djordjević et al., 2005). The dual-drainage models are physically-based models; they simulate water movement over the surface and in the sewers by solving the appropriate approximation of mass and momentum conservation equations, making the simulation of urban hydraulic features more realistic (Allitt et al., 2009). The traditional dual-drainage

models are however very computational demanding in order to estimate runoff details on the surface, which is usually composed of numerous 2-dimensional (2D) meshes; this is infeasible for real-time flood forecasting uses. Advanced techniques for analysing geographic information were therefore developed to accelerate the state-of-the-art dual-drainage modelling using improved 1-dimensional (1D) models for overland network, and at the same time to retain the necessary accuracy (Maksimović et al., 2009; Simões et al., 2010; Leitão et al., 2010).

In this section, the creation of the improved overland and sewer models and their interaction are described in order to account for the dual-drainage modelling. The resulting hydraulic model of the Cranbrook catchment, which was developed based upon the dual drainage concept in synergy with the Automatic Overland Flow Delineation (AOFD) technique (will be explained in Section 2.2.1), is then presented. This model was used to carry out the urban drainage modelling part of the case study.

2.2.1 Overland network modelling

In the last few years different approaches have been implemented to represent the flow on the urban surface (e.g. virtual reservoir, lost volume, rapid flood spreading models); however, none of these can realistically represent the hydraulic behaviour of the flow on the surface (Butler and Davies, 2011).

More recently, two ways of realistically modelling the surface or overland network of an urban catchment have been developed:

- As a 2-dimensional (2D) surface, using a mesh of triangular elements, or
- As a 1-dimensional (1D) system made up of ponds (modelled as storage nodes) and pathways (modelled as conduits with specific geometry computed from the Digital Elevation Model, or DEM).

Both models can reliably represent the overland network and the flow on it, but each of them has advantages and disadvantages. The 2D models provide a more detailed representation of the overland flow and allow for a better visualisation of the results; however, they tend to "spread" the flow over larger areas rather than conducting them following preferential pathways; they are therefore computationally demanding and their running time makes them unsuitable for real-time forecasting of urban pluvial flooding (given that short computational time is essential for this purpose). In contrast, the 1D models are

significantly faster and therefore suitable for real-time forecasting; however, they provide less detail and poorer visualisation of results, although they can still represent the overland flow reliably. It is therefore more feasible to use 2D models for detailed and off-line purposes, such as hydraulic infrastructure design and flood map generation); whilst to use 1D models for real-time uses, such as real-time flood forecasting and real-time control. For a more detailed comparison of 1D and 2D models for overland network the readers are referred to Allitt et al. (2009) and the Chapter 2 of Ochoa et al. (2011a).

Concerning the aim of this research (i.e., urban pluvial flood forecasting), the 1D overland model was employed to characterise the surface of the Cranbrook catchment. A GIS (Geographic Information Systems) tool, named Automatic Overland Flow Delineation (AOFD), was used herein to automatically analyse and generate 1D models of the overland network based on an accurate DEM (Digital Elevation Model) of the study area. Despite there being several commercial and Open Source software packages (e.g. InfoWorks CS, MOUSE, SOBEK, SWMM) which are capable of simulating the 1D flow over the surface; their methodology to estimate the overland flow in general assumes manual (hence subjective) definition of the surface flow paths, which is laborious and might lead to unreliable representations of surface flow processes (Maksimović et al., 2009).

In this work a detailed LiDAR (Light Detection And Ranging) DEM of the Cranbrook catchment with $1m$ horizontal resolution and approximately $\pm 0.15m$ accuracy for vertical elevation was used. The 1D models generated with the AOFD tool can realistically represent the overland flow, taking into account processes such as pond forming, flow through preferential pathways and surface drainage capacity. Furthermore, the models generated with the AOFD tool also take into account the interactions with the sewer system, which take place at the manholes, inlets and gullies. The output of the AOFD tools is a set of shapefiles which constitute the 1D model of the overland network. These files can be imported into InfoWorks CS model or several other hydraulic simulation software packages and can be easily coupled with 1D models of the sewer system (such as SWMM), thus allowing for the creation of 1D-1D dual drainage models. For further details of the AOFD tool, the readers are referred to Ochoa et al. (2011a) (Chapter 3), Maksimović et al. (2009) and Simões et al. (2010).

2.2.2 Sewer network modelling

All sewer network models are made up of nodes and conduits. Given that in these elements the flow direction is very well defined and the section within each conduit is constant, 1D

models can be used to represent its behaviour (in fact, sewer networks are always modelled as 1D models). An InfoWorks CS model of the sewer network of the Cranbrook catchment was obtained from Thames Water (the water company of the study area).

However, the original model obtained from Thames Water was missing some details, and some illogical connections of pipes were detected. These errors were firstly corrected manually through cross comparisons with the information provided by various local authorities of the London Borough of Redbridge. Then, the Engineering Validation tool in the InfoWorks CS model was used to a detailed check on the network data to ensure their consistency with engineering expectations; such as the logic of pipe connections, the heights of manholes (which shall not be higher than the ground surface) and the interactions with surface models. In addition, four events recorded during the monitoring period were used to verify the reliability of models (along with level data obtained from level gauges installed throughout the sewer system), and in general (as compared to the observations from level gauges) the errors of the simulated level estimates (by using raingauge records as input) are within 10%. A map of the corrected sewer network of Cranbrook is shown in Figure 2.5.

It is worth mentioning here that the validation steps conducted in this work were very simple and the associated uncertainty sources that could be diminished were limited. Because the focus of this work is mainly on rainfall data processing, a in-depth uncertainty analysis of the hydraulic models was not conducted (McIntyre et al., 2002) but is suggested to be carried out in the near future in order to have a more accurate assessment of the impact of proposed rainfall processing techniques on urban pluvial flood modelling.

2.2.3 Dual-drainage modelling

The interaction between these two systems is the key to properly coupling them in 1D-1D models. It takes place at the manholes, which are assigned a "Stored" flood type. In this case the flood water on the catchment surface is retained in the storage volume defined by the flood levels and areas (specified for each manhole). When the flood level is reached, the water flows from the manholes to the surface pathways (towards another manhole or a surface pond; thus originating surface flow). The flood water returns to the drainage system as the levels drop. The coupled overland and the sewer network dual-drainage models (in InfoWorks CS) of the Cranbrook catchment are shown as Figure 2.6.

The advantage of having a 1D model of the overland network (instead of a 2D model) is its short computational time, which makes it suitable for real time forecasting of plu-

vial urban flooding. Analyses conducted by Leitão et al. (2010) and Simões et al. (2010) justify the claim that a 1D model produces reasonable results as compared to 2D models, while requiring significantly less computational time. For more comparisons and new developments in dual-drainage modelling the readers are referred to Simões et al. (2011a).

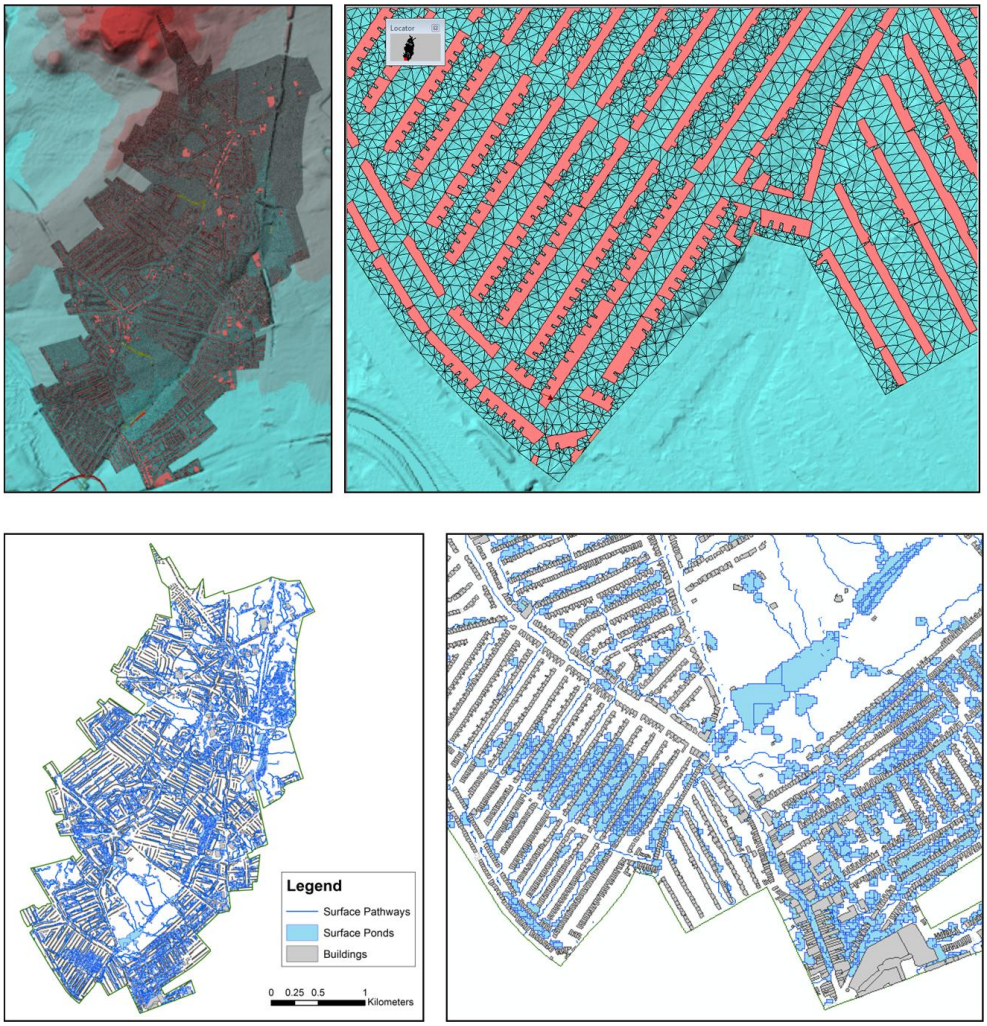


Figure 2.4: 2D (upper) and 1D (lower) model of the overland network of the Cranbrook catchment: entire catchment (left) and details (right) [source: Ochoa et al. (2011b)]

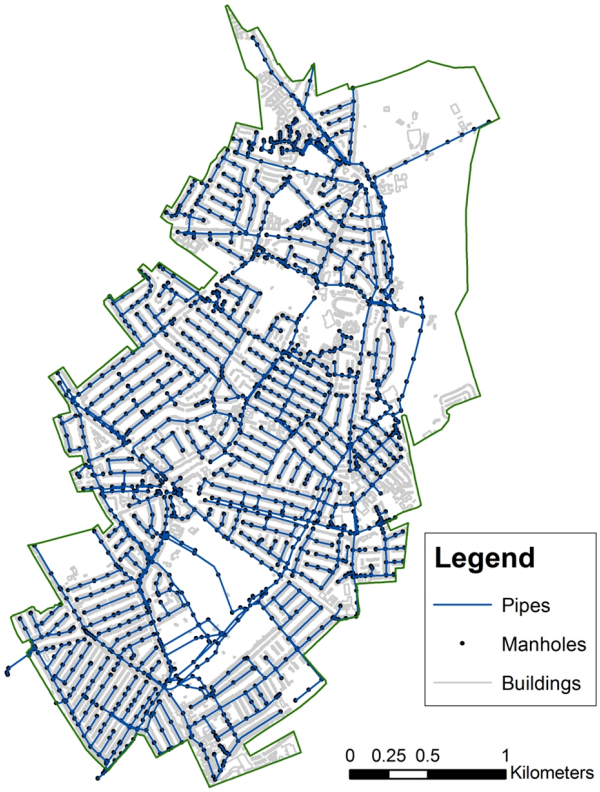


Figure 2.5: Sewer network of the Cranbrook catchment [source: Ochoa et al. (2011b)]

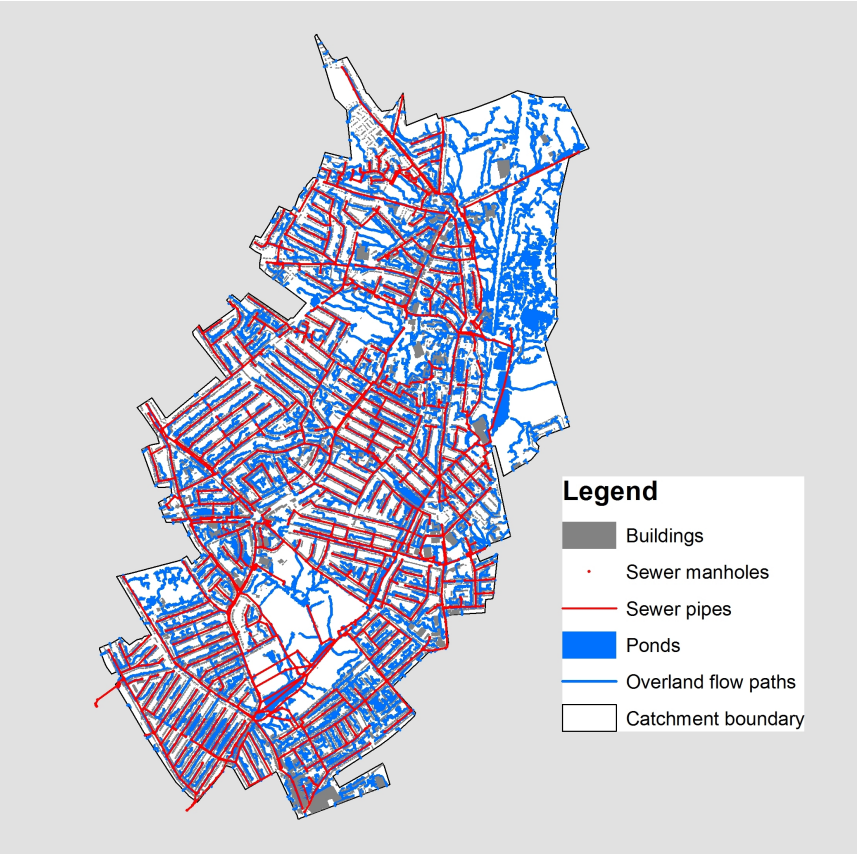


Figure 2.6: The 1D-1D dual drainage network of the Cranbrook catchment [source: Wang et al. (2011)]

2.3 Rainfall data sets

This section describes the rainfall data sets used in this work. The associated geographic information of these data sets and the study areas mentioned in the context are summarised in Table 2.1.

2.3.1 In-Situ Raingauge data

High-resolution raingauge data from the monitoring system installed in the Cranbrook catchment have been collected since April 2010 (please see Section 2.1.2). The conversion between the number of tips and rainfall volume was conducted based upon the default calibration result provided by the raingauge design company. The quality of raingauge data was maintained based upon a long-term comparison with the coincidental radar rainfall

estimates (i.e. the Nimrod composite rainfall product, which is consistently quality controlled by the UK Met Office. See Section 2.3.2 for the details of Nimrod rainfall product) and the cross comparison of the data between three in-situ raingauges. A high correlation was in general observed between in-situ raingauge and radar data (the correlation coefficient is approximately 0.7 on average, except for the 03/01/2012 raingauge records at the Chadwell Heath Foundation School). In addition, the original rainfall data are of 1-2 min temporal resolution; in order to increase the reliability, they have been post-processed (i.e. aggregated) into 5-min rainfall time series data in this work.

During the monitoring period, there are totally 8 events recorded; half of them were used to verify the hydraulic models (as mentioned in Section 2.2.2), and the rest were used to test the proposed downscaling methods, to be combined with the coincidental radar observations, and to carry out full-scale testing of the case study.

It is worth mentioning that, to evaluate the reliability of raingauge data, a more complete uncertainty analysis of raingauge observations should be carried out in the future; for example, re-calibration of the in-situ tipping bucket raingauges and the analyses of the potential uncertainty sources due to the siting and the exposure of raingauges (such as wind-related undercatch, which is caused by the location of gauges that change the pattern of wind turbulence). However, due to limited budget and time, only very preliminary activities were undertaken (i.e. the comparison with quality-controlled Nimrod data and the verification of the resulting hydraulic outputs with observations) to ensure the reliability of raingauge data to an acceptable extent.

2.3.2 Radar data

Radar rainfall data produced by UK Met Office's Nimrod system were used in this work. Nimrod is a fully automated system for weather analysis and nowcasting based around a network of 15 C-band rainfall radars. There are three main components in Nimrod: producing analyses and forecasts of precipitation, cloud and visibility. This rainfall product used in this work is generated from the producing analyses of precipitation and clouds. The precipitation part is implemented by using processed radar and satellite data, in synergy with surface reports and NWP estimates; while the cloud analysis is largely based upon satellite imagery and surface reports (for details of the Nimrod system and forecasting components, the readers are referred to Golding (1998)).

The Nimrod rainfall products include composite and single-site rainfall estimates. The operational resolutions are 1- and 5-km in space and 5- and 15-min in time. The coverage

of composite estimates includes the whole UK (1- and 5-km) and Northern Europe (5-km only). Nimrod data are routinely quality controlled by the Met Office; the processes include, for example, noise filtering, clutter, and occultation identification, and attenuation correction (for details, the readers are referred to Harrison et al. (2000, 2009)). In addition, the radar rainfall quantity is adjusted with coincidental ground raingauge data every one hour by applying an adjustment factor to reduce the mean filed bias between radar and raingauge observations (Harrison et al., 2009).

The type of Nimrod data used in this work is 1-km composite rainfall data in the 5-min time interval over the whole UK area (1725 km X 2175 km), and the data source is BADC (British Atmospheric Data Centre) website. A simple tool was implemented to clip the data respectively over the areas of Greater London (100 km X 100 km) and the Cranbrook catchment (5 km X 6 km) from the original data for further applications. In this work, Nimrod (radar) data were mainly used to provide the spatial structures of rainfall fields and their variations, to test the proposed methods of radar rainfall processing (in Chapters 3 and 4), and to carry out the case study (in Chapter 5).

Table 2.1: Summary of geometric information of the data sets used in this thesis (LL: lower left; TR: top right; RG: raingauge; RD: radar/Nimrod)

Data Set	Type	Coordinates (UK Reference)	Area (km^2)	Spatial/Temporal Resolution
Beal High School	RG	(542230.14,189444.28)	-	5 min
Chadwell Heath Foundation School	RG	(546812.4, 187992.11)	-	5 min
Ursuline High School	RG	(543565.67, 186866.61)	-	5 min
Whole UK	RD	LL(-405000, -625000) TR(1320000, 1550000)	1725 X 2175	1 km 5 min
Greater London	RD	LL(485000, 135000) TR (585000, 235000)	100 X 100	1 km 5 min
Cranbrook Catchment	RD	LL(541000, 186000) TR(546000, 192000)	5 X 6	1 km 5 min

2.3.3 Other data sources

Historical raingauge data in 5-min time intervals from the Greenwich site in the UK were used in the work to assess the developed rainfall time series downscaling methods (in Section 4.3.2 and 4.4). The period of the sequence from Greenwich station ranges 21/02/1987 to 21/02/2001 (i.e., 14 years $\approx$ 1471680 data). A summary of specific statistics of Greenwich data respectively at 5-min and 1-day time intervals is shown in Table 2.2. Certain facts were observed as follows. The 5-min rainfall data are expected to be much more dispersed than the daily data according to the remarkable increase of CVs. Moreover, the substantial rises of the lag-1, -2 and -3 autocorrelation (r_1, r_2 and r_3) and the proportion of dry periods indicate the changes in rainfall patterns whilst timescales reduce from daily to 5-min.

Table 2.2: Summary statistics of 5-min and daily rainfall data recorded in the Greenwich raingauge (CV: coefficient of variation; r_i : lag-i autocorrelation coefficient; dry period %: proportion of dry periods)

Scale interval	Mean (mm)	Variance (mm^2)	CV	r_1	r_2	r_3	Averages of dry period %
5-min	0.00542	0.00283	9.814	0.565	0.418	0.331	98.0
1-day	1.561	13.015	2.311	0.165	0.101	0.0895	56.2

2.4 Rainfall Events for Case Studies

As mentioned above, four rainfall events passing over the Cranbrook catchment in the period of Apr 2010 - Feb 2012 were selected to carry out full-scale testing for evaluating this work's developments. These rainfall events respectively occurred on 23/08/2010, 26/05/2011, 05-06/06/2011 and 03/01/2012. The raingauge rainfall totals and the recorded maximum rainfall rates at each in-situ raingauge site are shown in Figure 2.7. The associated information and statistics of these events are summarised in Table 2.3, where RG Total and Max RG Total are respectively the mean and maximum of three raingauge totals, and Max rainrate and Max RG rainrate are respectively the maximum catchment-averaged rainfall rate and individually-observed rainfall rate from three raingauges.

The 23/08/2010 event was associated with a warm front and the rainfall falling within the Cranbrook catchment was approximately 23.53 mm in around 8 hr, with more than 80% falling in a period of 3 hr. For this event, the total and maximum rainfall recorded by three in-situ raingauges are very similar, and the maximum catchment-averaged and individually-observed rainfall rates are also similar. This suggests a frontal feature of the 23/08/2010 event. Similarly, the 05-06/06/2011 event also shows the frontal feature. It lasted approximately 24 hr and produced over 20 mm of rainfall. The varitions of total and maximum precipitation between three raingauges are insignificant. The maximum rainfall rates observed in this event (approximately 7.20 mm/hr) are relatively small as compared to other events.

Unlike the two events mentioned above, the 26/05/2011 and 03/01/2012 events show relatively convective features. For example, although the 26/05/2011 event produced less rainfall totals than the 23/08/2011 event, but significantly larger rainfall maximums and larger variations of these maximums between raingauges can be observed. Over 60% rainfall

volumes were concentrated in a period of 1 hr (around 15.00 - 16.00) and one over 50 mm/hr rainfall rate was recorded by the Ursuline High School raingauge (see Figure 2.7 (bottom)). Similarly, the 03/01/2012 event also shows convective feature. According to the contact of local council , this event was reported as a small typhoon-like storm crossing the London Borough of Redbridge, resulting in minor flooding over the Cranbrook catchment. Although this event produced merely around 10 mm of rainfall in 13 hr, over 50% of it concentrated in a period of 1.5 hr and a 45.6 mm/hr rainfall rate was recorded by the Beal High School raingauge. For the 03/01/2012 event, the flow level peak at the location of study pipe was not especially high; however, among these four study events, the 03/01/2012 event was the only event causing property damage. A further look at the radar estimates of this event (shown in Figure E.4). It can be found that, at around 12.00 - 12.10, a very large spatial variation in rainfall was suddenly measured by radar. This suggests that, in addition to the total rainfall volume and maximum rainfall rate, the spatial variations in rainfall may also be a crucial factor that causes pluvial flooding.

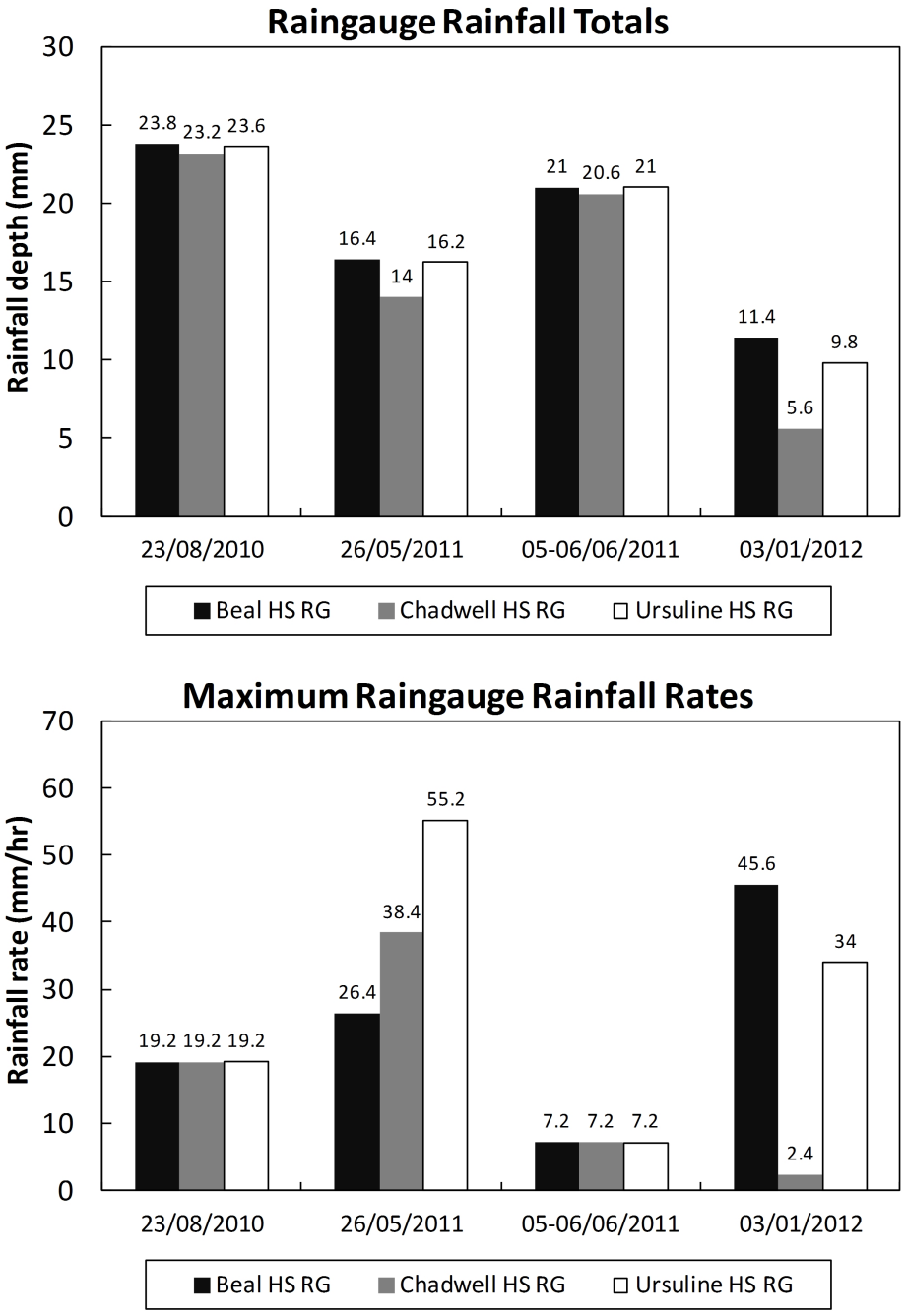


Figure 2.7: Rainfall information measured by the local in-situ raingauges for the selected events: rainfall totals (the upper) and maximum rainfall rates (the lower).

Table 2.3: Summary information of the four selected storms over the Cranbrook catchment during the monitoring period from August 2010 to January 2012, including storm date, duration, storm total rainfall (mean of raingauge observations; in mm), maximum individual raingauge accumulation over the catchment, maximum catchment-averaged rainfall rate (in mmh^{-1}), maximum individually-observed rainfall rate (in mmh^{-1}), flow level peaks observed at the Valentine Park sewer (in meter).

Date	Duration	RG Total (mm)	Max RG Total (mm)	Max Rainrate (mmh^{-1})	Max RG Rainrate (mmh^{-1})	Peak FL (m)
23/08/2010	8 hr	23.53	23.80	15.20	19.20	0.633
26/05/2011	9 hr	15.53	16.40	36.00	55.20	0.672
05-06/06/2011	24 hr	20.87	21.00	5.60	7.20	0.346
03/01/2012	13 hr	8.93	11.40	16.80	45.60	0.547

2.5 Summary

In this chapter, the environmental setting and the monitoring network of the experimental site, i.e., the Cranbrook catchment, in the London Borough of Redbridge was described; and the associated dual-drainage hydraulic models used in this work to simulate hydraulic behaviours of surface and sewer flows in the Cranbrook catchment were detailed.

In addition, the rainfall data sets used in this work were summarised. These sets include the in-situ raingauge data, radar (Nimrod) data, and the archived raingauge data in Greenwich (London). The in-situ raingauge network provides 5-min point rainfall observations over the Cranbrook catchment from April 2010; the radar network provides high-resolution (1-km and 5-min) rainfall measurements covering the whole UK area (therefore, the Greater London and the Cranbrook areas). Several rainfall events passing over the Greater London area after April 2010 were selected as case studies to compare with and to further assess the developments of this work, which is detailed in Chapters 3 - 5. The radar(Nimrod) data and archived raingauge data were also used in this work to carry out preliminary test of the proposed models at the stage of development.

Chapter 3

Urban Rainfall Estimation

The reliability of urban pluvial flood forecasting largely depends on the accuracy of rainfall forecasts (Golding, 2009b). The rainfall events that cause this type of flooding however are of small scale and high intensity and consequently highly unpredictable. Raingauge and radar are two sensors that are most ready for rainfall estimation at catchment scales (Cole and Moore, 2008); however, based upon the operational radar-raingauge networks, the applicability (i.e., achievable accuracy and resolution) for urban hydrological uses is insufficient. This chapter therefore focuses on the topic of enhancing the suitability of radar rainfall estimates for urban hydrological uses based upon radar-raingauge data combination techniques. The radar estimates with operational (or achievable) spatial (1 km) and/or temporal (5 min) resolutions are employed to test the proposed application and its impact on hydraulic outputs.

3.1 Raingauge measurements

Raingauges remain the most reliable sensor providing direct and accurate point rainfall measurements over the ground surface, which are widely used as "ground truth" for radar rainfall calibration (and/or adjustment). Quality control (QC) is the main issue for the application of raingauge data and it has been thoroughly studied (Einfalt et al., 2004). In general, raingauge data is also used to calibrate the hydraulic models of urban drainage systems, and the resulting hydraulic outputs (such as flow levels in the pipes) are regarded as the references to assess the performance of the hydraulic outputs resulting from other types of rainfall inputs (e.g. radar or satellite rainfall estimates).

The major drawback of raingauge data lies in its deficient capacity in characterising

the spatial variation in rainfall. Many studies have been conducted, aiming to synthesise the spatial structures of rainfall based upon point rainfall information in synergy with interpolation techniques (Tabios and Salas, 1985; Syed et al., 2003; Vischel et al., 2011). The results showed that this combination is very sensitive to the number of raingauges in the network and the interpolation techniques used (Looper and Vieux, 2011). In addition, as compared to radar observations, the temporal continuity of interpolated rainfall fields between successive time steps is usually insufficient since the temporal evolution of interpolated spatial structures is seldom modelled.

Instead of examining the reproducibility of spatial variation in rainfall, some works alternatively focus only on assessing the performance of the hydrological outputs resulting from the interpolated rainfall fields (Looper and Vieux, 2011; Simões et al., 2011b). Simões et al. (2011b), for example, employed the IDW (Inverse Distance Weighting) interpolation technique, coupled with time series prediction techniques, to undertake space-time rainfall and flood forecasting based upon a network of three raingauges in a very small catchment (approximately 1.5 km^2) in Coimbra (Portugal). Due to the size of the study catchment and the storm type, less spatial variation was found in rainfall and therefore promising results with approximately 15-30 min forecasting lead time were obtained. This work indicates that the combination of raingauge data and interpolation techniques could be useful for generating rainfall information in very small areas to the extent that spatial variability is less crucial. However, the drawback of this method (raingauge data plus interpolation techniques) is that the forecasting lead time is in general short and difficult to increase. It is because the raingauge-based prediction can be triggered only when the raingauges start to record non-zero rainfall measurements (i.e. rainfall storms reach the target catchments). Even in a larger catchment with a dense raingauge network, this method still shows poor reliability to forecast flooding with longer lead time (Looper and Vieux, 2011).

To summarise, raingauges provide reliable point rainfall time series records but lack the ability to satisfactorily describe the spatial structures of rainfall fields. The most important issue of raingauge data is to retain its quality. In this work, the quality of raingauge data used is regularly controlled by removing abnormal measurements and comparing with the coincidental radar (Nimrod) data, whose quality is continuously controlled by the Met Office (Harrison et al., 2000, 2009). The raingauge data used in this work is therefore assumed to be true point information and its resulting hydraulic and hydrological outputs are regarded as the reference to evaluate other rainfall inputs (i.e. radar rainfall estimates) if the hydraulic observations are unavailable.

3.2 Radar rainfall estimates

Radar rainfall data have been widely used in urban hydrological modelling due to their ability to characterise the spatial distribution of rainfall and its advection and evolution in high spatial (1-2 km) and temporal (5-15 min) resolutions. Their ability to reflect the spatial and temporal variability of rainfall in the corresponding hydrological and hydraulic simulation has been widely addressed in the literature (Fabry et al., 1994; Einfalt et al., 2004; Vieux and Bedient, 2004; Smith et al., 2007; Cole and Moore, 2008; Harrison et al., 2009). However, these works also concluded that the accuracy of radar rainfall estimates was in general insufficient, particularly for the case of extreme rainfall magnitudes. It is largely because, unlike raingauges which directly collect rain droplets, radar devices obtain rainfall measurements through an indirect process, which introduces more uncertainty.

As compared to the raingauge network, the advantage of radar is that it can provide broader and spatially and temporally continuous plane measurements. Radar rainfall therefore has the potential to significantly improve the predictability (e.g. longer forecast lead time) of short-term rainfall and flood forecasting. Some applications of radar rainfall to flood forecasting over urban or rural catchments have been recently studied (Krämer et al., 2007; Ehret et al., 2008; Wang et al., 2011). For example, Krämer et al. (2007) demonstrated the benefit of using radar rainfall forecasts for flow forecasting in the sewer system by quantifying their effectiveness for real time control. Although the predictability of radar-based rainfall and the subsequent hydrological modelling can be determined by many variables (such as the temporal and spatial scales of interest), these works all concluded that the most important variable was the accuracy of radar estimates that were used as starting points to project future rainfall quantities. In addition, radar observations have been widely used to calibrate or to be merged with precipitation outputs of Numerical Weather Prediction (NWP) models (such as the mesoscale NWP model MM5 in Liguori et al. (2011) and the operational UK Met Office Unified Model in Bowler et al. (2006) and Pierce (2009)) to conduct high-resolution rainfall forecasting with longer lead time (e.g. 1 km and 5 min resolution with 3-hr lead time in operational STEPS). This suggests additional need to be cautious in using radar data. The quality of radar rainfall and its suitability for hydrological applications are therefore the key to producing reliable flood forecasts. In the following, a brief description of radar rainfall production is given; then the techniques that have high potential to improve the applicability of radar rainfall to urban flood simulation are further explained.

Weather radar devices obtain rainfall measurements through sending horizontal (and/or

vertical) pulses of microwave radiation within a specific range of wavelengths, listening for return signals reflected by rain droplets (or other precipitation particles) and further analysing the propagation of these reflectivities. As mentioned above, this is an indirect process and in order to obtain rainfall estimates a series of quality control and correction techniques has to be applied (Golz et al., 2005). Based upon the production of operational radar rainfall estimates, these techniques generally include noise filtering, identification of clutter and occultation, removal of anomalous propagation, attenuation correction, conversion of reflectivity to rainfall rate and gauge-based adjustment (Fulton et al., 1998; Harrison et al., 2000, 2009). Since this work focuses on the application of radar rainfall product, rather than the processing of raw radar signals, special attention is therefore given to rainfall rate conversion (or calibration) and gauge-based adjustment techniques. For details of other techniques readers are referred to Collier (1996), Fulton et al. (1998), Harrison et al. (2000), Golz et al. (2005) and Germann et al. (2006).

3.2.1 $Z - R$ conversion

Through analysing the reflected radio energy from target, radar is able to detect and measure objects at a specific distance. This can be termed by the well known Radar Equation:

$$P_r = P_t \frac{G^2 \lambda^2 \sigma_T}{(4\pi)^3 r^4}, \tag{3.1}$$

where P_r and P_t are respectively received and transmitted power, G is the gain of the antenna, λ is the transmitted wavelength, σ_T is the radar cross section of the target and r is the distance to the target. If the particular properties of a given radar are known, this equation can be simplified and further derived as follows (for details, the reader is referred to Rinehart (2010) and Bringi and Chandrasekar (2001)):

$$P_r = \frac{Z_0}{r^2} \sum_{i=1}^{N(D)} D_i^6, , \tag{3.2}$$

where Z_0 is a constant related to the properties of a given radar and $N(D)$ is the raindrop-size distribution that tells us how many drops of each diameter D are contained in a unit

volume. Then the well known "radar reflectivity factor Z (in $\mathrm{mm}^6/\mathrm{m}^3$)" is defined as

$$Z = \sum_{i=1}^{N(D)} D_i^6 = \int_D D^6 N(D) dD. \tag{3.3}$$

Compared this equation with the definition of rainfall rate R (in mm/h),

$$R = \frac{\pi}{6} \int_D D^3 v(D) N(D) dD \tag{3.4}$$

where $v(D)$ is the terminal fall velocity; the radar rainrate can be estimated using a power-law $Z - R$ relation (known as the Marshall-Palmer relation):

$$R = aZ^b, \tag{3.5}$$

where a and b are constants to be determined. The values of a and b are in general subject to several factors, such as weather types (e.g. the convective or tropical types were employed in Fulton et al. (1998)) and the distances between specific locations and the centre of radar sites (see Sebastianelli et al. (2010) and Imgarten and Vieux (2012)). Due to the development of dual-polarisation in radar technologies, this conventional conversion between radar signals and rainfall rates has been improved. Dual-polarisation radar[1] allows retrieving extra information, such as differential reflectivity Z_{DR} and differential phase K_{DP}. In synergy with the conventional Z-R conversion, they are very useful in improving the accuracy of rainfall rate estimation.

However, these developments still largely rely on the calibration process to obtain rainfall rate. This means a large number of comparisons between coincidental radar and raingauge observations are required. Moreover, in order to obtain the statistically optimal results, the conversion process has to compromise the capacity of deriving extreme values since the frequency of their occurrence is relatively low; hence, the $Z - R$ conversion or the corresponding improved conversions are particularly poor at capturing intense rainfall rates (Einfalt et al., 2004, 2005; Jessen et al., 2005; Ryzhkov et al., 2005). This ability however is especially crucial to urban hydrological applications; further processing is therefore

[1]Different from the conventional radars that transmit only horizontal electromagnetic pulses, dual-polarisation radars transmit both horizontal and vertical signals.

necessary to overcome this deficiency.

3.2.2 Gauge-based adjustment

In order to enhance the suitability of radar rainfall estimates for hydrological or hydraulic applications, the gauge-based adjustment techniques are widely used to dynamically minimise the bias between radar estimates and the coincidental raingauge measurements (Fabry et al., 1994; Fulton et al., 1998; Seo et al., 1999; Harrison et al., 2009). Whereas "(electronic) calibration" relies on a long-term and large number of comparisons, "adjustment[2]" refers to dynamically (and/or locally) adjusting radar rainfall estimates using spatially and temporally coincidental raingauge measurements. For example, the operational Nimrod system employs an adjustment factor, based only upon the recent comparison between processed radar data and raingauge data, to the entire domain of each single radar site and updates it on an hourly basis to improve the suitability of radar rainfall estimates for hydrological uses (Seo et al., 1999; Harrison et al., 2009). The associated results demonstrated that hydrological applications indeed benefited from dynamically adjusting radar rainfall data; however, the study areas of these works are usually large compared to the general urban areas, and therefore their suitability for urban hydrological applications may be insufficient.

Smith et al. (2007) re-investigated 35 rainfall events selected from WSR-88D[3] rainfall products during the period 2003 - 2005, and compared them with the coincidental point observations recorded by a dense network of raingauges (one raingauge per km^2 on average) over a small urban area ($\approx 14.3km^2$). The results showed that large and event-varying biases were observed over the study catchment even though WSR-88D radar rainfall products had been dynamically adjusted with raingauge measurements over coarser spatial and temporal scales (similar to the Nimrod rainfall data, adjusted based upon hourly scales). Nonetheless, these biases could be effectively reduced by applying a simple ratio to scale up or down the radar rainfall rates to approximate the coincidental raingauge records. This simple ratio was derived from the comparison between the mean radar rainfall estimates and mean local raingauge measurements at the locations of raingauges over the period of

[2]In the literature, it is sometimes called "re-calibration", "combination" or "merging" (Todini, 2001b; Einfalt et al., 2004).

[3]WSR-88D, standing for Weather Surveillance Radar, 1988, Doppler, is the technical name of NEXRAD (Next-Generation Radar), which is a network of 159 high-resolution Doppler weather radars operated by the National Weather Service, an agency of the National Oceanic and Atmospheric Administration (NOAA) within the United States Department of Commerce (Fulton et al., 1998; Seo et al., 1999).

an event (it is therefore called the "mean bias" adjustment in the following context).

A similar work was carried out by Vieux and Bedient (2004) but over a relatively large urban catchment (≈ 260 km^2). Vieux and Bedient (2004) evaluated the hydrological prediction uncertainty caused by rainfall input errors through event re-construction. Five events were selected from the WSR-88D rainfall products during the period 1998 - 2003; the associated conversion between radar reflectivity and rainfall rate was implemented by using either tropical (i.e. $Z = 250R^{1.2}$) or convective (i.e. $Z = 300R^{1.4}$) Z-R relationships. Similarly, these events were re-constructed by employing a simple ratio to reduce the mean bias between radar and the co-located raingauge observations. Results, similar to Smith et al. (2007), also suggested that the corresponding flow prediction could be significantly improved by using mean bias adjusted (corrected) radar rainfall estimates as inputs.

These works suggested that "mean bias" (also termed "systematic error" in the literature) was the most important uncertainty source that decreased the suitability of radar rainfall for the urban hydrological or hydraulic applications, and the performance of these applications could be massively improved through locally and dynamically adjusting radar rainfall estimates using co-located raingauge records. However, this simple mean bias adjustment was carried out by post-event (or historical rainfall records) comparisons. A ratio is first obtained by comparing the coincidental radar and raingauge accumulations over a specific period and then applied to the rainfall rate at each radar grid. It is therefore more suitable for improving the applicability of historical rainfall events to hydrological or hydraulic design, other than short-term forecasting in real time. If further applied to real-time flood forecasting uses, this method requires a very wide-range raingauge network (over a large area) and a longer temporal comparison basis (i.e. hourly) to obtain a more reliable ratio to scale the radar rainfall (Anagnostou and Krajewski, 1999; Seo et al., 1999). It is therefore more suitable for coarser spatial- and temporal-resolution rainfall adjustment.

A local calibration methodology was initiated by Moore et al. (1989), and further modified by Wood et al. (2000), to improve the local and dynamic capacity of conventional mean bias adjustment. A dynamic calibration factor c was introduced to carry out 15-min radar rainfall adjustment in real time (Wood et al., 2000):

$$c = \frac{R_g + \epsilon}{\kappa R_r + \epsilon}, \tag{3.6}$$

where R_g and R_r are the raingauge and coincidental radar rainfall values (in mm) for a 15 minute time interval. This factor is constituted by the comparison of raingauge

and radar estimates at each time step in synergy with a positive correction value ϵ and a static calibration factor κ (determined from long-term study of radar-raingauge bias), where ϵ and κ are both empirically derived constants. Cole and Moore (2008) further examined the applicability of this methodology over two UK catchments (Darwen and Kent, respectively 135.7 and 212.3 km^2). Three types of gauge-based adjustment techniques were used to correct radar estimates. They were respectively static adjustment, standard dynamic adjustment, and dynamic adjustment including mean bias. The first one was similar to the aforementioned simple mean-bias adjustment, but based upon a long-term radar-raingauge comparison. The second and third techniques are respectively based upon the original local calibration methodology (Moore et al., 1989) and the modified one (Wood et al., 2000). Results suggested that the applicability of radar rainfall estimates can be significantly improved by the local calibration methodology (i.e. the second and third techniques). It was found that, compared to the hydrological outputs resulting from the static adjusted radar estimates, those resulting from the dynamically local-calibrated radar estimates had much better agreement with in-situ observations.

Similarly to the techniques described above which focus on reducing mean bias, a geostatistical merging method was developed by Ehret et al. (2008) and applied to real-time small-scale flood forecasting in Goldersbach catchment, Germany ($\approx$ 75km^2). At each time step, the point raingauge records are interpolated to a rainfall field and further merged with the coincidental radar image. The Block Kriging interpolation technique was employed to ensure that the synthetic rainfall field is unbiased. A deviation field can be then constituted by the ratios of the interpolated rainfall to radar rainfall at each radar grid. This field is then corrected to ensure the ratios are symmetric to 1.0 and consequently the mean raingauge totals are retained and further applied to the interpolated rainfall field. A merged rainfall field is therefore obtained at each time step and further used as input for flood forecasting. The quality of radar rainfall was significantly improved through this merging process and consequently the accuracy of rainfall and flood forecasting was largely improved.

However, some common drawbacks are found in all the mean-bias adjustment methods mentioned above. First, the spatial structure (e.g. spatial variability) of radar rainfall fields could be altered by multiplying a ratio by the estimate in each radar grid square. The ability to characterise the spatial variations in rainfall is however one of the most reliable feature of radar sensors and should be retained. Second, the mean-bias adjustment has difficulty in correcting the temporal profiles of radar rainfall. For example, if the

original radar rainfall estimates fail to capture the rainfall peaks with the right timing, this failure will not be corrected by the mean-bias adjustment since this method focuses on the correction of quantitative difference (see Figure 4 of Ehret et al. (2008)).

Whereas the above techniques focus on diminishing the mean bias, another type of adjustment technique focuses on minimising the error variances. The error herein represents the difference between true (or raingauge) and radar rainfall estimates. The concept of minimising the error variances is similar to maximum likelihood approaches; therefore, in addition to mean bias, the spatial and temporal patterns of rainfall are also taken into account in the adjustment methods (Krajewski, 1987; Todini, 2001b; Mazzetti, 2004; Gerstner and Heinemann, 2008). These techniques in general assume that there is a true rainfall field at each time step, of which the rainfall volume at each grid is the (linear) combination of the coincidental radar and raingauge estimates; and the rainfall total of this true rainfall field is equal to the raingauge total (this means that the raingauge records are unbiased). However, it is not always possible to have at least one raingauge in each radar grid square. Some further assumptions are therefore necessary. For example, Gerstner and Heinemann (2008) defined that the rainfall volume at a specific grid square of the true (or called best estimated) rainfall field as follows:

$$P_a(x_i, y_i) = P_r(x_i, y_i) + \sum_{k=1}^{K} w_{ik}[P_g(x_k, y_k) - P_r(x_i, y_i)], \tag{3.7}$$

where $P_a(x_i, y_i)$ and $P_r(x_i, y_i)$ are respectively the best estimated and radar rainfall at the grid point (x_i, y_i), $P_g(x_k, y_k)$ is the raingauge measurement at the position (x_k, y_k) from a network of K raingauges and w_{ik} is the to-be-determined weight. Through minimising the error variances between each radar grid rainfall and raingauge record, w_{ik}'s can be estimated and their values are in general inversely proportional to the distance between raingauge and radar grids. Results showed that this weighting technique could effectively reflect the local point information to radar rainfall. However, the study was carried out on a daily basis; its applicability to sub-daily and sub-hourly radar rainfall adjustment is therefore unknown.

Differently from Gerstner and Heinemann (2008), Krajewski (1987) and Todini (2001b) employed the (Block-) Kriging interpolation technique to generate point raingauge information at each radar grid square for merging with radar estimates. In the Cokriging technique proposed by Krajewski (1987), the best rainfall estimate $V^*(x_0, y_0)$ at a specific

location was defined as follows:

$$V^*(x_0, y_0) = \sum_{i=1}^{N_G} \lambda_{G_i} G_i(x_i, y_i) + \sum_{i=1}^{N_R} \lambda_{R_i} R_i(x_i, y_i), \tag{3.8}$$

where N_G and N_R are the numbers of raingauges and radar grid squares around location (x_0, y_0) and G_i and R_i are the associated measurements. In the process of deriving λ_{G_i} and λ_{R_i}, the information of the covariances between true and raingauge rainfall Cov_{VG} and between true and radar rainfall Cov_{VR} are however required; but it is impossible to obtain them. They are therefore approximated by the forms $Cov_{VG} = \beta_G Cov_{GG}$ and $Cov_{VR} = \beta_R Cov_{RR}$, where Cov_{GG} and Cov_{RR} are the covariances respectively between raingauges and radar grids and β_G and β_R are two to-be-determined constants ranging from 0 to 1. This approximation however largely decreases the applicability of the Cokriging technique because the optimal values of β_G and β_R are usually determined subjectively or through a large number of simulations.

Todini (2001b), unlike Krajewski (1987), employed the Kalman filter algorithm to merge the interpolated and radar rainfall field to obtain the "true" rainfall field at each time step. This method (called Bayesian combination), instead of using Cov_{VG} and Cov_{VR}, uses the covariance of errors Cov_{ϵ_t} to help derive the true rainfall field. The error ϵ_t is estimated by comparing the co-located Block-Kriged and radar rainfall estimates, an empirical Cov_{ϵ_t} matrix is then constructed and further fitted to a theoretical covariance model (the exponential variogram was used in Todini (2001b)) in real time to update the original radar estimates to produce the "true" rainfall field. This Bayesian combination method has been applied to a 1051 km^2 river catchment near Bologna (Italy), where 1 km^2 C-band radar images and point rainfall information recored by a network of 26 raingauges are available. Results showed that the bias and variance between radar and observed rainfall estimates were significantly reduced. This application however was undertaken on a hourly basis and its potential for use in sub-hourly rainfall adjustment needs to be further examined.

This work will further study the applicability of this Bayesian combination method to sub-hourly and small-scale urban catchment the following section. This method was selected and applied to urban rainfall processing due to the following reasons:

1. It has strong theoretical background and relatively few approximations;

2. It does not require numerous simulations and historical rainfall events to determine parameters;

3.3 Applications of gauge-based adjustment to urban rainfall processing

The aim of this section is to evaluate the applicability of the Bayesian combination method to urban flood forecasting/modelling and to study the major factors that determine the suitability of radar rainfall estimates for urban hydrological uses. The simple mean bias adjustment was also implemented in this section to compare it with the Bayesian method. The comparison between the adjusted and the original radar rainfall and the raingauge observations is firstly given. The corresponding hydraulic outputs are then compared to demonstrate the impact of rainfall adjustment on urban flood modelling.

3.3.1 Mean bias adjustment

As previously mentioned above, the bias between raingauge and radar rainfall estimates is widely regarded as the dominant factor in the uncertainty of the corresponding hydrological or hydraulic modelling. The mean bias adjustment was therefore implemented in this work to evaluate the impact of bias reduction on the four selected events and the corresponding hydraulic outputs.

The idea of the mean bias adjustment is to analyse the differences between raingauge observations and the coincidental radar measurements over the duration of a given event, and then apply this event-varying difference directly to each radar rainfall grid of the event. A quantity, named the sample bias, is defined here as the ratio of the mean raingauge accumulations to the co-located mean radar rainfall accumulations on an event total basis, i.e.,

$$B_i = \frac{(\sum_{j=1}^{m} RG_{ij})/m}{(\sum_{j=1}^{m} R_i(T_i, x_j))/m}, \tag{3.9}$$

where B_i is the sample bias for the i-th event with duration T_i, m is the number of raingauges, x_j is the geographical location of the j-th raingauge, and $R_i(T_i, x_j)$ and RG_{ij} respectively represent the radar and raingauge rainfall accumulations (in mm) over period

T_i at the coincidental location x_j.

Table 3.1 summarises the results of raingauge, radar rainfall accumulations and the associated sample bias B_i obtained by using Eq. (3.9) for four selected events in this work. It can be observed that there are in general large and event-varying bias (ranging from 1.16 to 3.23) between raingauge (denoted "RG") and the original 1-km Nimrod radar (denoted "Radar 1 km") rainfall measurements. This result is consistent with the finding of Smith et al. (2007) and Vieux and Bedient (2004).

Table 3.1: Summary of raingauge and the coincidental radar accumulations and the sample bias for the selected events, where RG Total is the mean raingauge accumulations $\sum_{j=1}^{m} RG_{ij}/m$, Radar@RG Total is the co-located mean radar rainfall accumulation $\sum_{j=1}^{m} R_i(T_i, x_j)/m$ and Radar Total is the mean radar accumulation over the whole Cranbrook catchment

Event	RG Total (1) (mm)	Radar@RG Total (2) (mm)	Radar Total (mm)	B_i
23/08/2010	23.53	7.29	6.80	3.23
26/05/2011	15.53	5.10	4.88	3.04
05-06/06/2011	20.87	9.43	9.48	2.21
03/01/2012	8.93	7.72	7.55	1.16

The obtained sample bias was then applied to each radar rainfall grid over the Cranbrook catchment respectively for each selected event to correct the mean bias (the radar data adjusted by the sample bias are denoted "Corrected Radar 1 km estimates" in the following context). Figure 3.7 shows the 5-min rainfall profiles and accumulations of the Corrected Radar 1 km estimates (the dashed gray lines), the coincidental raingauge records (denoted "RG" and plotted as the brown bars and the lines with square markers) and the original radar rainfall estimates (denoted "Radar 1km" estimates and plotted as the gray solid lines) at the location of each in-situ raingauge site for the 23/08/2010 event. It is observed that the radar rainfall accumulations at each raingauge location are largely improved by the mean bias adjustment. For the rainfall profiles, however, some underestimation (e.g. around 00:05 - 02:05), overestimation (e.g. around 03:05 - 04:05) and faulty timings of rainfall peaks are observed.

Further comparisons of the rainfall over the whole Cranbrook catchment for four selected event are shown in Figures E.1-E.4. Similarly to Figure 3.7, the radar rainfall accumulations of these events are substantially improved, but the 5-min profiles are not always well reproduced. This is because the mean bias adjustment fully relies on correct-

ing the accumulated difference between radar and raingauge measurements over the overall event period without taking into account the temporal variation within a storm process. In addition, Figures E.1 -E.4(middle) also demonstrate that the spatial structures of rainfall fields are largely altered by simply multiplying a given constant (i.e. the sample bias) to the original radar rainfall fields.

The corresponding flow levels of the pipes, respectively located at the up-, mid- and downstream of the Cranbrook catchment, by using the Corrected Radar 1 km estimates as inputs are shown in Figures E.5-E.8. It is observed the Corrected Radar 1 km outputs (the gray solid lines) are quantitatively much more similar to the RGs outputs (the solid dark lines) and the observations (the round markers) than the Radar 1km outputs (the gray dashed lines). However, the results also show that the faulty reproduction of rainfall profiles indeed affects the hydraulic outputs. For example, due to the poor reproduction of rainfall profile, the level peak in the period of 03:00 - 04:00 of the 23/08/2010 event (see Figure E.5) was not well matched, and this mismatch does not disappear in the downstream pipe. This suggests that, although rainfall bias plays an important role in flood modelling, the spatial and temporal variations of radar rainfall estimates should not be ignored and their impact on hydraulic outputs is of importance. More sophisticated methods are therefore necessary to effectively reduce rainfall bias as well as to appropriately reproduce rainfall profiles.

3.3.2 Bayesian-based adjustment

The Bayesian-based adjustment employed in this work was developed based upon the data combination technique proposed by Todini (2001b). The aim is to combine the advantages of two different sensors: raingauge and radar; the prior provides accurate and local point rainfall information, whilst the latter has a better description of the spatial structure of rainfall processes and its temporal evolution. The idea of this Bayesian-based adjustment method is shown in Figure 3.1. At each time step (say Time = t), the raingauge data are firstly interpolated into a synthetic rainfall field in real time by the Block Kriging interpolation method, then merged with the coincidental radar image based upon the Kalman filter algorithm (Todini, 2001b; Mazzetti, 2004). As highlighted in Figure 3.1, the key techniques included in this method are the Block-Kriging interpolation, the Kalman Filter algorithm and the characterisation of error fields.

The idea of the Block Kriging interpolation method is to generate a synthetic rainfall field whose semi-variogram curve is very similar to the semi-variogram curve empirically

estimated from the associated point rainfall information, where the semi-variogram curve is a function used to characterise the degree of spatial dependence of a spatial random field (e.g. the rainfall field). The semi-variogram is defined as the variance of the difference between random field values at two locations across realizations of the field and can be expressed as,

$$\gamma(x_i, x_j) = \frac{1}{2} var[Z(x_i) - Z(x_j)], \tag{3.10}$$

where $Z(x_i)$ and $Z(x_j)$ are two random values (e.g. rainfall volumes) at locations x_i and x_j. If $Z(x_i)$ and $Z(x_j)$ follow the same probability distribution (known as "stationary" in mathematical sciences), Eq.(3.10) can be simplified as $\gamma(h_{i,j})$ where $h_{i,j}$ is the distance between two locations x_i and x_j and $\gamma(h_{i,j})$ can be further derived and linked to the covariance matrix Cov of the random field Z:

$$\gamma(h_{i,j}) = \frac{1}{2}[Cov(x_i, x_i) + Cov(x_j, x_j) - 2Cov(x_i, x_j)], \tag{3.11}$$

Based upon Eq.(3.11), the empirical $\gamma(h_{i,j})$ can be estimated from a number of point observations and further fitted to a given mathematical model to obtain a continuous theoretical $\gamma(h_{i,j})$. Therefore, the covariance between each two points can be estimated and In this work, as suggested in Todini (2001b) and Mazzetti (2004), the Gaussian semi-variogram is employed, which is a function of three parameters, p the nugget, ω the sill and a the range:

$$\gamma(h) = p + \omega(1 - \exp^{-(h/a)^2}). \tag{3.12}$$

Based upon this summary of the theory of Kriging interpolation, it can be seen that by taking into account the semi-variogram in the interpolation process the (Block) Kriged rainfall fields provide not only accurate point rainfall estimates but also the spatial dependences between these point estimates over a specific area. This information can reflect the spatial structure of rainfall right above the ground; it is therefore very useful to correct the spatial structure observed by radar, which is at a specific elevation above the ground and could be horizontally shifted by wind advection. This idea of using spatial dependences

estimated from raingauge observations to improve the generation of rainfall processes has been widely applied in hydrology (Wheater et al., 2005; Yang et al., 2005).

After the Kriged rainfall field is computed, at the location of each radar grid square there are one radar estimate and one co-located Kriged rainfall estimate; the Kalman filter algorithm is then employed to produce an output rainfall field by merging the Kriged rainfall field and the coincidental radar image. To complete the Kalman filter, there are in general two steps: predict and update (Kalman, 1960). In the "predict" step, the "a priori" estimates and status at current time step (say Time = t) are firstly predicted based upon the estimates and status at the previous time step (Time = $t-1$). These "a priori" estimates and status are then "updated" using the real-time observations, and the "a posteriori" estimates and status can be obtained by characterising the differences (or called errors) between the "a priori" estimates and observations. The characterisation of the errors is usually implemented by fitting the variances of these errors (termed "error variance") to a specific mathematical model.

In the method proposed by Todini (2001b), at each time step the radar image represents the "a priori" estimates and the Kriged rainfall field is used as the observations to update the "a priori" estimates to obtain the output field (the "a posteriori" estimates). The "update" is conducted by characterising the empirical error field using a given mathematical model, where the empirical error field is composed of the differences between the co-located radar and Kriged rainfall estimates and can be expressed as

$$\epsilon_t = R_t - RG_t, \tag{3.13}$$

where R_t and RG_t are respectively the radar and raingauge estimates. As suggested by Todini (2001a), the ϵ_t field here is characterised by using an exponential variogram model to fit its covariance matrix. Similarly to the Gaussian variogram, the exponential variogram model is also a function of p the nugget, ω the sill and a the range:

$$\gamma(h) = p + \omega(1 - \exp^{-(h/a)}). \tag{3.14}$$

The fitted error field (termed "theoretical error field" in Figure 3.1) is then added back to the radar image ("a prior" estimates) to obtain the output rainfall field (the "a posteriori" estimates). Unlike the conventional Kalman filter that predicts the "a priori" estimates

at each time step based upon the "a posteriori" estimates from the previous time step, this method uses the real-time measured radar images as the "a priori" estimates. It is because that the "predict" step of the original Kalman Filter is conducted based upon a linear model, which is not a suitable tool to predict the highly nonlinear atmospheric process. The status of the Kalman Filter is therefore re-calculated and the error field is re-fitted in real time at each time step. For further details of this data merging method and the associated techniques, the reader is referred to Kalman (1960), Cressie (1993), Todini (2001b) and Mazzetti (2004).

This Bayesian method was then applied to the four events selected in this work. Figures 3.2-3.5 show the spatial distributions of rainfall rates of the original radar data, Block-Kriged and Bayesian-based adjusted rainfall estimates at the time steps in the vicinity of peaks over the Cranbrook catchment (i.e. a 5 km X 6 km gridded square as shown in Figure 2.2). It can be seen that in general the "Bayesian radar 1 km" images show similar colours to the "BK-RGs 1 km" (i.e. Block-Kriged Raingauge rainfall fields) images but are of more variable patterns, which are similar to the "Radar 1 km" images. This can also be reflected in the associated statistics (i.e. the means and standard deviations shown under each image in Figures 3.2-3.5). This indicates that the Bayesian-based adjustment technique indeed has the ability to combine the advantages of different rainfall sensors, i.e., the mean rainfall volume from raingauges and the spatial representativeness of radars.

For the 23/08/2010 and 05-06/06/2011 events (Figures 3.2 and 3.4 and Figure 3.6 (a) and (c)), around 5-10 min inconsistency in time can be observed between the original radar and the block-Kriged raingauge rainfall estimates. The peak of the 23/08/2010 event, for example, was recorded by radar at 00:25 but was recorded by raingauges at 00:30. For the 05-06/06/2011 event, a cluster of rainfall cells with a clear peak was observed by radar, passing the Cranbrook catchment from the time step 17:05; however the similar peak of the Block-Kriged raingauge estimates was observed at 17:15. This temporal inconsistency could be caused by the frontal feature of these two events; i.e., the strong vertical gradient of wind advection causes the inconsistency on the movement of rainfall cells at different heights. Since the rainfall image observed by radar is at a specific elevation above the ground, it is very likely to have a temporal lag between radar and raingauge observations.

It can be seen that, in the Bayesian-based adjusted images of these two events, the rainfall volumes measured by radars are largely adjusted to fit to raingauge records to diminish the temporal lag of the mean bias, whilst the spatial distributions observed by radar are remained. This is actually incorrect in a physical sense and could be an uncertainty

source when this Bayesian-based adjustment technique is applied; however, in practise the associated impact could be insignificant since the spatial variability of frontal storms and its variation with time are in general low.

For the 26/05/2011 and 03/01/2012 events, which were recognised as convective systems, the temporal lag between the radar and raingauge measurements is less significant (see Figures 3.3 and 3.5 and Figure 3.6 (b) and (d)). As compared to the 23/08/2010 and 05-06/06/2011 events, some rainfall snapshots of relatively high spatial variability can be observed from both radar and interpolated raingauge estimates of these two events; for example, the radar and Block-Kriged raingauge images at the time step 12:00 of 03/01/2012 event and the time steps 15:15 and 15:20 of the 26/05/2011 events. In addition, the gradients of the spatial variabilities between these snapshots and their previous ones are in general large; this means the occurrence of these highly variable snapshots is very sudden, which is a typical feature of convective weather systems.

It can be found that if the point rainfall information is sufficient, the interpolated rainfall estimates have the potential to somewhat represent the spatial variability of convective storms in local areas, and the quality of the associated adjusted rainfall estimates is also better, in terms of the performance in merging the advantages of raingauge and radar measurements (i.e. the representativeness of mean volumes and spatial distribution of rainfall fields, respectively). For example, according to the results of the Bayesian-based adjusted rainfall estimates for the 26/05/2011 event (see Figure 3.3), the features of raingauges and radars observations are consistently combined; whilst, for the 03/01/2012 event, because one in-situ raingauge broke during the event period and consequently less point rainfall information was provided, the Bayesian adjustment technique used herein failed consistently merging the advantages of radar and raingauge observations. This means that the quality of the Bayesian-based adjusted estimates is sensitive to the density and the geographic deployment of raingauge networks, particularly for convective storms. This could be an uncertainty source that affects the corresponding hydrological and hydraulic applications and needs to be further evaluated in the future work.

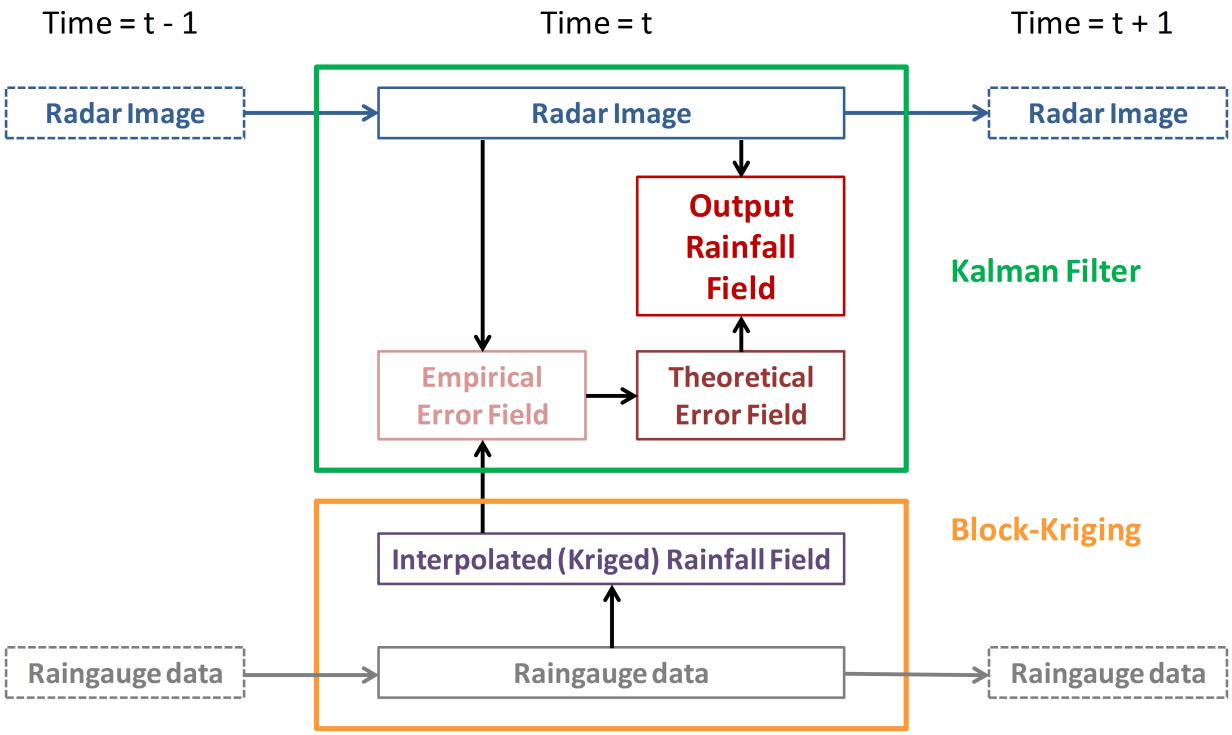


Figure 3.1: Schematic of the Bayesian-based adjustment proposed by Todini (2001b)

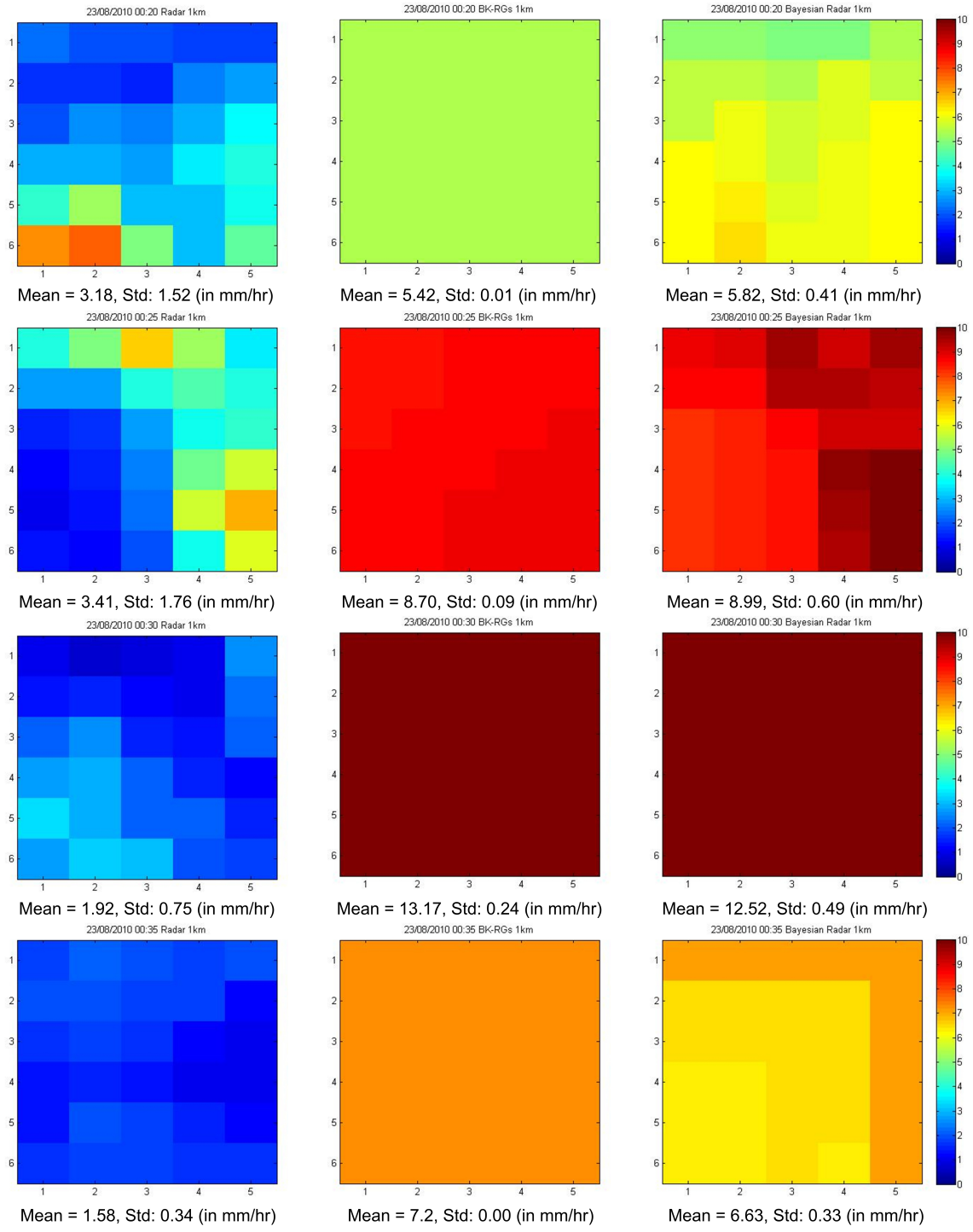


Figure 3.2: Images of radar, Block-Kriged and Bayesian-based adjusted radar rainfall fields (from left to right) between time steps 00:20 and 00:35 (from top to bottom) for the 23/08/2010 event

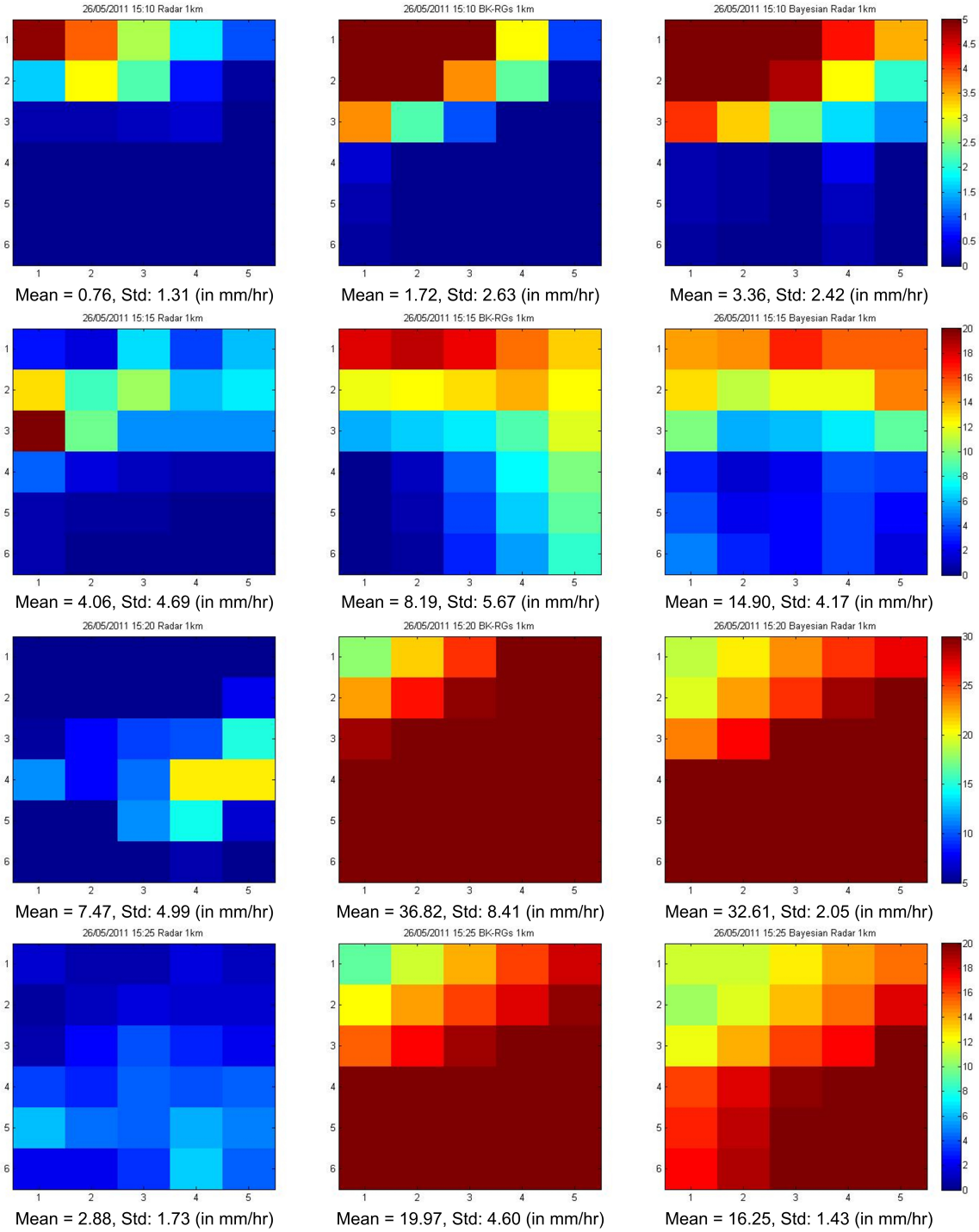


Figure 3.3: Images of radar, Block-Kriged and Bayesian-based adjusted radar rainfall fields (from left to right) between time steps 15:10 and 15:25 (from top to bottom) for the 26/05/2011 event

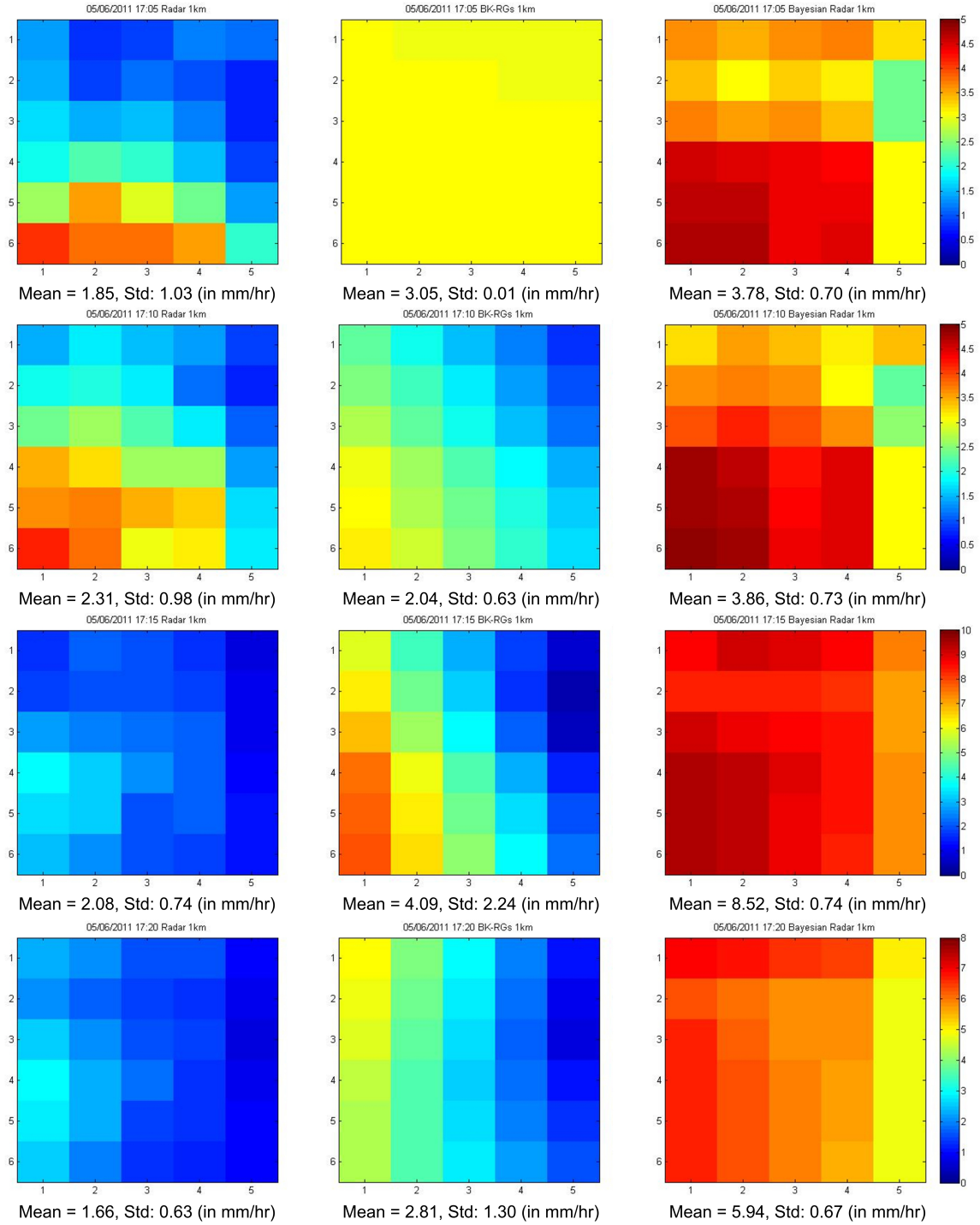


Figure 3.4: Images of radar, Block-Kriged and Bayesian-based adjusted radar rainfall fields (from left to right) between time steps 17:05 and 17:20 (from top to bottom) on 05/06/2011 for the 05-06/06/2011 event

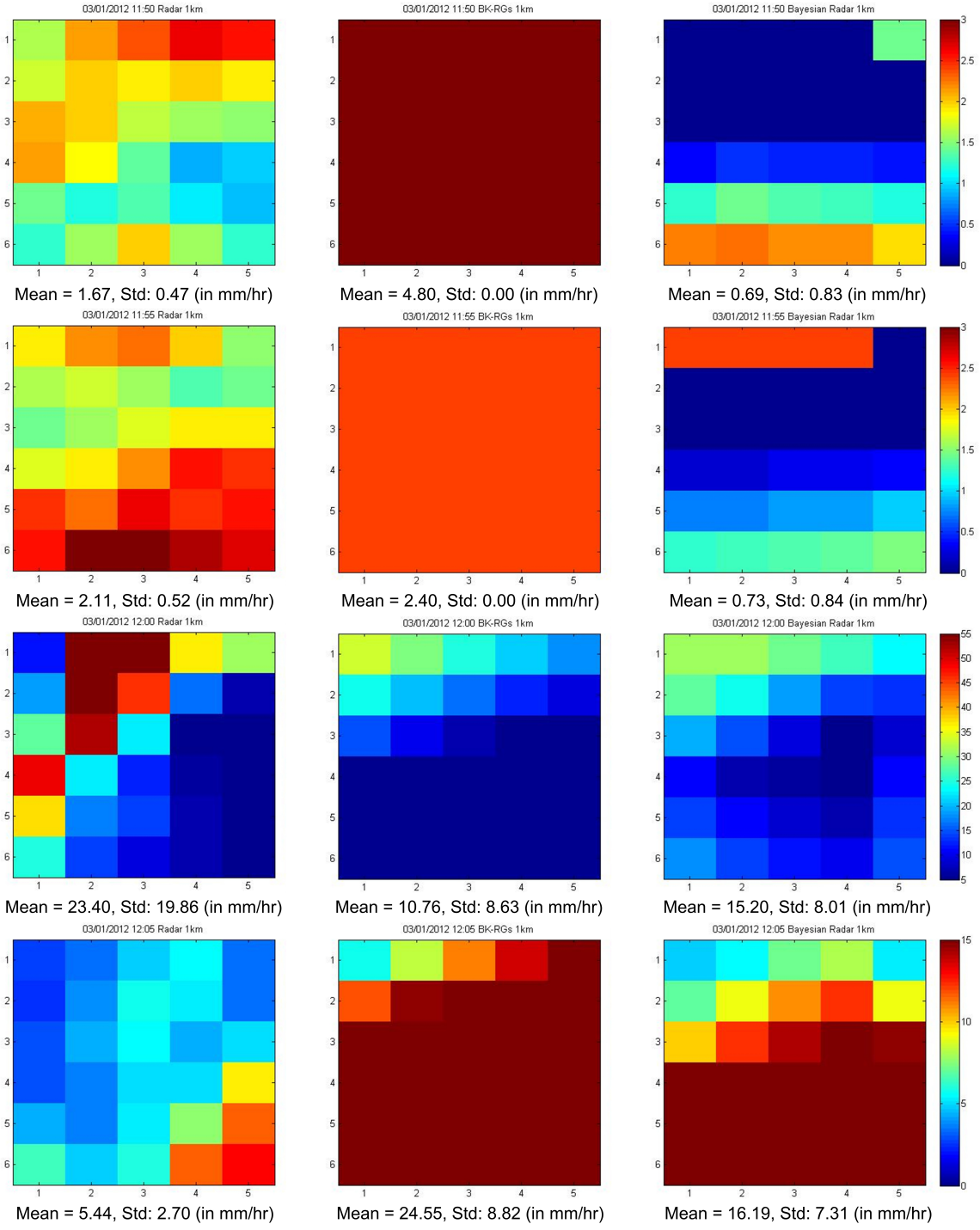


Figure 3.5: Images of radar, Block-Kriged and Bayesian-based adjusted radar rainfall fields (from left to right) between time steps 11:50 and 12:05 (from top to bottom) for the 03/01/2012 event

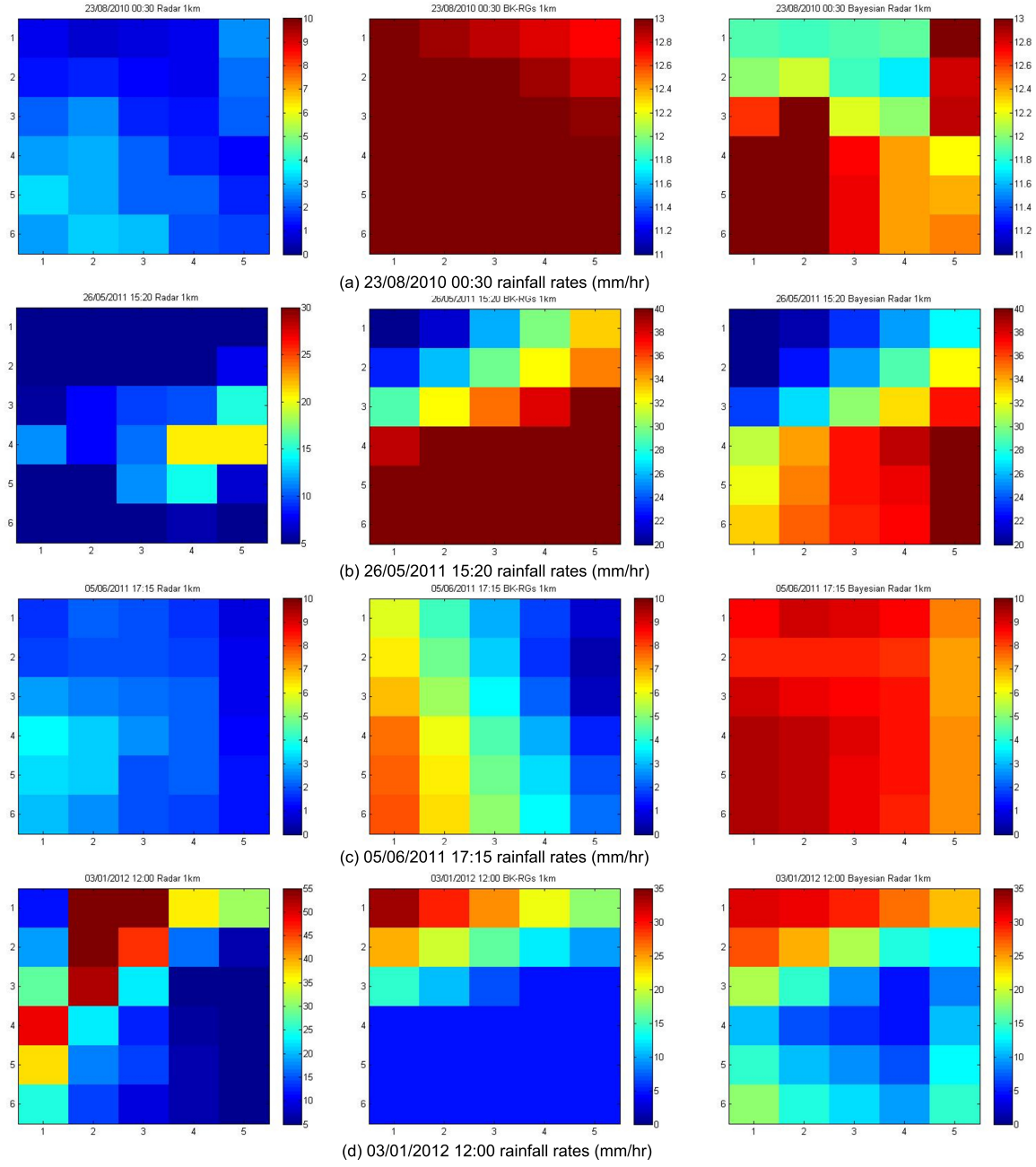


Figure 3.6: Images of radar, Block-Kriged and Bayesian-based adjusted radar rainfall fields (from left to right) at time steps where peaks were observed for four selected events on (a) 23/08/2012, (b) 26/05/2011, (c) 05-06/06/2011 and (d) 03/01/2012

3.3.3 Comparison of adjustment techniques

A detailed statistical analysis and comparison between the original radar rainfall, the raingauge records and the adjusted radar estimates, and their impacts on hydraulic outputs are carried out in this section.

Figures E.1-E.4 show the 5-min profiles and accumulations of the Bayesian-based adjusted radar rainfall (the dark solid lines), the coincidental raingauge records (the brown bars and the lines with square markers), the original radar rainfall estimates (the gray solid lines) and the mean bias corrected radar rainfall estimates at the locations of in-situ raingauges for four selected events over the Cranbrook catchment. It is found that the accumulations of the Radar 1km estimates are in general largely improved by both the Bayesian and mean bias adjustment techniques (the Bayesian Radar 1km estimates are slightly lower than the Corrected Radar 1km estimates). Nonetheless the 5-min profiles of the Bayesian Radar 1km estimates are in general more consistent with the RG observations. For example, the peaks of mean rainfall volumes at around 00:30 and 00:55 which had not been correctly detected by the radar due to the frontal feature of this event were properly corrected by the Bayesian adjustment (see the dark solid and the gray dashed lines in Figure E.1 (upper)). Moreover, unlike the mean bias adjustment, the Bayesian adjustment better retains the spatial variability of the original radar observations. This ability to reflect the spatial variability of a rainfall field is in general regarded as the strength of radar estimates and will be kept (see the dark and gray solid lines in Figures E.1-E.4 (middle)).

Further quantile-quantile analyses were conducted to assess the performance of different types of radar estimates in profile fitting against the RG observations (shown in Figure 3.8). It can be seen that in most events the Bayesian Radar 1 km estimates (the filled round markers) show a better fit to the raingauge observations, particularly the peaks of the events. Furthermore, compared to the Radar 1 km (the triangular markers) and the Corrected Radar 1km estimates (the round markers), the markers of Bayesian Radar 1 km estimates are relatively concentrated and closer to the straight lines with slope equal to 1. A further assessment of the goodness of the quantile-quantile comparisons can be quantified using the linear regression analysis. Two key coefficients of the linear regression are used here: the coefficient of determination (R^2) and the regression coefficient (β). The R^2, ranging from 0 to 1, is used here to measure the correlation (i.e. the geometrical similarity) of the raingauge observations and the specific radar rainfall estimates. It therefore cannot reflect the quantitative difference (i.e. bias) between two different types of data. The β

is the slope of the line obtained from the liner regression analysis. For quantile-quantile comparisons, it represents the quantitative similarity of raingauge and radar estimates, and it indicates a good fit as its value closes to 1.

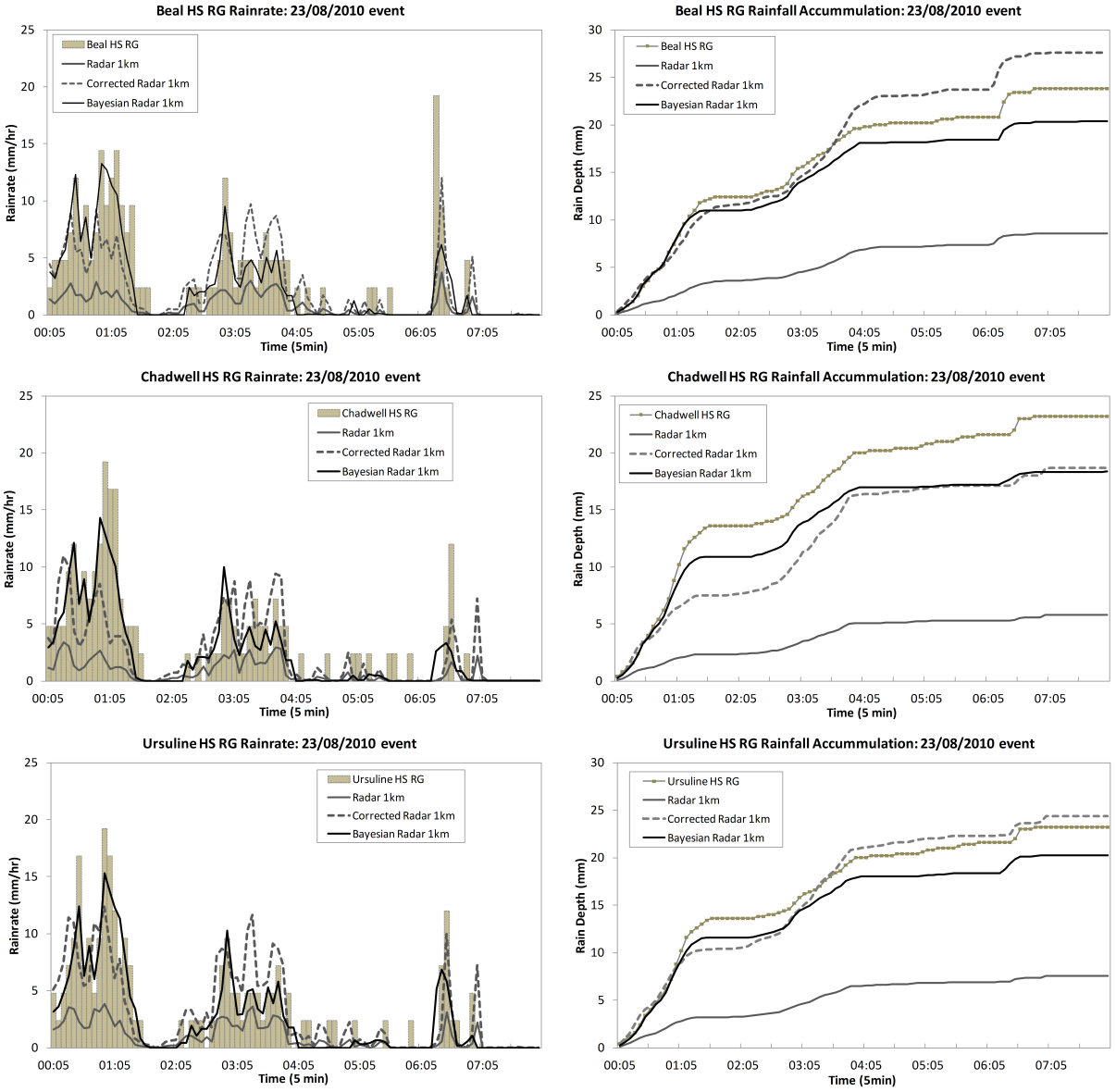


Figure 3.7: The comparison of raingauge observations, the coincidental radar and merged radar estimates in the rainfall event taking place on 23/08/2010 in the Cranbrook catchment, London

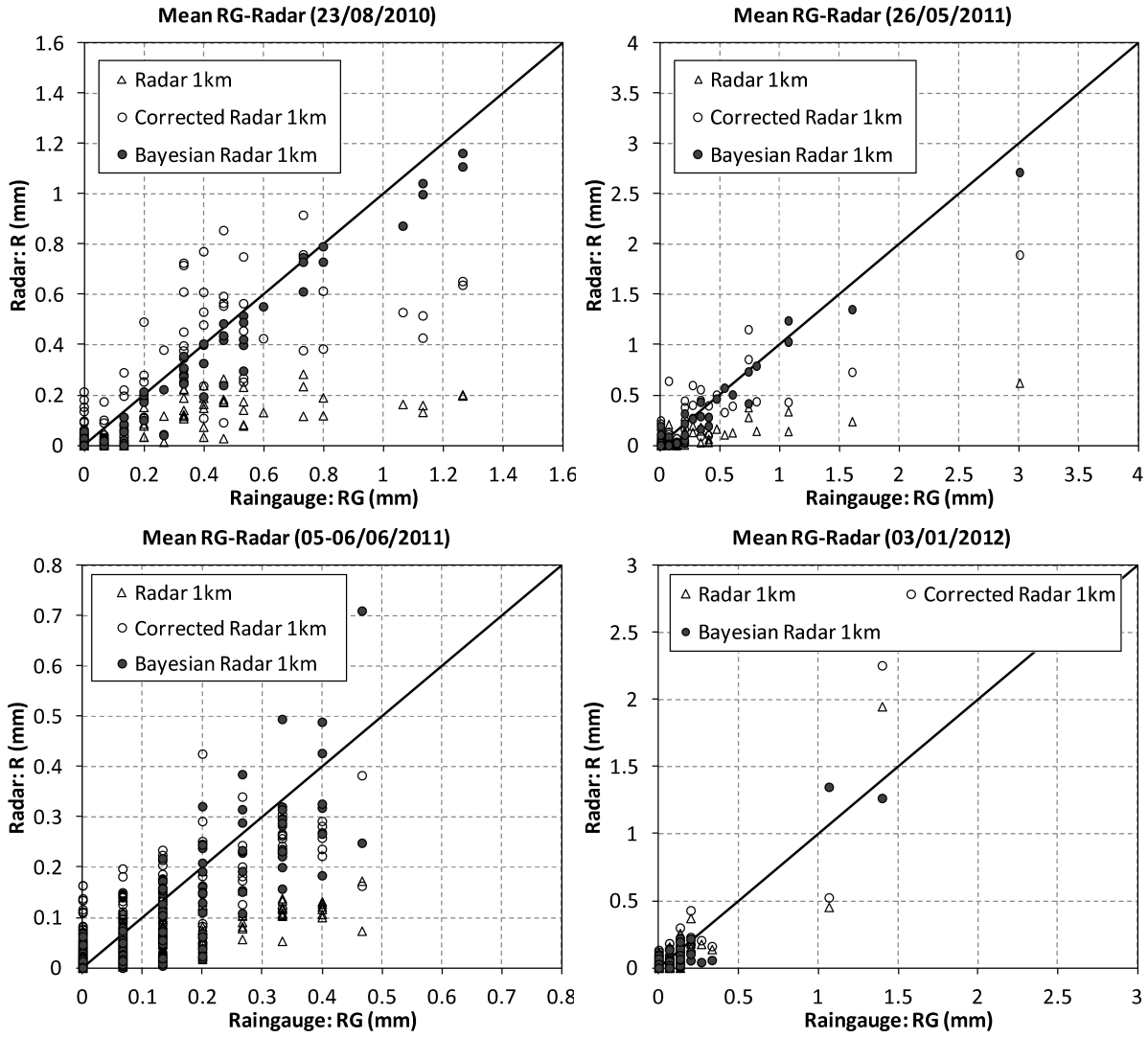


Figure 3.8: The quantile comparison of the raingauge observations and the various radar rainfall estimates (each point represents the instantaneous rainfall depth in 5-min time intervals. The original radar data: triangular markers; the mean-field bias corrected radar estimates: round markers; the Bayesian-based adjusted radar estimates: filled round markers) over the Cranbrook catchment for the four selected events

The results of the linear regression analysis are given in Tables 3.2-3.5. It can be observed that the R^2's of the Radar 1 km estimates are in general around 0.5, but the β's are in general far from 1. This means that the Radar 1 km estimates have geometrically similar pattern to the RG observations; however, there is a big quantitative difference (i.e. bias) between them. Through mean-field bias adjustment, the β's are largely improved, but the R^2's are the same. This means that in the aspect of pattern similarity, the mean

bias adjustment fully relies on the Radar 1 km estimates, and has no ability to correct the pattern based upon local RG information. For the Bayesian Radar 1 km estimates, both measures are in general improved. This means that the Bayesian adjustment can not only adjust the quantitative bias, but also correct the geometric pattern of radar rainfall estimates by merging local RG information.

In addition, the rmse (root mean squared error) measure was also used to evaluate the overall similarity between raingauge observations and different radar estimates. The results show that, whether over the locations of raingauges or the whole catchment, the Bayesian Radar 1 km estimates in generally give significantly improved similarity, as compared to the Radar 1 km and the Corrected Radar 1 km estimates. This suggests that the Bayesian-based adjustment has a better ability to adjust the original radar estimates with the local rainfall information.

The corresponding flow levels of the up-, mid- and downstream pipes resulting from the Bayesian Radar 1 km inputs are shown as the dashed-dotted lines in Figures E.5-E.8. It can be seen that, except the 03/01/2012 event, the Bayesian Radar 1 km hydraulic outputs in general have a better agreement with the RG outputs and the level observations, particularly in terms of the timing and the quantity of peaks. It is mainly due to the better reproduction of rainfall profiles in both quantity and geometry. This suggests that, in addition to rainfall mean bias, the variability of rainfall is another important factor and shall not be ignored.

Table 3.6 summarises the observed (Obs) and estimated (RG, Radar 1km, Corrected Radar 1km and Bayesian Radar 1km) flow depth peaks and their differences (in percentage) at the level gauge in the sewer system of the Valentine Park (termed "pipe 463.1" in the hydraulic model) for each event[4]. It can be observed that performance of the RG and adjusted Radar hydraulic outputs is much better than the Radar 1 km outputs; and the RG and the Bayesian Radar 1 km estimates in general produce better flow level peaks than the Corrected Radar 1 km estimates, particularly when the peaks are higher.

A summary of the flow level peaks respectively at the up-, mid- and down-stream of the catchment by using various rainfall estimates as input is provided in Table 3.7. It can be seen that due to the large bias between the mean RG and the Radar 1 km estimates, the differences between their hydraulic outputs are significant. Nonetheless, through the mean bias adjustment (see the "Corrected Radar 1km" column), these differences can be largely reduced. This suggests that the rainfall mean bias is the major factor dominating

[4]Due to the breakdown of the level gauge, the observations of the 03/01/2012 event are unavailable.

the performance of flood modelling. However, it can be seen that the Bayesian Radar 1km outputs in general have a better agreement with the RG outputs than the Corrected Radar 1km outputs (except the 03/01/2012 event). This indicates that the spatial variations in rainfall will propagate through hydraulic modelling; therefore, the ability to reproduce spatial variability must be assessed.

The R^2 and β coefficients are used here again to measure the geometrical and quantitative similarities of the hydraulic outputs using the RG and various radar rainfall estimates as inputs (see Table 3.8). From the Radar 1km and the Corrected Radar 1km columns, it can be observed that the mean bias adjustment causes significant improvements in β but no obvious improvements in R^2. This suggests that the geometrical similarity between the RG and the Radar 1km outputs cannot be improved through mean bias correction, and therefore the faulty timing for capturing rainfall peaks is not fully smoothed away after the rainfall-runoff conversion and the hydraulic process. Nonetheless, the timing problem can be effectively improved by better reproducing rainfall profiles using the Bayesian-based adjustment.

In addition, it can be seen that, even though the Corrected Radar 1km estimates perform better in the reduction of total rainfall bias than the Bayesian Radar 1km estimates, the β's of the associated hydraulic outputs are not always better. For example, for the 23/08/2010 and 26/05/2011 events, significant improvements on the β's can be observed when using Bayesian Radar 1km as input. These results suggest the importance of capturing rainfall variability, which is equally critical as the bias correction, in particular for the short-term flood simulation.

3.4 Summary

In this chapter, raingauge and radar rainfall estimates, most widely-used rainfall data sources for urban hydrology, are introduced; the former gives accurate point rainfall information, whilst the latter provides a better and broader description of the spatial and temporal variations in rainfall and has better potential to produce urban rainfall forecasts in longer lead time. A combination of the information from these two sensor has the potential to extract their advantages and consequently to improve the suitability of radar rainfall estimates for urban flood modelling/forecasting

This work reviews the theoretical background of state-of-the-art gauge-based radar rainfall adjustment techniques, which are in general developed for coarser spatial- and

temporal-scale hydrological applications. It can be found that the key subject of these techniques is to effectively characterise the error fields (i.e. the quantitative differences between radar and the coincidental raingauge rainfall estimates). Based upon the methods used to characterise the error fields, these techniques can be categorised by this work into two types: mean bias correction and error minimisation. The former focuses on diminishing the averaged bias between raingauge and the co-located radar estimates, whilst the latter focuses on characterising the variances of the error (or difference) between two types of estimates using a given mathematical model.

This work implements two different adjustment methods: mean bias adjustment and Bayesian-based adjustment, respectively based upon two types of adjustment techniques, and applies them to the study site (Cranbrook catchment) to evaluate their capacity to improve operational radar measurements and consequently flood modelling.

The associated results suggest that, although the total rainfall volume (or mean bias) is in general regarded as the most important factor in hydrological modelling , the rainfall variation shall not be negligible; and actually, for short-term urban flood modelling, it may be as important as rainfall volume. Therefore, the Bayesian-based adjustment technique, which not only corrects the bias between radar and raingauge rainfall but also well reproduces the (5-min) rainfall profiles of the events, is more suitable than the mean bias adjustment for urban flood simulation in this work.

However, a further study of the Bayesian-based adjustment is necessary, which can be two aspects. In the theoretical aspect, the mathematical models (i.e. Gaussian and exponential semi-variograms) that are respectively used to characterise spatial feature of point rainfall information and the error fields in the Block-Kriging interpolation and the Kalman filter algorithm can be further researched. For example, the impact of using different mathematical models shall be evaluated or the possibility to dynamically alter mathematical models can be explored. In addition, with the increase of spatial and temporal resolutions, the distributions of error fields tend towards high nonlinearity and therefore the conventional mathematical models (e.g. Gaussian semi-variograms) could be insufficient to satisfactorily characterise them. Alternative mathematical models (such as Multifractals) are suggested in order to better capture the features of error fields.

In the practical aspect, the applicability of the Bayesian-based adjustment to different types of storms (i.e. frontal and convective storms and probably their mixtures) can be further explored. According to the results of this work, different uncertainty sources could be found when radar and raingauge measurements of different types of storms are being

merged. The associated impacts on the accuracy of subsequent hydrological and hydraulic modelling shall be assessed in the future work.

Table 3.2: Summary statistics of the raingauge observations and the coincidental radar estimates for the 23/08/2010 event at the locations of local raingauges and over the Cranbrook Catchment (R^2: coefficient of determination; β: the regression coefficient; rmse: root mean squared error)

Data Type	Total (mm)	Maximum (mm/hr)	R^2	β	rmse (mm/hr)
Cranbrook Catchment					
RG	23.53	11.09	-	-	-
Radar 1km	6.80	3.41	0.57	0.18	3.71
Corrected Radar 1km	21.95	14.08	0.57	0.57	2.47
Bayesian Radar 1km	19.49	13.96	0.88	0.78	0.91
Beal HS					
RG	23.80	19.20	-	-	-
Radar 1km	8.54	3.73	0.43	0.15	4.13
Corrected Radar 1km	27.56	12.04	0.43	0.49	3.08
Bayesian Radar 1km	20.36	13.25	0.74	0.71	2.14
Chadwell HS					
RG	23.20	19.20	-	-	-
Radar 1km	5.79	3.39	0.36	0.14	3.38
Corrected Radar 1km	18.69	10.94	0.36	0.44	4.23
Bayesian Radar 1km	18.35	14.32	0.79	0.72	1.99
Ursuline HS					
RG	23.60	19.20	-	-	-
Radar 1km	7.55	3.83	0.56	0.21	3.89
Corrected Radar 1km	24.37	12.36	0.56	0.66	2.79
Bayesian Radar 1km	20.25	15.28	0.86	0.81	1.60

Table 3.3: Summary statistics of the raingauge observations and the coincidental radar estimates for the 26/05/2011 event at the locations of local raingauges and over the Cranbrook Catchment (R^2: coefficient of determination; β: the regression coefficient; rmse: root mean squared error)

Data Type	Total (mm)	Maximum (mm/hr)	R^2	β	rmse (mm/hr)
Cranbrook Catchment					
RG	15.53	36.00	-	-	-
Radar 1km	4.88	7.47	0.66	0.14	3.80
Corrected Radar 1km	14.85	22.76	0.66	0.42	2.28
Bayesian Radar 1km	13.84	32.61	0.75	0.55	0.90
Beal HS					
RG	16.40	26.40	-	-	-
Radar 1km	4.31	8.48	0.71	0.23	3.63
Corrected Radar 1km	13.12	25.81	0.71	0.71	2.34
Bayesian Radar 1km	17.83	29.83	0.74	0.83	2.26
Chadwell HS					
RG	14.00	38.40	-	-	-
Radar 1km	4.70	7.53	0.46	0.18	4.20
Corrected Radar 1km	14.32	22.93	0.46	0.54	3.60
Bayesian Radar 1km	14.37	30.70	0.87	0.78	1.79
Ursuline HS					
RG	16.20	55.20	-	-	-
Radar 1km	6.29	10.89	0.52	0.20	5.50
Corrected Radar 1km	19.16	33.16	0.52	0.62	4.66
Bayesian Radar 1km	13.76	34.40	0.83	0.60	3.19

Table 3.4: Summary statistics of the raingauge observations and the coincidental radar estimates for the 05-06/06/2011 event at the locations of local raingauges and over the Cranbrook Catchment (R^2: coefficient of determination; β: the regression coefficient; rmse: root mean squared error)

Data Type	Total (mm)	Maximum (mm/hr)	R^2	β	rmse (mm/hr)
Cranbrook Catchment					
RG	20.87	5.60	-	-	-
Radar 1km	9.48	2.31	0.64	0.28	1.07
Corrected Radar 1km	20.97	5.11	0.64	0.61	0.76
Bayesian Radar 1km	16.89	8.52	0.74	0.79	0.68
Beal HS					
RG	21.00	7.20	-	-	-
Radar 1km	8.24	2.15	0.42	0.18	1.39
Corrected Radar 1km	18.23	4.75	0.42	0.39	1.16
Bayesian Radar 1km	14.74	8.55	0.64	0.60	0.95
Chadwell HS					
RG	20.60	7.20	-	-	-
Radar 1km	8.80	2.28	0.40	0.18	1.44
Corrected Radar 1km	19.47	5.55	0.40	0.41	1.24
Bayesian Radar 1km	15.63	6.94	0.30	0.36	1.37
Ursuline HS					
RG	21.00	7.20	-	-	-
Radar 1km	11.25	3.23	0.43	0.24	1.29
Corrected Radar 1km	24.89	7.14	0.43	0.53	1.18
Bayesian Radar 1km	18.77	8.61	0.73	0.68	0.80

Table 3.5: Summary statistics of the raingauge observations and the coincidental radar estimates for the 03/01/2012 event at the locations of local raingauges and over the Cranbrook Catchment (R^2: coefficient of determination; β: the regression coefficient; rmse: root mean squared error)

Data Type	Total (mm)	Maximum (mm/hr)	R^2	β	rmse (mm/hr)
Cranbrook Catchment					
RG	8.93	16.80	-	-	
Radar 1km	7.55	23.40	0.76	0.98	0.99
Corrected Radar 1km	8.73	27.07	0.76	1.13	1.16
Bayesian* Radar 1km	6.88	16.19	0.86	0.94	0.69
Beal HS					
RG	11.40	45.60	-	-	-
Radar 1km	9.66	49.52	0.94	1.02	1.07
Corrected Radar 1km	11.17	57.28	0.94	1.18	1.55
Bayesian* Radar 1km	6.29	16.67	0.70	0.37	3.24
Ursuline HS					
RG	9.80	34.00	-	-	-
Radar 1km	6.25	7.63	0.45	0.26	2.87
Corrected Radar 1km	7.23	8.83	0.45	0.30	2.79
Bayesian* Radar 1km	7.23	24.40	0.86	0.68	1.44

Table 3.6: Summary of the observed (Obs) and estimated (RG, Radar 1km, Corrected Radar 1km and Bayesian Radar 1km) peak water levels at the Valentine Park sewer (pipe 463.1 in the hydraulic model) for each event and the relative differences with the observed data

Events	Obs (m)	RG (m)	Radar 1km (m)	Corrected Radar 1km (m)	Bayesian Radar 1km (m)
23/08/2011	0.633	0.655	0.287	0.550	0.640
	-	(3.51)	(-52.9)	(-29.1)	(1.27)
26/05/2011	0.672	0.710	0.308	0.600	0.721
	-	(5.65)	(51.3)	(-23.4)	(8.16)
05-06/06/2011	0.346	0.395	0.226	0.344	0.412
	-	(14.1)	(-30.3)	(-1.09)	(19.1)

Table 3.7: Summary of the estimated (RG, Radar 1km, Corrected Radar 1km and Bayesian Radar 1km) peak water levels at three selected pipes (pipe 1455.1, 463.1 and 307.1, respectively located at the up-, mid- and down- streams of the Cranbrook catchment) for each event and the relative differences (%)with the peak water levels obtained by using raingauge data as inputs

Pipe No.	RG (m)	Radar 1km (m)	Corrected Radar 1km (m)	Bayesian Radar 1km (m)
23/08/2011 event				
1455.1 (Upstream)	0.210	0.117	0.191	0.204
	-	(-79.8)	(-10.1)	(-2.91)
463.1 (Midstream)	0.655	0.287	0.550	0.640
	-	(-128.6)	(-19.2)	(-2.38)
307.1 (Downstream)	0.761	0.355	0.635	0.746
	-	(-114.2)	(-19.9)	(-2.04)
26/05/2011 event				
1455.1 (Upstream)	0.245	0.135	0.213	0.269
	-	(-81.3)	(-15.3)	(8.81)
463.1 (Midstream)	0.710	0.308	0.600	0.721
	-	(-130.7)	(-8.3)	(1.53)
307.1 (Downstream)	0.810	0.371	0.692	0.795
	-	(-118.4)	(-17.0)	(-1.87)
05-06/06/2011 event				
1455.1 (Upstream)	0.159	0.088	0.120	0.159
	-	(-80.5)	(-32.7)	(-0.45)
463.1 (Midstream)	0.395	0.226	0.344	0.412
	-	(-74.3)	(-14.9)	(4.15)
307.1 (Downstream)	0.459	0.293	0.436	0.491
	-	(-56.8)	(-5.18)	(6.51)
03/01/2012 event				
1455.1 (Upstream)	0.271	0.232	0.251	0.194
	-	(-17.1)	(-8.20)	(-39.8)
463.1 (Midstream)	0.547	0.426	0.463	0.354
	-	(-28.3)	(-18.2)	(-54.4)
307.1 (Downstream)	0.650	0.470	0.505	0.443
	-	(-38.2)	(-28.6)	(-46.7)

Table 3.8: Summary statistics of the estimated (RG, Radar 1km, Corrected Radar 1km and Bayesian Radar 1km) water levels at the three selected pipes (pipe 1455.1, 463.1 and 307.1, respectively located at the up-, mid- and down- streams of the Cranbrook catchment) compared to the water levels obtained by using raingauge data as inputs

Pipe No.	Radar 1km		Corrected Radar 1km		Bayesian Radar 1km	
	R^2	β	R^2	β	R^2	β
23/08/2011 event						
1455.1 (Upstream)	0.724	0.346	0.740	0.770	0.892	0.894
463.1 (Midstream)	0.879	0.399	0.856	0.830	0.955	0.962
307.1 (Downstream)	0.888	0.416	0.873	0.866	0.964	0.975
26/05/2011 event						
1455.1 (Upstream)	0.787	0.289	0.839	0.655	0.888	0.899
463.1 (Midstream)	0.904	0.368	0.898	0.784	0.961	0.953
307.1 (Downstream)	0.865	0.377	0.886	0.813	0.969	0.947
05-06/06/2011 event						
1455.1 (Upstream)	0.702	0.322	0.707	0.603	0.763	0.728
463.1 (Midstream)	0.904	0.451	0.903	0.781	0.830	0.777
307.1 (Downstream)	0.923	0.474	0.915	0.822	0.869	0.802
03/01/2012 event						
1455.1 (Upstream)	0.903	0.754	0.905	0.828	0.790	0.575
463.1 (Midstream)	0.891	0.725	0.898	0.801	0.902	0.638
307.1 (Downstream)	0.922	0.722	0.926	0.796	0.934	0.663

Chapter 4

Rainfall Downscaling

This chapter describes the major contribution of this PhD programme; that is, the development of rainfall downscaling models based upon the cascade process. In order to provide essential background of rainfall downscaling, a brief review will be firstly given of statistically-based rainfall downscaling techniques over different scales and their applications in the hydrological field. Then, a detailed review of the theory of multifractals will be presented to establish the theoretical background for the new cascade-based models developed in this work. Afterwards, the idea of two new downscaling models are detailed. One of them can be used for both spatial and temporal downscaling, whilst the other is only for temporal downscaling. These models will be further applied to historical rainfall events (recorded by radar and raingauge sensors, respectively) in the Greater London area to evaluate their applicability to short-term and small-scale urban hydrological applications.

However, in the process of rainfall downscaling, it is inevitable to cause additional uncertainty. A further study of the uncertainty issues induced by the proposed techniques and their combination with the adjustment techniques (in Chapter 3) will be conducted in Chapter 5.

4.1 Reviews of downscaling techniques for hydrological applications

4.1.1 Generalised Linear Models

There are a multitude of rainfall disaggregation models in the literature which can be classified into three categories based upon the theories respectively used. The first cat-

egory of disaggregation models are purely statistical models, among which for example Generalised Linear Models (GLMs, shown as Figure 4.1) have been successfully applied to the studies of disaggregation processes of rainfall sequences, particularly at daily time scales (Segond et al., 2006; Chandler and Wheater, 2002; Stern and Coe, 1984). GLMs are extended from the simple linear regression models, of which the idea is to predict a probability distribution for a rainfall sequence at a specific site of interest by linking the mean of that distribution to the values of a certain number of associated quantities known as "covariates" or "predictors." A two-stage approach, constituting the Occurrence and Amounts models, has been widely adopted to analyse daily or coarser rainfall data. In the first stage (Occurrence model), the pattern of dry and wet days from a single rainfall sequence is modelled using logistic regression. Then, in the second stage (Amounts model), the amount of rain on wet days is analysed by fitting gamma distributions. The advantage of GLMs is that they enable not only to profile the daily variability of rainfall sequences but also to reflect the effects of long-term climatic trends and orographic variability on rainfall patterns by considering the seasonal cycles and location-dependent coefficients in covariates (Chandler and Wheater, 2002).

Moreover, the conventional GLMs for individual sites have been extended to generate simultaneous rainfall sequences at several sites by considering the spatial dependence among these sites (Yang et al., 2005). Joint distributions, instead of individual distributions, for next day's rainfall at all sites are respectively specified for the Occurrence and Amount models, to implement GLMs with spatial dependence structures. The results show that GLMs have not only the abilities to reproduce a number of important statistical features of daily rainfall sequences at individual sites, but also the potential to simulate those at a network of sites. However, the quality of simulation/prediction results of GLMs relies strongly upon the selection of an appropriate set of predictors. This means that predictor vectors have to be reconstructed site by site; moreover, some factors may be difficult to quantify as predictors. The estimation of the predictors' parameters also affects simulation/prediction results. A multitude of diagnostic methods has been developed to assess this estimation. Each of these methods however targets different uncertainty issues and may generate different results (Chandler and Wheater, 2002). Therefore, to attain a proper diagnostic method, it may need a iterative process. Moreover, although GLMs with spatial dependence structures have been developed to simulate multi-site rainfall sequences, their applicability and generalisation are limited due to the fact that the spatial dependence is strongly associated with the scales of the area of interest. The proposed method in Yang

et al. (2005) therefore may not satisfactorily cope with the spatial dependence of rainfall sequences over a larger area.

4.1.2 Poisson cluster models

Second, Poisson-cluster models were developed based upon a theory of stochastic point processes by considering physically-based parameters which constitute the hierarchical structure of the rainfall process. The Bartlett-Lewis rectangular pulse models (shown as Figure 4.2) are one specific class of the widely-used individual-site rainfall models based upon a Poisson-cluster process. The general assumptions of these models are: origins of storms t_i arrive according to a Poisson process; cell origins t_{ij} of each storm arrive following another Poisson process starting with the storm; the duration of each storm (v_i) after its arrival is exponentially distributed; and each cell's duration w_{ij} and intensity X_{ij} are exponentially distributed (Koutsoyiannis, 2003; Onof et al., 2000). All these distributions are assumed independent, and the parameters associated with these assumptions are generally estimated using standard model fitting techniques (e.g. the method of moments in Onof and Wheater (1993), considering six statistics: mean, variance, lag-one autocorrelation, and proportion of dry periods at hourly and daily intervals). The selection of fitting statistics however is somewhat subjective. This may result in problems for parameter estimation; thus, improvements in the fitting method have been further proposed, and for details the reader is referred to the discussion in Onof et al. (2000).

Poisson-based models have been widely improved and applied to rainfall modelling. They are also useful to disaggregate daily rainfall sequences to hourly ones (Koutsoyiannis and Onof, 2001; Onof and Wheater, 1993, 1994; Onof and Arnbjerg-Nielsen, 2009). For example, Onof and Wheater (1993) and Onof and Wheater (1994) improved the basic Bartlett-Lewis rectangular pulse model by randomising the duration of cells and applying a gamma instead of an exponential distribution to the cell intensity. These two modifications respectively address the general problems in Poisson-based models, i.e., the overestimation of the proportions of dry periods and relatively poor performance in reproducing the extreme values of the distribution of rainfall depth. Furthermore, the conventional Poisson-based models for individual sites have been extended by considering the cross-correlation among the raingauge station of interest and its neighbouring stations to generate spatially and temporally consistent hourly rainfall sequences at multiple sites (Koutsoyiannis, 2003). This achievement may be applied to generate spatially consistent hourly rainfall sequences in raingauges where merely daily data are available.

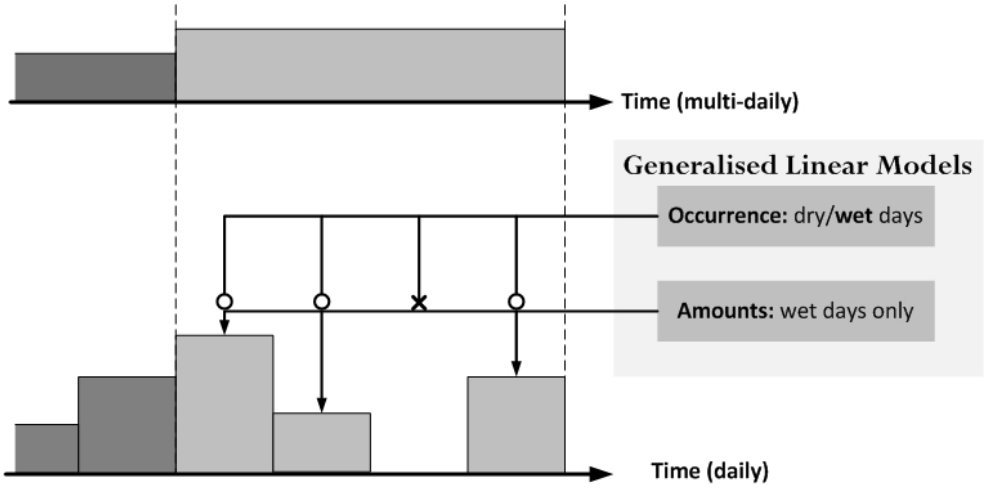


Figure 4.1: The sketch for the two-stage Generalised Linear Models: Occurrence and Amounts models

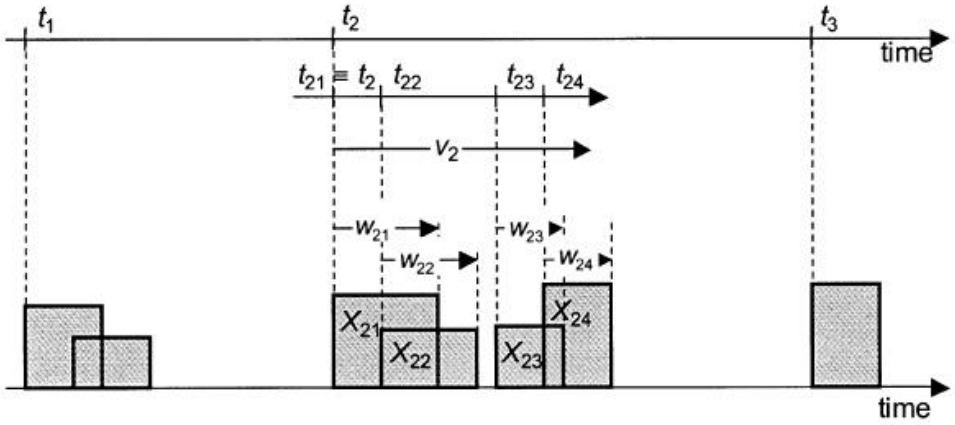


Figure 4.2: The sketch for the Bartlett-Lewis rectangular pulse model (Koutsoyiannis and Onof, 2001)

4.1.3 Cascade-based models

The third type of disaggregation models are cascade methods, which are developed by investigating the scale-invariant behaviour of complex nonlinear processes. Random multiplicative cascade methods have been successfully applied to rainfall modelling, particularly the distribution of high-resolution rainfall observations both in space and time. This type of model is basically constructed based upon the multiplicative cascade process, which has been thoroughly characterised using the theory of multifractals (see Section 4.2 for details), and the random cascade is the most widely-used process to develop this type of

models. The idea of the multiplicative cascade process is to distribute rainfall volumes on successive regular subdivisions of an interval in a randomly or deterministically multiplicative manner. In order to simulate the process of multiplicative cascades, discrete- and continuous-in-scale schemes are respectively developed. The former provides an efficient framework to reproduce the structures (i.e. specific statistical features) of fine-scale rainfall processes. For example, aiming to integrate disaggregation models at various timescales, Onof and Arnbjerg-Nielsen (2009) adopted a canonical cascade generator, based upon log-Poisson distributed random variables, to generate 5-min rainfall sequences from hourly ones; Molnar and Burlando (2005) used the intermittent lognormal β-model, developed by Over and Gupta (1996), to generate 10-min rainfall sequences. Although this type of methods, based upon the discrete-in-scale scheme, was critisised for the artificially constructed results because it is merely scaling for integer powers, they are however pragmatic choices when employed to produce high-resolution rainfall information because they are relatively efficient and have been widely verified to be able to preserve specific statistical features (Gupta and Waymire, 1993; Over and Gupta, 1996; Deidda et al., 1999; Pathirana et al., 2003; Shrestha et al., 2004; Molnar and Burlando, 2005; Onof and Arnbjerg-Nielsen, 2009; Kang and Ramírez, 2010).

Whereas the discrete-in-scale scheme carries out an efficient simulation with a somewhat artificial pattern, the continuous-in-scale scheme provides a promising framework to generate more realistic and visually smooth rainfall distributions for it is scaling not only for integer powers (Lovejoy and Schertzer, 1990, 2010a,b). To generate realistic rainfall distributions, fractional integration is however necessary to simulate the rainfall structures at all intermediate scales via numerical calculation. This suggests that, although the efficiency of the calculation has been somewhat improved (Lovejoy and Schertzer, 2010a,b), the total simulation time is still too long for some practical uses, e.g., the Nearly Real-Time (NRT) flood modelling. Moreover, although it has been validated that the continuous-in-scale Universal multifractal cascade are able to satisfactorily reproduce the (multi-) scaling features of the observed rainfall, its ability to reproduce other (statistical) features is seldom explored (Bellone, 2004). The latter ability however is very crucial for hydrological modelling uses (e.g. ground runoff and sewer network simulation), and has been demonstrated in a number of previous works that the discrete-in-scale cascade models are feasible techniques with this ability. Concerning efficiency and applicability for urban hydrological uses, this work therefore focuses on the development of discrete-in-scale cascade methods.

The construction of discrete-in-scale cascade-based downscaling models is based upon

the multiplicative cascade process. A more detailed introduction of this process is necessary and therefore carried out as follows. The multiplicative cascade is a single process to generate fine-scale data by subdividing a unit set into a fixed number of smaller and smaller subsets according to a fixed set of fragmentation (contracting) ratios and at the same time subdividing the associated unit measure by another set of fragmentation ratios. A random process can therefore be created based upon a self-similar process with a deterministic set of fragmentation ratios (Mandelbrot, 1989), such that the mass of measures is exactly or statistically conserved.

Figure 4.3 is the schematic of a binomial multiplicative cascade process. When it is applied to rainfall time series downscaling, the aforementioned set and measure are respectively mapped to the timescale and the rainfall volume of a given rainfall series. Between two successive levels, each timescale is subdivided into two smaller sub-timescales with equal length (the number of subdivisions is termed the branching number b, where $b \geq 2$ and is usually assumed to be 2); at the same time, the associated rainfall volume, denoted V, are subdivided into two sub-volumes (e.g. V_1 and V_2 at level $n = 1$) according to given fragmentation ratios or weights (denoted w_i^n, where n represents the cascade level and i is the index of the corresponding weights to given sub-volumes, $i = 1, \ldots, b$ and $b = 2$); for example, w_1^1 and w_2^1 are the weights for cascade levels between $n = 0$ and $n = 1$; w_1^2 and w_2^2 for the weights between $n = 1$ and $n = 2$. In each branching, constraints are further applied to these weights in order to conserve the rainfall volume; they are $w_1^1 + w_2^1 = 1$ and $w_1^2 + w_2^2 = 1$ (consequently, $V_1 + V_2 = V \cdot w_1^1 + V \cdot w_2^1 = V$ and $V_{21} + V_{22} = V_2 \cdot w_1^2 + V_2 \cdot w_2^2 = V_2$).

To implement this application, it is crucial to derive these fragmentation ratios in order to construct the multiplicative cascade processes that can be used to reproduce the observed temporal (or/and spatial) rainfall structures. These fragmentation ratios could be a set of constants or follow a specific probability distribution; and the function used to generate these ratios is called the cascade generator. As aforementioned, the random cascade is the most widely-used process to develop cascade methods and it is usually assumed to follow a given theoretical probability distribution, such as log-Poisson or log-Normal distributions; however, the type and parameters of generators strongly depend upon the probability distribution of specific rainfall features. This indicates that a generator may radically alter when a different rainfall field/sequence starts. Thus, it is difficult to find a promising and general generator. New methodologies were therefore developed in this work, which decouples the dependence of existing cascade models from specific probability

distributions and consequently provides a simpler and more general form of the generator. Similar to conventional cascade methods, the proposed methodologies are mainly based upon the theory of multifractals, which provides the promising framework to satisfactorily characterise the process of cascading. A detailed review of the theory of multifractals and its link to cascade methods are therefore given first in the following Section 4.2 for providing necessary theoretical background to enable further explanation of the new development in this work.

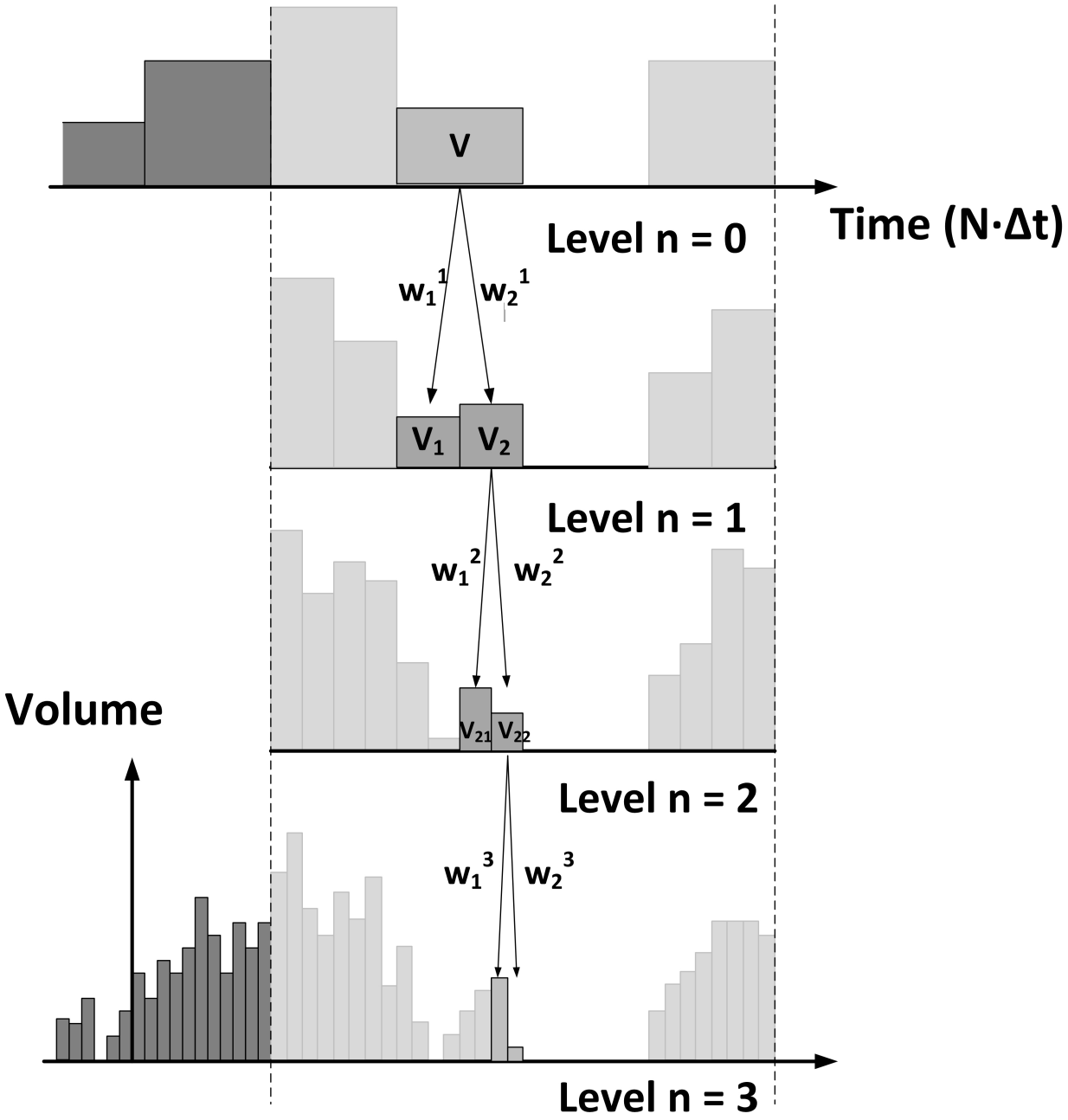


Figure 4.3: The diagram for a multiplicative cascade process

4.2 Theory of Multifractals

4.2.1 Euclidean Dimension

In Euclidean geometry, any object has a characteristic number associated with it called a dimension. The estimation of the Euclidean dimension requires complex mathematical formalism but can be explained using a simple example as follows. There are for example a line (1-dimension, length L), a square (2-dimension, sidelength L and area L^2) and a cube (3-dimension, sidelength L and volume L^3). If the line is divided into m equal segments, the length of each segment is L/m; in other words, it needs $N = m$ segments (length L/m) to cover the line and the contracting ratio (or called the scaling ratio) against the original line is $r = (L/m)/L = 1/m = 1/N$. If each side of the square is divided into m segments, it needs $N = m^2$ small squares (area $(L/m)^2$) to cover the original square and the contracting ratio for each side is $r = \sqrt[2]{(L/m)^2/L^2} = \sqrt{(1/N)}$. Similarly, it needs $N = m^3$ small cubes (volume $(L/m)^3$) to cover the original cube (the contracting ratio of each side is $r = \sqrt[3]{1/N}$) if each side of the cube is subdivided into m segments. This example can be extended to a E-dimension object, and it needs $N = m^E$ small objects to cover the original object. Based upon this derivation, it can be found that,

$$N = m^E = (\frac{1}{r})^E, \tag{4.1}$$

or

$$E = \frac{\ln N}{\ln 1/r}. \tag{4.2}$$

Based upon this definition, we may however meet some problems, such as the Cantor set, which is constructed by repeatedly deleting the open middle thirds of a set of line segments. The associated Euclidean dimension is therefore $E = \ln N/\ln 1/r = \ln 2/\ln 3 = 0.631$, which conflicts with the definition of integer dimension in Euclidean Geometry. Therefore, further theories were developed to explain dimension in a more general idea.

4.2.2 Monofractals

Fractals, or Monofractals, provide a simple framework to characterise the scale-invariant features of a given natural process primarily based upon a simple scaling relationship (Mandelbrot, 1983):

$$N(\epsilon) \sim \epsilon^{-D_F}, \tag{4.3}$$

where $N(\epsilon)$ is some property of the natural process observed at a specific scale ϵ (or so-called box, which is the same as r in Eq.(4.1)), and D_F is a scaling exponent. This relationship has been widely used to analyse the geometric structures of certain processes by defining $N(\epsilon)$ as the number of boxes needed to cover the whole structure. The corresponding scaling exponent D_F thus is known as a fractal dimension. It is obvious that this dimension is not necessarily an integer; in other words, it could be a fraction, which is an extension of the dimension defined in Euclidean Geometry (Eq. (4.2)). The fractal dimension of the Cantor set, i.e., $\ln 2/\ln 3 = 0.631$, which is estimated by rearranging Eq. (4.3), no longer conflicts with the definition of fractal dimension.

The structure of rainfall quantities and the fluctuations thereof have been studied based upon this simple scaling relationship (Lovejoy and Mandelbrot, 1985; Schertzer and Lovejoy, 1987; Olsson et al., 1992, 1993). For example, Lovejoy and Mandelbrot (1985) defined this simple scaling feature in terms of the probability distribution of a random function $X(t)$ and its fluctuations $\Delta X(t)$ respectively as $X(\lambda t) \stackrel{d}{=} \lambda^H X(t)$ and $\Delta X(\lambda \Delta t) \stackrel{d}{=} \lambda^H \Delta X(\Delta t)$. Here, for arbitrary t_0 and t_1, $\Delta t = t_1 - t_0$, $\Delta X = X(t_1) - X(t_0)$, $t_2 = t_0 + \lambda(t_1 - t_0)$ and $\Delta X(\lambda \Delta t) = X(t_2) - X(t_0)$. The parameter λ is the resolution with corresponding scale $\epsilon = L/\lambda$, where L is the largest scale of the structure and is obtained when $\lambda = 1$; H is a scaling exponent related to the fractal dimension (D_F); and the symbol $\stackrel{d}{=}$ denotes identity statistical distribution. This definition indicates a relation that the probability distribution of rainfall or its fluctuations will change according to the ratio λ^H when the measurement scale or its fluctuations are rescaled by a factor λ. Olsson et al. (1992) also analysed the simple scaling feature of rainfall sequences observed in Lund, Sweden, using box-counting methods. The results showed that the same fractal dimensions were investigated in minute, daily, and monthly observations when proper threshold values were respectively applied.

These works generally conclude that the scale invariance that is characterised by a single fractal dimension indeed exists at a specific scale interval; however, for the structures of

most natural phenomena, scaling features cannot be entirely illustrated using merely one quantity, or a set of them. The theory of Multifractal Measures, or Multifractals, therefore was developed to generalise the concept of fractal sets to measures. This generalisation is implemented by characterising the scale-invariant features of multifractal measures by a function instead of a single number (Evertsz and Mandelbrot, 1992).

4.2.3 Multifractals

In order to explain Multifractals, a quantity, namely the coarse Hölder exponent, is introduced herein:

$$\alpha = \frac{\log \mu(\epsilon)}{\log \epsilon}, \tag{4.4}$$

which is the logarithm of the measure within a given box, $\mu(\epsilon)$, divided by the logarithm of the sidelength of that box ϵ. This quantity describes the scaling behaviour of a local μ located within a certain finite interval ϵ in the support of the measure. Whilst fractals are useful to represent whether an event belongs to a fractal set or not, multifractals represent how intensely an event behaves fractally. This intensity is generally measured by counting the number of boxes of side ϵ having a coarse Hölder exponent equal to a given α. Based upon this number $N_\epsilon(\alpha)$, an analysis of the frequency distribution of this α could be carried out by introducing

$$f_\epsilon(\alpha) = -\frac{\log N_\epsilon(\alpha)}{\log \epsilon}, \tag{4.5}$$

where $f_\epsilon(\alpha)$ is the logarithm of $N_\epsilon(\alpha)$ divided by the logarithm of the box size ϵ. The points $(\alpha, f_\epsilon(\alpha))$ compose a plane domain of singular measures, of which the upper boundary is a concave curve shaped like the symbol $\cap$ and leaning to one side in most cases (shown as Figure 4.4). This upper boundary defines the function $f(\alpha)$, which is loosely similar to the fractal dimension D_F but is defined within the subsets of the size ϵ having coarse Hölder exponent α. In other words, the whole $f(\alpha)$ curve, known as a multifractal spectrum, represents an infinite number of fractal dimensions (Evertsz and Mandelbrot, 1992; Mandelbrot, 1989).

Some basic properties of the $f(\alpha)$ curve can be briefly reviewed herein by letting $A^\alpha(\epsilon)$

be a subset of boxes covering the support of the measure having a coarse Hölder exponent between α and $\alpha + d\alpha$; then, the corresponding measure within this subset is $\mu(A^{\alpha}(\epsilon)) = N_{\epsilon}(\alpha)\epsilon^{\alpha}d\alpha = \epsilon^{-f(\alpha)_{\epsilon}+\alpha}d\alpha \sim \epsilon^{-f(\alpha)+\alpha}d\alpha$. Due to the fact that the total measure in all boxes is one, a relation $f(\alpha) \leq \alpha$ can be derived. This implies that the $f(\alpha)$ curve always lies under the bisector (i.e. the straight dotted line $\alpha = f(\alpha)$, shown in Figure 4.4), and there is a unique point intersecting this bisector where $f'(\alpha) = 1$ (Evertsz and Mandelbrot, 1992). Further mathematical formalism of the function $f(\alpha)$, has been well established, and for details the reader is referred to previous literatures (Falconer, 2003; Riedi, 1995; Riedi and Mandelbrot, 1995).

If the size of the space that supports the whole measure is assumed to be unity, the probability of having the coarse Hölder exponent equal to α can be derived as $P_{\epsilon}(\alpha) = N_{\epsilon}(\alpha)/\epsilon^{-E}$, where E denotes a Euclidean dimension and ϵ^{-E} is proportional to the total number of the boxes (with the side ϵ). Replace the $N_{\epsilon}(\alpha)$ term in Eq. (4.5) by this probability term; then a domain of singular densities can be estimated by defining

$$C_{\epsilon}(\alpha) = \frac{\log P_{\epsilon}(\alpha)}{\log \epsilon}, \tag{4.6}$$

As $\epsilon \to 0$, the exponent $C_{\epsilon}(\alpha)$ converges to the limit $C(\alpha)$. This function $C(\alpha)$ is termed the codimension function of singular measures due to its simple relation to $f(\alpha)$, i.e., $C(\alpha) = E - f(\alpha)$. A detailed formalism of $C(\alpha)$ and its further relations to $f(\alpha)$ have been well studied in previous research (Harte, 2001; Schertzer et al., 1997; Tessier et al., 1993).

Note that, according to the convention in previous research related to hydrological or geophysical applications, the codimension function is usually termed $C(\gamma)$ instead of $C(\alpha)$, where γ is a quantity with similar idea to α and termed the order of singularity (Schertzer and Lovejoy, 1987). A modified relationship of the codimension function and probability distributions of measures then is expressed as (Tessier et al., 1993)

$$P(\mu(\epsilon) \geq \lambda^{\gamma}) \sim \lambda^{-C(\gamma)}. \tag{4.7}$$

This equation entails that the probability distribution of the measure above a threshold quantity λ^{γ} (namely a singularity of order γ, where λ, the same as aforementioned, is the resolution) could be characterised by the associated codimension function. This relation

provides a theoretical framework for constructing random cascade models. A prototype of this type of models can be demonstrated by introducing a simplified equality deduced from Eq. (4.7):

$$P(\mu(\epsilon)/\epsilon = \lambda^{\gamma}) = P(\epsilon, \gamma) = \lambda^{-C(\gamma)}, \tag{4.8}$$

where $\mu(\epsilon)$, in a physical sense, can be explained as (normalised) rainfall quantities at a given temporal/spatial scale (ϵ) and $\mu(\epsilon)/\epsilon$ is the associated intensity. This equation has been evolved into various rainfall models which are used to generate rainfall sequences or fields (Deidda, 2000; Deidda et al., 1999; Gupta and Waymire, 1993; Molnar and Burlando, 2005; Onof and Arnbjerg-Nielsen, 2009; Onof et al., 2005; Over and Gupta, 1994, 1996; Pathirana and Herath, 2002; Pathirana et al., 2003; Shrestha et al., 2004). A β-model, for example, was implemented based upon Eq. (4.8) to define two states:

$$\begin{aligned} P(\mu(\epsilon)/\epsilon = \lambda^{\beta}) &= \lambda^{-\beta} \\ P(\mu(\epsilon)/\epsilon = 0) \quad &= 1 - \lambda^{-\beta} \end{aligned} \tag{4.9}$$

This β-model was originally developed to simulate the complex turbulent process of generating eddies and has been further used to construct space-time mesoscale rainfall generators based upon the with/without rainfall dichotomy determined by the exponent β (please see Appendix C.3 for detailed construction of β-model). Although being substantially simplified, this model produces acceptable results (Molnar and Burlando, 2005; Over and Gupta, 1996; Pathirana and Herath, 2002; Pathirana et al., 2003). Similar to the β-model that was developed based upon Eq. (4.6), the α-model and the log-Poisson model are discrete-in-scale random cascade models but are constructed by characterising cascade processes based upon more complex probability distributions; particularly the latter (the log-Poisson model) was widely used in hydrological and geophysical applications (Deidda, 2000; Deidda et al., 1999; Onof and Arnbjerg-Nielsen, 2009; Onof et al., 2005). For detailed construction of these two models, the readers are referred to Appendices C.4 and C.5. However, most of this type of models preserve only the statistical ensemble while generating successive cascades, which means that the measures (e.g. rainfall quantities) are not exactly conserved between successive cascades in these models (Olsson, 1998). This inconsistency of measures may be amplified as a finer scale or/and a short-term event is studied, which may

massively increase the input uncertainty for urban pluvial flood modelling or forecasting.

Unlike the wide applications of codimension function $C(\gamma)$ in the realm of natural phenomena, the applications of multifractal spectrum $f(\alpha)$ seem to be relatively limited due to its being deterministic. This feature could be traced back to the earlier development of the multifractal spectrum, which was based upon the study of multiplicative cascades (Mandelbrot, 1990). A deterministic multiplicative cascade is a process to generate random sequences. This process fragments a geometric set (e.g., the time scale in Figure 4.3) into smaller and smaller components according to a given set of ratios (s_1 and s_2) and at the same time fragments the associated measure of the components (e.g., the rainfall intensity or depth) by another set of ratios (w_1 and w_2). However, these ratios are unnecessary to be applied in sequence when used to fragment scales and measures. This means the sequence of ratios could be randomly altered at each branching. Nonetheless, due to the fact that the ratios used are fixed, this process can be satisfactorily characterised by the theory of self-similar multifractals and the complexities induced by randomness can be therefore circumvented through working with non-random measures (Mandelbrot, 1990).

4.2.4 Self-similar and Left-sided Multifractals

The connection between multiplicative cascade and the theory of multifractals can be linked by characterising an important feature of cascade process: self-similarity. In this section, self-similar multifractals are derived by considering a self-similar measure μ supported by a self-similar subset F of $\mathbb{R}$ (Falconer, 2003), where the self-similar measure and subset respectively represent the fragmented measure and geometric set in a self-similar multiplicative cascade process. Let $S_1, \ldots, S_b : \mathbb{R} \to \mathbb{R}$ be contracting similarities with ratios $s_1, \ldots, s_b$, where $b \geq 2$. These ratios are used to fragment the self-similar set by repeatedly divide a given interval on F into a series of subintervals, of which each is a closed interval I such that $S_i(I) \subset I$ for all i, and $S_i(I) \cap S_j(I) = \emptyset$ whenever $i \neq j$. These subintervals could be then indexed by the finite sequences $\mathcal{I}_k = \{(i_1, \ldots, i_k) : 1 \leq i_j \ \leq b\}$. Thus

$$I_{\mathbf{i}} = I_{i_1, i_2, \ldots, i_k} = S_{i_1} \circ \cdots \circ S_{i_k}(I), \tag{4.10}$$

where $\circ$ denotes the composition operator, and $\mathbf{i} = (i_1, \ldots, i_k)$, termed "address"(Evertsz and Mandelbrot, 1992), is a typical b-adic sequence of $\mathcal{I}$. The address helps determine the whereabouts of each interval, and the length of the address (k) indicates the number of

times that subdivision is carried out on subset F. If $|I| = 1$ is further assumed herein, thus

$$|I_{\mathbf{i}}| = s_{\mathbf{i}} \equiv s_{i_1} s_{i_2} \cdots s_{i_k}. \tag{4.11}$$

Let $w_1, \ldots, w_b$ be fragmentation ratios, satisfying $w_i > 0$ for all i and $\sum_{i=1}^{b} w_i = 1$. The pertinent measure with support F then can be derived as

$$\mu(I_{i_1,i_2,\ldots,i_k}) = w_{\mathbf{i}} \equiv w_{i_1} w_{i_2} \cdots w_{i_k}. \tag{4.12}$$

This measure can be easily regarded as a self-similar measure, in the sense that

$$\mu(A) = \sum_{i=1}^{m} w_i \mu(S_i^{-1}(A)). \tag{4.13}$$

for all sets A. This equation represents the process to evaluate the measure for a given subset A at a specific level in a self-similar multiplicative cascade (shown as Figure 4.3). First the measure of the associated subset at the previous level is obtained by evaluating μ on the "presubset" of A, i.e., $S_i^{-1}(A)$. Then, multiply this previous measure with fragmentation ratios w_i and finally add up the results to obtain the measure of A. By repeating this process, a self-similar multifractal measure is generated.

The properties of self-similar multifractals have been studied by previous research based upon a scaling relation between the measures and their interval size (Halsey et al., 1986; Mandelbrot, 1990):

$$\chi(q, \epsilon) = \sum_{j} \mu_j^q(\epsilon) \sim \epsilon^{\tau(q)}, \tag{4.14}$$

where the partition function $\chi(q, \epsilon)$ is the q-th order moment of the measures within a box of side ϵ. In a physical sense, $\chi(q, \epsilon)$ represents specific statistical features of the measures at the scale ϵ; for example, the first two moments (i.e. $q = 1$ and $q = 2$) of the measures are respectively related to the mean and the variance of the measures. This scaling relation performs an important feature of self-similar multifractals that the moment of measures $\chi(q, \epsilon)$ scales a power law of the form $\epsilon^{\tau(q)}$ for all $-\infty < q < \infty$. By applying with

various sizes of the box and orders of moments, the curve $\tau(q)$, shown as Figure 4.5 then can estimated and has been known as the characteristic function of multifractal measures. Moreover, the function $\tau(q)$ has been further proved to be the Legendre transform of the multifractal spectrum $f(\alpha)$, and vice versa (Falconer, 2003; Halsey et al., 1986; Mandelbrot et al., 1990):

$$f(\alpha) = \min_{-\infty<q<\infty} \{q\alpha - \tau(q)\}. \tag{4.15}$$

Analogous to multifractal spectra, codimension functions $C(\gamma)$ also has the associated Legendre transform, which is usually denoted as $K(q)$ [1] and has been widely used to demonstrate the scaling features of rainfall (Lovejoy and Schertzer, 1990; Tessier et al., 1993; Schertzer et al., 1997; Molnar and Burlando, 2005).

Since $\tau(q)$ curve is strictly convex (see the proof on page 287 in Falconer (2003)), for a given α there is a unique $q_\alpha = q(\alpha)$ to attain the minimum in equation (4.15). Differentiate $q\alpha - \tau(q)$ with respect to q and equate it to 0, thus

$$\alpha = \left.\frac{\mathrm{d}\tau}{\mathrm{d}q}\right|_{q=q_\alpha} = \alpha(q_\alpha). \tag{4.16}$$

Substituting it into Eq. (4.15) gives

$$f(\alpha) = q_\alpha \alpha(q_\alpha) - \tau(q_\alpha). \tag{4.17}$$

This equation helps understand properties of the $f(\alpha)$ curve; for example, the extremum of the $f(\alpha)$ curve for the value $\alpha = \alpha(q)$ can be derived by satisfying

$$\left.\frac{\partial}{\partial\alpha} f(\alpha)\right|_{\alpha=\alpha(q)} = q. \tag{4.18}$$

If the $f(\alpha)$ curve is differentiable, the maximum of it can be attained where $q = 0$ (shown as Figure 4.4).

[1] $K(q)$ is usually termed the structure function, and its relation with $\tau(q)$ is $K(q) = q - \tau(q) - 1$ (See Appendix C.2 for detailed derivation)

Due to the fact that $\tau(q)$ is a unique mapping to its corresponding multifractal spectrum, the features of $f(\alpha)$ could be indirectly determined by profiling the function $\tau(q)$. Previous research has studied the function $\tau(q)$ in two senses according to the range of q (Mandelbrot, 1989, 1990; Mandelbrot et al., 1990). In a restricted sense, the function $\tau(q)$ is defined for all $-\infty < q < \infty$, which indicates that the scale-invariant relation depicted by equation (4.14) is required to hold for all real number q (shown as Figure 4.15), and its corresponding "restricted" multifractal spectrum is shown as Figure 4.5. However, in a general sense, the function $\tau(q)$ is defined only for $0 \leq q < \infty$, which means that the scaling relation in equation (4.14) fails to hold for $q < 0$. As for $f(\alpha)$, only the left side of a "general" multifractal spectrum looks like it does in a "restricted" multifractal spectrum (i.e., the segment between $q \to \infty$ and $q = 0$ of the curve in Figure 4.5). The multifractal spectrum in a general sense, thus, is named the left-sided multifractal spectrum, which could be characterised by $\alpha_{max} = \infty$ with $f(\alpha_{max}) = D_0$ (a constant) and, in theory, the constant D_0 could be obtained from equation (4.14) and (4.15) as $q = 0$ (Mandelbrot, 1990).

A deterministic multiplicative cascade has been proved to behave "left-sided" in previous research (Mandelbrot, 1989, 1990; Mandelbrot et al., 1990). This suggests that the left-sided multifractal spectrum may provide a theoretically reliable framework for studying rainfall, which is implicitly consistent with previous research which considered merely the case $q > 0$ when analysing rainfall based upon the scaling relation in equation (4.14) (Olsson, 1995). However, it is still an open problem to generate rainfall sequences or fields based upon these left-sided multifractal features even though the theory has been well established.

4.2.5 The Generating Equation

A possible solution to deriving a general generator/generating methodology in synergy with left-sided multifractals is the "generating equation,"

$$\sum_{i=1}^{b} s_i^{-\tau(q)} w_i^q = 1, \tag{4.19}$$

where $s_1, \ldots, s_b$ and $w_1, \ldots, w_b$ are the fragmentation ratios respectively for the set and measure, the same as those in Eqs. (4.11) and (4.12), to repeatedly divide a self-similar set and its associated self-similar measure into b subsets and sub-measures. This equation is

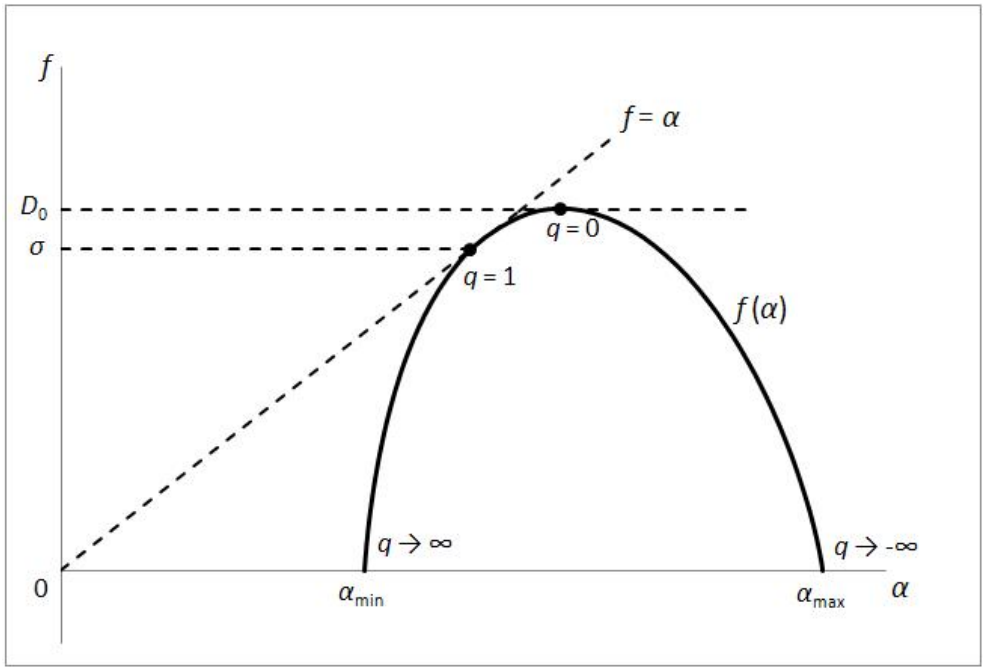


Figure 4.4: The multifractal spectrum $f(\alpha)$ estimated from a typical self-similar measure (Falconer, 2003)

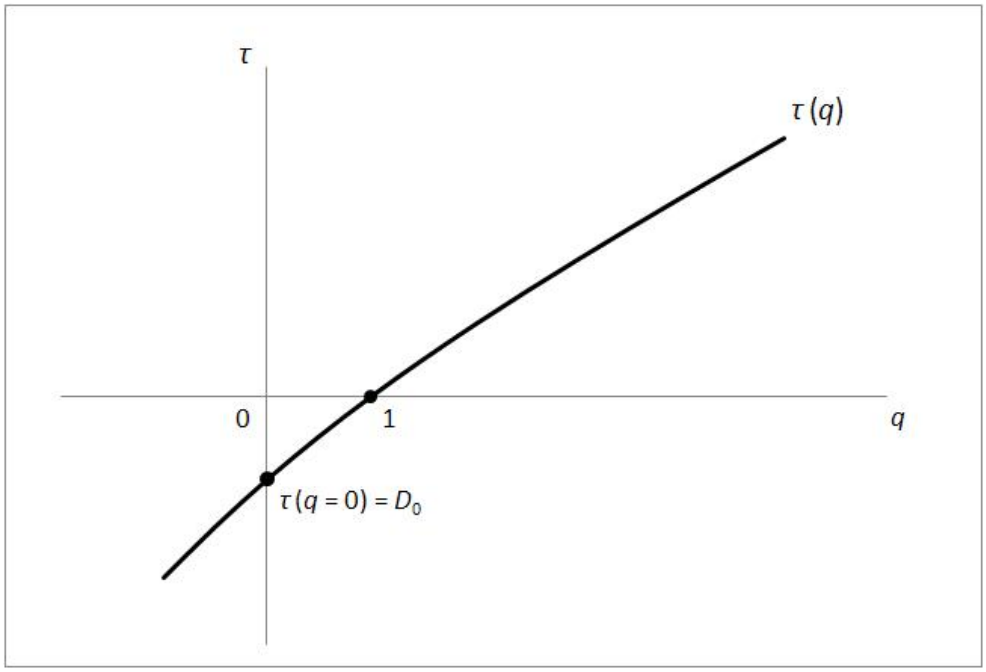


Figure 4.5: The associated Legendre transform ($\tau(q)$) of the multifractal spectrum in Figure 4.4

a simple framework to describe a multiplicative cascade with deterministic fragmentation ratios and was derived from the process of rescaling transformation on self-similar measures; for details of its derivation and further relation to a multifractal spectrum $f(\alpha)$ the reader is referred to Hentschel and Procaccia (1983) and pp. 277 - 297 of Falconer (2003).

The reason Eq. (4.19) is known as the generating equation is that one could implicitly generate the theoretical values of $\tau(q)$ via numerically solving it if all the values of s_i and w_i were known; whilst the inverse task, i.e., to derive the s_i and w_i from known $\tau(q)$, is relatively difficult and seldom explored. These ratios are the key elements to construct a general rainfall generator/generating methodology; an explicit/analytic solution of these ratios cannot, however, be obtained. A further study therefore is necessary to profile this generating equation, particularly focusing on the composition of these ratios.

It is obvious that difficulties primarily arise out of the unknown branching number b and the quantities and orders of these fragmentation ratios. An assumption of single-scaled multifractal measures (i.e., $s_i = 1/b$ for all i) is made herein to simplify these parametric problems, which gives

$$\tau(q) = -\log_b \sum_{i=1}^{b} w_i^q. \tag{4.20}$$

Harte (2001) discussed this equation using an example considering the case of the multinomial measure with $b = 10$ to implicitly demonstrate the links between a $\tau(q)$ curve and the associated fragmentation ratios (the example on page 51 in Harte (2001)). Three scenarios were considered: the first was where $w_i = s_i = 1/b = 0.1$ for all i, which would produce a uniform distribution. The associated $\tau(q)$ curve, by substituting $w_i = 1/b$ into Eq. (4.20) could be derived as

$$\tau(q) = q - 1, \tag{4.21}$$

a straight line with slope one (the solid line in Figure 4.6). The second scenario was where all values of $w_i = 0.111$, except one equal to 0.001, of which the distribution was uniform but with small areas having very small (non-zero) measures. The associated $\tau(q)$ curve was a line substantially dropping for $q < 0$ but similar to that of the first scenario for $q > 0$ (shown as the dashed line in Figure 4.6). The last scenario was all w_i's equal to 0.07,

except one equal to 0.37. The corresponding plot of $\tau(q)$ sharply dropped for $q > 0$, but was somewhat similar to that of the first scenario for $q < 0$ (the dotted line in Figure 4.6). These examples provides an understanding of the behaviour of the generating equation. They also provides guidance as to the possible composition of the associated fragmentation ratios. When all values of w_i are equal, the measure is expected to be uniformly distributed over the support set and the associated $\tau(q)$ curve is a straight line. However, when the measure is not uniformly distributed, the associated $\tau(q)$ curve is concave downwards. According to the section where $\tau(q)$ drops down, the relative composition of w_i's values could be roughly foreseen. For $q > 0$, it is expected that the relatively large measures would dominate the trend of the $\tau(q)$; whilst for $q < 0$, the relatively small non-zero measures would dominate it. In other words, the $\tau(q)$ curve can be used to investigate the extent to which the measure deviates from a uniformly distributed measure (Harte, 2001). This information may help reduce the solution domain when numerically solving Eq. (4.19).

In previous research, a further simplified case of single-scaled binomial multifractal measures, i.e., $b = 2$ and $s_i = 1/b = 1/2$, is in general applied to rainfall downscaling (Gupta and Waymire, 1993; Olsson, 1995, 1998; Over and Gupta, 1994, 1996). However, this parametric assumption may oversimplify the complex patterns of high-resolution rainfall sequences according to the preliminary results of Wang (2005) and Wang et al. (2009a) indicating that a relatively complex cascade, i.e., $b \geq 2$, has the potential to provide a more promising description of rainfall sequences. Limited research was also carried out on this inverse work by assuming b to be an infinite number (Mandelbrot, 1989, 1990; Mandelbrot et al., 1990). Although these studies theoretically yield encouraging results, the assumption of an infinite branching number, however, is impractical for realistic use.

Moreover, it is also an open problem to generate zero-values for rainfall sequences and fields since in the theory of cascade methods fragmentation ratios are usually assumed to be $0 < w_i < 1$ for all i. A widely-used idea is to present zero-values by empirically employing some threshold values in the post-processing stage, e.g. (Lovejoy and Schertzer, 1990). However, the determination of threshold values may strongly depend upon the weather systems and some associated factors at the sites of interest. The model developed in Over and Gupta (1994), analogous to the aforementioned β-model, is able to generate zero-values, but the patterns of the synthetic rainfall fields are less continuous comparing to those of observed rainfall fields due to its simplification of the wet/dry (or with/without rainfall) pattern. Considering two more states (respectively denoted as 1/0 and 0/1) in synergy with the conventional "non-zero" single-scaled binomial multifractal measures

(denoted as x/x), Olsson (1998) developed a generator of hourly rainfall sequences able to produce zero-values. The state of 1/0, i.e., $w_1 = 1$ and $w_2 = 0$, represents that all the rainfall volume is distributed into the branching at position 1; whilst the 0/1 state is the reverse. Then, the associated probabilities of each state between successive cascade levels are estimated to understand the cascade processes of rainfall. The results of this work show that the associated probabilities are scale-invariant over a certain range of scales. This implies that there may be a fixed proportion of w_i equal to zero when cascading in this scaling range. This derivation could be applied to the generating equation to help improve the conventional cascade models in generating zero-values. In the ordinary definition of Eq. (4.19), no w_i values are allowed to be zero since it does not hold for $q < 0$. However, according to the explanation in Section 4.2.4, the zero-ratios may be involved if the definition domain of left-sided multifractals is applied, i.e., considering merely the case of $q \geq 0$.

4.2.6 Applications of multifractals to rainfall downscaling

A general methodology to apply the theory of multifractals to cascade-based rainfall downscaling can be summarised here (shown in Figure 4.7). The idea is first to pre-define the form of the cascade generator; conventionally it is based upon the random variable of a given theoretical probability distribution (e.g. log-Poisson or log-normal distributions); however, it could also be the deterministic variables solved from the generating equation Eq.(4.19), as proposed in this work. Then, through analysing the scaling features of historical temporal or spatial rainfall observations (in Figure 4.7, they are rainfall time series) within a certain range of scales (e.g. 5 min to 1 hour), the parameters of the generator can be empirically estimated; then the generator can be further used to disaggregate the coarser-scale rainfall estimates into finer scales through synthesising the associated cascade process.

In this methodology, the theory of multifractals is employed to implement the steps of characterising historical rainfall observations over a proper range of (temporal or spatial) scales and consequently deriving generator's parameters. The scaling features of the historical observations are captured using Eq.(4.14) and the associated $\tau(q)$ curve can be empirically deduced (which is therefore called the empirical $\tau(q)$ curve in this work and can be regarded as a "characteristic" curve of the data being analysed; to obtain the empirical $\tau(q)$ from real data, the readers are referred to Appendix B for detailed steps). In the other hand, a theoretical $\tau(q)$ curve (denoted $\tau^*(q)$ in Figure 4.7) can be deduced accord-

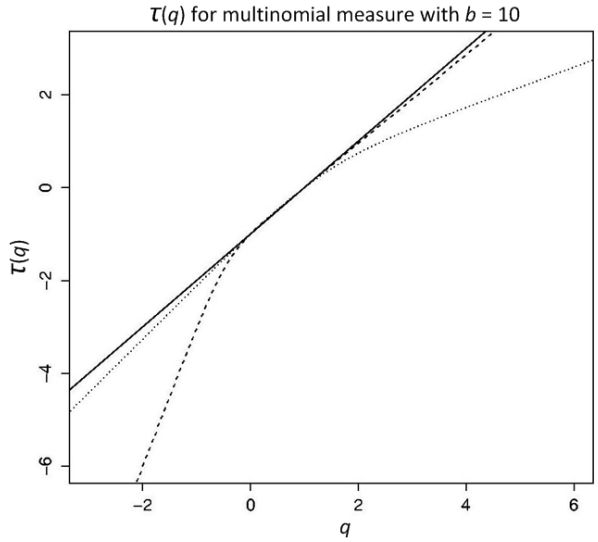


Figure 4.6: The solid line denotes the first scenario where $w_i = 0.1$ for all i; the dashed line represents the second scenario where $w_i = 0.111$ for all i, except one equal to 0.001; and the dotted line is where $w_i = 0.07$ for all i, except one equal to 0.37 (Harte, 2001).

ing to the form of pre-defined generators, such as Eq. (C.15) for the β-model, Eq.(C.20) for the α-model and Eq.(C.27) for the log-Poisson model. Through fitting the empirical and theoretical $\tau(q)$ curves, the parameters of the generator used can be therefore derived for further downscaling applications.

One of the biggest advantages to use the theory of multifractals is that it can be applied to the characterisation of different types of rainfall structures (e.g. 1-Dimension raingauge series and 2-Dimension radar rainfall fields) without massively increasing the computational and theoretical complexity. The methodology described can be therefore followed to implement both spatial and temporal rainfall downscaling.

4.2.7 Summary

This section reviewed the theory of multifractals and its links to the applications of discrete-in-scale cascade models to rainfall observations. In addition to the widely-used random cascade models whose generators are constructed based upon pre-defined probability distributions, this work, through re-investigating the multiplicative cascade process, proposed a potentially new cascade generator which, instead of depending on a given theoretical probability distribution, is constructed based upon the generating equation. The generating equation has been derived and has been shown to be the key to producing cascade process

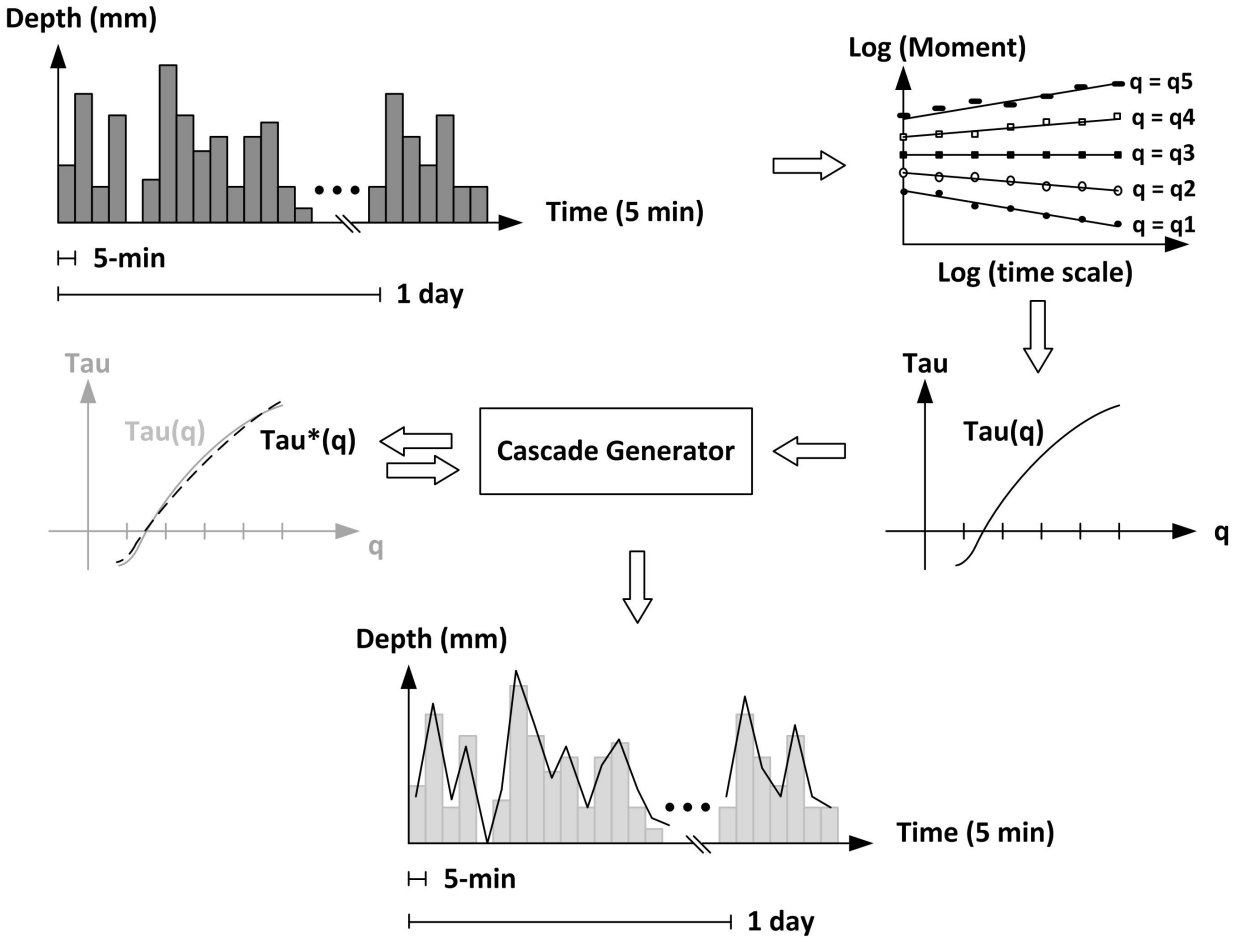


Figure 4.7: General schematic of the construction of cascade models

in literature; however, the associated discussion and understanding about its applications was insufficient or impractical. In this section, some derivations were conducted to demonstrate that the generating equation has the potential to help improve rainfall modelling in synergy with the left-sided multifractals. In the next section, the applications of this new generator to temporal and spatial rainfall downscaling will be detailed and validated.

4.3 Semi-deterministic cascade model

A new cascade model, called semi-deterministic cascade model (denoted SD model in the following context), is proposed in this work. Employing the generating equation as the cascade generator, this model is able to produce random cascade processes (such as rainfall) by using deterministic fragmentation ratios (i.e. s_i and w_i); the statistical features (e.g. mean and variance) of the produced processes are therefore invariant (hence named the semi-deterministic cascade model). The associated validation of the statistically deterministic nature of the semi-deterministic cascade model is detailed in Appendix D).

In the generating equation (Eq.(4.19)), it is intuitive that the theoretical $\tau(q)$ curve could be obtained if s_i and w_i were known. However, the inverse task, i.e., to derive the s_i and w_i from known $\tau(q)$, is relatively difficult because of the non-linearity of the generating equation and the unknown number of s_i and w_i (i.e. unknown b); but this inverse derivation is the key to constructing the cascade generator of the SD model. Following the general methodology of applying the theory of multifractals to cascade-based rainfall downscaling, mentioned in Section 4.2.6, the proposed SD model first analyses the scaling features of historical rainfall data over the scales of interest to obtain the empirical $\tau(q)$ curve. This curve is then substituted into the generating equation to iteratively and inversely derive the "best" set of s_i and w_i by fitting the theoretical and empirical $\tau(q)$ curves (e.g. the likelihood method) subject to the constraints $\sum_{i=1}^{b} s_i = 1$ and $\sum_{i=1}^{b} w_i = 1$. Finally, this set of s_i and w_i is further used to synthesise (or downscale) rainfall estimates (in space or time) that have similar structures (i.e. statistical features) to the associated historical observations through the cascade process.

To implement the SD model, one of the key parameters that needs to be identified is b, which largely dominates the applicability of the theoretical $\tau(q)$ curve (See Section 4.2.5) and consequently affects the fitting results of the $\tau(q)$ curves. In conventional discrete-in-scale random cascade models, the value of b is in general assumed to be 2 because it can directly generate more intermediate cascade levels (i.e. more intermediate timescales)

and is easier to be implemented and formalised [2]. However, based upon the analyses in Wang et al. (2009a,b), a better fitting is obtained if the branching number is assumed to be 4. This indicates that, instead of the binomial (i.e. $b = 2$) cascade model, a more general "multinomial" (i.e. $b \leq 2$) cascade model shall be employed in the SD model in order to conduct more accurate rainfall downscaling. A schematic of the multinomial cascade process is shown in Figure 4.8. The components at level g, for example, can be assumed to be an hourly rainfall sequence, and each component of it thus represents an 1-h rainfall volume. Subdivision is then continuously carried out for each component at level g to obtain b sub-components at level $g+1$, which could be regarded as the corresponding sub-hourly rainfall sequence. Repeat the same fragmentation several times till level h; the associated high-resolution (e.g. 5-min) rainfall sequence can be obtained.

As mentioned above, an advantage of the theory of multifractals (see Section 4.2.6) is that this schematic can be also applied to spatial rainfall downscaling. The components at level g can be regarded as, for example, the radar image at a given time step and each component represents one rainfall volume in the coarser spatial scale (e.g. 8×8 km^2 grid, or 8 km grid length). According to the determined set of s_i and w_i by solving the generating equation, these coarser volumes can be iteratively subdivided into finer-scale rainfall volumes (e.g. in 1×1 km^2), which are assumed to be the sub-components at cascade level h.

[2]Due to the complimentary nature between two fragmentation ratios, i.e., $w_1 + w_2 = 1$, they always follow the same distribution or behaviour

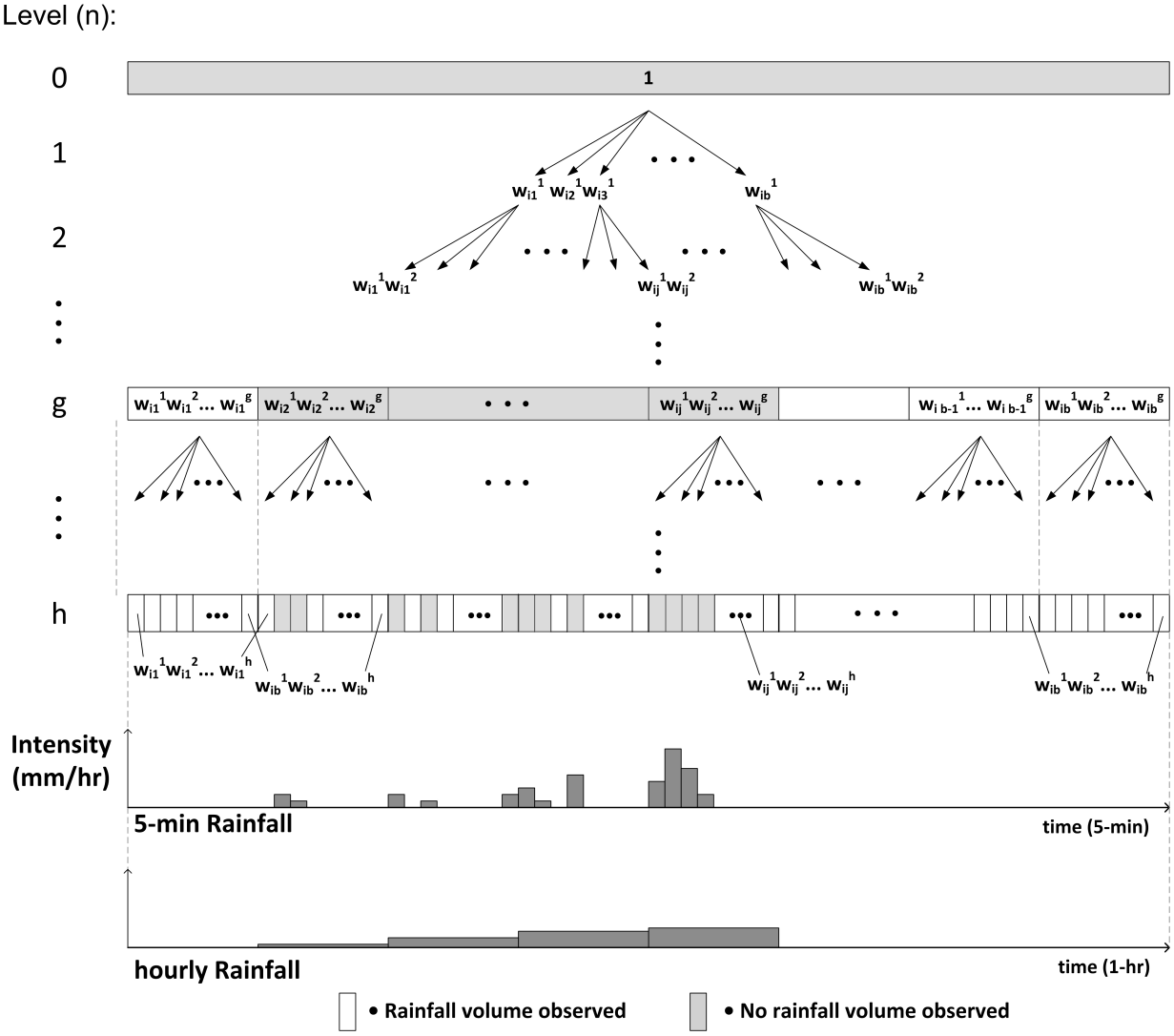


Figure 4.8: Schematic of the multinomial multiplicative cascade process

4.3.1 Quad-nomial cascade model

In the following sections, the applications of the proposed SD model to temporal and spatial rainfall downscaling are demonstrated. To simplify the complexity of solving the generating equation, the value of s_i is assumed to be constant (i.e. equal to $1/b$, where $b = 4$ following the suggestion in Wang et al. (2009a,b, 2010)); the cascade generator used in this model is therefore the single-scaled generating equation (i.e. Eq. (4.20)). The cascadings between successive levels over the range of temporal and spatial scales of interest in this work (e.g. from 80-min to 5-min time intervals or from 8×8 km^2 to 1×1 km^2) are respectively shown

in Figure 4.9 and 4.12.

Archived raingauge and radar data in the vicinity of Greater London area (see the description of dataset in Section 2.3) were used to assess the proposed SD model. In addition, in order to understand and highlight the features of the SD model and its difference from the conventional random cascade models, this work employed the log-Poisson cascade model (denoted LP model in the following context), a widely-used discrete-in-scale random cascade model (Deidda et al., 1999; Onof and Arnbjerg-Nielsen, 2009). Comparison between these two models were carried out, particularly focusing on its capacity to reproduce certain statistical features that may affect the corresponding urban hydraulic modelling; the associated results are demonstrated as follows.

4.3.2 Temporal downscaling

Historical time series data from Greenwich raingauge site in London were used to assess the proposed SD model. The original raingauge data is in the 5-min resolution and 14 years long (from 1st Jul 1987 to 30th Jun 2001); in this work, only the last two years of data (from 1st Jul 1999 to 30th Jun 2001) were used because some extreme temporal structure may be smoothened if too many data are used. In order to assess SD model's capacity of reproducing the temporal structure of the rainfall time series, the original 5-min data were aggregated to 80 min; then these coarser data were downscaled back into 5-min using the SD model (Figure 4.9). These downscaled rainfall estimates were then compared with the original 5-min raingauge observations and the downscaled 5-min estimates generated by the LP model.

The scaling feature was firstly analysed over the range from 5 min to 1 month by using Eq. (4.14) and the result is shown in Figure 4.10 (left). A scaling break can be observed in the vicinity of timescale equal to 1 day; this means that the scale-invariant behaviours between the timescale ranging from 5 min to 1 day and from 1 day to 1 month (or longer) are different and consequently need to be characterised by different $\tau(q)$ curves. Bearing in mind the aim of this research, the scale-invariance over the 5-min to 1-day timescale range has therefore been captured (Figure 4.10 (right)) and the associated empirical $\tau(q)$ curve can be obtained and plotted as the round markers in Figure 4.11. According to the trend of the curve (which is similar to the dotted line in Figure 4.6, where a sharp drop is observed for $q \geq 0$), it can be expected that the distribution of w_i will be similar to the associated scenario: one relatively large fragmentation ratio and several equally small ratios. An abnormal rise however can be observed for $0 \leq q < 1$, which is not seen in

Figure 4.6 and only occurs when zero values partly exist in the distribution of w_i (Wang et al., 2009b).

Based upon the proposed SD model, the "best-fitting" theoretical $\tau(q)$ curve can be derived and plotted as the solid line (denoted SD model) in Figure 4.11; the associated fragmentation ratios are $\mathbf{W} = (0.0, 0.114, 0.247, 0.639)$, which is somewhat similar to the expected distribution of w_i. The best-fitting theoretical $\tau(q)$ curve (the dashed line, denoted LP model) derived from the LP model can also be obtained by fitting Eq. (C.27) and the associated parameters (i.e. C and β; see Appendix C.5 for the details) in the LP model are obtained: $C = 0.638$ and $\beta = 0.282$. Good fits can be observed between the empirical $\tau(q)$ and two theoretical $\tau(q)$ curves, particularly for $q \leq 1$; and for $0 \leq q < 1$, a slightly better fitting is achieved by SD model. This indicates that SD model may have a relatively better ability to characterise smaller rainfall volumes because for $q < 1$ the effect of the rainfall quantities that are less than one is magnified.

Downscaled results are summarised in Figure 4.23, where the solid lines are plotted based upon the 2-year observations at the Greenwich gauge site and the dashed-dotted line and the gray areas with gray dashed border are respectively based upon the SD and LP models. Due to the aforementioned deterministic nature, SD model produces a series of constant STDs (standard deviations) and Dry period %'s (percentage of zero rainfall volumes); whilst LP model produces an envelope of STDs and Dry period %'s due to its stochastic nature. It is observed that the SD model well captures the STDs in some months but in general tends to underestimate variability of rainfall time series, particularly when the values of STDs are relatively larger, such as in May; whilst the LP model tends to overestimate STDs and produces a larger uncertainty range as the values of STDs are larger, such as in May and September, despite that it envelopes the observed STDs in most months.

A similar result is observed for the Dry period %. The LP model envelopes the observed Dry period %'s in most months, whilst the SD model in general underestimates them. However, it is worthwhile to mention that, because the LP model is unable to directly produce zero values, a physically-meaningful thresholding was actually applied to the LP model in this work (as in most previous works that used the LP model) to filter out the rainfall depths smaller than 0.1 mm (which is the best resolution of the widely-used tipping bucket raingauges); whilst the proposed SD model is able to directly generate zero rainfall volumes. However, a poor performance in reproducing the values and trends of lag-1 and 2 autocorrelations is observed in Figure 4.23. This means that, as compared to

the observations and the estimates generated by the LP model, each rainfall volume within the time series synthesised by the SD model is on average less correlated to the volumes at past 1 and 2 time steps.

These results show that the proposed quad-nomial SD model, which is based upon a fixed number of constant fragmentation ratios, is able to characterise and somewhat reproduce the "quantity" feature of high-resolution rainfall time series; but it is insufficient to generate the temporal correlation that exists in the observed 5-min rainfall series. This correlation is a very important feature of time series, particularly for short-term high-resolution time series; however it is seldom implemented in the discrete-in-scale cascade models (Lovejoy, 2010). By re-investigating the construction of SD and LP model, the major difference lies in that the prior uses a finite number of constants to represent fragmentation ratios, whilst the latter uses a probability distribution to characterise them; a stronger correlation between the volumes generated by the LP model is therefore observed. An improved cascade model, which is developed particularly for temporal downscaling by introducing this correlation, will be described later in Section 4.4.

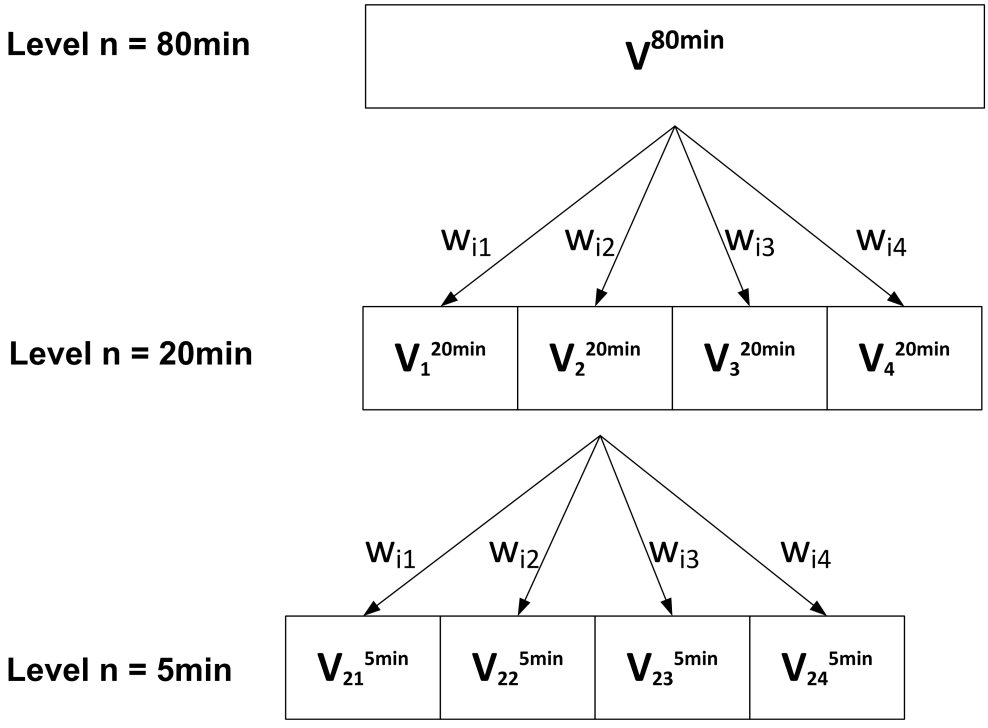


Figure 4.9: Application of the quad-nomial cascade to rainfall time series downscaling

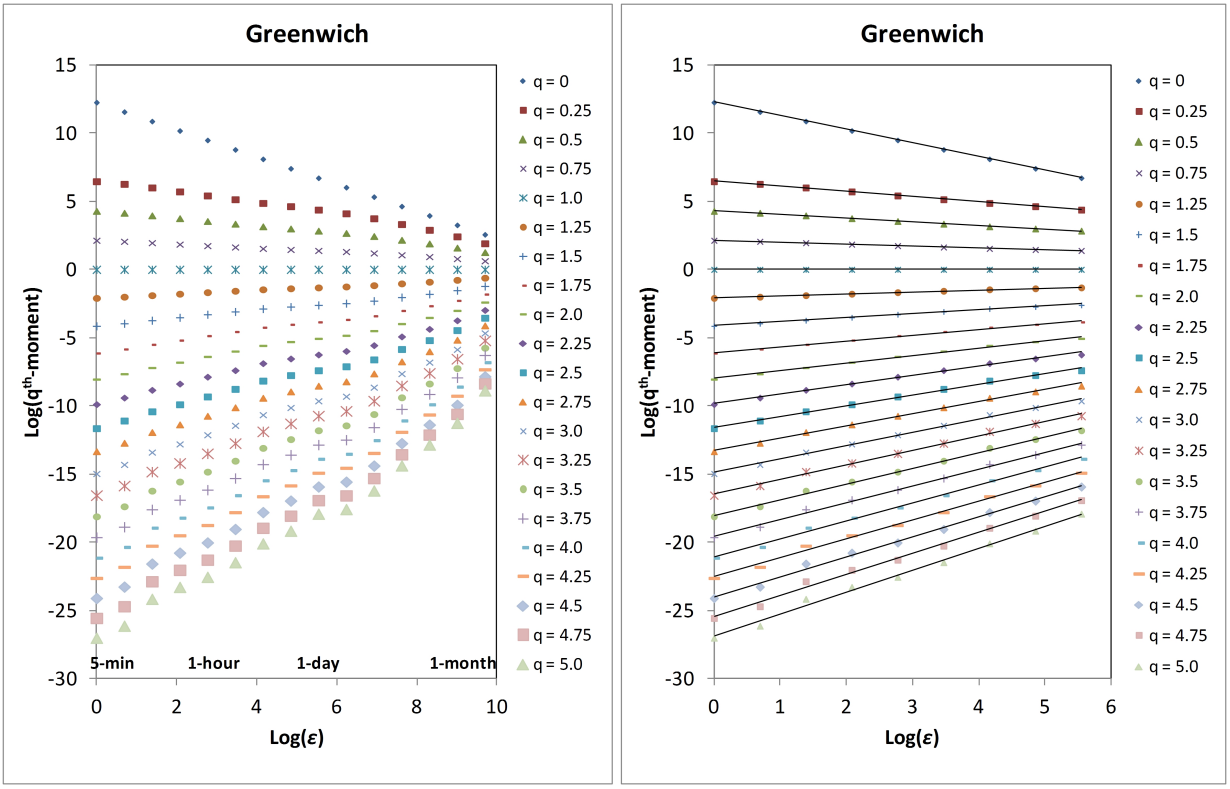


Figure 4.10: The q-th moment $\chi(q, \epsilon)$ as a function of time scale ϵ over the range from 5 min to 1 month (left) and the range from 5 min to 1 day (right) for $0 \leq q \leq 5$ from Greenwich raingauge data. A scaling break can be observed around $\epsilon = 1$ day and a well straight-line behaviour can be characterised over 5 min to 1 day scales.

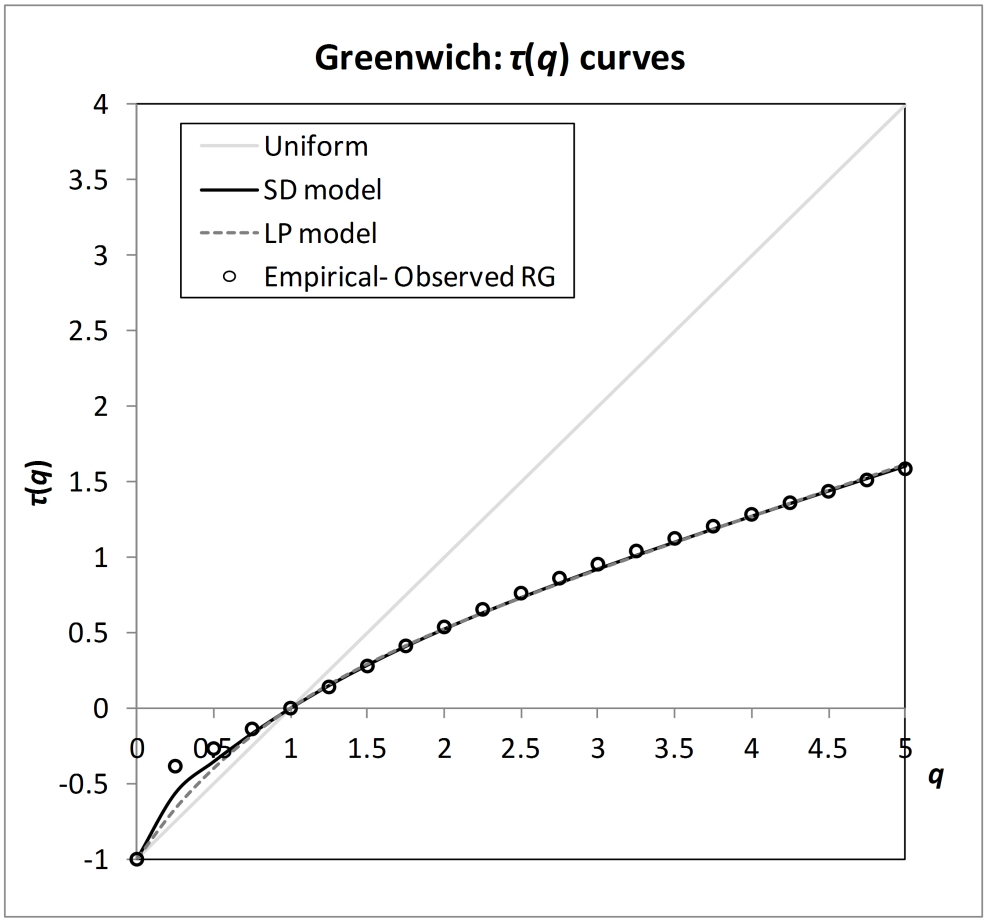


Figure 4.11: Empirical and theoretical $\tau(q)$ curves from Greenwich raingauge data over the time scales 5 min to 1 day; the round markers are empirical $\tau(q)$ curves, whilst the solid and dashed lines are theoretical $\tau(q)$ curves derived respectively from SD and LP models

4.3.3 Spatial downscaling

The storm taking place on 9th Feb 2009 (termed 20090209 10:00-17:00 event) over the Greater London was studied herein since it induced surface water flooding around Victoria Rail Station in the Central London. The data used in this work is 1-km, 5-min UK Met Office composite Nimrod data over a 64×64 km^2 squared area clipped from the original 100×100 km^2 Greater London area[3]. In order to assess the applicability of the proposed SD model to spatial rainfall downscaling, the original 1-km Nimrod data were aggregated into 8-km; then these coarser data were downscaled back to 1-km using SD model (the schematic is shown in Figure 4.12, where the same fragmentation ratios were used to downscale a given 8-km rainfall volume to 1-km ones). These downscaled rainfall estimates were then compared with the original 1-km Nimrod data and the downscaled 1-km estimates generated by the LP model.

The spatial structure (i.e. empirical $\tau(q)$ curves) of each snapshot of rainfall fields was first analysed over 8 to 1 km spatial scales. Their temporal evolution against different q's is shown as the gray dotted lines in Figure 4.13, and the associated "best-fitting" theoretical $\tau(q)$ curves were derived from the SD model (by solving the generating equation) and shown as the solid lines in Figure 4.13. Only very little differences between the empirical and theoretical $\tau(q)$ curves are observed here, which validates new model's capacity of reproducing specific statistical features of real rainfall fields.

Two snapshots, respectively at time steps 14:55 and 16:25, were especially selected here to demonstrate the fitting results of spatial scaling features (shown in Figure 4.14). At time step 16:25, a very good fit can be observed between the empirical (the round markers, denoted Empirical-16:25) and theoretical $\tau(q)$ curves, obtained both for the SD (the gray solid line, denoted SD-16:25) and the LP (the dark solid line, denoted LP-16:25) cascade models; whilst at time step 14:55, poorer results can be observed when q increases, particularly the theoretical $\tau(q)$ curve derived from the LP model (the dark dashed line, denoted LP-14:55). According to the trend of $\tau(q)$ curves at these two time steps and the analyses of the features of $\tau(q)$ curves in Section 4.2.5, it can be expected that the spatial structure of the rainfall field at 14:55 is more variable compared to the rainfall field at 16:25 because an obvious drop can be observed in the plot of $\tau(q)$ curve at 14:55 when q increases for $q > 0$.

[3]The UK Easting/Northing coordinates of the lower left (LL) and the top right (TR) grids of the original Greater London area are respectively (485000, 135000) and (585000, 235000). The clipped area is LL (485000, 171000) and RR (549000, 235000).

The associated parameters of the cascade generators for the SD and LP models were therefore derived and the generators were further used to generate 1-km rainfall fields from 8-km Nimrod data for the 20090209 10:00-17:00 event. The corresponding mean rainrates and the spatial variations over the 64×64 km^2 Greater London area are shown in Figure 4.15. Because the SD model follows the microcanonical cascade process, the mean rainrate generated by it (denoted SD model ($8 \rightarrow 1$km)) is exactly the same as the observed measurement (denoted Nimrod 1km); whilst the LP model provides an uncertainty range for estimated mean rainrates and well envelopes the observed mean rates.

Due to its deterministic nature, although the SD model generates random rainfall fields, the resulting standard deviation over the 64×64 km^2 Greater London area is constant at each time step; whilst the LP model provides an uncertainty range that envelopes the observed STDs for most time steps. However, the SD model exhibits a better ability to reproduce STDs, particularly when rainfall fields of relatively higher variability occur; for example, at time steps 14:55 and 16:25, the SD model ($8 \rightarrow 1$km) STDs are very similar to the Nimrod 1km STDs, as compared to the LP model ($8 \rightarrow 1$km) STDs.

In order to evaluate the SD model's capacity for being used for urban pluvial flood modelling, the rainfall fields over the 5×6 km^2 Cranbrook catchment area were clipped and the corresponding performance is shown in Figure 4.16. Since this area is smaller than 8×8 km^2 (i.e. the coarsest scale used in this work's spatial downscaling), the mean rates and STDs generated by the SD model are no longer fully coincidental with the observed ones; in other words, similar to the LP model, the SD model also generates an uncertainty range for each statistic. In this event, the SD model is found to be able to produce smaller and less fluctuant uncertainty bands than the LP model for mean rainfall rates and STDs in the Cranbrook catchment. This suggested that the SD model has the potential to be a suitable tool to generate less uncertain high spatial-resolution rainfall fields over very small areas.

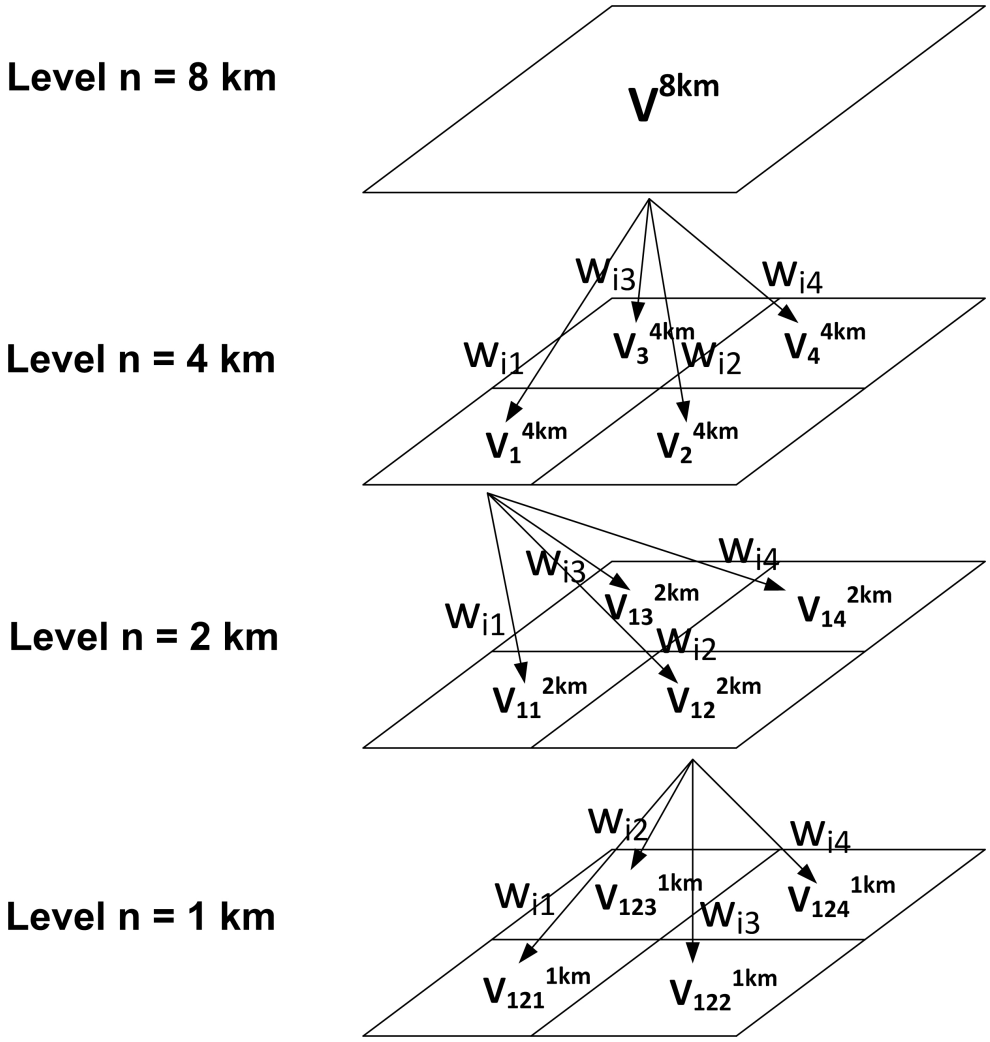


Figure 4.12: Application of the quad-nomial cascade to rainfall field downscaling

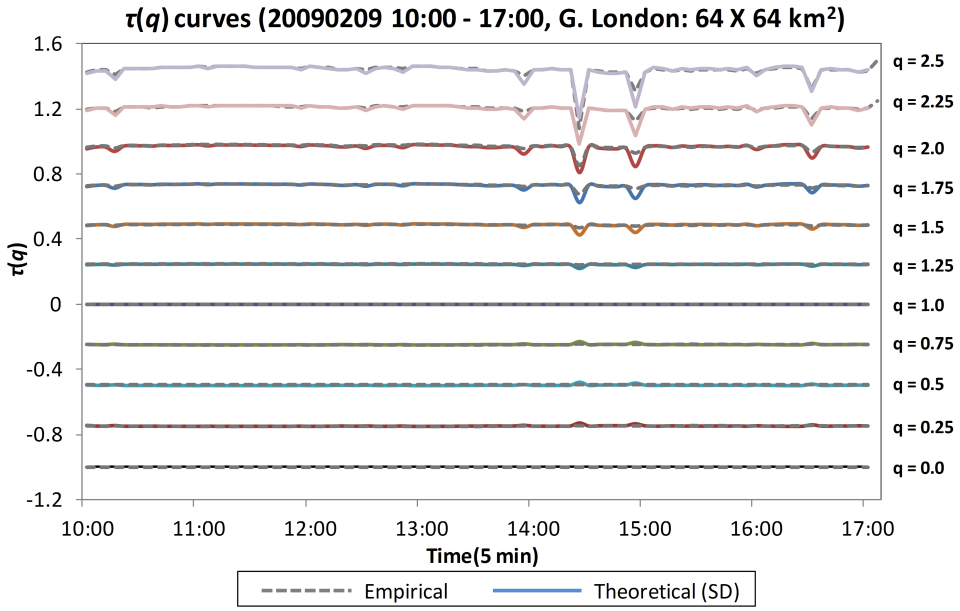


Figure 4.13: Evolution of $\tau(q)$ curves in the 20090209 10:00-17:00 event over 64×64 km^2 Greater London area; the dashed lines are empirical $\tau(q)$ curves and the solid lines are theoretical $\tau(q)$ curves estimated by solving the generating equation

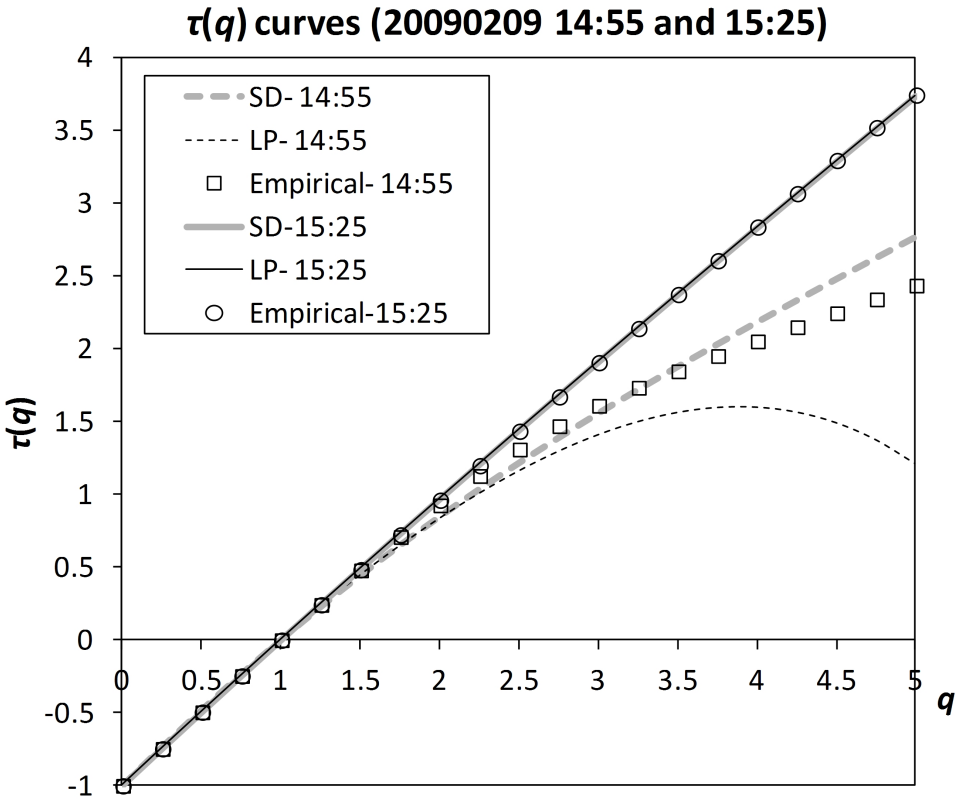


Figure 4.14: Empirical and theoretical $\tau(q)$ curves at time steps 14:55 and 15:25 in the 20090209 10:00-17:00 event over 64×64 km^2 Greater London area; the round (15:25) and square (14:55) markers are empirical$\tau(q)$ curves, whilst the solid (15:25) and dashed (14:55) lines are theoretical $\tau(q)$ curves derived respectively from SD and LP models

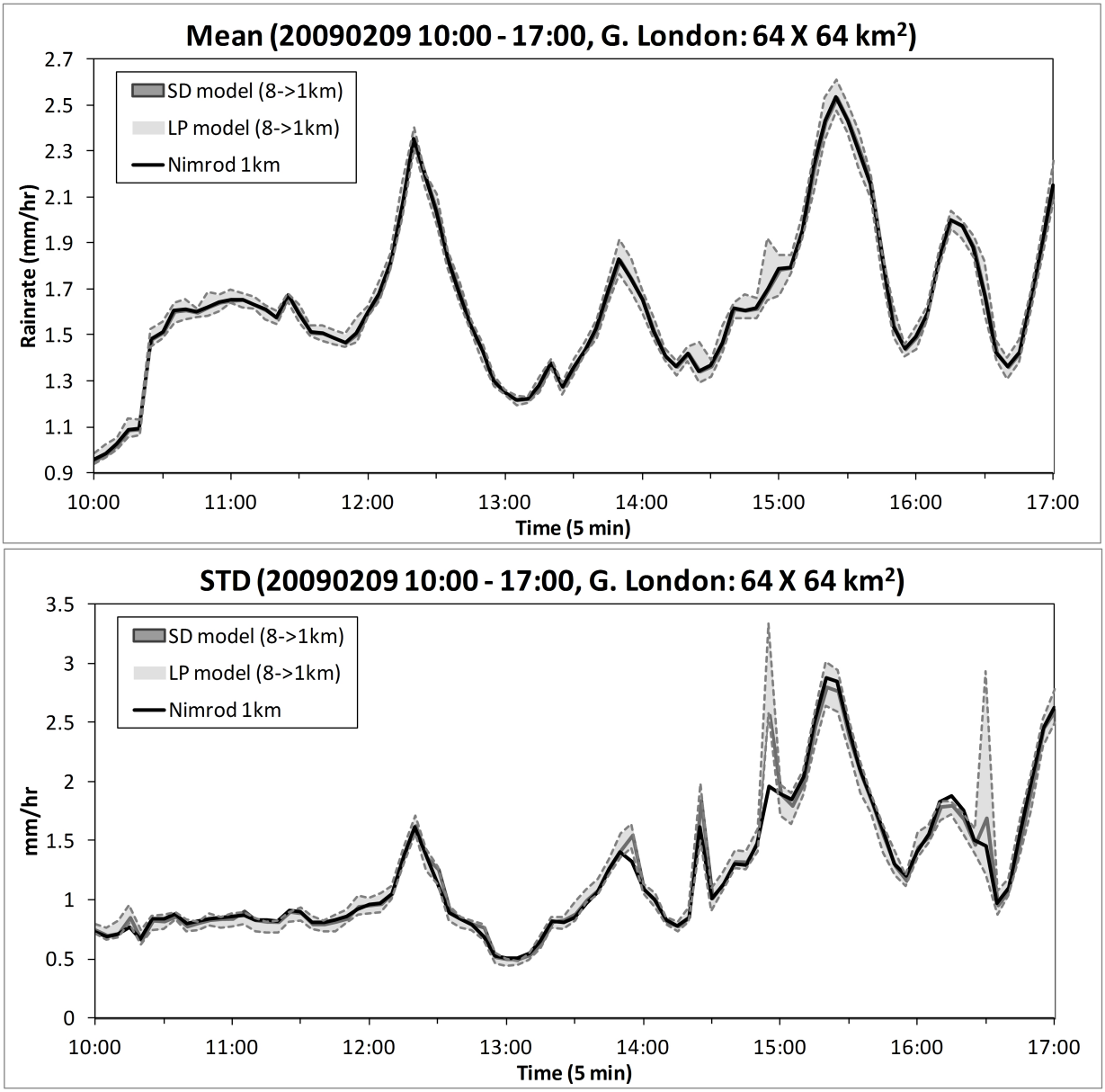


Figure 4.15: Mean and spatial variation (Std, standard deviation) of rainrates in the 20090209 10:00-17:00 event. The dark solid lines were estimated from 1-km Nimrod data over 64×64 km^2 Greater London area; the gray solid lines and the gray areas with gray dashed border lines were estimated from the downscaled rainfall fields (8 km to 1 km) in the coincidental area, respectively generated by the SD and LP models

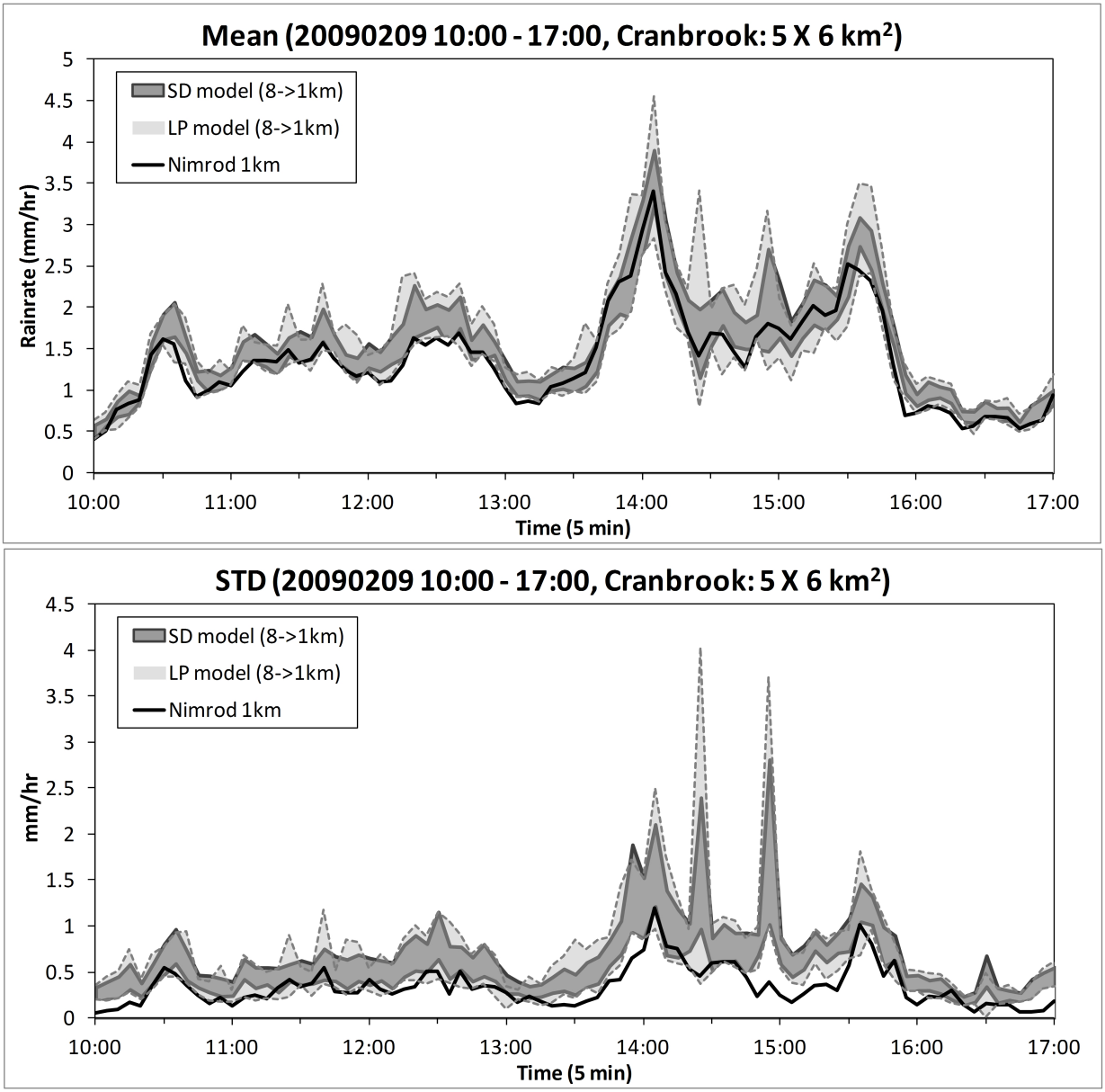


Figure 4.16: Mean and spatial variation (Std, standard deviation) of rainrates in the 20090209 10:00-17:00 event. The dark solid lines were estimated from 1-km Nimrod data over 5×6 km^2 Cranbrook catchment; the gray areas with gray solid border lines and with gray dashed border lines were estimated from the downscaled rainfall fields (8 km to 1 km) in the coincidental area, respectively generated by the SD and LP models

4.4 Fully-empirical cascade model

In this section, the development of a new cascade model is described. This model was developed because of quad-nomial SD model's insufficient ability to satisfactorily reproduce the causality of rainfall time series. Despite the fact that the quad-nomial cascade process demonstrated promising performance in fitting scaling features of historical rainfall time series measurements, there is however a big drawback of this type of model, which follows the "standard" multiplicative cascade process to downscale time series; that is, this type of model lacks the ability to characterise "causality," a property particularly important in short-term high-resolution time series (e.g. 5-min raingauge data). In other words, what SD and LP models characterised is the scaling feature of rainfall "quantities" between various timescales (or cascade levels); however, when two neighbouring rainfall volumes at the parent cascade level are branched into finer-scale volumes, these two branchings (or cascadings) are in general assumed to be sampled independently (based upon the same set or distribution of fragmentation ratios). This consequently generates acausal patterns (i.e. left-right symmetric on the time axis); however, the structures of temporal rainfall are not acausal because the past affects the future but not vice versa. Although the LP model generates temporally-correlated rainfall structures, they are still acausal due to the symmetric nature of the Poisson distribution (i.e. the past affects the future "and" vice versa); this is unrealistic in a physical sense (Lovejoy, 2010). In fact, many studies have demonstrated the "causality" (i.e. left-right asymmetric on the time axis) of rainfall time series and addressed its importance in rainfall time series downscaling (Cârsteanu and Foufoula-Georgiou, 1996; Marsan et al., 1996).

In addition to causality, Olsson (1998) demonstrated that the behaviour of each branching between two successive cascade levels also depends on some physical factors (such as the relative position of the rainfall volume being subdivided) and therefore proposed a methodology able to apply these physical factors to "hourly" time series downscaling. This work extended the methodology proposed by Olsson (1998) to construct a microcanonical cascade model and further took into account the causality to therefore develop a cascade model for "sub-hourly" rainfall time series downscaling. Different from the aforementioned cascade models, the proposed model therefore does not strictly follow the theory of multifractals; that is, instead of deriving only one set of fragmentation ratios[4] to represent the structures of rainfall data through the overall timescale range (or cascade levels) of in-

[4]Notice that the term "one set of fragmentation ratios" here indicates one set of constants or random variables of a given probability distribution

terest, the proposed cascade model characterises scaling features of rainfall measurements for each two successive cascade levels. In other words, there is "one set of fragmentation ratios" to represent the scaling feature of each two successive cascade levels. Furthermore, these features were estimated empirically and, instead of being intentionally fitted to any theoretical probability distribution (as Olsson (1998) did), they were directly applied to the cascading process (hence named the fully-empirical cascade model and denoted FE model in the following context).

The schematic of the FE model is shown in Figure 4.17; it is a microcanonical binomial cascade process. Following the methodology proposed by Olsson (1998), the FE model considers three states for each branching (or cascading); they are denoted 1/0, 0/1 and x/x, where 0 represents a dry (i.e. zero) volume whilst 1 and x represent wet (i.e. non-zero) volumes. The 1/0 state ($w_1 = 1$ and $w_2 = 0$ in a binomial cascade process) represents the condition that the rainfall volume at the parent cascade level is fully distributed into the prior branching, whilst 0/1 ($w_1 = 0$ and $w_2 = 1$) represents the reverse condition; and the x/x state represents the condition that the rainfall volume at the parent cascade level is partially distributed into two branchings (i.e. $w_1 \neq 0$ and $w_2 \neq 0$). The probabilities of the occurrence of these three states are therefore denoted $P(1/0)$, $P(0/1)$ and $P(x/x)$, and their sum is naturally equal to 1.

In addition to "quantity", according to the analyses made by Olsson (1998), the relative position of rainfall volumes is also an important physical factor affecting the process of temporal downscaling. In order to consider this factor, two types of non-zero (or wet) rainfall volumes were particularly categorised based upon their relative positions:

1. The "starting" volumes: preceded by a dry volume and succeeded by a wet volume; and

2. The "isolated" volumes: preceded and succeeded by dry volumes.

In order to obtain the parameters for implementing the schematic and for taking into account the physical factors of interest (i.e. relative positions and causality), preliminary analyses were conducted and are described in the following sections. The data set used here is the same as the one used in section 4.3.2 (i.e. archived 5-min raingauge measurements from Greenwich between 1st Jul 1999 and 30th Jun 2001) in order to enable further comparisons between different cascade models.

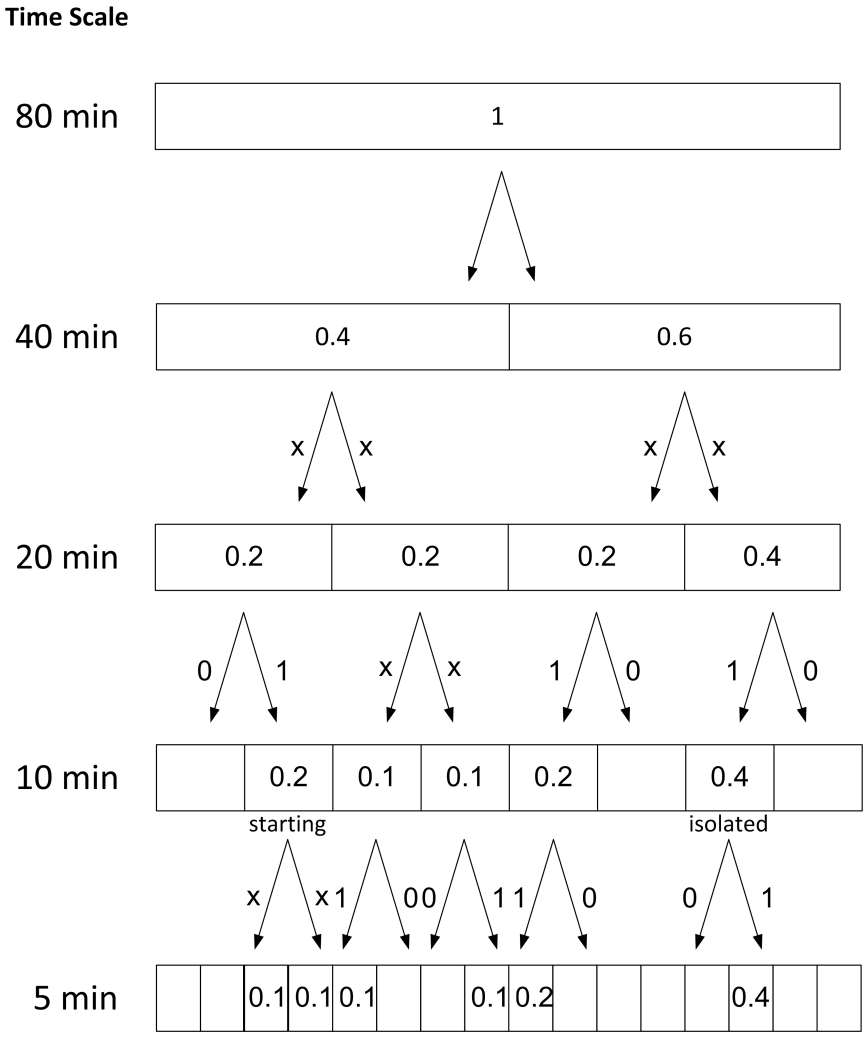


Figure 4.17: Schematic of the binomial fully empirical multiplicative cascade process

4.4.1 Derivation of fragmentation ratios

Figure 4.18 is the schematic of given two successive cascading levels (10 min and 5 min levels). An arbitrary component at level 10 min (i.e. the parent level) is termed $V_i^{10\text{min}}$ and the sub-components thereof are termed $V_{i,1}^{5min}$ and $V_{i,2}^{5min}$. The associated fragmentation ratios at level 5 min can be therefore calculated by $w_1^{5min} = V_{i,1}^{5min}/V_i^{10min}$ and $w_2^{5min} = V_{i,2}^{5min}/V_i^{10min}$, where $V_i^{10min} \neq 0$. By repeating this calculation, fragmentation ratios for all non-zero components can be estimated and their weight distributions (also termed empirical probability distribution to be distinguished from a theoretical probability distribution) can be illustrated in Figure 4.21. From the upper to the lower in Figure 4.21 are the weight distributions of the cascading levels between 80 and 40, 40 and 20, 20 and

10, and 20 and 5 mins. It is observed that the weight distributions change slightly over different timescale ranges. At the level 10 min - 5 min, the probability of the occurrence of the states 1/0 or 0/1 exceeds 70%; whilst it decreases to less than 60% at the level 80 min - 40 min.

If only the state x/x is seen (i.e. $0 < w_1^{5min}, w_2^{5min} < 1$), at the level 10 min - 5 min, over 60% of fragmentation ratios concentrate in the vicinity of 0.5, whilst this proportion decreases to approximately 25% at the level 80 min - 40 min, and at the same time the probability distribibition of the quantity of fragmentation ratios is relatively even (see Figure 4.22). This indicates that a greater variability of ways in which 80-min rainfall is distributed at 40 min than 10-min rainfall at 5 min.

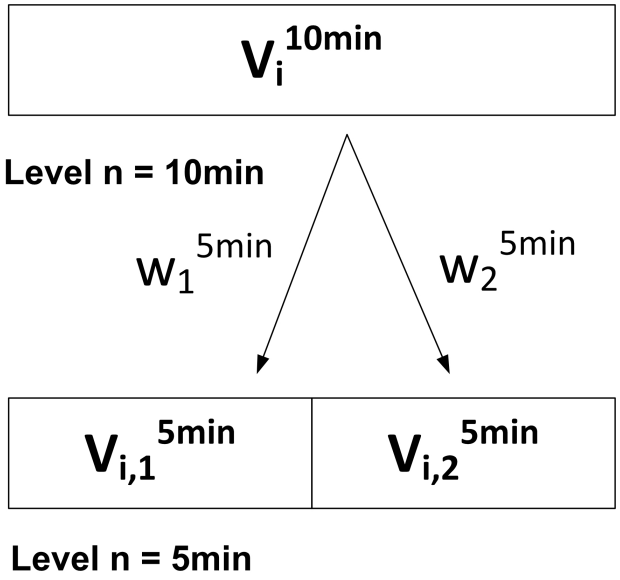


Figure 4.18: Schematic of estimation of fragmentation ratios between two successive cascade levels

4.4.2 Relative positions of rainfall volumes

Following Olsson (1998)'s study on the relative position of rainfall volumes, in the FE model the occurrence of three cascading states (0/1, 1/0 and x/x) of two specially categorised types of rainfall volumes (i.e., the "starting" and "isolated" volumes) were studied and the result is illustrated in Figure 4.19. It shows the probability distribution of the occurrence of the cascading states between two successive cascade levels given that a rainfall volume at the parent level is classified into the "starting" or "isolated" types. For "starting" type of rainfall volumes, the probability distribution of the occurrence of three cascading states

substantially alters with timescale ranges; it is observed that $P(0/1)$ and $P(x/x)$ increase when the rainfall time series is observed at coarser timescales; whilst $P(1/0)$ decreases. In a physical sense, $P(1/0)$ here represents the probability that a given "starting" rainfall volume at the parent level becomes "isolated" after one cascading; this consequently increases the intermittency of time series. The finest temporal resolution of the raingauge data used in this work is 5 min; it therefore makes sense that the 5-min rainfall time series is more intermittent than coarser-resolution series, and therefore the $P(1/0)$ is relatively high at the level 10 min - 5 min.

For "isolated" type of rainfall volumes, similar distributions are observed over the timescale ranges of study. $P(1/0)$ and $P(0/1)$ are always much bigger than $P(x/x)$. This means that it is very unlikely for a given "isolated" rainfall volume to evolve into two "unisolated" sub-volumes. However, it is observed that $P(x/x)$ gradually increases from the level 10 min - 5 min to 80 min - 40 min; whilst $P(0/1)$ and $P(1/0)$ decrease slightly. This depicts that the probability of a given "isolated" volume becoming "unisolated" increases when the rainfall time series is observed at coarser timescales; this variation, in a physical sense, means that the time series is more intermittent at finer timescales, which is consistent with the result for "starting" type of rainfall volumes.

These results show that the occurrence of cascading states is largely related to the two types of rainfall volumes defined in the FE model, sand it is therefore reasonable to take into account this physical factor in temporal rainfall downscaling.

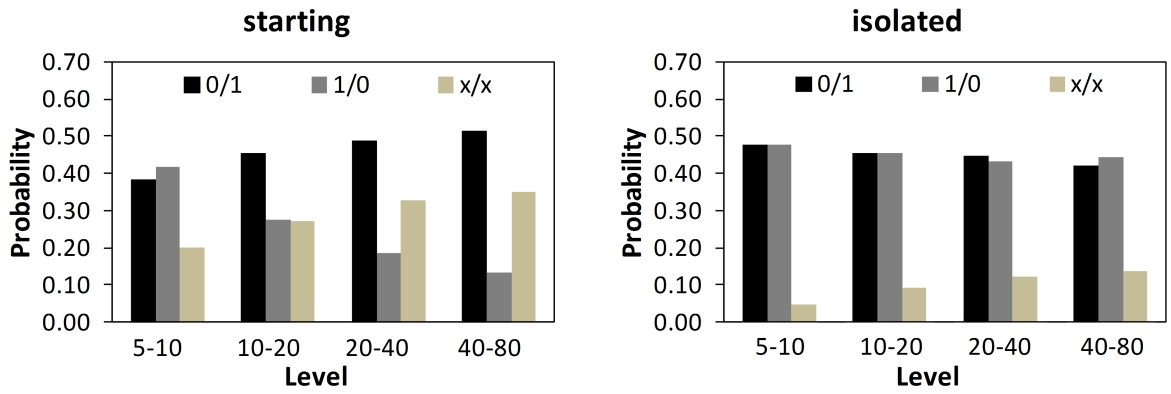


Figure 4.19: Probability of the occurrence of three cascading states (i.e. $P(0/1)$, $P(1/0)$ and $P(x/x)$) according to different positions: "starting" and "isolated"

4.4.3 Causality

Cârsteanu and Foufoula-Georgiou (1996) analysed the autocorrelation of a series of fragmentation ratios estimated from high-resolution historical raingauge data and demonstrated the existence of causal relations between temporally consecutive fragmentation ratios. This indicates the importance of applying causality, a physical factor that was in general not explicitly taken into account in discrete-in-scale cascade models, to temporal downscaling. This work proposed a methodology to implement causality in the FE model, which is shown in Figure 4.20 (top-right). There are, for example, two consecutive 10-min rainfall volumes respectively at time steps T and T+1, and the associated fragmentation ratio pairs to downscale these two volumes to 5-min are denoted $w_{T,1}/w_{T,2}$ and $w_{T+1,1}/w_{T+1,2}$. The idea of the proposed methodology is to condition the occurrence of $w_{T+1,1}/w_{T+1,2}$ by its previous state (i.e. $w_{T,1}/w_{T,2}$).

Analyses of the temporal dependence of the cascading states over the timescale ranges of interest were then carried out. Figure 4.20 (top-left) shows the probability distribution of $w_{T+1,1}/w_{T+1,2}$ in various timescale ranges given that $w_{T,1}/w_{T,2}$ is 0/1. It is observed that $P(0/1)$ at the time step T+1 decreases when the timescale range is coarser; in contrast, $P(x/x)$ substantially increases when coarser timescale ranges are studied. However, for the conditions of $w_{T,1}/w_{T,2}$ equal to 1/0 and x/x, the resulting probability distributions of cascading states and their variation with different timescale ranges change. For example, given that the state x/x occurs at the time step T (shown as Figure 4.20 (lower-right)), state x/x is always more likely to take place at the time step T+1 over the whole timescale ranges. These results show that the cascading state of a pair of fragmentation ratios at a given time step indeed correlates to its previous state, and it is therefore necessary to take into account the causality and its variation with different timescale ranges.

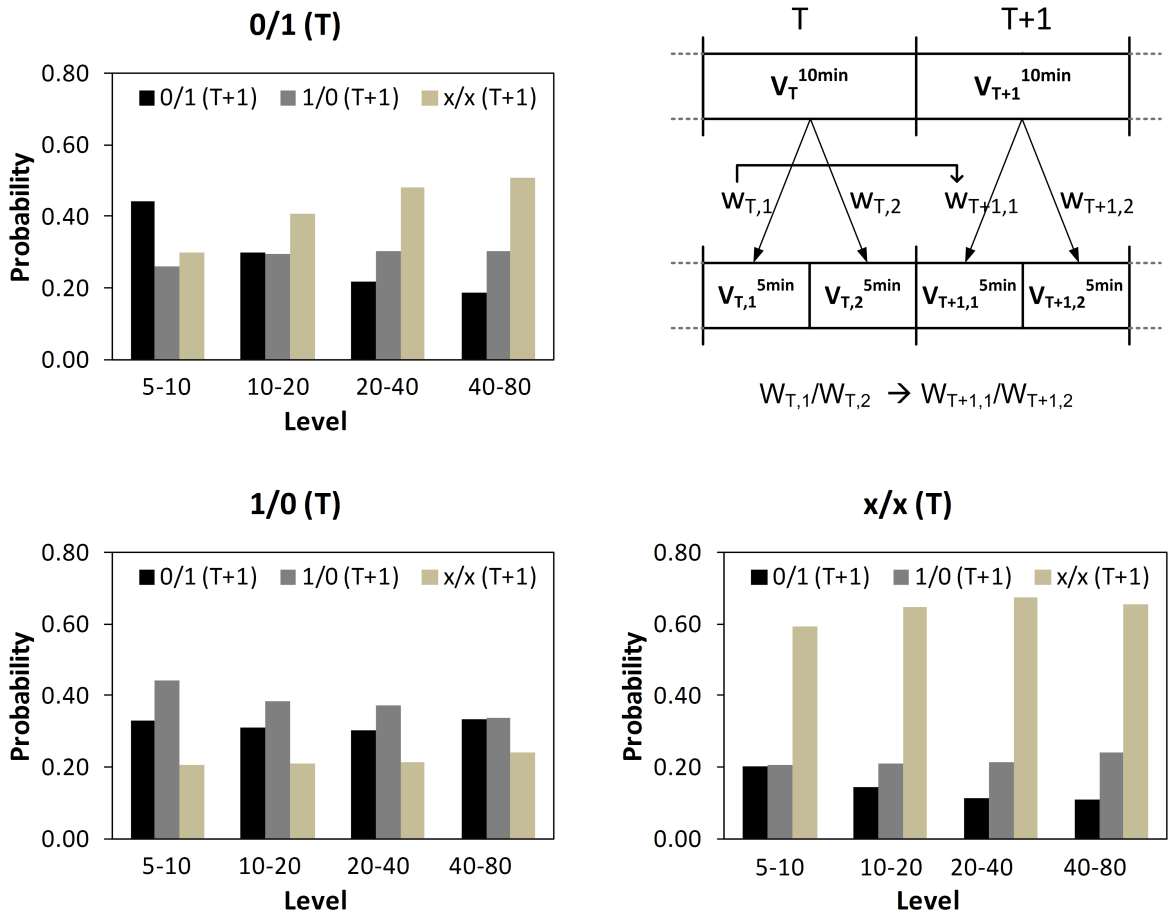


Figure 4.20: Schematic of causality between two pairs of temporally consecutive fragmentation ratios (top-right), and their variations according to different cascading states and timescale ranges

4.4.4 Applications of the FE model to temporal rainfall downscaling

In order to apply the aforementioned physical factors and their results to the schematic of the FE model, the following algorithm was proposed. This algorithm was initially based upon Olsson (1998)'s cascade model but it was further modified in order to appropriately take into account the causality factor.

Consider two successive cascade levels, e.g., timescales 10 min and 5 min in Figure 4.17, where the rainfall volumes at the level 10 min (i.e. the parent level) are assumed to be known ; the 5-min rainfall volumes (at the child level) are then stochastically obtained through repeating the following steps on each 10-min volumes.

1. Identify non-zero rainfall volumes: if the given volume at the parent level is zero, then skip it till the first non-zero volume is detected;

2. Confirm the type of the given non-zero volume according to its relative position:

   (a) For the case "isolated", sample the cascading state from the probability distribution shown in Figure 4.19 (right); if the cascading state is 1/0 (or 0/1), distribute whole volume to the prior (or the latter) sub-volumes at the child level; and if the cascading state is x/x, sample the fragmentation ratios from its weight distribution at the associated timescale range (shown in Figure 4.22;

   (b) for the case "starting", sample the cascading state from the probability distribution shown in Figure 4.19 (left); if the cascading state is 1/0 (or 0/1), distribute whole volume to the prior (or the latter) sub-volumes at the child level; and if the cascading state is x/x, sample the fragmentation ratios from its weight distribution at the associated timescale range (shown in Figure 4.22

   (c) for neither "isolated" nor "staring" cases, go to the "Causality" step.

3. Causality (for neither "isolated" nor "staring" volumes): sample the cascading state according to the state of previous cascading from the associated probability distribution shown in Figure 4.20. If the cascading state is 1/0 (or 0/1), distribute whole volume to the prior (or the latter) sub-volumes at the child level; and if the obtained state is x/x, sample the fragmentation ratios from the associated weight distribution (shown in Figure 4.22).

Based upon this algorithm, 5-min rainfall estimates of the Greenwich gauge were stochastically generated by downscaling 80-min rainfall data (which are aggregated from the original 5-min rainfall measurements). Statistical results of this algorithm for the FE model and their comparisons with the SD and LP models are shown in Figure 4.23. It is observed that the FE model in general underestimates the STDs less compared to the SD model, and with the same number of downscalings the FE model results in a relatively small uncertainty envelope of STD variables as compared to the LP model. However, similarly to the SD model, the FE model somewhat underestimates the Dry period percentage in the overall study period (note that there is no thresholding applied in the FE model to filter out the rainfall volumes smaller than 0.1 mm). Nonetheless, obvious improvements in reproducing the auto-correlation variables can be observed, particularly the estimated

lag-2 auto-correlations which well envelope the observed lag-2 auto-correlations in most months.

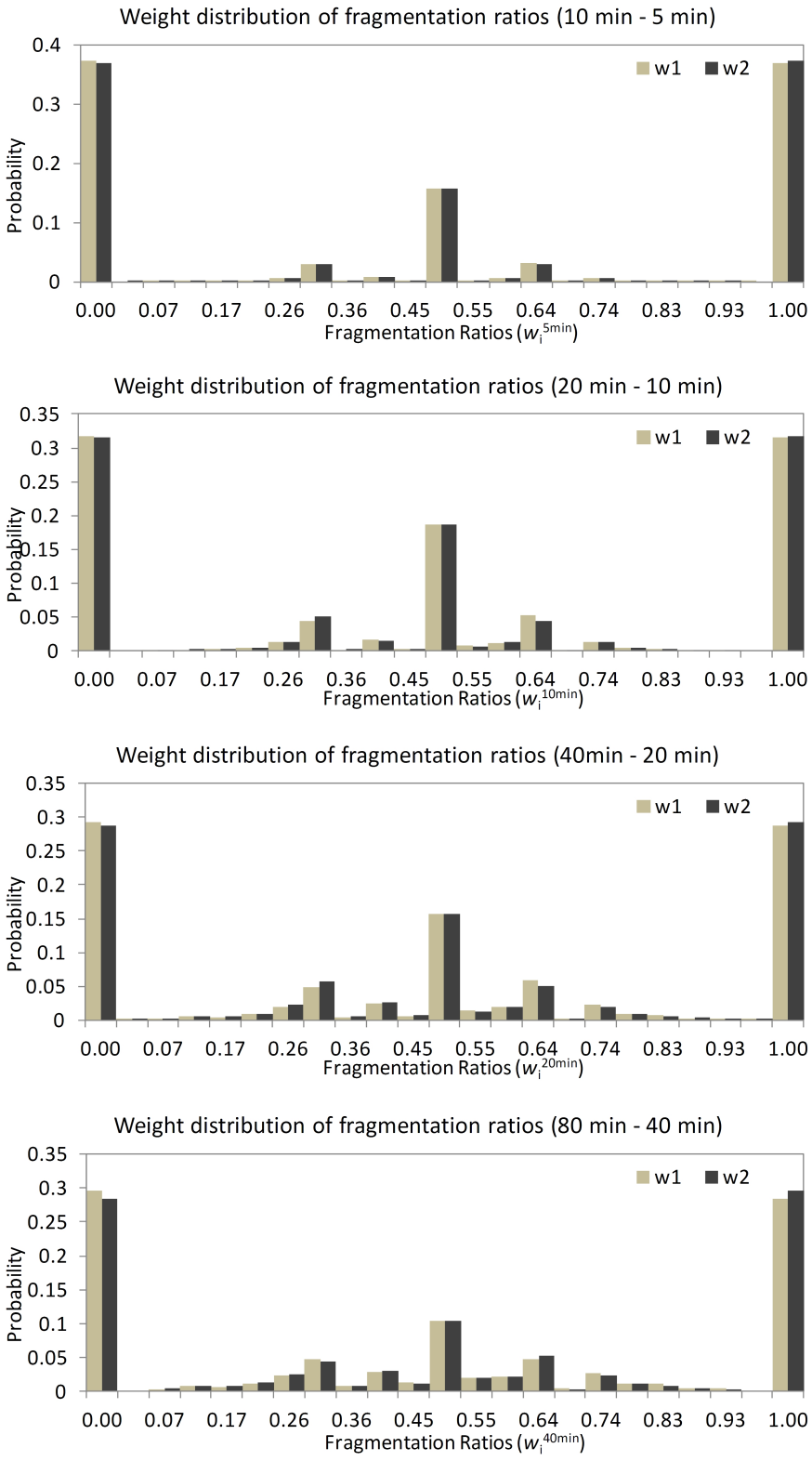


Figure 4.21: Weight distributions of fragmentation ratios between two successive cascade levels for all states (1/0, 0/1 and x/x) over timescales ranging from 80 min to 5 min

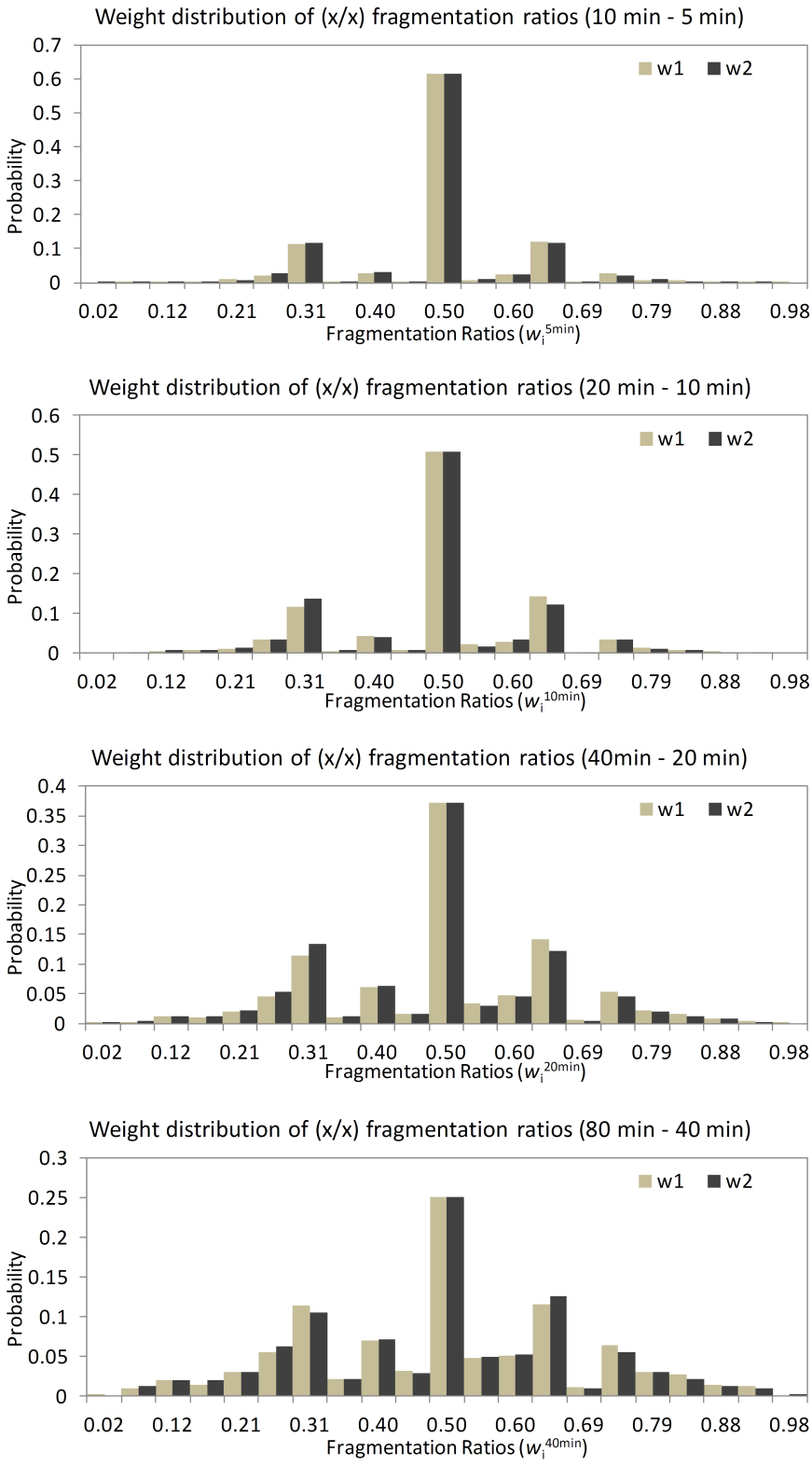


Figure 4.22: Weight distributions of non-zero fragmentation ratios between two successive cascade levels (i.e. x/x state) over timescales ranging from 80 min to 5 min

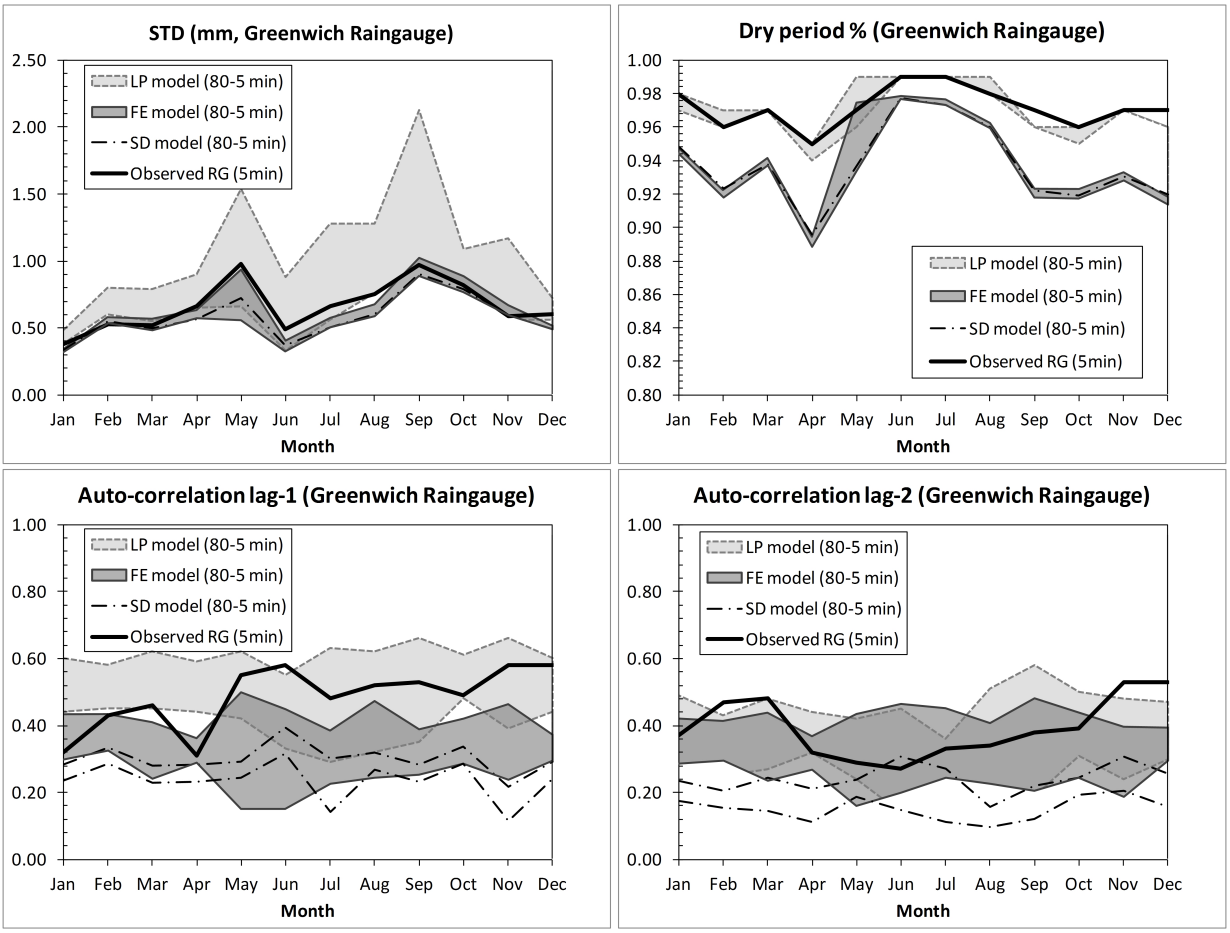


Figure 4.23: Comparison of monthly statistics of 5-min rainfall observations and synthetic time series generated respectively by SD, FE and LP models

4.5 Applications of cascade-based downscaling to urban hydrology

4.5.1 Temporal downscaling of raingauge measurements

A comparison between the FE and LP models' ability to produce short-term high-resolution rainfall time series is carried out here. Two historical 6-hour events (denoted event A and event B), extracted from the two-year Greenwich raingauge data, were used; the associated results are shown in Figure 4.24. In Figure 4.24, the profiles of the 5-min rainfall observations (the dark solid line) and the envelopes of 100 realisations of rainfall estimates generated by the FE (the area with the gray solid border) and LP (the area

with the gray dashed border) models are compared. In event A, the envelopes generated by the FE and LP models are similar; both models somewhat underestimate the peak rainfall rate, and some realisations miss the right timings to capture the peak. In event B, the realisations generated by both models can well envelop the rainfall observations; an envelope generated by the FE model of better sharpness can be observed, particularly in the vicinity of the peak.

The associated statistics of these two events are summarised in Table 4.1. In event A, the STDs generated from the LP model successfully envelope the observed STD; however, a relatively small STD range is generated from the FE model. Similarly, smaller ranges of lag-1 and 2 auto-correlations are generated from the FE models, and both models successfully envelope the observed auto-correlation variables. In the event B, the FE model shows a promising result in reproducing STDs, where a substantially smaller range is observed as compared to the LP model; and both models successfully envelope the observed auto-correlation variables of event B.

In order to understand the impact of these two cascade models on urban hydraulic outputs, the realisations of rainfall time series generated from the FE and LP models and the observed time series are used as inputs for hydraulic modelling in the Cranbrook catchment, where the outputs resulting from the observations are reckoned as reference. The resulting flows (in m^3/s) of the pipes respectively located at the up-, mid- and down-stream of the catchment are shown in Figures 4.25 and 4.26. It can be seen that, although the LP outputs have higher reliability (they always successfully envelop the reference flow outputs), the FE outputs have much higher sharpness (the width of envelope is relatively narrow) and acceptable reliability.

Some statistics of flow outputs are summarised in Tables 4.2-4.3. It can be seen that both models perform very well; the statistics of reference outputs are in general well reproduced. Similarly to the profiles of flows, the statistics of the FE outputs are much sharper, whilst the statistics of the LP outputs are slightly more reliable. This suggests that the FE model can be a useful tool to stochastically generate sub-hourly rainfall estimates that result in a sharper and reliable enough uncertainty range for flow outputs.

Table 4.1: Summary statistics of the observed and estimated rainfall estimates for events A and B in the Greenwich gauge (STD: standard deviation in mm/hr; r_i : lag-i autocorrelation coefficient in the 5-min temporal resolution)

Statistics		Mean (mm/hr)	STD (mm/hr)	r_1	r_2	r_3
Event A						
Observed	-	2.40	5.543	0.389	0.003	-0.029
LP model	Max	3.649	7.690	0.743	0.490	0.402
	min	0.592	1.022	0.114	-0.014	0.056
FE model	Max	-	4.868	0.396	0.376	0.404
	min		3.127	-0.038	-0.088	-0.081
Event B						
Observed	-	3.748	5.396	0.306	0.360	0.305
LP model	Max	8.022	19.391	0.703	0.488	0.406
	min	1.677	3.621	0.172	-0.017	-0.049
FE model	Max	-	8.555	0.385	0.548	0.386
	min		5.093	-0.138	-0.134	-0.021

Table 4.2: Summary statistics of the flow rates resulting from observed and estimated rainfall time series for events A (STD: standard deviation in m^3/s; r_i : lag-i autocorrelation coefficient in the 5-min temporal resolution)

Statistics Event A		Mean (m^3/s)	STD (m^3/s)	r_1	r_2	r_3
Up-stream (1455.1)						
RG flow	-	0.117	0.072	0.968	0.885	0.773
LP model	Max	0.164	0.156	0.991	0.968	0.932
	min	0.060	0.028	0.967	0.872	0.718
FE model	Max	0.119	0.070	0.991	0.964	0.923
	min	0.115	0.055	0.973	0.902	0.807
Mid-stream (463.1)						
RG flow	-	1.224	0.788	0.985	0.942	0.880
LP model	Max	1.774	1.354	0.995	0.980	0.956
	min	0.592	0.254	0.977	0.912	0.807
FE model	Max	1.243	0.748	0.994	0.976	0.949
	min	1.204	0.636	0.986	0.947	0.891
Down-stream (307.1)						
RG flow	-	1.687	0.936	0.993	0.976	0.949
LP model	Max	2.227	1.529	0.998	0.994	0.988
	min	0.879	0.409	0.985	0.941	0.872
FE model	Max	1.781	0.978	0.997	0.987	0.973
	min	1.691	0.898	0.994	0.977	0.951

Table 4.3: Summary statistics of the flows resulting from observed and estimated rainfall time series for events B (STD: standard deviation in m^3/s; r_i : lag-i autocorrelation coefficient in the 5-min temporal resolution)

Statistics Event B		Mean (m^3/s)	STD (m^3/s)	r_1	r_2	r_3
Up-stream (1455.1)						
RG flow	-	0.170	0.109	0.991	0.964	0.924
LP model	Max	0.344	0.317	0.989	0.961	0.918
	min	0.090	0.058	0.956	0.839	0.681
FE model	Max	0.175	0.113	0.992	0.969	0.933
	min	0.167	0.094	0.973	0.900	0.798
Mid-stream (463.1)						
RG flow	-	1.880	1.191	0.996	0.985	0.965
LP model	Max	2.571	1.690	0.996	0.987	0.973
	min	0.915	0.559	0.974	0.899	0.788
FE model	Max	1.919	1.186	0.996	0.985	0.967
	min	1.830	1.061	0.993	0.972	0.941
Down-stream (307.1)						
RG flow	-	2.431	1.378	0.998	0.991	0.982
LP model	Max	3.121	2.186	0.997	0.990	0.979
	min	1.337	0.741	0.988	0.952	0.895
FE model	Max	2.514	1.355	0.998	0.993	0.985
	min	2.370	1.233	0.995	0.982	0.961

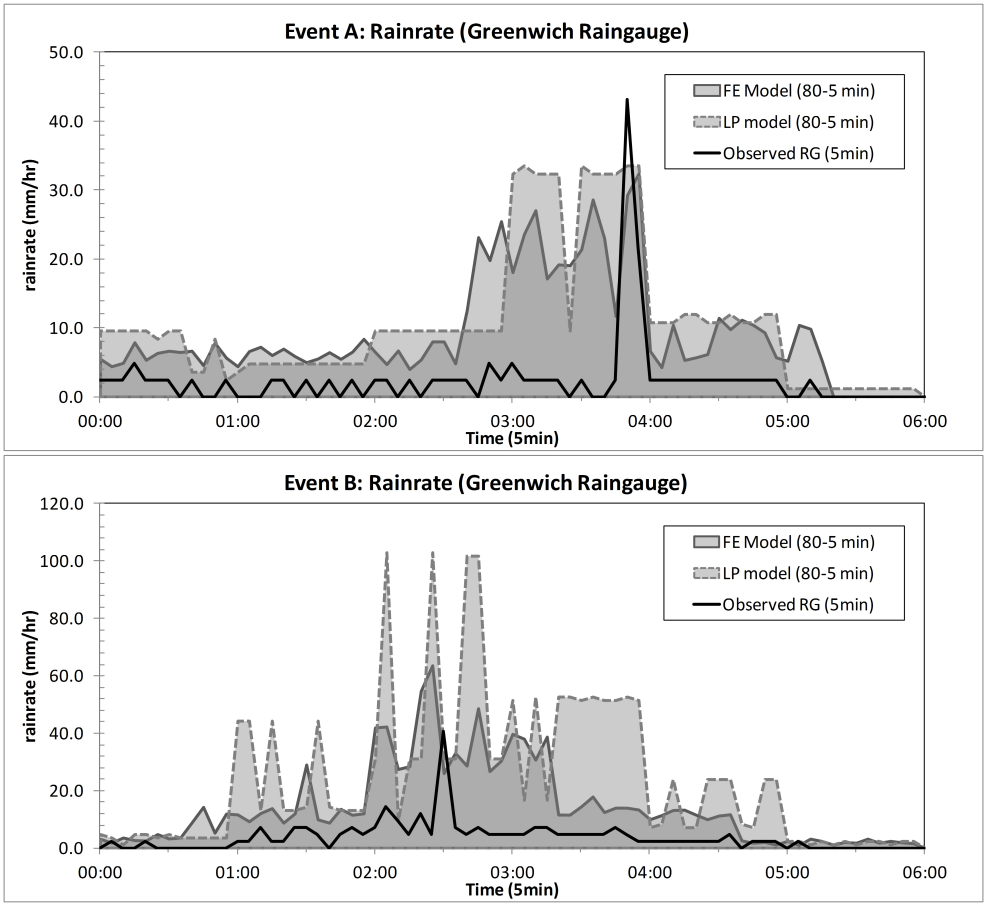


Figure 4.24: Comparison of 5-min rainfall observations and synthetic time series of two selected events generated by FE and LP models

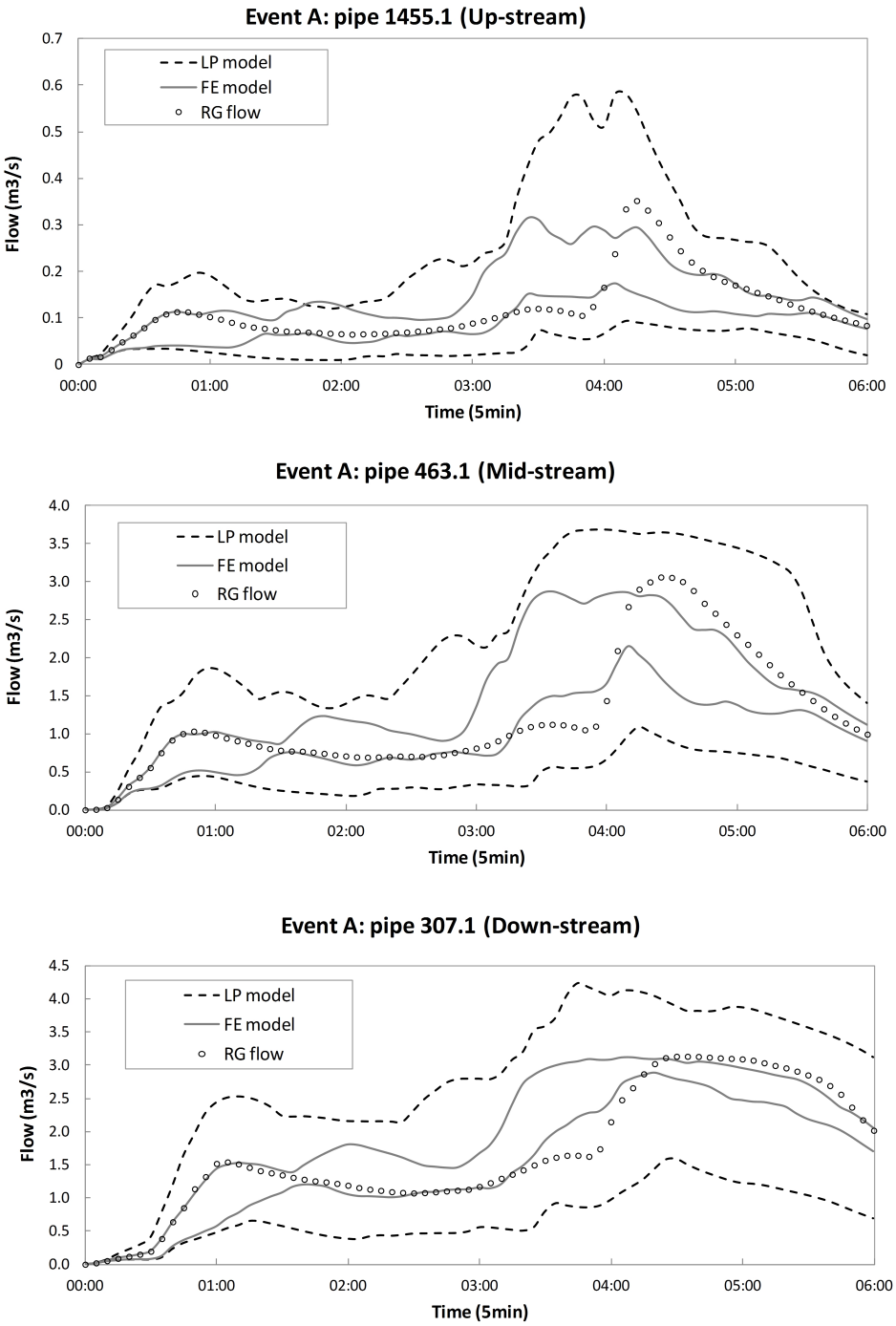


Figure 4.25: Comparison of flow rates (in m^3/s) resulting from observed 5-min rainfall observations (round markers) and the stochastically downscaled 5-min time series for event A using the FE (the area with dark dashed border) and LP (the area with gray solid border) models

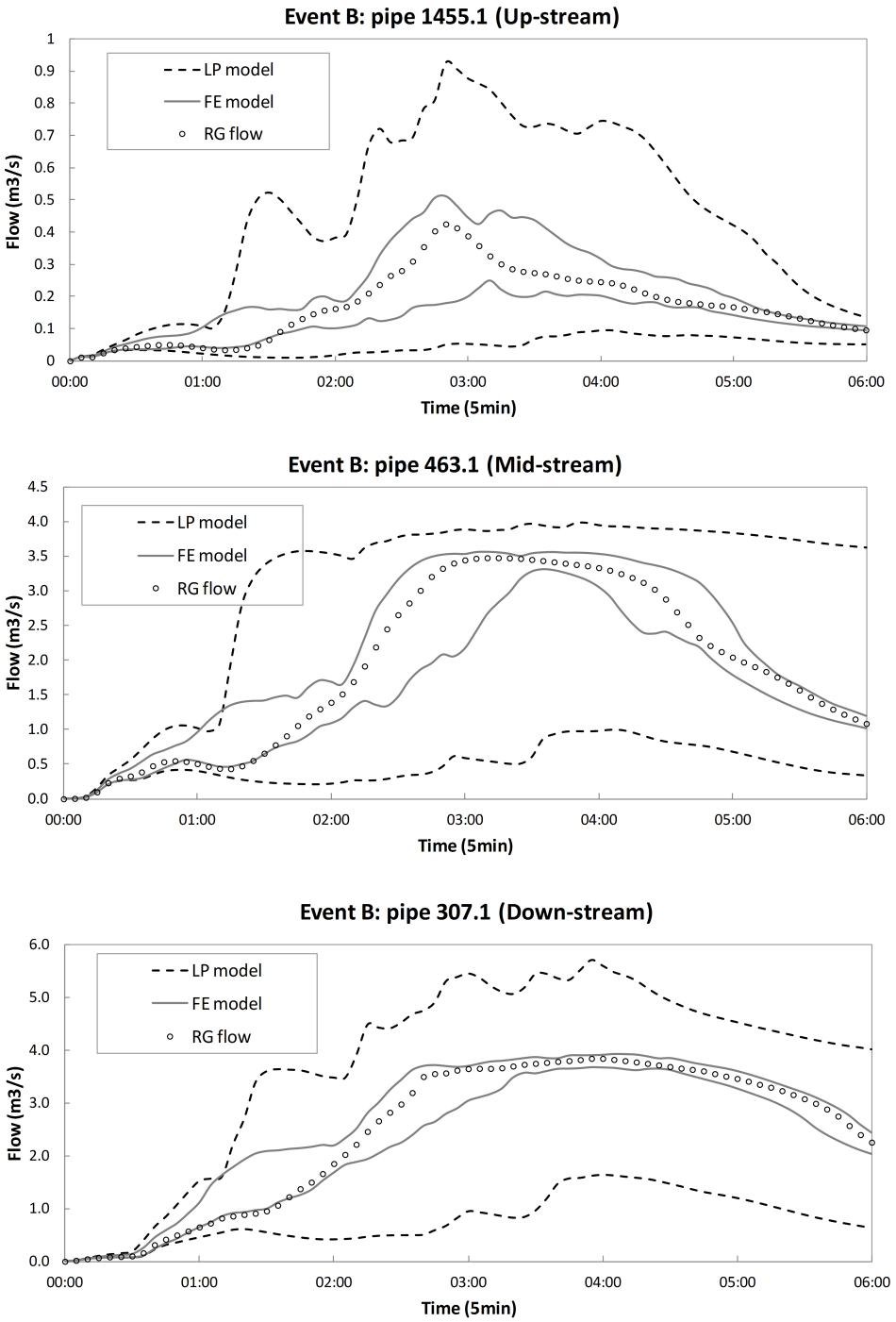


Figure 4.26: Comparison of flows (in m^3/s) resulting from observed 5-min rainfall observations (round markers) and the stochastically downscaled 5-min time series for event B using the FE (the area with dark dashed border) and LP (the area with gray solid border) models

4.5.2 Spatial downscaling of radar images

The SD model is used here to further verify its ability to accurately reproduce specific statistics of rainfall in the spatial downscaling process. The 5-min, 1-km radar data of four selected events in this work are used to carry out this verification. Similarly to Section 4.3.3, the original radar data are firstly aggregated to 8-km and downscaled back to 1-km using the SD model to obtain downscaled radar rainfall estimates.

Figures 4.27-4.30 show the variation of mean (upper) and standard deviation (lower) profiles of the original (gray solid line), downscaled (gray area with solid boundary) and ensemble (dark dashed line) radar rainfall estimates in the Cranbrook catchment for four selected events. For the event 23/08/2010, good agreement of mean rainfall rates between the downscaled and the observed rainfall estimates can be observed; while the spatial variability (standard deviation) is in general overestimated. In addition, because of the averaging process the ensemble rainfall estimates, whose mean profile is very similar to observations, are spatially smoother (less variable). However, it can be found that the overestimation of spatial variability does not influence the accuracy of the corresponding hydraulic outputs (see Figure 4.31). This suggests that the accuracy of the hydraulic outputs mainly depends on the ability to reproduce the magnitude of rainfall. The impact of spatial variability of rainfall actually lies in the uncertainty of flow outputs; this however will be further studied in the next Chapter.

Similarly, the mean and standard deviation profiles of the event 03/01/2012 are somewhat well reproduced; the means are slightly overestimated, while the standard deviations are slightly underestimated. Again, it can be seen that ability to reproduce mean rainfall rates is the major factor affecting the accuracy of the corresponding hydraulic outputs. In Figure 4.34, the flow depths are in general overestimated due to the overestimate of mean rainfall rates.

However, the performance of the SD model in events 26/05/2011 and 05-06/06/2011 is poor. It can be seen that some substantial overestimates of mean and standard deviation in specific periods of events lead to serious overestimates of the corresponding hydraulic outputs (see Figures 4.32 and 4.33). The possible reason to have these overestimates is that, in the SD model (and all other cascade models), the scaling features are obtained through an optimal fitting process over the scale range of interest. In other words, the derived fragmentation ratios represent the optimal (or averaged) scaling behaviour over the study range of spatial scales and over the study area (i.e. the Greater London, which is much larger than the Cranbrook catchment). When the forcing from the pattern of coarser-

resolution rainfall (e.g. in 8-km) and of larger area are stronger, the generated rainfall patterns in the finer resolutions and in a specific small area could be largely altered. This result reveals the tradeoff between accuracy and capacity in using downscaling techniques. If a coarser-resolution volume is used as the starting level of the cascading process, the capacity is larger because it can be applied to, for example, larger areas; however, it requires more cascade levels to produce finer-resolution volumes. This will increase the uncertainty of the downscaled estimates and therefore decrease the accuracy.

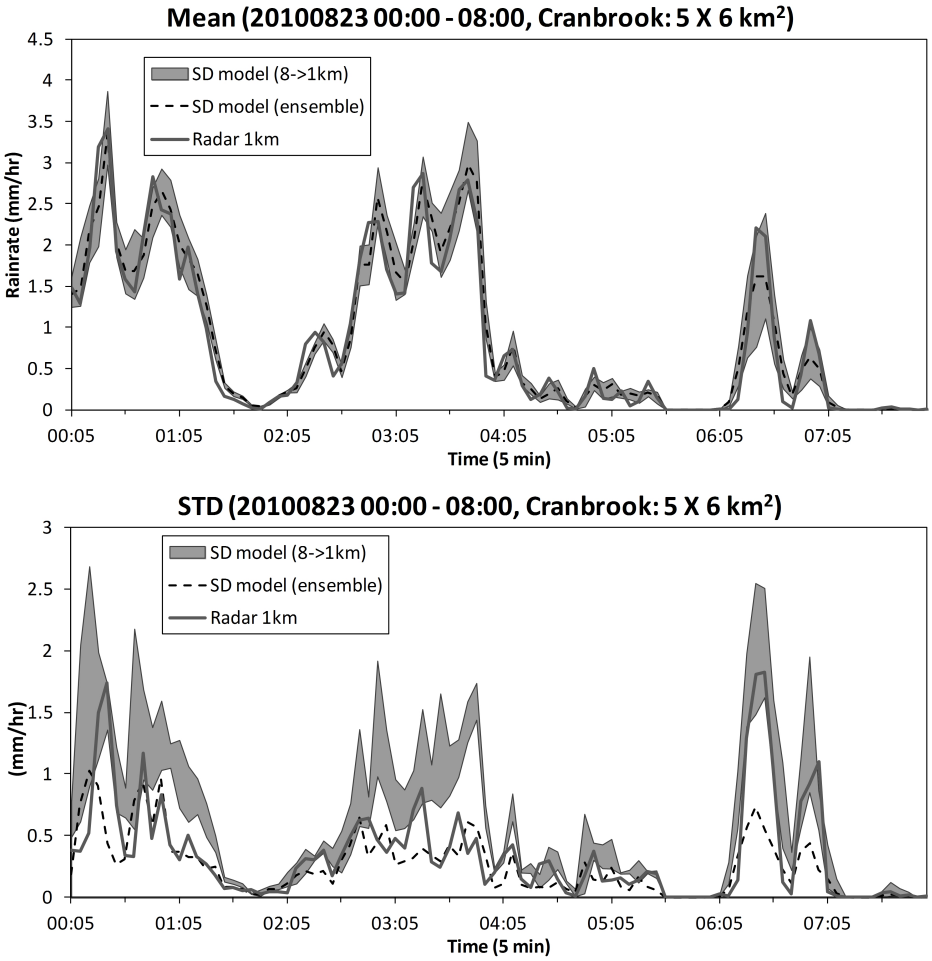


Figure 4.27: Mean (upper) and Standard deviation (lower) profiles of the original (gray solid line), stochastically downscaled (gray area with solid boundary) and ensemble (dark dashed line) radar rainfall estimates (from 8 km to 1 km scale) in the Cranbrook catchment for the event 23/08/2010

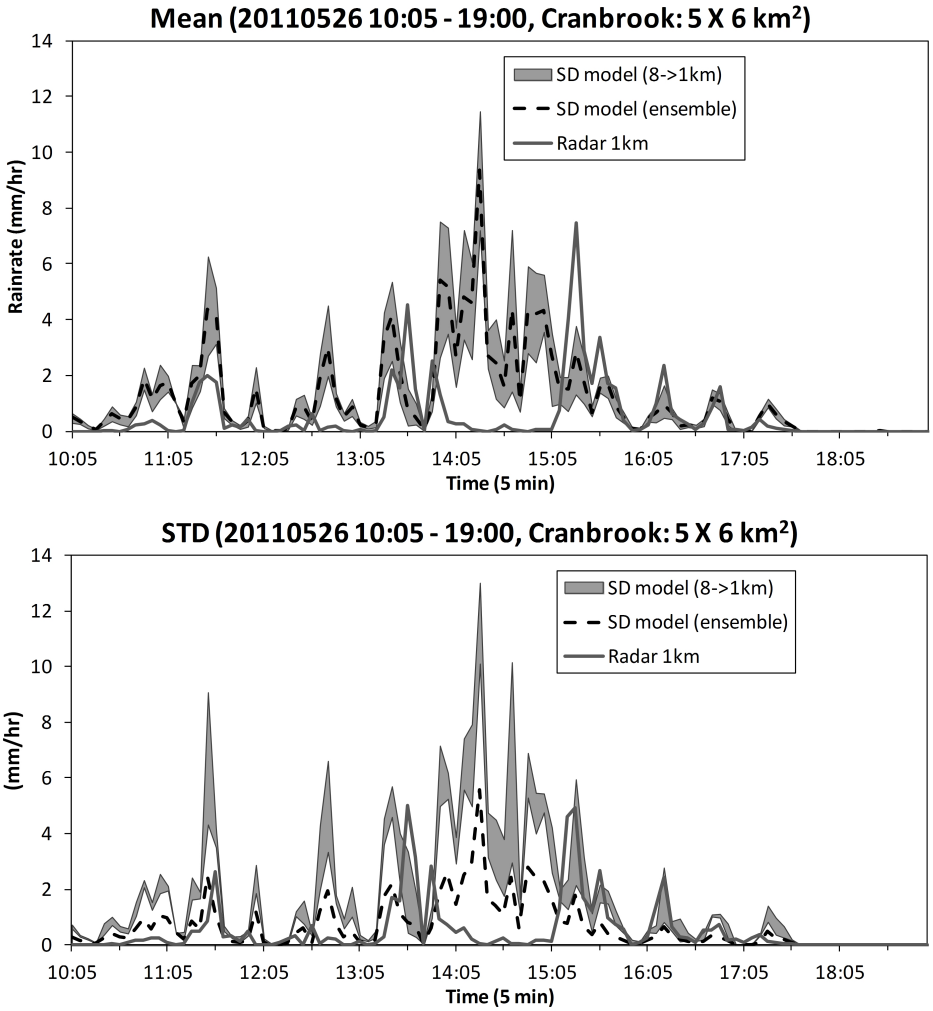


Figure 4.28: Mean (upper) and Standard deviation (lower) profiles of the original (gray solid line), stochastically downscaled (gray area with solid boundary) and ensemble (dark dashed line) radar rainfall estimates (from 8 km to 1 km scale) in the Cranbrook catchment for the event 26/05/2011

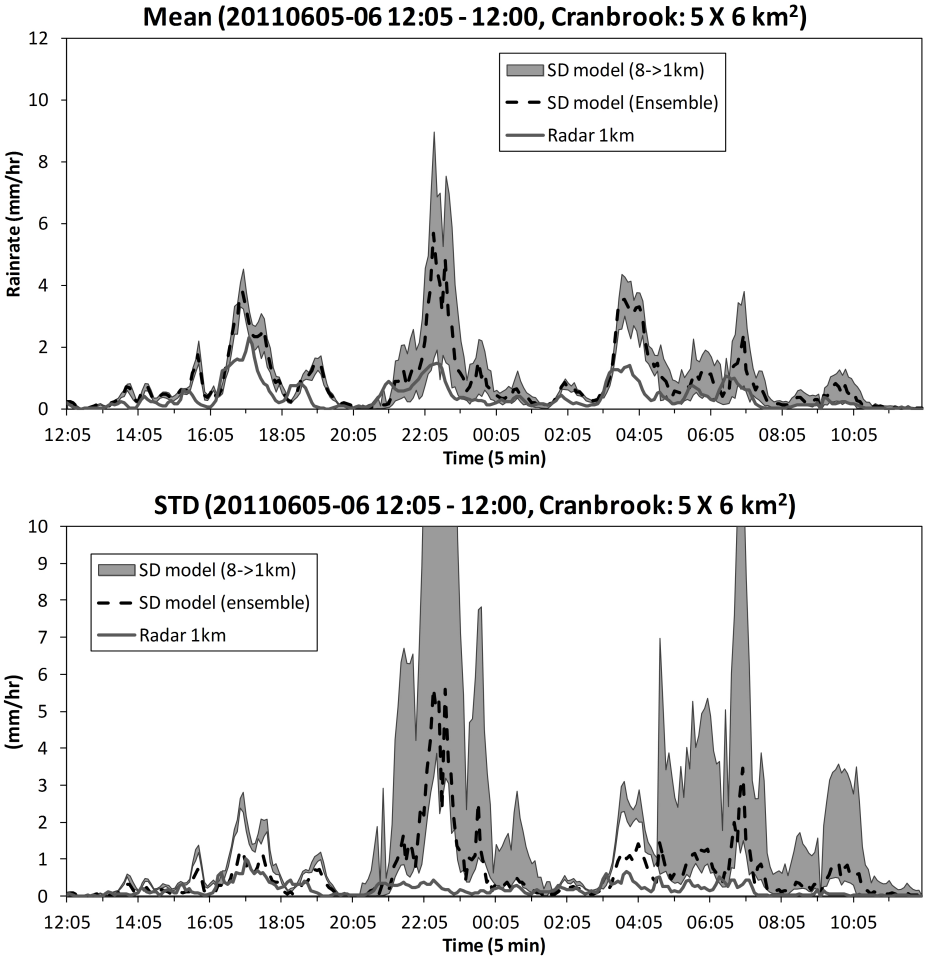


Figure 4.29: Mean (upper) and Standard deviation (lower) profiles of the original (gray solid line), stochastically downscaled (gray area with solid boundary) and ensemble (dark dashed line) radar rainfall estimates (from 8 km to 1 km scale) in the Cranbrook catchment for the event 05-06/06/2011

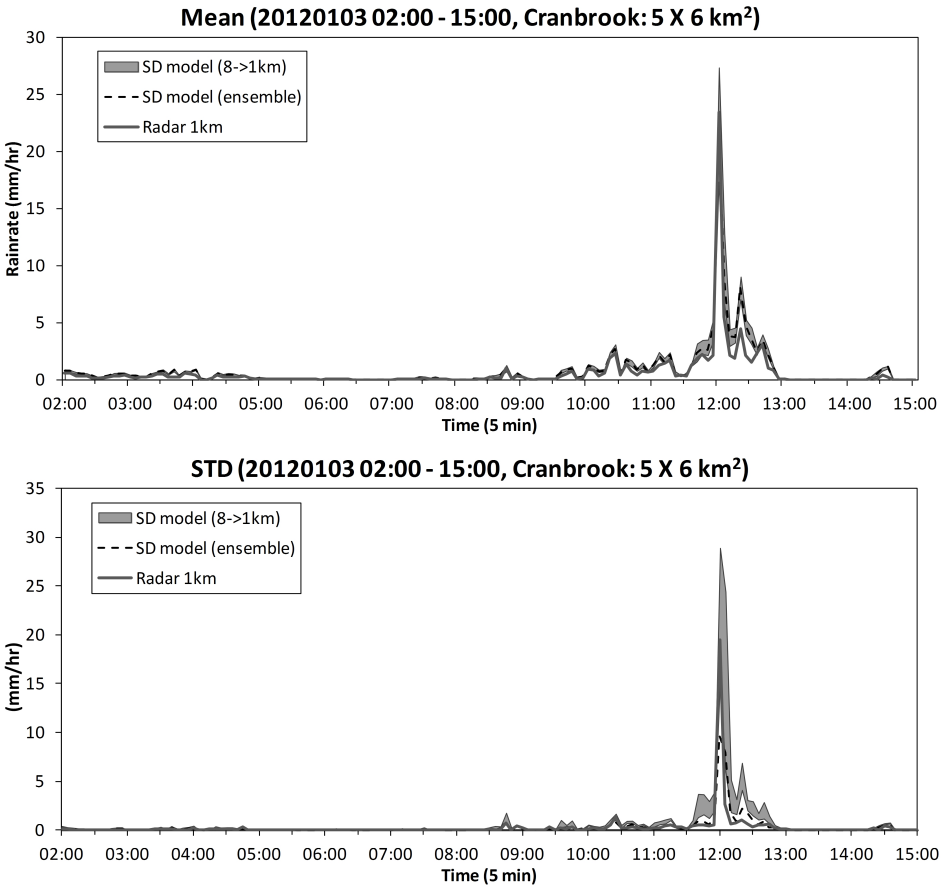


Figure 4.30: Mean (upper) and Standard deviation (lower) profiles of the original (gray solid line), stochastically downscaled (gray area with solid boundary) and ensemble (dark dashed line) radar rainfall estimates (from 8 km to 1 km scale) in the Cranbrook catchment for the event 03/01/2012

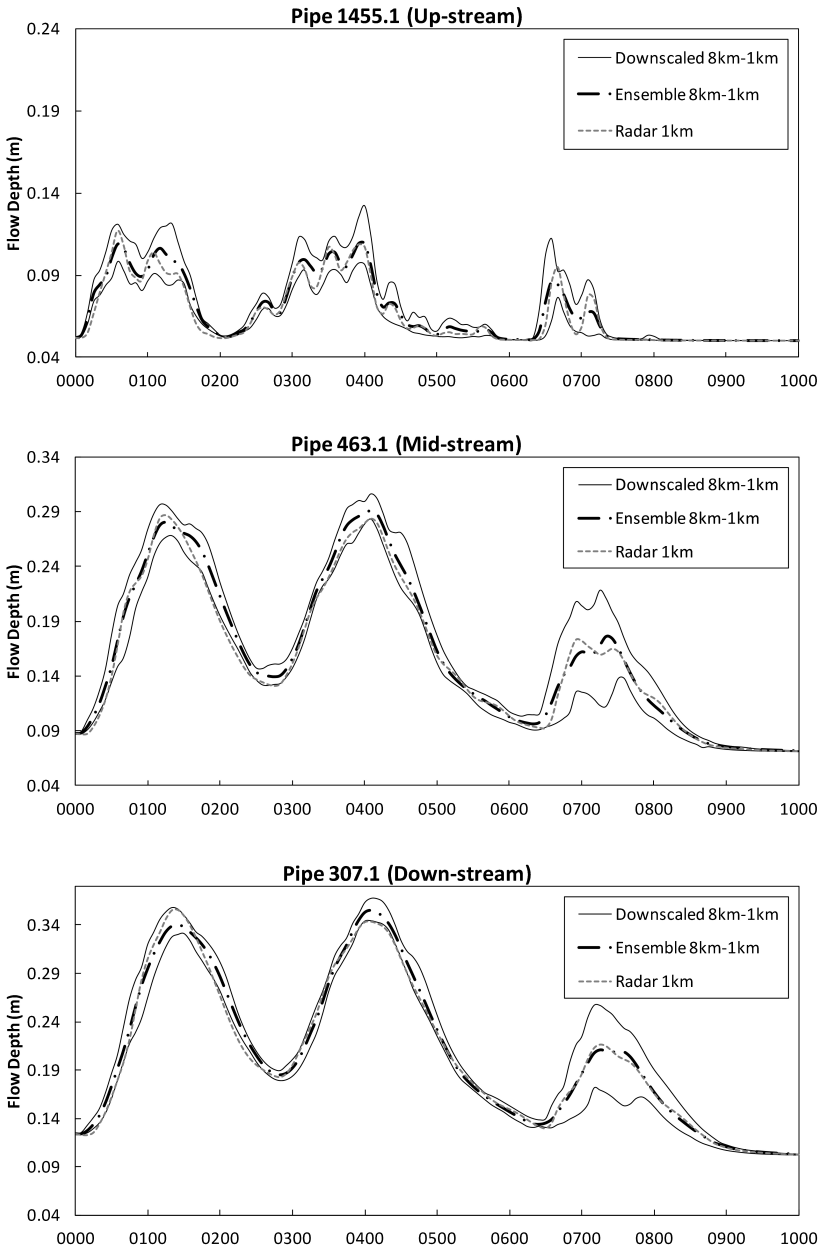


Figure 4.31: The comparison of the estimated flow depths at three selected pipes (from upper to lower figures: 1455.1 up-stream; 463.1 mid-stream; 307.1 down-stream) in the Cranbrook catchment for the event 23/08/2010. The estimated flow depths were obtained respectively using the original radar rainfall (gray dashed lines) and the stochastically downscaled (8 km to 1 km) radar rainfall estimates (enveloped by the dark solid lines) and their ensemble estimates (dark dashed-dotted lines) as inputs

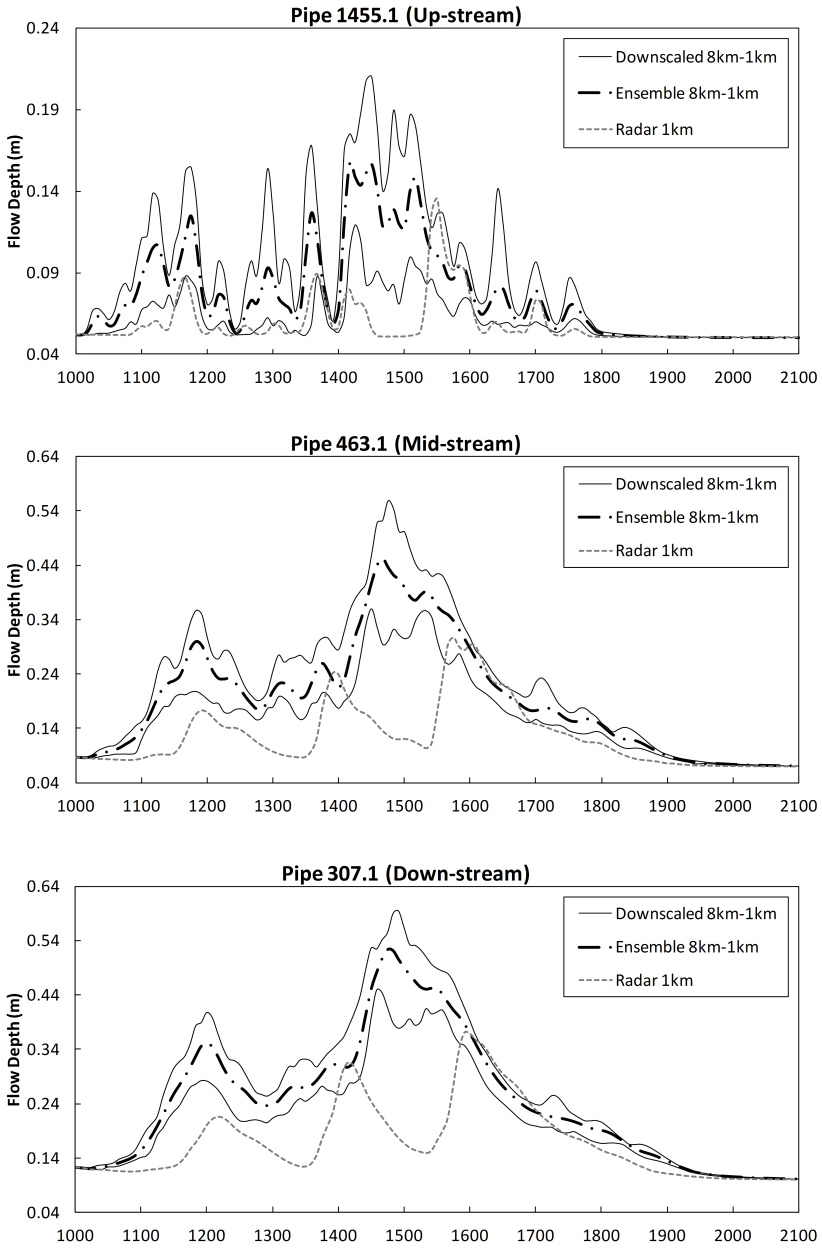


Figure 4.32: The comparison of the estimated flow depths at three selected pipes (from upper to lower figures: 1455.1 up-stream; 463.1 mid-stream; 307.1 down-stream) in the Cranbrook catchment for the event 26/05/2011. The estimated flow depths were obtained respectively using the original radar rainfall (gray dashed lines) and the stochastically downscaled (8 km to 1 km) radar rainfall estimates (enveloped by the dark solid lines) and their ensemble estimates (dark dashed-dotted lines) as inputs

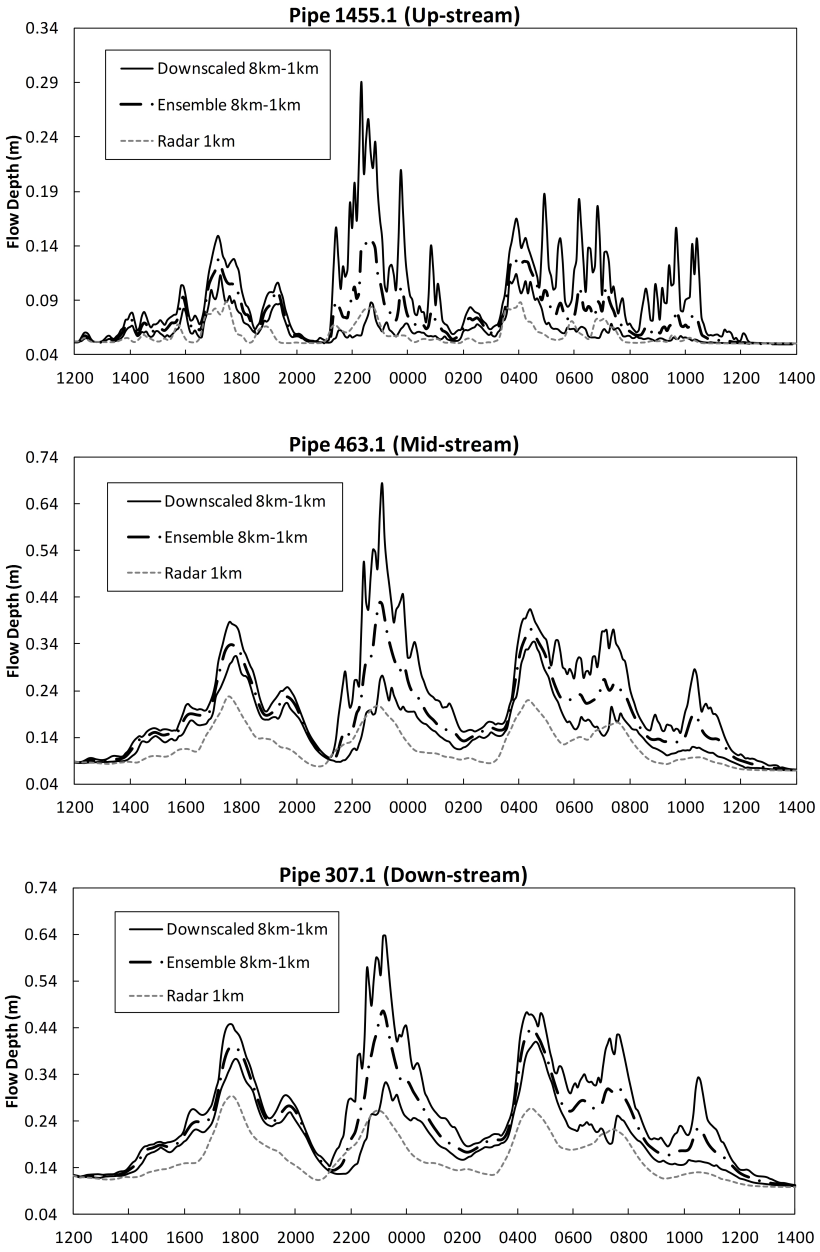


Figure 4.33: The comparison of the estimated flow depths at three selected pipes (from upper to lower figures: 1455.1 up-stream; 463.1 mid-stream; 307.1 down-stream) in the Cranbrook catchment for the event 05-06/06/2011. The estimated flow depths were obtained respectively using the original radar rainfall (gray dashed lines) and the stochastically downscaled (8 km to 1 km) radar rainfall estimates (enveloped by the dark solid lines) and their ensemble estimates (dark dashed-dotted lines) as inputs

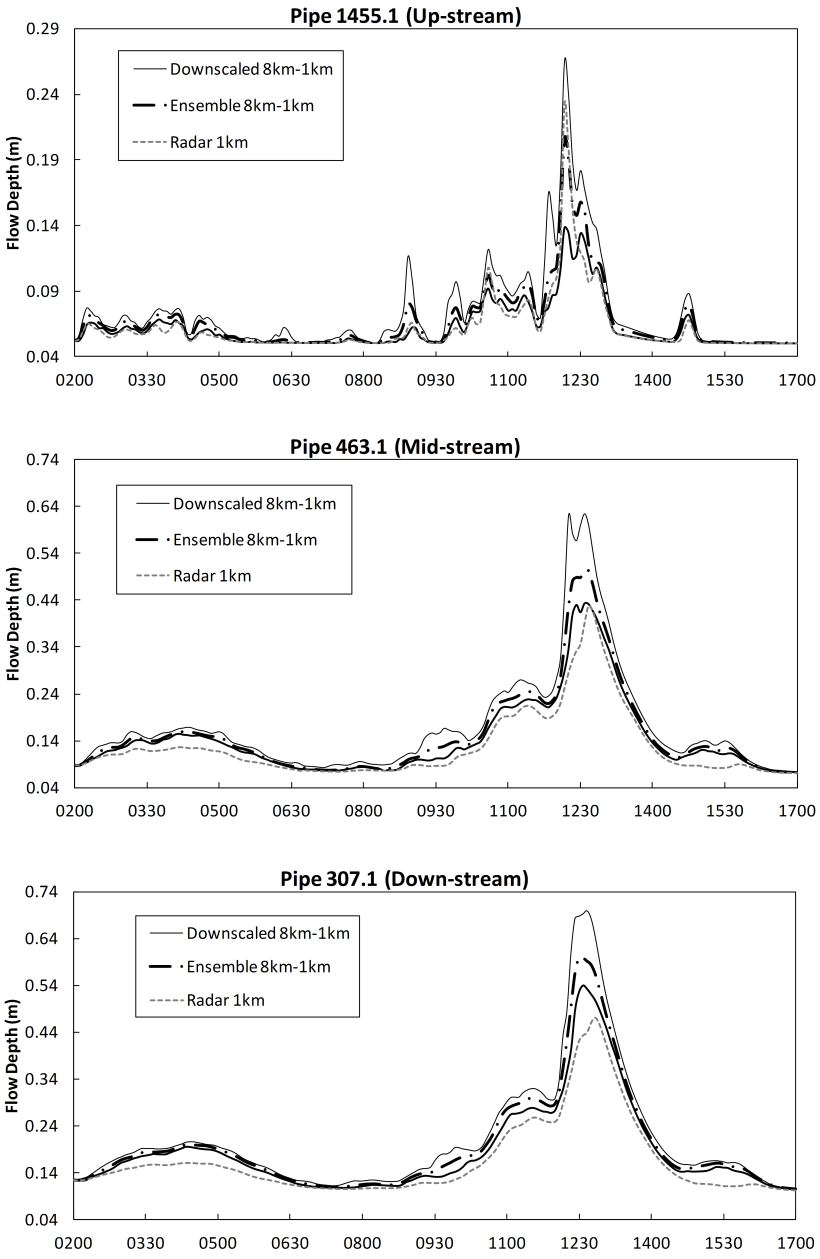


Figure 4.34: The comparison of the estimated flow depths at three selected pipes (from upper to lower figures: 1455.1 up-stream; 463.1 mid-stream; 307.1 down-stream) in the Cranbrook catchment for the event 03/01/2012. The estimated flow depths were obtained respectively using the original radar rainfall (gray dashed lines) and the stochastically downscaled (8 km to 1 km) radar rainfall estimates (enveloped by the dark solid lines) and their ensemble estimates (dark dashed-dotted lines) as inputs

4.6 Summary

In this chapter, a review of widely-used downscaling techniques was firstly given; then according to the requirement of urban hydrological applications, cascade-based techniques were further reviewed, including the associated category (i.e. discrete- and continuous-in-scale schemes) and theoretical background (i.e. the theory of multifractals). Two new discrete-in-scale cascade models were developed.

The semi-deterministic cascade model (denoted SD model) was developed based upon the theory of left-sided multifractals and was implemented by inversely solving the generating equation. The advantage of the SD model lies in its independence from any theoretical probability distributions and it can easily be extended to the reproduction of cascade processes in any dimension. Based upon the preliminary analyses, it shows particularly promising results in small-scale spatial rainfall downscaling as compared to the Log-Poisson cascade model (denoted LP model), a widely-used discrete-in-scale cascade model. It is however poor at reproducing the asymmetric temporal correlation that exists in rainfall time series and is particularly crucial in high temporal-resolution rainfall downscaling.

The second cascade model was therefore developed, which was named the fully empirical cascade model (denoted FE model). The FE model aims to introduce the "causality" and other physical factors into discrete-in-scale cascade models. As compared to the temporal SD model, the FE model shows improvement, particularly on the reproduction of temporal correlation between successive rainfall volumes within historical raingauge measurements. In addition, it shows promising results in short-term rainfall downscaling and therefore demonstrates its potentials to be used in urban hydrological applications.

These two models were respectively verified in this chapter using historical spatial and temporal rainfall data. The FE model was used to downscale raingauge data from hourly to sub-hourly scales, and the downscaled rainfall estimates were further used as inputs for urban hydrological simulation. The results show that, as compared to the LP model, the resulting hydraulic outputs from the FE model are sharper. This suggests that the FE model may be more suitable for urban hydraulic uses.

The SD model was used to downscale rainfall estimates from 8-km to 1-km scales. The downscaled 1-km estimates show good agreement with the observed 1-km radar rainfall measurements in some cases. The downscaled and observed 1-km radar estimates were further used as inputs for urban hydrological simulation to study the associated impact of the proposed SD model. The results demonstrate that the SD model has the potential to generate less uncertain high-resolution rainfall estimates than the LP model.

However, there is a generic drawback of cascade-based spatial downscaling models; that is, during the cascading (or branching) process, the spatial dependence between the sampled fragmentation ratios is not explicitly considered. Therefore, the cluster feature that is in general observed in the rainfall cells of storms cannot be satisfactorily reproduced. This could be an uncertainty source when the cascade-based downscaling techniques are used to generate high-resolution rainfall estimates. This drawback needs to be addressed and improved in the future.

In the next chapter, the SD model is used to further generate street-scale (smaller than 1 km grid length) rainfall estimates and to combine with the Bayesian-based adjustment technique (see Chapter 3) to estimate the associated uncertainty of hydraulic outputs caused by the spatial downscaling process.

Chapter 5

Combined Applications of Downscaling and Adjustment Techniques

A new procedure to process the operational rainfall estimates and therefore to enhance their applicability to urban flood modelling is proposed in this chapter. In this procedure, a combination of downscaling and adjustment is implemented, aiming to produce high accuracy and resolution rainfall estimates. However, unlike the adjustment process that reduces the rainfall input uncertainty through merging rainfall information from different sensors, the stochastic process of generating street-scale rainfall estimates, based upon the proposed SD model, actually causes additional uncertainty. This additional uncertainty will further propagate through hydraulic modelling and consequently affect the reliability of the resulting hydraulic outputs. It is therefore crucial to estimate the uncertainty caused by rainfall downscaling and its combination with the adjustment technique.

The 1-km radar data of four selected events crossing Greater London area (summarised in Section 2.4) were used herein as case studies. The original data were firstly downscaled to street-scale (500/250/125 m), based upon the proposed SD model, and further used as inputs for the hydraulic models of Cranbrook catchment (detailed in Section 2.2) to simulate the flow outputs (i.e. flow depths in mm) and to assess the associated uncertainty caused by this downscaling process. The same procedure was then applied to the Bayesian-based adjusted radar rainfall estimates to evaluate the impact of downscaling process on the adjusted rainfall estimates and consequently the hydraulic outputs.

In the following, the measure used to quantify the associated uncertainty will firstly be

explained. Then, the results of street-scale rainfall estimates downscaled respectively from the original and Bayesian-based adjusted radar rainfall data and their resulting hydraulic outputs will be shown and evaluated in term of the defined measure. Finally, key findings of this case study will be summarised.

5.1 Measurement of impact

This chapter focuses on evaluating the impact of the generation of street-scale rainfall estimates on urban hydrological/hydraulic modelling; the measures used here are therefore derived based upon the variation of hydraulic outputs (flow depth in a given pipe) resulting from 5-min rainfall estimates at various street scales (i.e. 500/250/125 m).

For a given urban drainage system, the flow depth of a given pipe results from many factors, such as total volume of input (mainly rainfall) and its spatial and temporal distribution and hydraulic characteristics (e.g. drainage area). In the case of urban pluvial flooding, the uncertainty of flow outputs is mainly propagated from rainfall inputs (Collier, 2009). A 1^{st}-order approximation is employed here to give a sense of the relation of rainfall input and flow output. Assume that, for a given rainfall event, the estimated flow depth of a pipe at a specific time step t is a joint contribution of the flow depths resulting from the total rainfall volume and its spatial distribution (or variation), which can be formed as follows:

$$F_{est,t} = F_{mean,t} + F_{sv,t}, \tag{5.1}$$

where $F_{mean,t}$ and $F_{sv,t}$ respectively represent the flow depth components resulting from rainfall volume and its spatial variation[1]. For the "rainfall volume" component, the flow depth results from rainfall that, at each time step, is uniformly-distributed over the catchment and of the same mean rainfall rate as the study event. The difference between $F_{est,t}$ and $F_{mean,t}$, namely $F_{sv,t}$, is therefore considered to be the contribution from spatial variations.

Based upon Eq. (5.1), the estimated flow depth (of a given pipe at time step t) resulting

[1] $F_{mean,t}$ and $F_{sv,t}$, however, are not fully independent; some further modifications will be made later.

from the 1-km radar rainfall estimates (of a given event) can be formed as follows:

$$F_{R_{1km},t} = F_{mean_{1km},t} + F_{sv_{1km},t}, \tag{5.2}$$

and this can be further extended to be a flow depth resulting from rainfall estimates in a specific spatial resolution s:

$$F_{est_s,t} = F_{mean_s,t} + F_{sv_s,t}, \tag{5.3}$$

where $F_{mean_{1km},t}$ and $F_{mean_s,t}$ represent the flow depths resulting from the uniformly-distributed rainfall estimates respectively in 1-km and s resolutions; and $F_{sv_{1km},t}$ and $F_{sv_s,t}$ represent the contributions from their spatial variations.

For the proposed SD model, because the mass of total rainfall is microcanonically conserved over a specific scale range, $F_{mean_s,t}$ is therefore constant within this scale range. For example, during the spatial downscaling process from 1 km to 250 m, $F_{mean_{1km},t}$ is the same as $F_{mean_{250m},t}$.

By rearranging Eq.(5.2) and substituting it and $F_{mean_{1km},t} = F_{mean_s,t}$ into Eq. (5.3), the following equation can be obtained:

$$F_{est_s,t} = F_{R_{1km},t} + \Delta F_{sv_s,t}, \tag{5.4}$$

where $\Delta F_{sv_s,t} = F_{sv_s,t} - F_{sv_{1km},t}$. Here, if s is defined within the street scale range (i.e. 500/250/125 m) that this research is interested in, $\Delta F_{sv_s,t}$ can be regarded as the flow depth increment (or decrement) resulting from the spatial variation component of rainfall estimates at a given street scale s, as compared to the spatial variation component resulting from 1-km radar rainfall estimates.

For a stochastic downscaling process, a certain number of realisations of downscaled rainfall estimates are generated. When they are further used as inputs for hydraulic modelling, the same number of realisations of flow depths will be obtained. For each time step, the maximum and minimum realisations of the estimated flow depths of a given pipe can

be termed

$$F_{max_s,t} = F_{R_{1km},t} + \Delta F_{sv_{s^+},t}, \tag{5.5}$$

and

$$F_{min_s,t} = F_{R_{1km},t} + \Delta F_{sv_{s^-},t}, \tag{5.6}$$

where $\Delta F_{sv_{s^+},t}$ and $\Delta F_{sv_{s^-},t}$ are the maximum and minimum increment (or decrement) resulting from the spatial variation of stochastically downscaled rainfall estimates at the street-scale resolution s, as compared to the spatial variation component resulting from 1-km radar rainfall estimates. The flow depth uncertainty resulting from the spatial variation component of downscaled rainfall estimates (as compared to the original 1-km radar) can therefore be quantified using $\Delta F_{sv_{s^+},t} - \Delta F_{sv_{s^-},t}$. However, as mentioned above, $F_{mean,t}$ and $F_{sv,t}$ are not fully independent; it can be expected that $\Delta F_{sv_{s^+},t} - \Delta F_{sv_{s^-},t}$ are not fully independent from $F_{R_{1km},t}$ either. Some preliminary tests were carried out, and the result actually shows that they are highly correlated (correlation is ≈ 0.7).

In order to remove the effect of $F_{R_{1km},t}$ from $\Delta F_{sv_{s^+},t} - \Delta F_{sv_{s^-},t}$, a dimensionless measure is therefore defined to evaluate the proportion of this uncertainty to the flow depth resulting from the original 1-km radar data:

$$U_s = \frac{\Delta F_{sv_{s^+},t} - \Delta F_{sv_{s^-},t}}{F_{R_{1km},t}} \times 100, \tag{5.7}$$

which can be reformulated as follows (by rearranging Eqs. (5.5) and (5.6) and substituting them into Eq. (5.7)):

$$U_s = \frac{F_{max_s,t} - F_{min_s,t}}{F_{R_{1km},t}} \times 100. \tag{5.8}$$

In the following sections, this measure, called uncertainty range, is used to represent the uncertainty range of flow outputs caused by the spatial variation of downscaled rainfall estimates.

5.2 Applications of downscaled rainfall estimates

In this section, the street-scale rainfall estimates are generated by downscaling the **original** 1-km radar data to 500/250/125 m, rather than downscaling from 8-km data (as in Section 4.5.2). This is because this section focuses on the uncertainty caused by the spatial variability only; the use of 8-km data will introduce other uncertainty caused by rainfall volume bias. For this downscaling range (i.e. from 1 km to 500/250/125 m), due to the semi-deterministic nature of the SD model, the mean rainfall volumes are micro-canonically conserved and the standard deviation is deterministic at each scale (see Appendix D for details). Therefore, the profiles of mean rainfall rates at different scales are the same and will not be shown, and the profiles of standard deviations are shaped as lines, rather than envelopes with specific bandwidths.

The generation of street-scale rainfall estimates is conducted based upon the assumption that the scale-invariance feature, establishing over the spatial scales ranging from 8 km to 1 km, can be extended to finer scales. This assumption has been studied and in theory the scaling can be invariant between 8-km and 30-cm scales (Lovejoy and Mandelbrot, 1985; Lovejoy and Schertzer, 1990; Tessier et al., 1993). This means that the associated fragmentation ratios (those employed in Section 4.5.2) can be directly applied to the 1-km radar data to produce 500/250/125 m (or even higher resolutions) rainfall estimates.

Figures 5.9-5.12 (upper) show the variation of standard deviation profiles of rainfall estimates at scales: 500 m (gray dashed lines), 250 m (yellow solid lines) and 125 m (red solid lines), over the Cranbrook catchment for four selected events. Standard deviations (or spatial variability) reasonably increase when higher-resolution rainfall estimates are studied. This quantitative increment of standard deviations between any two successive scales however is not invariant. This is due to the nonlinear nature of the SD model, which is indicated in Eq. D.5. In addition, for some time steps, it is observed that the patterns of standard deviations are gradually altering. This is because, in the SD model, the fragmentation ratios are obtained from an optimal fitting process between scales 8 km and 1 km. For those time steps at which the patterns change, the forcing from coarser-resolution rainfall is stronger than the 1-km rainfall and therefore the patterns are gradually altered in order to follow the theoretically optimal patterns at given scales.

Figures 5.1-5.4 show the estimated flow depths resulting from the original radar rainfall (gray dashed lines) and the stochastically downscaled (1 km to 500 m) radar rainfall estimates (enveloped by the dark solid lines) and their ensemble estimates (dark dashed-dotted lines) as inputs. The flow depths at three pipes (from upper to lower figures: 1455.1 up-

stream; 463.1 mid-stream; 307.1 down-stream) in the Cranbrook catchment are selected. Good agreement between the flow depths resulting from the 1-km radar data and the ensemble 500-m rainfall estimates are in general observed. A specific (uncertainty) band, namely the difference between maximum and minimum flow depths, can be seen throughout each event. This band indicates the uncertainty induced by the spatial variation of downscaled rainfall estimates.

Eq.5.8 is further employed here to evaluate the defined uncertainty range U_s and its evolution with time and different scales, which are shown in Figures 5.5-5.8. The variation of uncertainty range profiles at three selected pipes (from upper to lower figures: 1455.1 up-stream; 463.1 mid-stream; 307.1 down-stream) in the Cranbrook catchment can be seen. It can be found that there is no specific relation between the value of flow depths and the coincidental uncertainty ranges. The associated statistics are given in Table 5.1, where the mean, standard deviation (std) and maximum (max) of U_s at three selected pipes for four selected events are summarised. It can be observed that in general the averaged value (i.e. mean) and variability (i.e. std) of U_s decrease from upstream to downstream, and increase from coarser (500 m) to finer scales (125 m). The maxima of U_s also decrease from upstream to downstream; however, they do not always increase from coarser (500 m) to finer scales (125 m). For some cases (see Figures 5.5-5.8), although 125-m rainfall estimates always have higher spatial variability than 250-m rainfall estimates, the maxima of U_s were caused by the rainfall inputs downscaled from 1-km to 250-m, instead of 125-m. One possibility is that the number of realisations used in this work is merely 30, which may be insufficient to completely represent the behaviour of the maxima of U_s against rainfall inputs at different scales. However, it can be concluded that in general higher-resolution rainfall inputs will lead to higher uncertainty in flood modelling.

Table 5.1: Summary statistics of uncertainty ranges U_s resulting from rainfall estimates, down-scaled from 1-km to 500/250/125 m, at three selected pipes (pipe 1455.1, 463.1 and 307.1, respectively located at the up-, mid- and down- streams of the Cranbrook catchment) for four selected events

scale	Upstream (1455.1)			Midstream (463.1)			Downstream (307.1)		
	mean	std	max	mean	std	max	mean	std	max
23/08/2011 event									
1km-500m	5.05	6.07	34.85	4.50	4.31	25.89	2.91	2.66	15.51
1km-250m	6.14	7.87	50.43	7.95	8.09	50.03	7.40	6.99	31.53
1km-125m	5.40	6.18	34.29	5.64	6.40	39.08	3.39	3.57	16.32
26/05/2011 event									
1km-500m	5.50	8.01	41.19	5.73	6.08	31.24	3.97	3.79	22.28
1km-250m	6.85	9.43	55.25	7.07	7.39	52.28	4.73	4.46	24.59
1km-125m	6.65	8.60	47.55	6.31	7.06	48.70	4.41	4.41	23.72
05-06/06/2011 event									
1km-500m	6.40	7.81	38.93	5.57	4.62	19.99	3.40	2.58	12.01
1km-250m	8.15	10.16	59.07	6.81	5.75	23.58	4.33	3.62	16.11
1km-125m	9.55	11.94	50.06	8.15	7.55	39.22	4.84	4.13	20.05
03/01/2012 event									
1km-500m	3.61	4.57	30.94	2.95	2.38	14.42	1.72	1.64	11.52
1km-250m	4.23	5.60	44.81	3.16	2.40	12.56	1.91	1.59	9.05
1km-125m	4.45	5.58	42.33	2.96	2.29	14.64	1.64	1.40	7.79

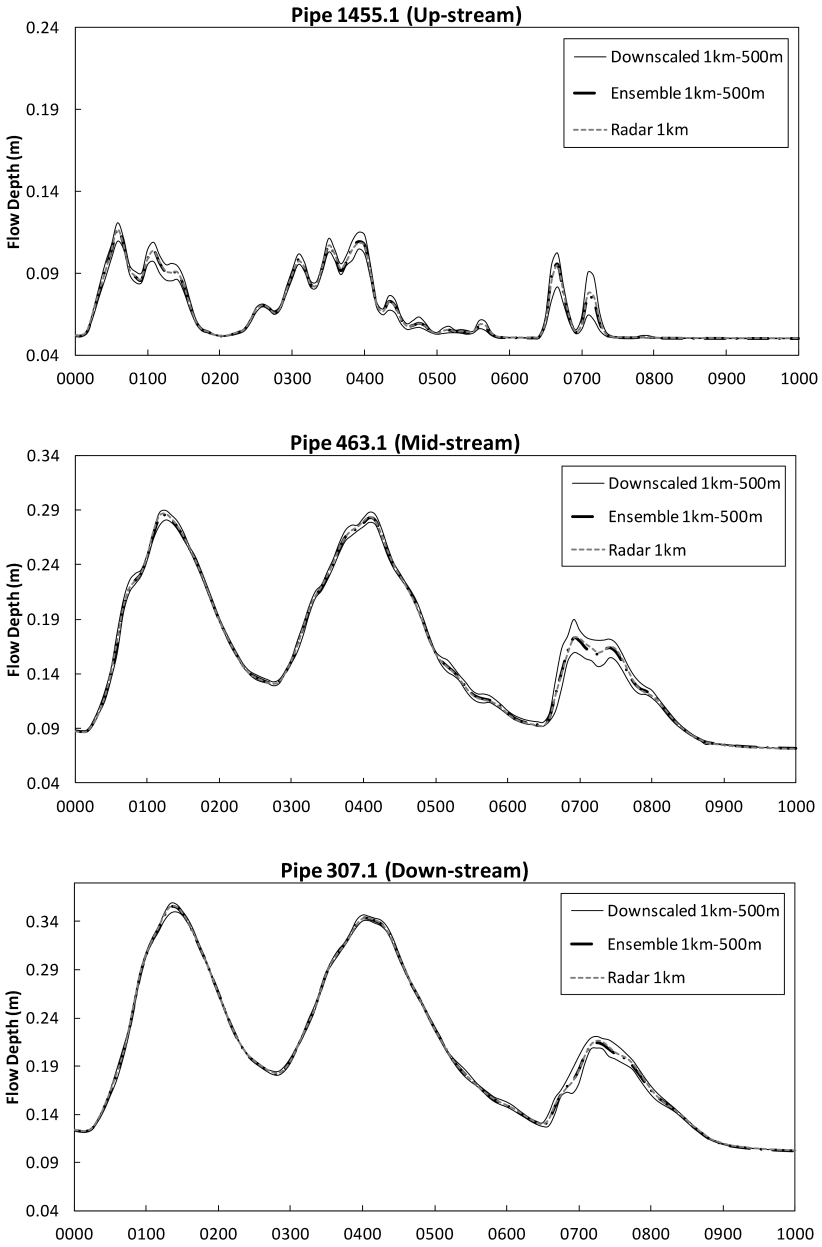


Figure 5.1: The comparison of the estimated flow depths at three selected pipes (from upper to lower figures: 1455.1 up-stream; 463.1 mid-stream; 307.1 down-stream) in the Cranbrook catchment for the event 23/08/2010. The estimated flow depths were obtained by using the original radar rainfall (gray dashed lines) and the stochastically downscaled (1 km to 500 m) radar rainfall estimates (enveloped by the dark solid lines) and their ensemble estimates (dark dashed-dotted lines) as inputs

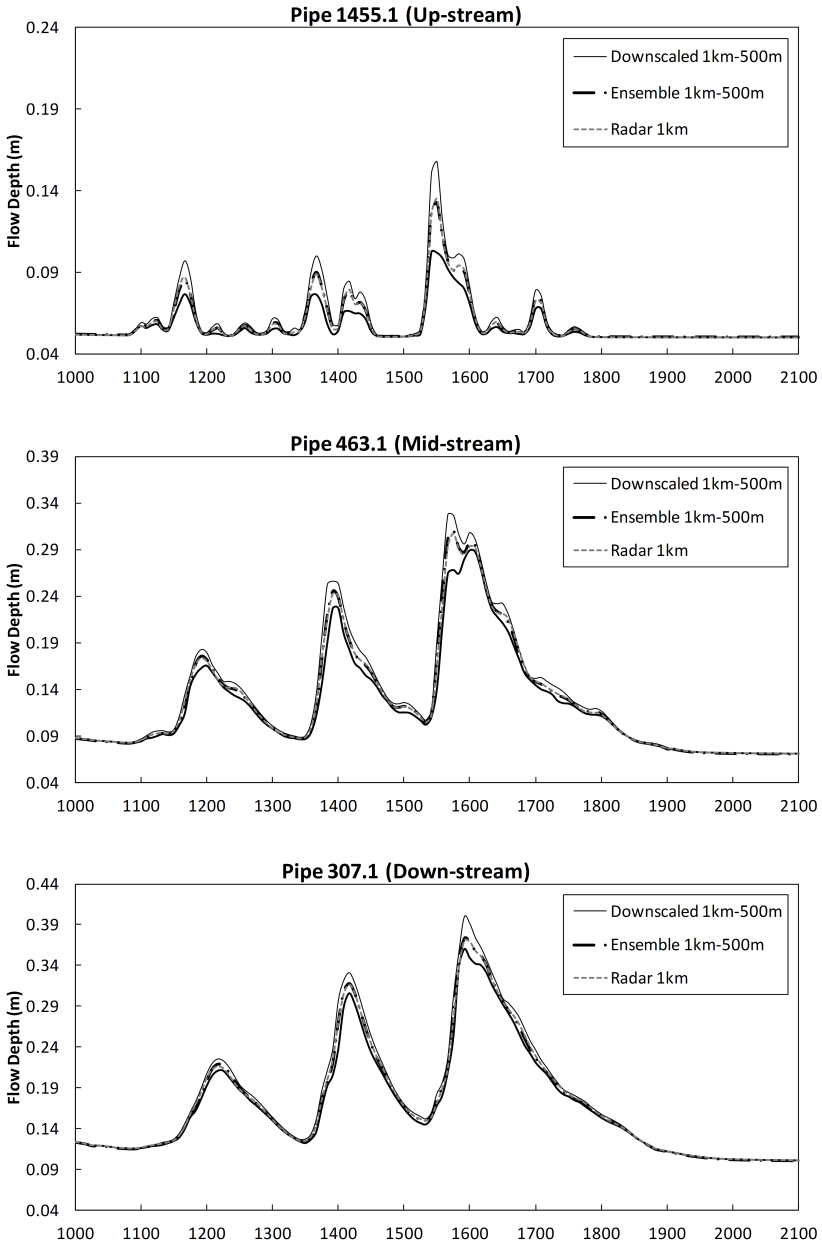


Figure 5.2: The comparison of the estimated flow depths at three selected pipes (from upper to lower figures: 1455.1 up-stream; 463.1 mid-stream; 307.1 down-stream) in the Cranbrook catchment for the event 26/05/2011. The estimated flow depths were obtained by using the original radar rainfall (gray dashed lines) and the stochastically downscaled (1 km to 500 m) radar rainfall estimates (enveloped by the dark solid lines) and their ensemble estimates (dark dashed-dotted lines) as inputs

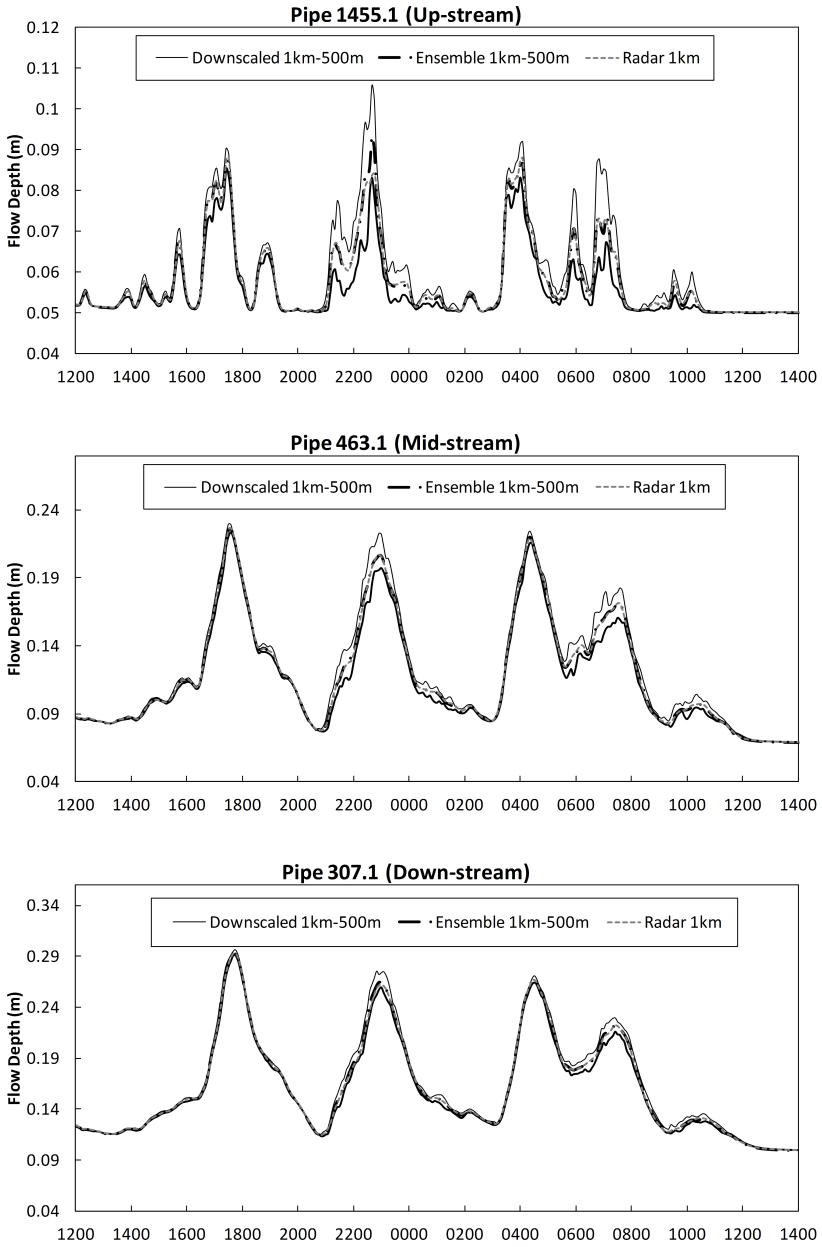


Figure 5.3: The comparison of the estimated flow depths at three selected pipes (from upper to lower figures: 1455.1 up-stream; 463.1 mid-stream; 307.1 down-stream) in the Cranbrook catchment for the event 05-06/06/2011. The estimated flow depths were obtained by using the original radar rainfall (gray dashed lines) and the stochastically downscaled (1 km to 500 m) radar rainfall estimates (enveloped by the dark solid lines) and their ensemble estimates (dark dashed-dotted lines) as inputs

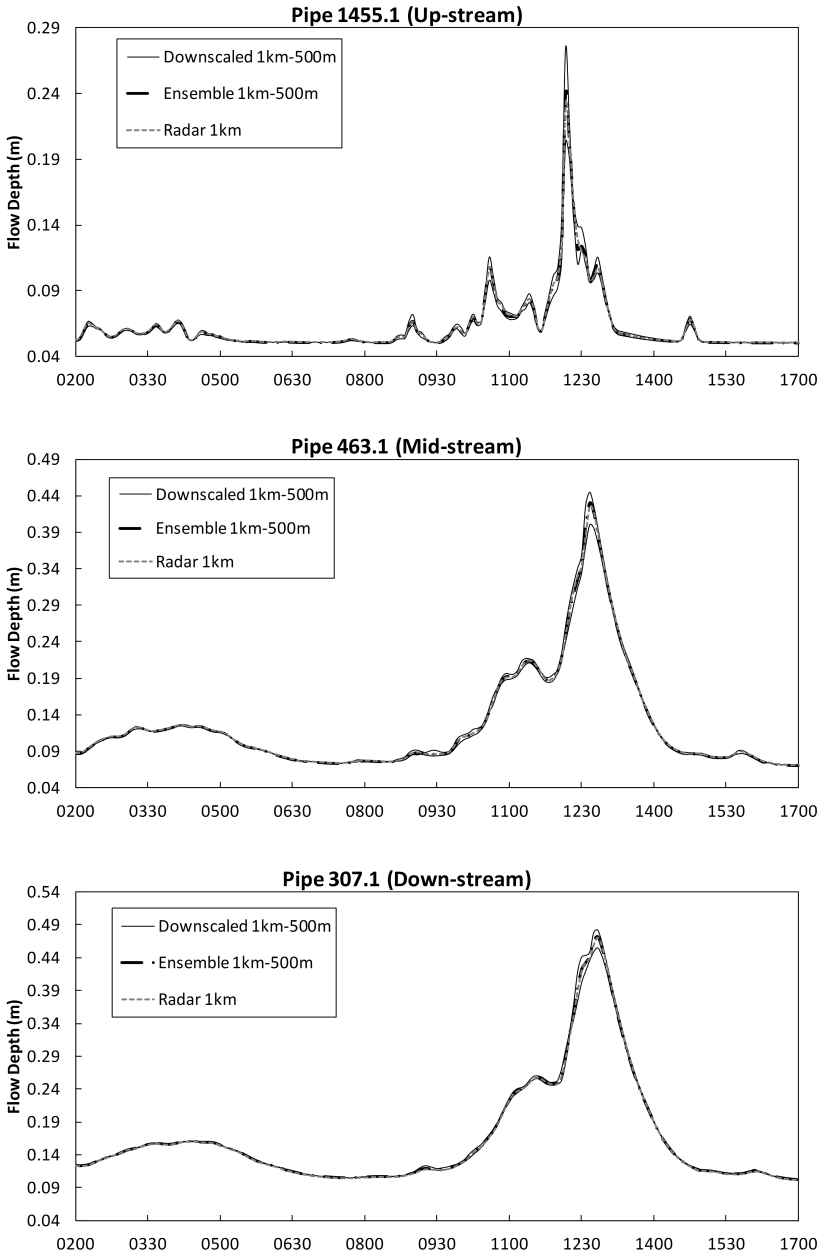


Figure 5.4: The comparison of the estimated flow depths at three selected pipes (from upper to lower figures: 1455.1 up-stream; 463.1 mid-stream; 307.1 down-stream) in the Cranbrook catchment for the event 03/01/2012. The estimated flow depths were obtained by using the original radar rainfall (gray dashed lines) and the stochastically downscaled (1 km to 500 m) radar rainfall estimates (enveloped by the dark solid lines) and their ensemble estimates (dark dashed-dotted lines) as inputs

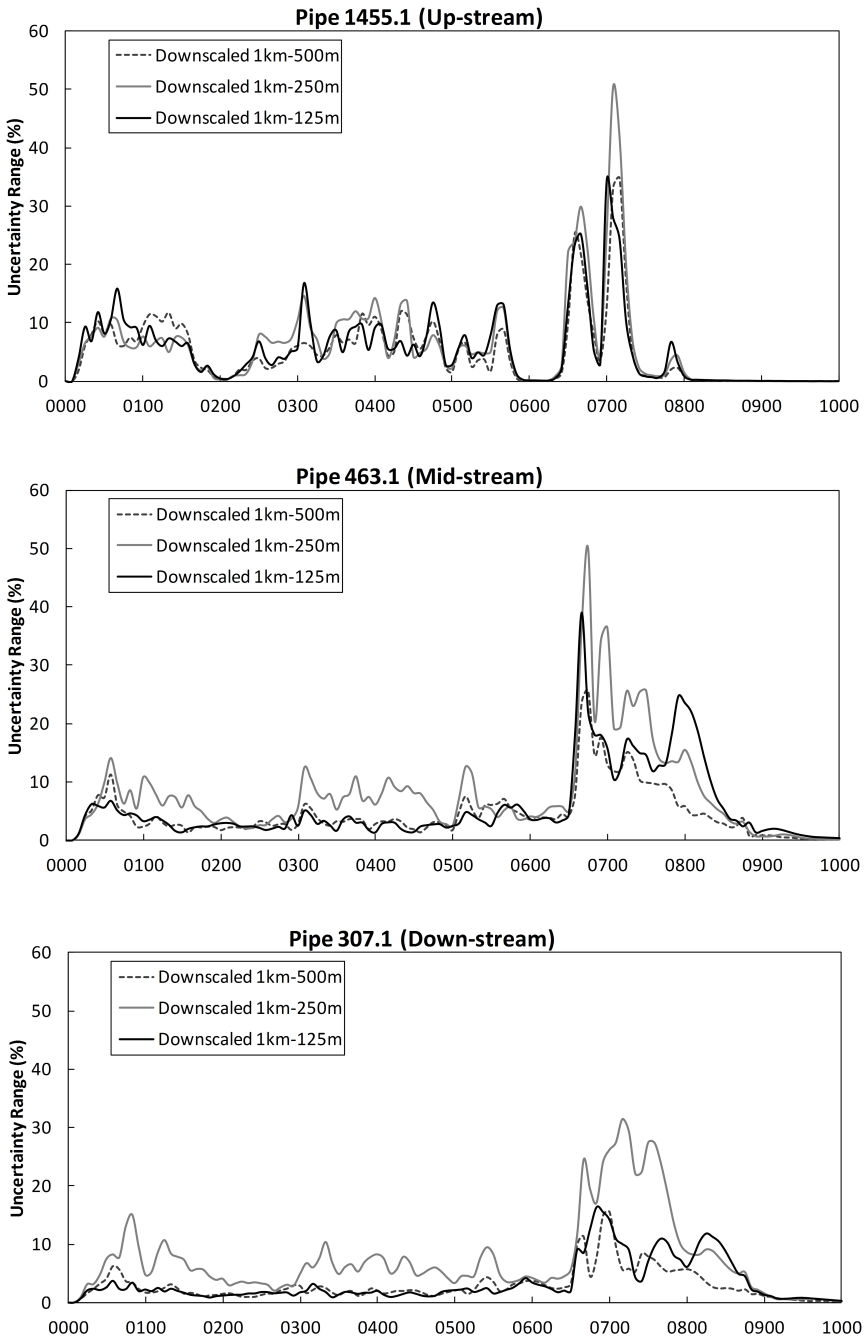


Figure 5.5: Variation of uncertainty range profiles at three selected pipes (from upper to lower figures: 1455.1 up-stream; 463.1 mid-stream; 307.1 down-stream) in the Cranbrook catchment for the event 23/08/2010. The estimated ranges were obtained by using the rainfall estimates, downscaled from the **original** 1 km radar rainfall to 500 (gray dashed lines), 250 (gray solid lines) and 125 (dark solid lines) m, as inputs

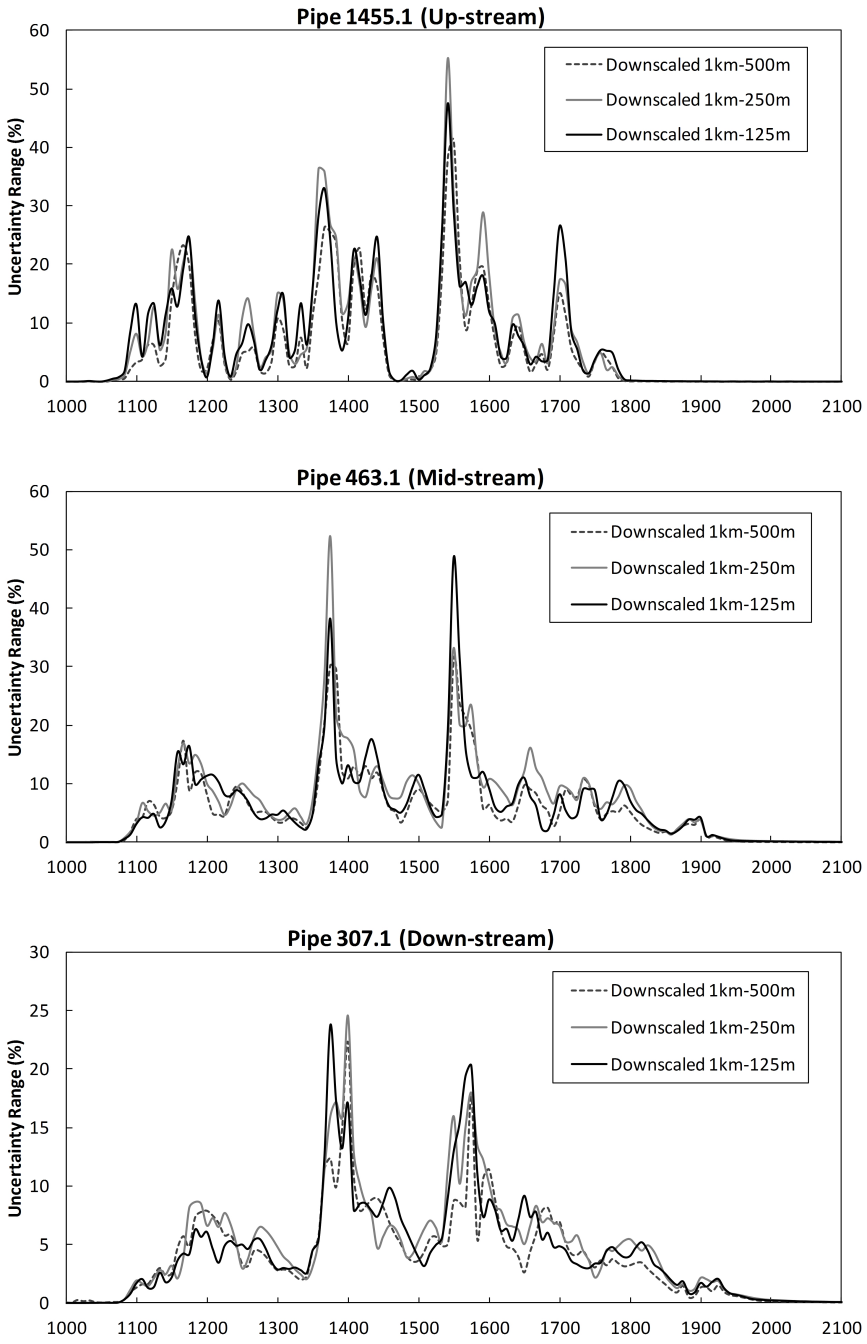


Figure 5.6: Variation of uncertainty range profiles at three selected pipes (from upper to lower figures: 1455.1 up-stream; 463.1 mid-stream; 307.1 down-stream) in the Cranbrook catchment for the event 26/05/2011. The estimated ranges were obtained by using the rainfall estimates, downscaled from the **original** 1 km radar rainfall to 500 (gray dashed lines), 250 (gray solid lines) and 125 (dark solid lines) m, as inputs

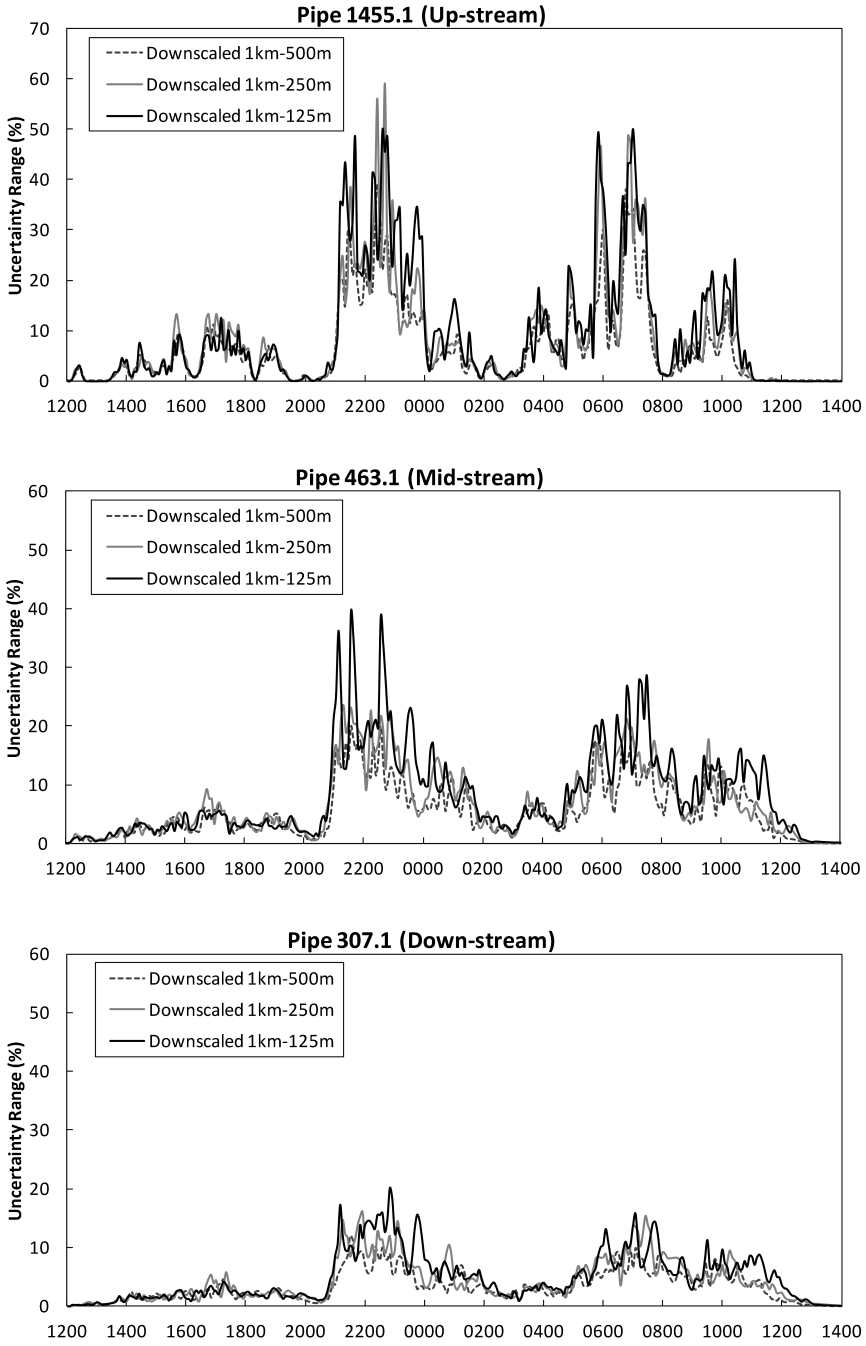


Figure 5.7: Variation of uncertainty range profiles at three selected pipes (from upper to lower figures: 1455.1 up-stream; 463.1 mid-stream; 307.1 down-stream) in the Cranbrook catchment for the event 05-06/06/2011. The estimated ranges were obtained by using the rainfall estimates, downscaled from the **original** 1 km radar rainfall to 500 (gray dashed lines), 250 (gray solid lines) and 125 (dark solid lines) m, as inputs

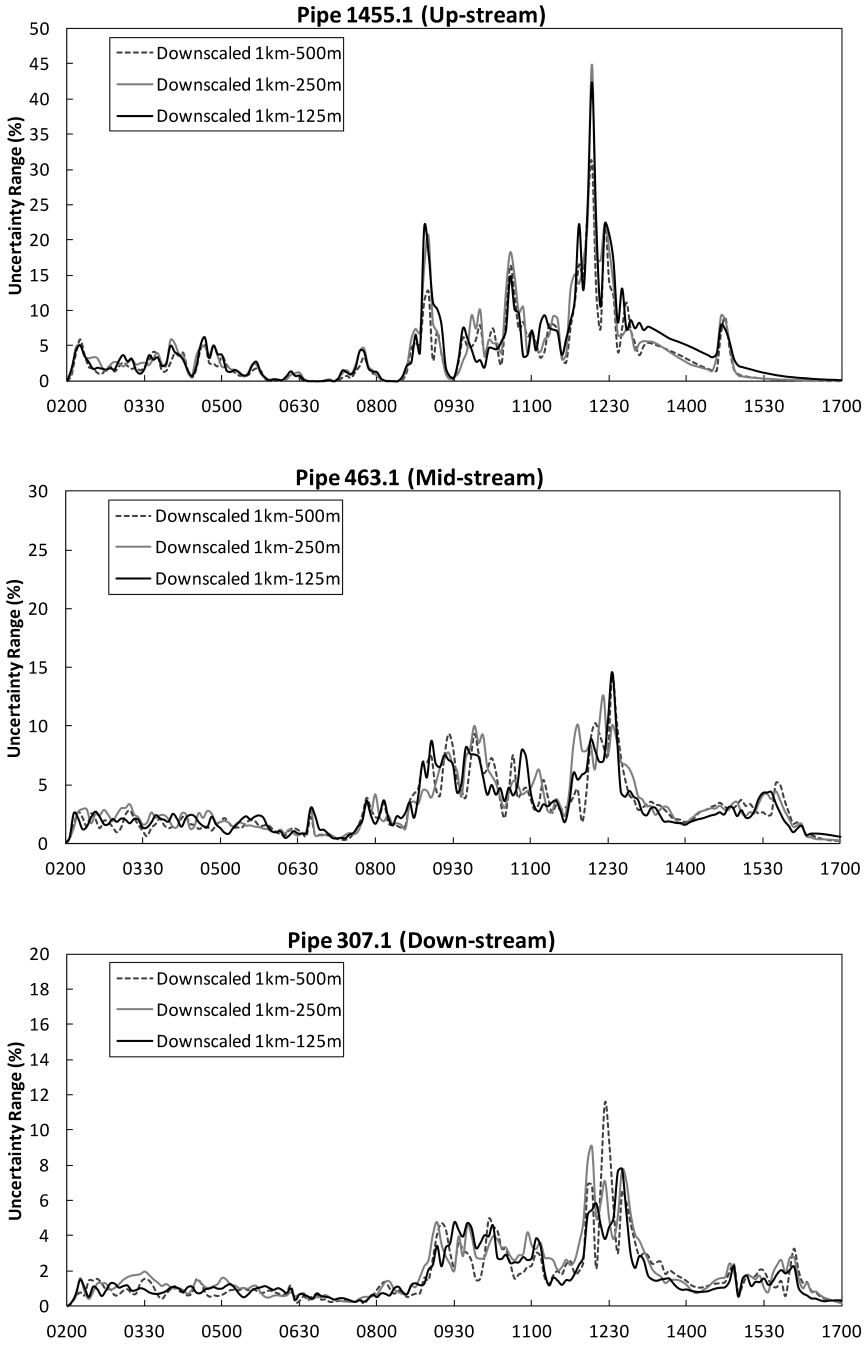


Figure 5.8: Variation of uncertainty range profiles at three selected pipes (from upper to lower figures: 1455.1 up-stream; 463.1 mid-stream; 307.1 down-stream) in the Cranbrook catchment for the event 03/01/2012. The estimated ranges were obtained by using the rainfall estimates, downscaled from the **original** 1 km radar rainfall to 500 (gray dashed lines), 250 (gray solid lines) and 125 (dark solid lines) m, as inputs

5.3 Applications of downscaled and adjusted rainfall estimates

Similarly to the previous section, the fragmentation ratios, obtained from fitting the scale-invariance feature over the spatial scales ranging from 8 km to 1 km, are used here to generate street-scale rainfall estimates; however, they are downscaled from the 1-km **Bayesian-adjusted** radar rainfall estimates. Note that the fragmentation ratios used in this section were derived from the original radar data because the raingauge network used to adjust radar rainfall in this work only covers the Cranbrook catchment (within 5 X 6 1-km radar grids), which is not large enough to derive meaningful scaling feature from 8 km to 1km.

Figures 5.9-5.12 (lower) show the variation of standard deviation profiles of rainfall estimates at different street scales: 500 (gray dashed lines), 250 (yellow solid lines) and 125 (red solid lines) m, over the Cranbrook catchment for four selected events. It can be found that, although the spatial variability is only slightly altered through the Bayesian adjustment (see the gray and dark solid lines), the difference however is magnified when finer rainfall estimates are generated. This demonstrates the nonlinearity of the proposed SD model. A clear view of these differences can be seen in Figures 5.14-5.17. These figures show the results of a comparison of the spatial variability (i.e. standard deviation) and its variation of the original (gray solid lines) and the adjusted (dark solid lines) radar rainfall rates, respectively at 500, 250 and 125-m resolutions (from upper to lower).

In order to evaluate the impact of the downscaled rainfall estimates on the adjustment processes, the downscaled adjusted rainfall estimates are used as inputs for the hydraulic models of Cranbrook catchment. In the following, the focuses will be on the verification of the impact and on the comparison of the contribution (could be positive or negative) to the uncertainty of flow simulation between the adjustment and downscaling processes.

Figures 5.13-5.20 show the estimated flow depths at three selected pipes for four selected events. The estimated flow depths are obtained respectively using the original (gray dashed lines), the Bayesian adjusted 1-km radar rainfall (gray solid lines) and the associated downscaled (1 km to 500 m) adjusted radar rainfall estimates (enveloped by the dark solid lines) and their ensemble estimates (dark dashed-dotted lines) as inputs. It can be found that, due to the microcanonical nature of the SD model, good agreement can be observed of the flow depths resulting from the adjusted 1-km and 500-m rainfall estimates. In addition, a wider envelope of flow depths resulting from stochastically downscaled adjusted estimates is in general observed, as compared to the envelope resulting from the rainfall estimates

downscaled from the original radar data.

The associated uncertainty ranges U_s can be estimated[2] and shown in Figures 5.21-5.24. The estimated uncertainty ranges resulted from the rainfall estimates, respectively downscaled from the **adjusted** 1 km radar rainfall to 500 (gray dashed lines), 250 (gray solid lines) and 125 (dark solid lines) m. The associated statistics are provided in Table 5.2. It can be seen that the behaviour of U_s obtained from the downscaled adjusted rainfall estimates is very similar to the U_s obtained from downscaled unadjusted rainfall estimates (see Table 5.1 for comparison). However, in general, the values of the statistics of U_s increase when the Bayesian adjusted rainfall estimates are downscaled. This means that, in this case, the combination of the adjustment and downscaling indeed introduces additional uncertainty to the hydraulic outputs. The possible source is that the parameters (i.e. fragmentation ratios) used to downscale the Bayesian adjusted estimates were the same as the parameters for the original rainfall estimates; however these parameters, in theory, should be re-derived.

These uncertainty ranges U_s caused by the downscaling process can be then compared with the uncertainty reduced by the adjustment, which is formed as follows:

$$U_{adjusted} = \frac{\left|F_{R_{adjusted-s},t} - F_{R_{1km},t}\right|}{F_{R_{adjusted-1km},t}} \times 100. \tag{5.9}$$

Some statistics of $U_{adjusted}$ are summarised in Table 5.3. They are in general larger than U_s, particularly for the pipes located at mid- and down-stream. A comparison is then carried out by calculating the proportion of these two measures, i.e., $U_s/U_{adjusted}$, to estimate the variation of the contribution from these two processes to the uncertainty. The results of the comparison are provided in Table 5.4, where the mean proportion and the proportion when the maximum $U_{adjusted}$ take place are summarised. It can be observed that both proportions decrease from up- to down-stream, and in most cases the mean proportions increase from coarser (500 m) to finer (125 m) scales; however the trend of the latter is not as strong as the former. This suggests that the uncertainty caused by the downscaling process is smoothed when the drainage area increases (i.e. downstream); however, it may diminish the reduction of uncertainty contributed by the adjustment process when the drainage area is very small. This result indicates that the impact of the spatial variability of rainfall inputs on the subsequent hydraulic outputs could be small when the catchment

[2]Note that, when calculating the uncertainty ranges U_s resulting from downscaled adjusted estimates, the term $F_{R_{1km},t}$ in Eq. (5.8) is replaced by $F_{R_{adjusted-1km},t}$

size is relatively large; the uncertainty is mainly dominated by the accuracy of rainfall volumes. However, when the catchment size is very small (such as urban catchments), the impact of the spatial variability of rainfall inputs on flood modelling becomes significant and may even dominates its uncertainty.

Table 5.2: Summary statistics of uncertainty ranges U_s resulting from adjusted rainfall estimates, downscaled from 1-km to 500/250/125 m, at three selected pipes (pipe 1455.1, 463.1 and 307.1, respectively located at the up-, mid- and down- streams of the Cranbrook catchment) for four selected events

scale	Upstream (1455.1)			Midstream (463.1)			Downstream (307.1)		
	mean	std	max	mean	std	max	mean	std	max
23/08/2011 event									
1km-500m	7.16	6.68	32.61	3.83	3.62	26.39	2.86	2.51	16.72
1km-250m	8.32	8.37	56.30	4.64	4.56	35.95	3.31	3.10	16.63
1km-125m	7.13	7.06	34.06	4.95	4.31	29.89	3.08	2.26	10.61
26/05/2011 event									
1km-500m	7.40	9.33	41.90	5.39	5.92	34.25	4.15	4.01	20.76
1km-250m	8.25	9.89	47.67	6.91	7.24	44.27	4.46	5.01	23.22
1km-125m	9.96	9.10	45.00	6.34	6.07	36.23	4.70	4.45	25.24
05-06/06/2011 event									
1km-500m	8.46	10.72	50.27	6.86	5.80	25.98	4.22	3.45	16.06
1km-250m	10.86	14.01	84.72	8.46	7.19	31.79	5.26	4.42	18.11
1km-125m	13.67	17.92	97.36	10.10	9.43	44.61	5.89	5.35	25.22
03/01/2012 event									
1km-500m	3.73	5.22	39.33	2.87	2.55	15.35	1.69	1.66	10.17
1km-250m	4.41	6.32	44.32	3.44	3.22	20.93	2.12	1.92	11.64
1km-125m	4.63	6.66	43.04	3.00	2.35	14.41	1.71	1.41	8.11

Table 5.3: Summary statistics of uncertainty reduction resulting from the radar rainfall adjustment process at three selected pipes (pipe 1455.1, 463.1 and 307.1, respectively located at the up-, mid- and down- streams of the Cranbrook catchment) for four selected events

event	Upstream (1455.1)			Midstream (463.1)			Downstream (307.1)		
	mean	std	max	mean	std	max	mean	std	max
23/08/2010	18.97	16.00	54.64	28.57	14.60	57.25	26.46	14.05	53.07
26/05/2011	15.52	17.10	62.21	22.44	17.30	60.53	19.18	16.02	63.12
05-06/06/2011	8.02	10.81	44.36	13.97	13.48	45.24	12.66	12.04	40.38
03/01/2012	3.73	7.54	41.96	9.21	13.18	81.33	8.58	11.23	60.72

Table 5.4: Summary of the proportion of the contributions from downscaling and adjustment processes to uncertainty in flood modelling, i.e., $U_s/U_{adjusted}$, at three selected pipes (pipe 1455.1, 463.1 and 307.1, respectively located at the up-, mid- and down- streams of the Cranbrook catchment) for four selected events

scale	Upstream (1455.1)		Midstream (463.1)		Downstream (307.1)	
	mean	max	mean	max	mean	max
23/08/2011 event						
1km-500m	37.74	59.68	13.42	46.10	10.81	31.52
1km-250m	43.89	103.03	16.23	62.80	12.50	31.34
1km-125m	37.59	62.32	17.34	52.21	11.63	20.00
26/05/2011 event						
1km-500m	47.66	67.35	24.04	56.59	21.61	32.89
1km-250m	53.14	76.62	30.79	73.13	28.45	36.78
1km-125m	64.14	72.34	28.28	60.35	24.53	39.98
05-06/06/2011 event						
1km-500m	105.47	113.33	49.09	57.43	33.28	39.78
1km-250m	135.40	190.98	60.53	70.27	41.57	44.85
1km-125m	170.46	219.50	72.26	98.61	46.49	62.45
03/01/2012 event						
1km-500m	100.15	93.73	31.18	18.87	19.76	16.75
1km-250m	118.29	105.62	37.31	25.74	24.72	19.17
1km-125m	124.20	102.58	32.54	17.72	19.95	13.35

5.4 Summary

In this chapter, a combination of downscaling and adjustment techniques was carried out, which is a new rainfall processing procedure proposed by this work that enable the improvement of the suitability of the operational rainfall estimates for urban pluvial flood modelling. In addition, the uncertainty in urban pluvial modelling caused by the downscaling process and its combination with the adjustment technique was estimated.

Some interesting findings are summarised as follows:

1. Impact of rainfall downscaling on flow simulation decreases from up- to down-stream. This indicates that the effect of rainfall variation on hydrological/hydraulic modelling could be smoothed when drainage areas increase; however this also means, for very small catchments, the importance of spatial variation of rainfall could substantially rise.

2. Adjustment processes can largely reduce the uncertainty caused by rainfall estimates in urban flood modelling; aside from some cases of very small areas where the uncertainty caused by the downscaling process could be larger than that reduced by the adjustment. This indicates that the uncertainty of flow simulation could be dominated by the spatial variation of rainfall in very small catchments. It shall therefore not be ignored in urban hydrological applications.

3. The combination of the adjustment and downscaling processes introduces additional uncertainty. This could be due to the difference of the background theories of these two techniques or insufficient raingauge information. To reduce this additional uncertainty, new processing techniques are necessary to have a better theoretical connection between these two processes; in addition, raingauge data over larger areas can also improve the estimation of the parameters for the downscaling process.

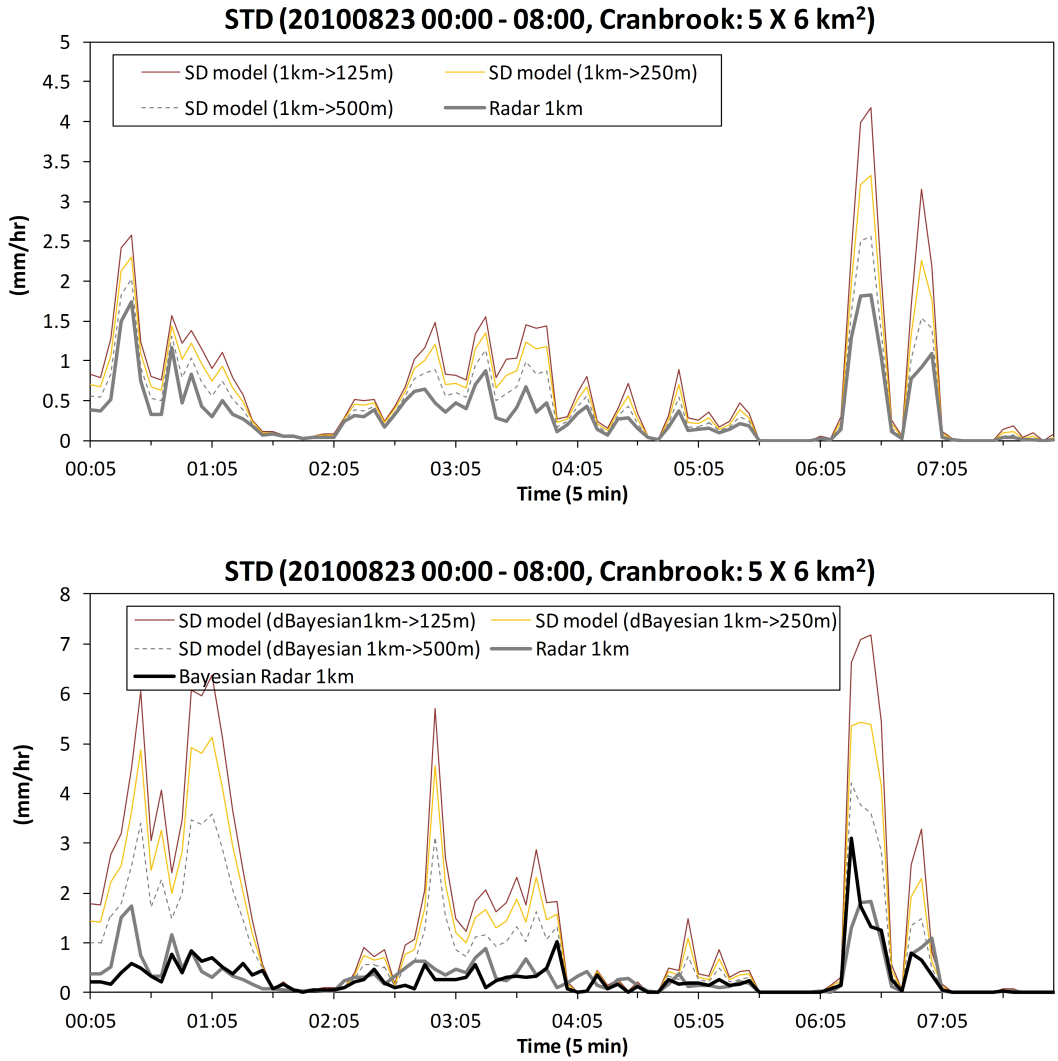


Figure 5.9: Variation of standard deviation profiles of the radar rainfall rates, downscaled from 1 km to 500 (gray dashed lines), 250 (yellow solid lines) and 125 (red solid lines) m in the Cranbrook catchment for the event 23/08/2010. The gray dashed lines are from the original radar data, and the dark dashed line is from the adjusted radar estimates

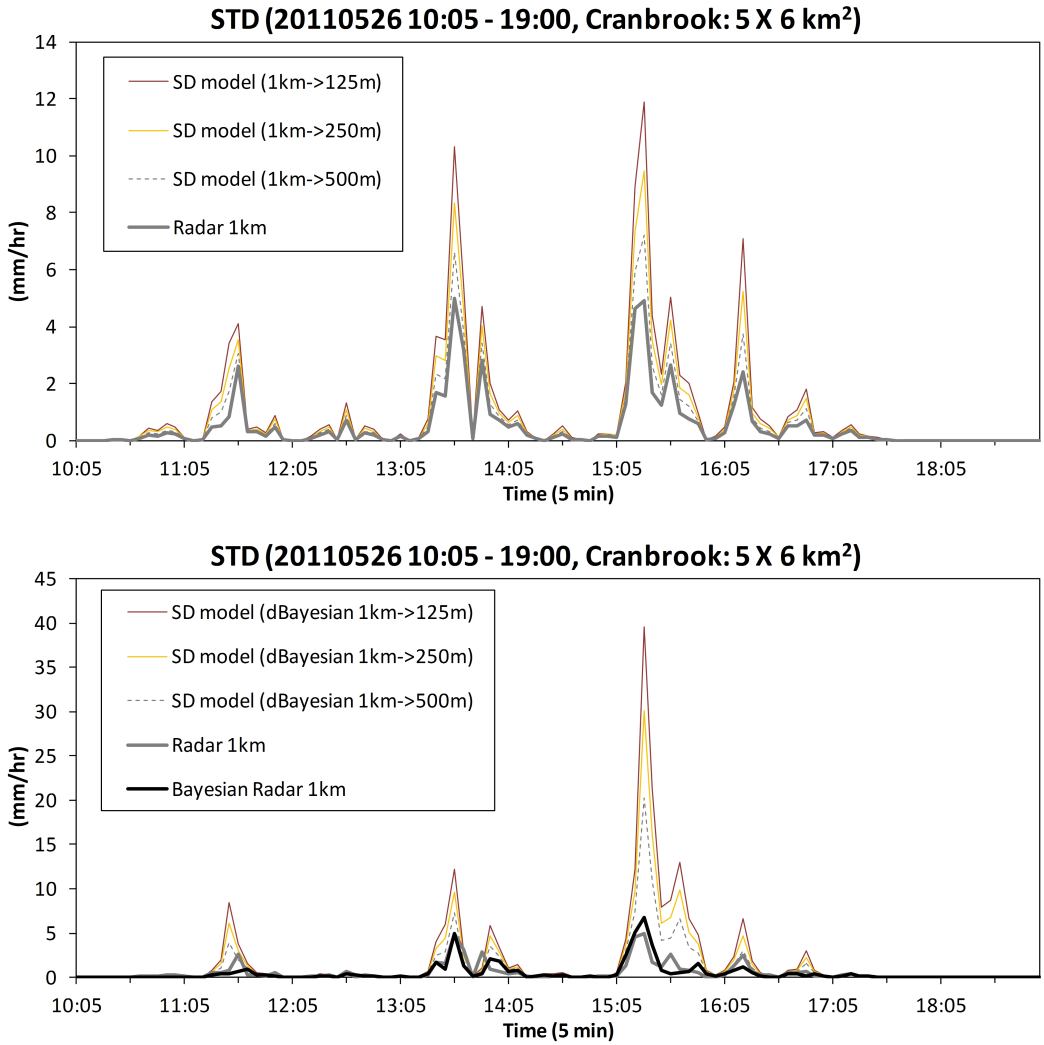


Figure 5.10: Variation of standard deviation profiles of the radar rainfall rates, downscaled from 1 km to 500 (gray dashed lines), 250 (yellow solid lines) and 125 (red solid lines) m in the Cranbrook catchment for the event 26/05/2011. The gray dashed lines are from the original radar data, and the dark dashed line is from the adjusted radar estimates

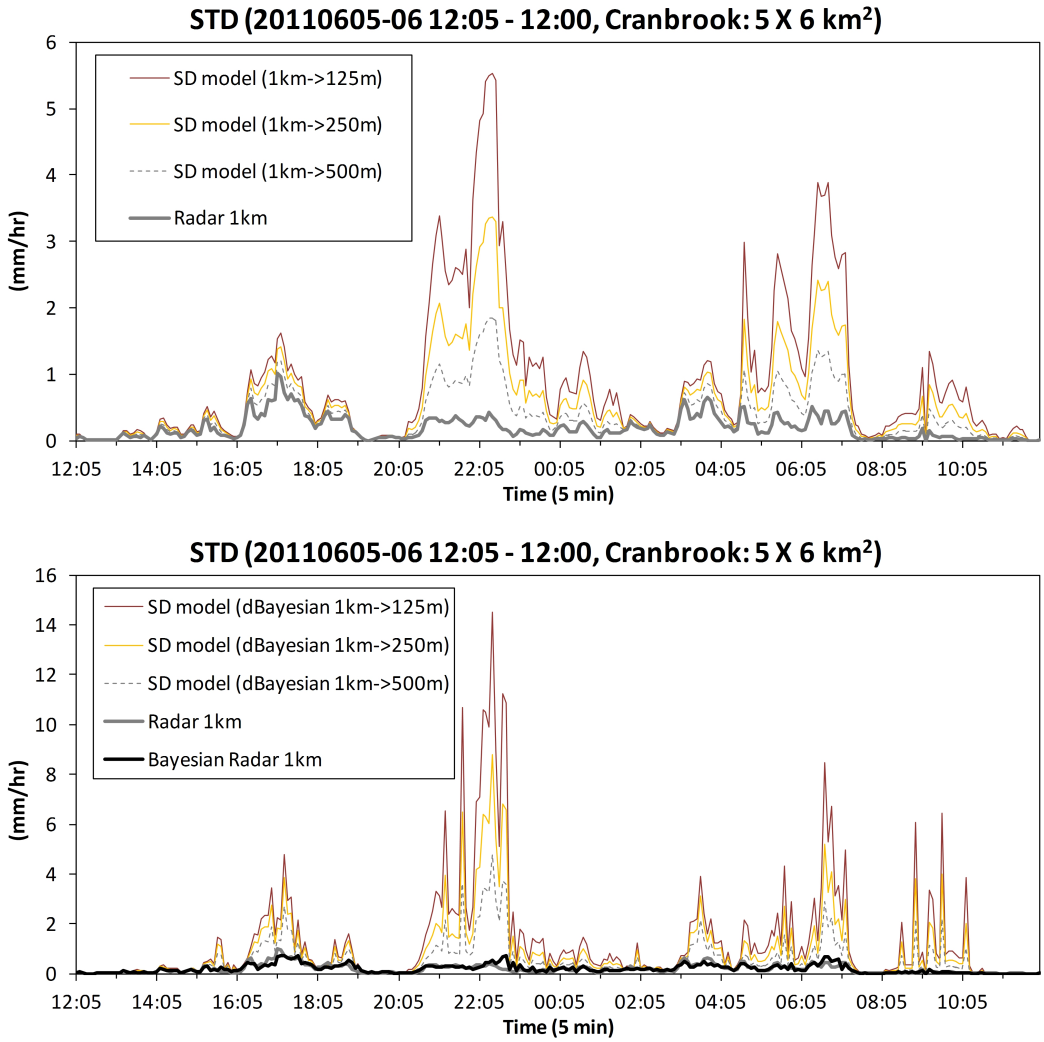


Figure 5.11: Variation of standard deviation profiles of the radar rainfall rates, downscaled from 1 km to 500 (gray dashed lines), 250 (yellow solid lines) and 125 (red solid lines) m in the Cranbrook catchment for the event 05-06/06/2011. The gray dashed lines are from the original radar data, and the dark dashed line is from the adjusted radar estimates

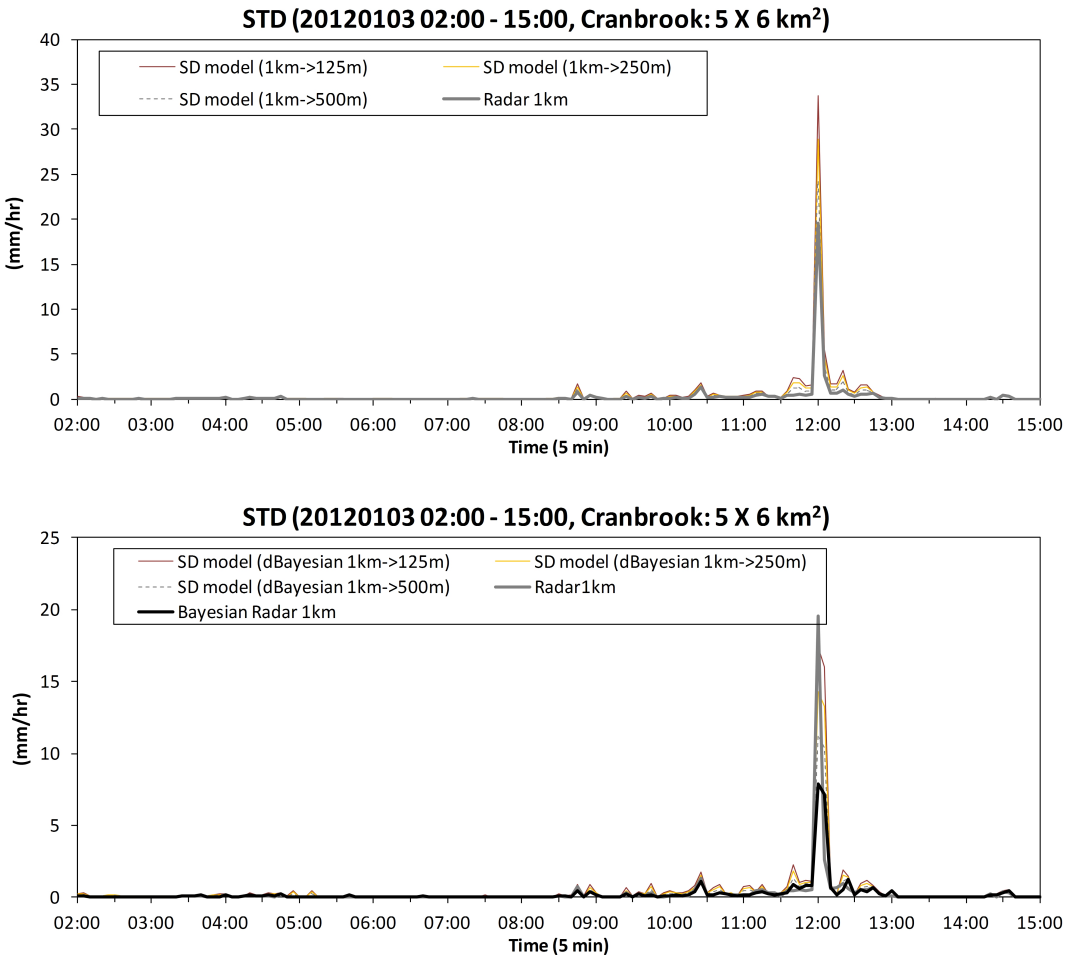


Figure 5.12: Variation of standard deviation profiles of the radar rainfall rates, downscaled from 1 km to 500 (gray dashed lines), 250 (yellow solid lines) and 125 (red solid lines) m in the Cranbrook catchment for the event 03/01/2012. The gray dashed lines are from the original radar data, and the dark dashed line is from the adjusted radar estimates

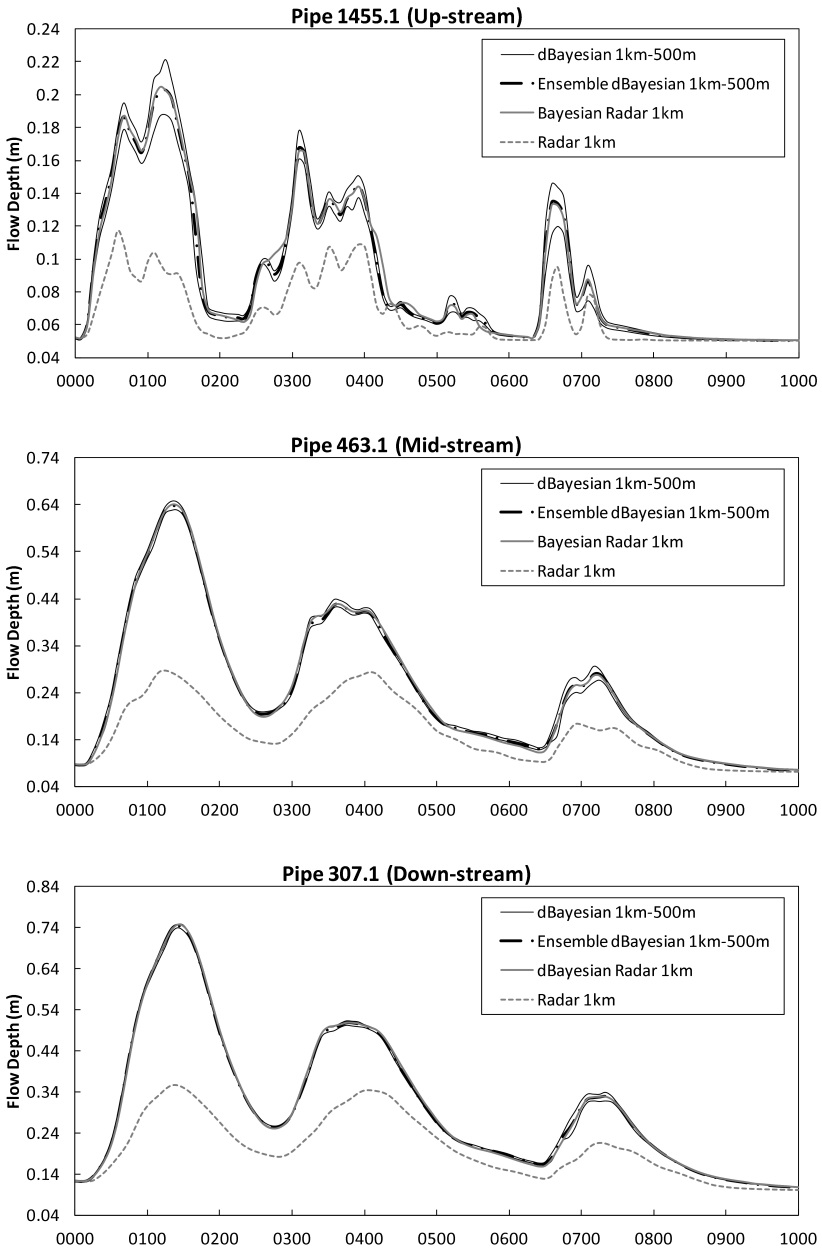


Figure 5.13: The comparison of the estimated flow depths at three selected pipes (from upper to lower figures: 1455.1 up-stream; 463.1 mid-stream; 307.1 down-stream) in the Cranbrook catchment for the event 23/08/2010. The estimated flow depths were obtained by using the original radar rainfall (gray dashed lines), the adjusted radar rainfall (gray solid lines) and the stochastically downscaled (1 km to 500 m) adjusted radar rainfall estimates (enveloped by the dark solid lines) and their ensemble estimates (dark dashed-dotted lines) as inputs

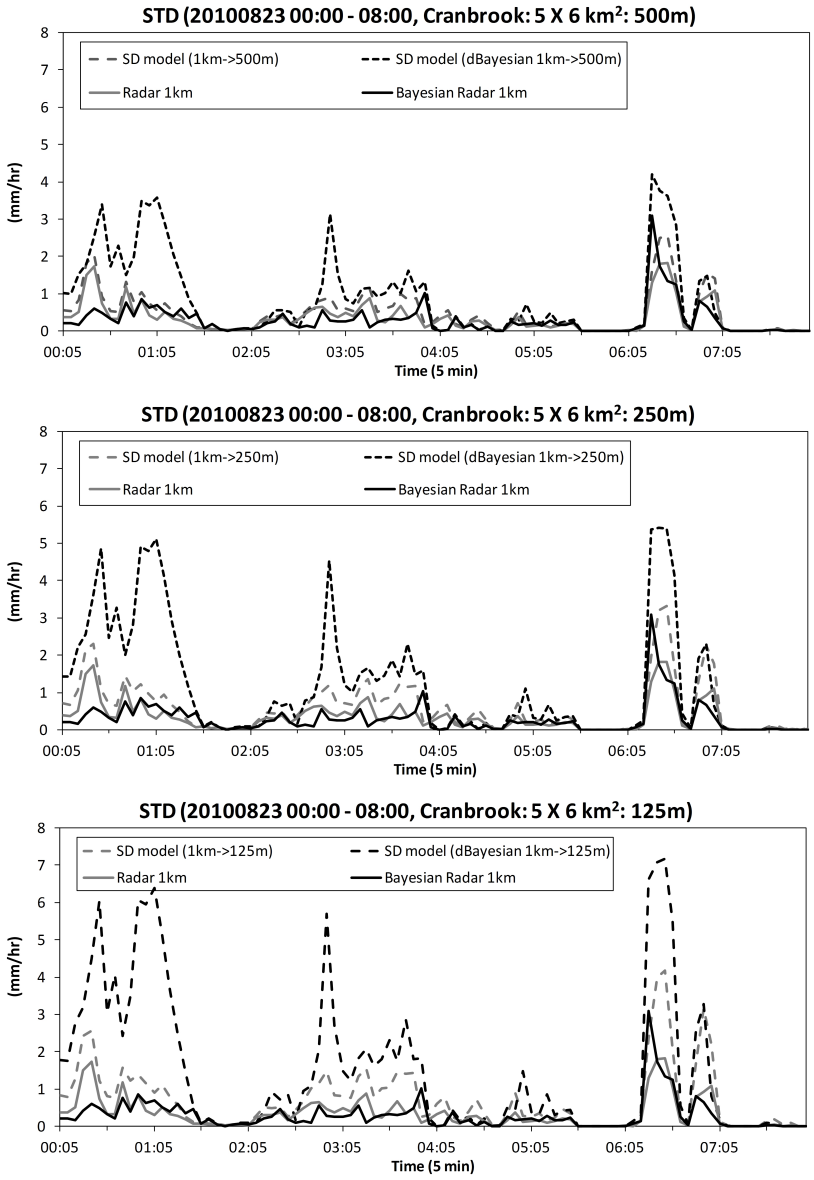


Figure 5.14: Standard deviation profiles of the original (gray solid lines) and adjusted (dark solid lines) radar rainfall rates at various downscaling scales in the Cranbrook catchment for the event 23/08/2010 (from upper to lower): from 1 km to 500, 250 and 125 m. The gray dashed lines are downscaled from the original radar data, while the dark dashed lines are from the adjusted radar estimates

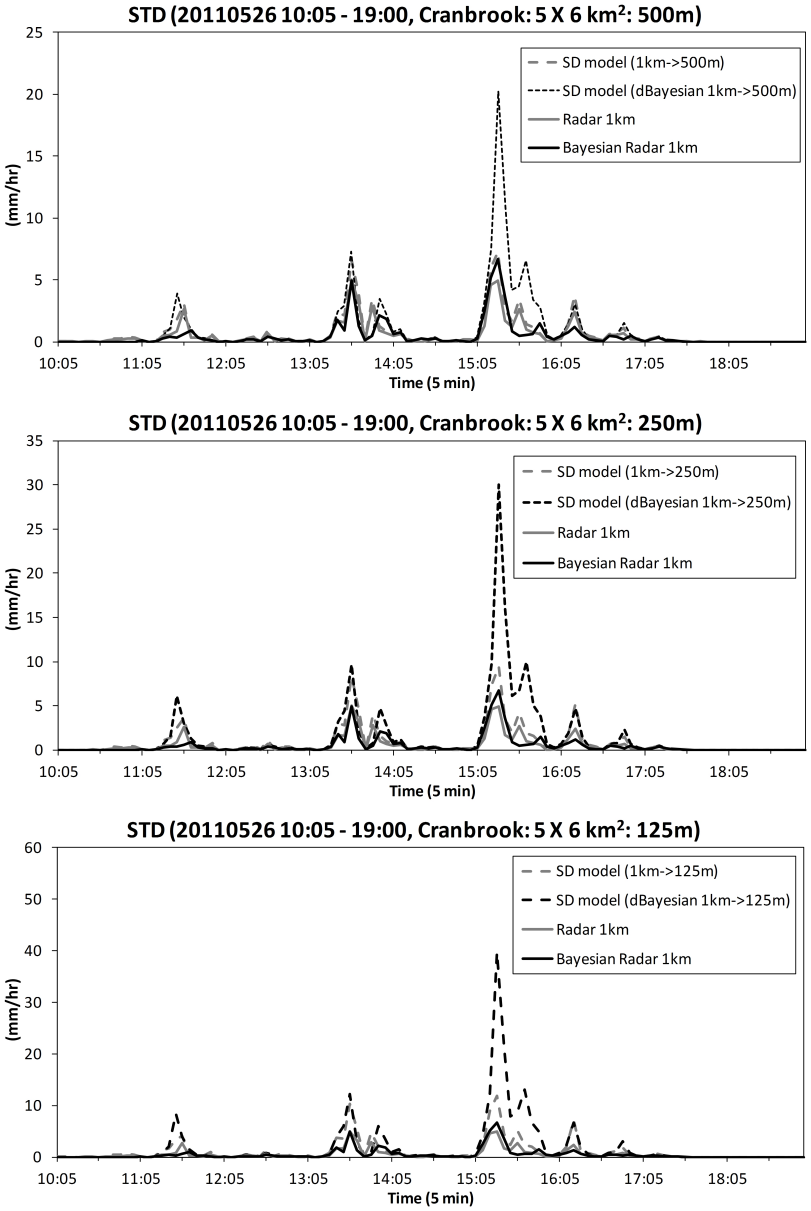


Figure 5.15: Standard deviation profiles of the original (gray solid lines) and adjusted (dark solid lines) radar rainfall rates at various downscaling scales in the Cranbrook catchment for the event 26/05/2011 (from upper to lower): from 1 km to 500, 250 and 125 m. The gray dashed lines are downscaled from the original radar data, while the dark dashed lines are from the adjusted radar estimates

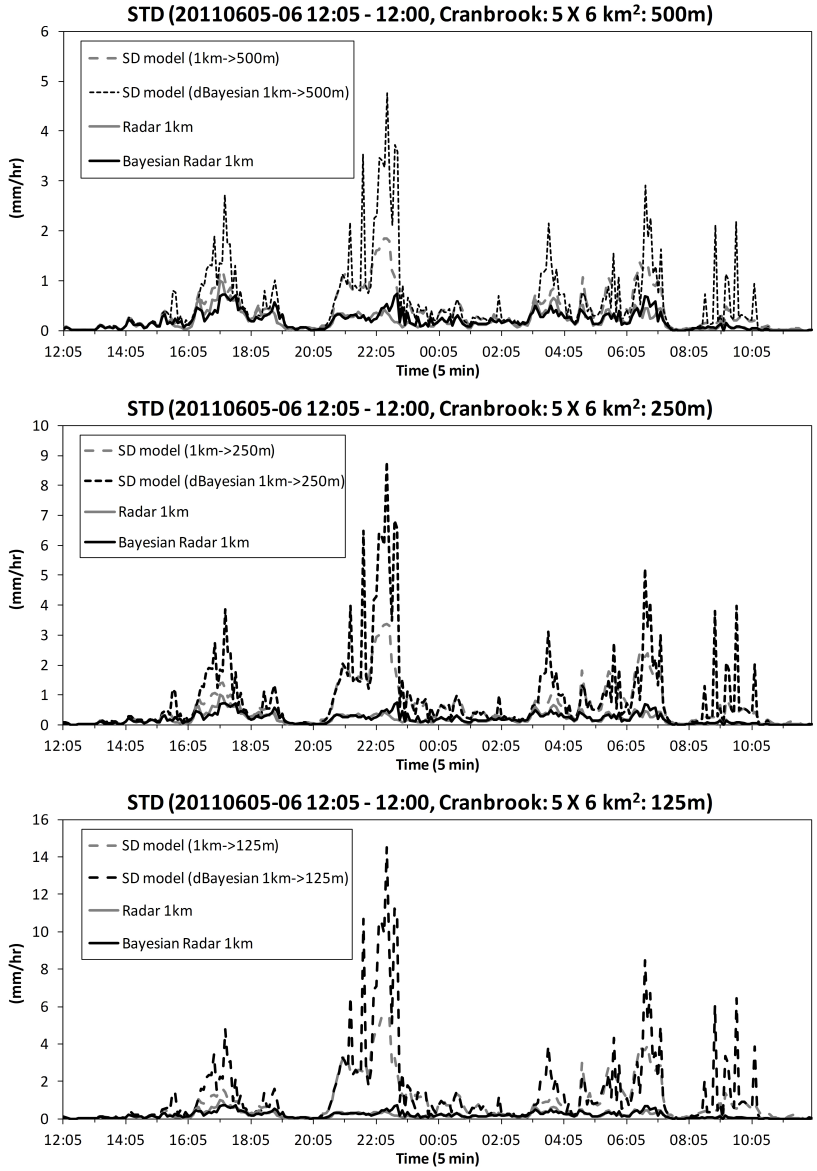


Figure 5.16: Standard deviation profiles of the original (gray solid lines) and adjusted (dark solid lines) radar rainfall rates at various downscaling scales in the Cranbrook catchment for the event 05-06/06/2011 (from upper to lower): from 1 km to 500, 250 and 125 m. The gray dashed lines are downscaled from the original radar data, while the dark dashed lines are from the adjusted radar estimates

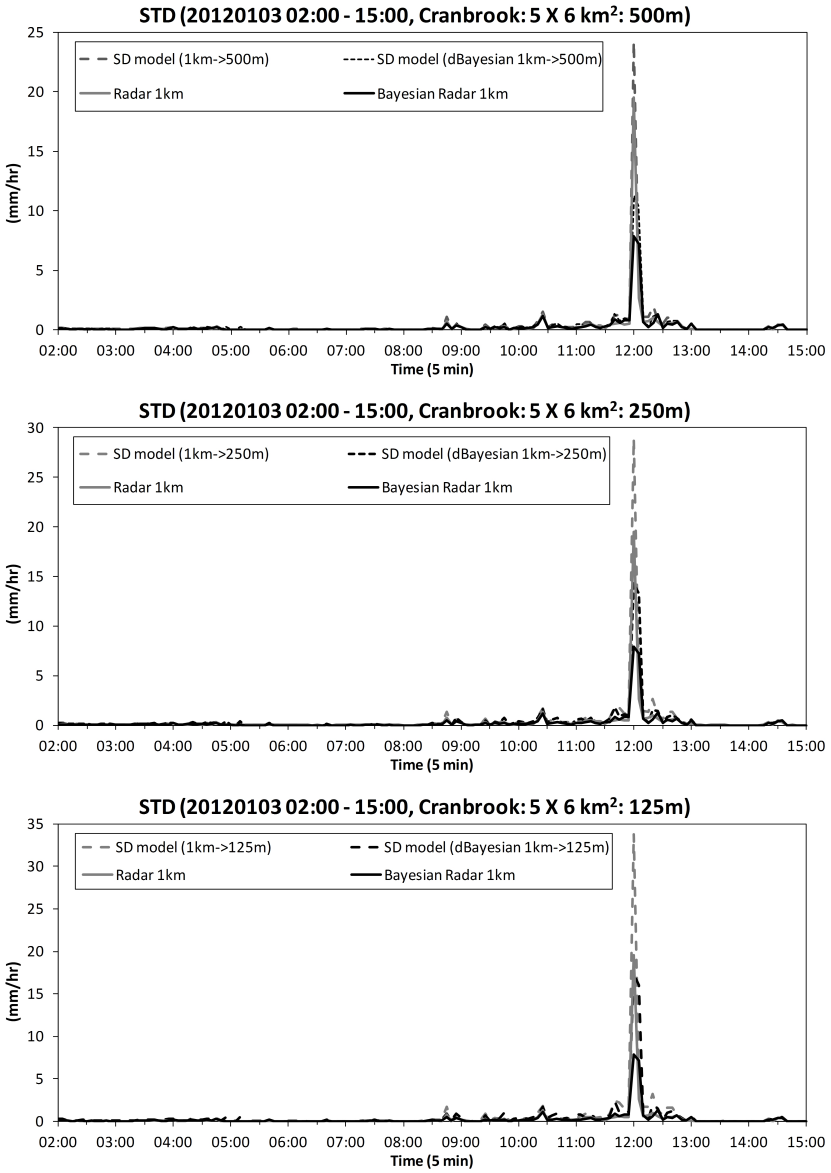


Figure 5.17: Standard deviation profiles of the original (gray solid lines) and adjusted (dark solid lines) radar rainfall rates at various downscaling scales in the Cranbrook catchment for the event 03/01/2012 (from upper to lower): from 1 km to 500, 250 and 125 m. The gray dashed lines are downscaled from the original radar data, while the dark dashed lines are from the adjusted radar estimates

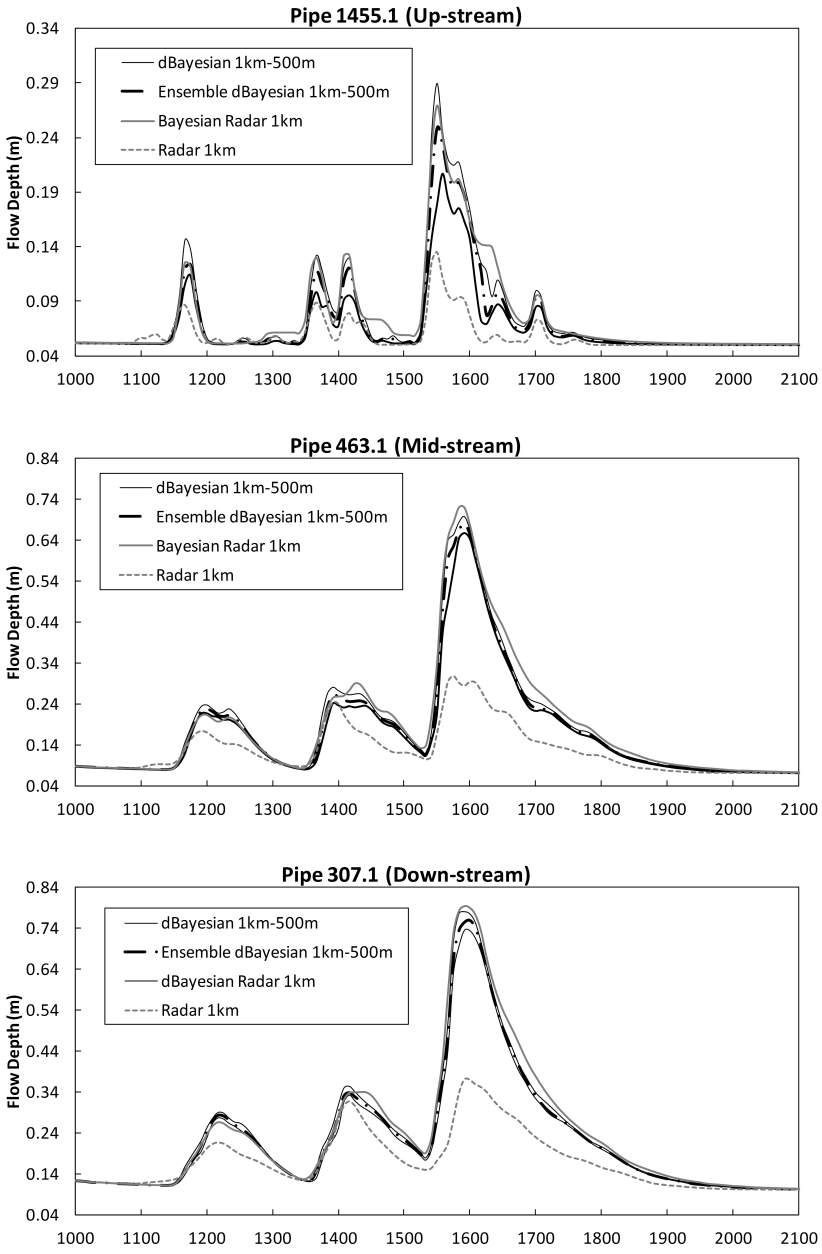


Figure 5.18: The comparison of the estimated flow depths at three selected pipes (from upper to lower figures: 1455.1 up-stream; 463.1 mid-stream; 307.1 down-stream) in the Cranbrook catchment for the event 26/05/2011. The estimated flow depths were obtained by using the original radar rainfall (gray dashed lines), the adjusted radar rainfall (gray solid lines) and the stochastically downscaled (1 km to 500 m) adjusted radar rainfall estimates (enveloped by the dark solid lines) and their ensemble estimates (dark dashed-dotted lines) as inputs

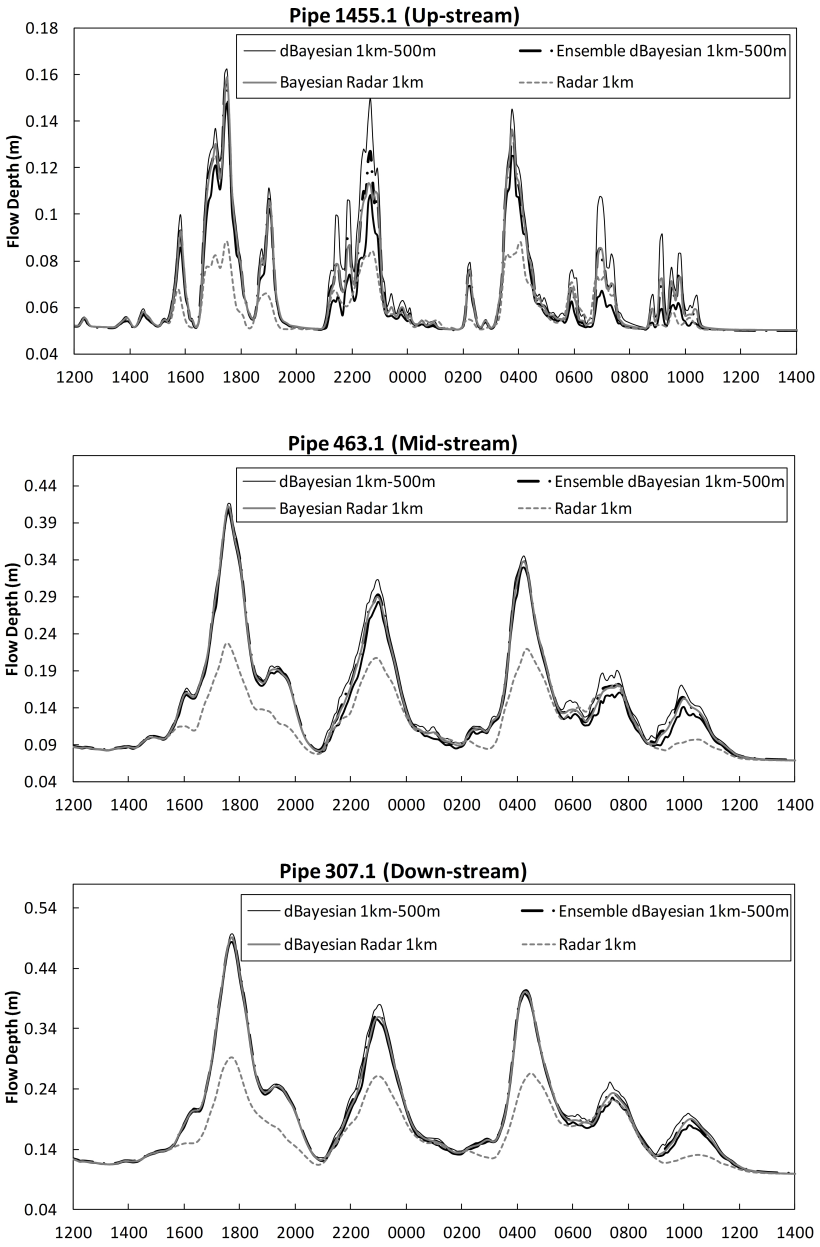


Figure 5.19: The comparison of the estimated flow depths at three selected pipes (from upper to lower figures: 1455.1 up-stream; 463.1 mid-stream; 307.1 down-stream) in the Cranbrook catchment for the event 05-06/06/2011. The estimated flow depths were obtained by using the original radar rainfall (gray dashed lines), the adjusted radar rainfall (gray solid lines) and the stochastically downscaled (1 km to 500 m) adjusted radar rainfall estimates (enveloped by the dark solid lines) and their ensemble estimates (dark dashed-dotted lines) as inputs

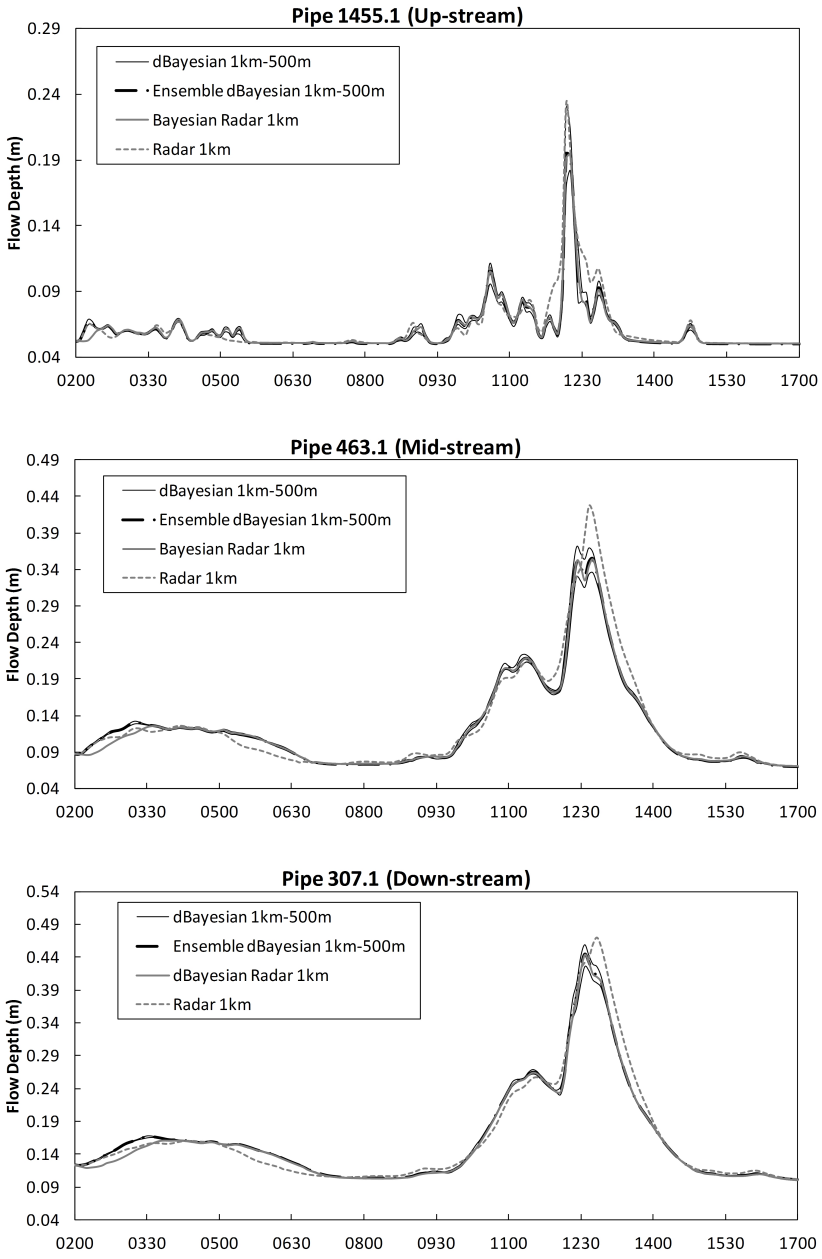


Figure 5.20: The comparison of the estimated flow depths at three selected pipes (from upper to lower figures: 1455.1 up-stream; 463.1 mid-stream; 307.1 down-stream) in the Cranbrook catchment for the event 03/01/2012. The estimated flow depths were obtained by using the original radar rainfall (gray dashed lines), the adjusted radar rainfall (gray solid lines) and the stochastically downscaled (1 km to 500 m) adjusted radar rainfall estimates (enveloped by the dark solid lines) and their ensemble estimates (dark dashed-dotted lines) as inputs

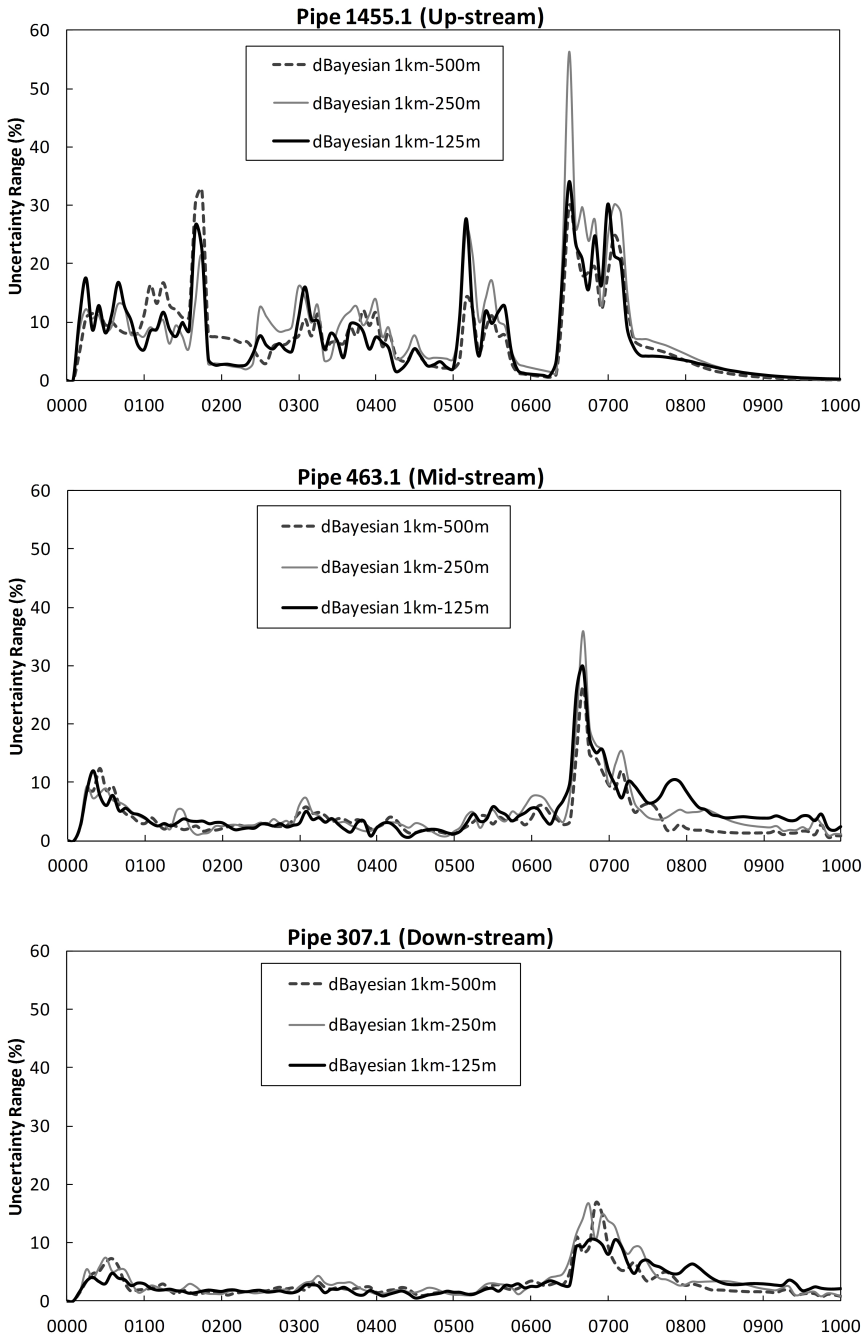


Figure 5.21: Variation of uncertainty range profiles at three selected pipes (from upper to lower figures: 1455.1 up-stream; 463.1 mid-stream; 307.1 down-stream) in the Cranbrook catchment for the event 23/08/2010. The estimated ranges were obtained by using the rainfall estimates, downscaled from the **adjusted** 1 km radar rainfall to 500 (gray dashed lines), 250 (gray solid lines) and 125 (dark solid lines) m, as inputs

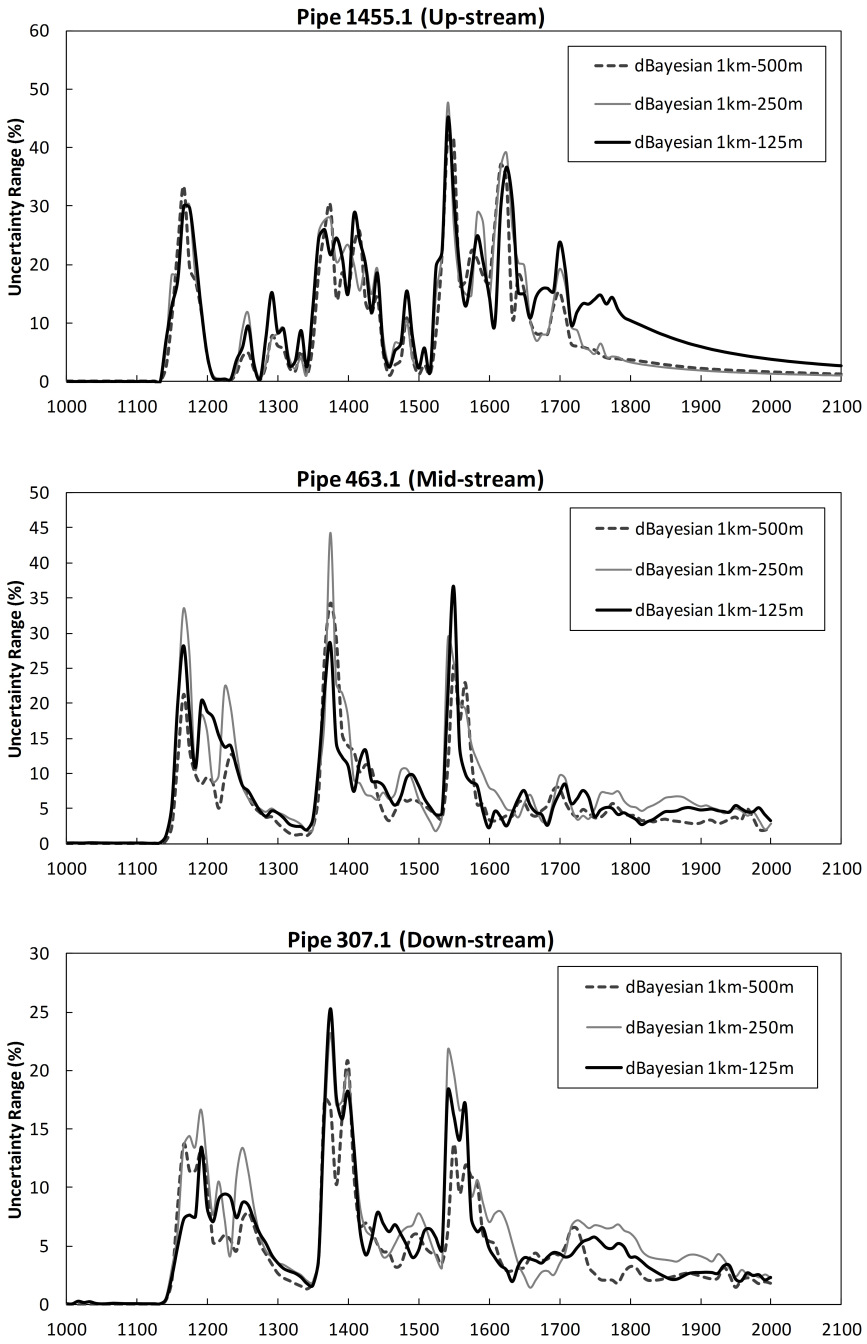


Figure 5.22: Variation of uncertainty ranges (in mm) at three selected pipes (from upper to lower figures: 1455.1 up-stream; 463.1 mid-stream; 307.1 down-stream) in the Cranbrook catchment for the event 26/05/2011. The estimated ranges were obtained by using the rainfall estimates, downscaled from the **adjusted** 1 km radar rainfall to 500 (gray dashed lines), 250 (gray solid lines) and 125 (dark solid lines) m, as inputs

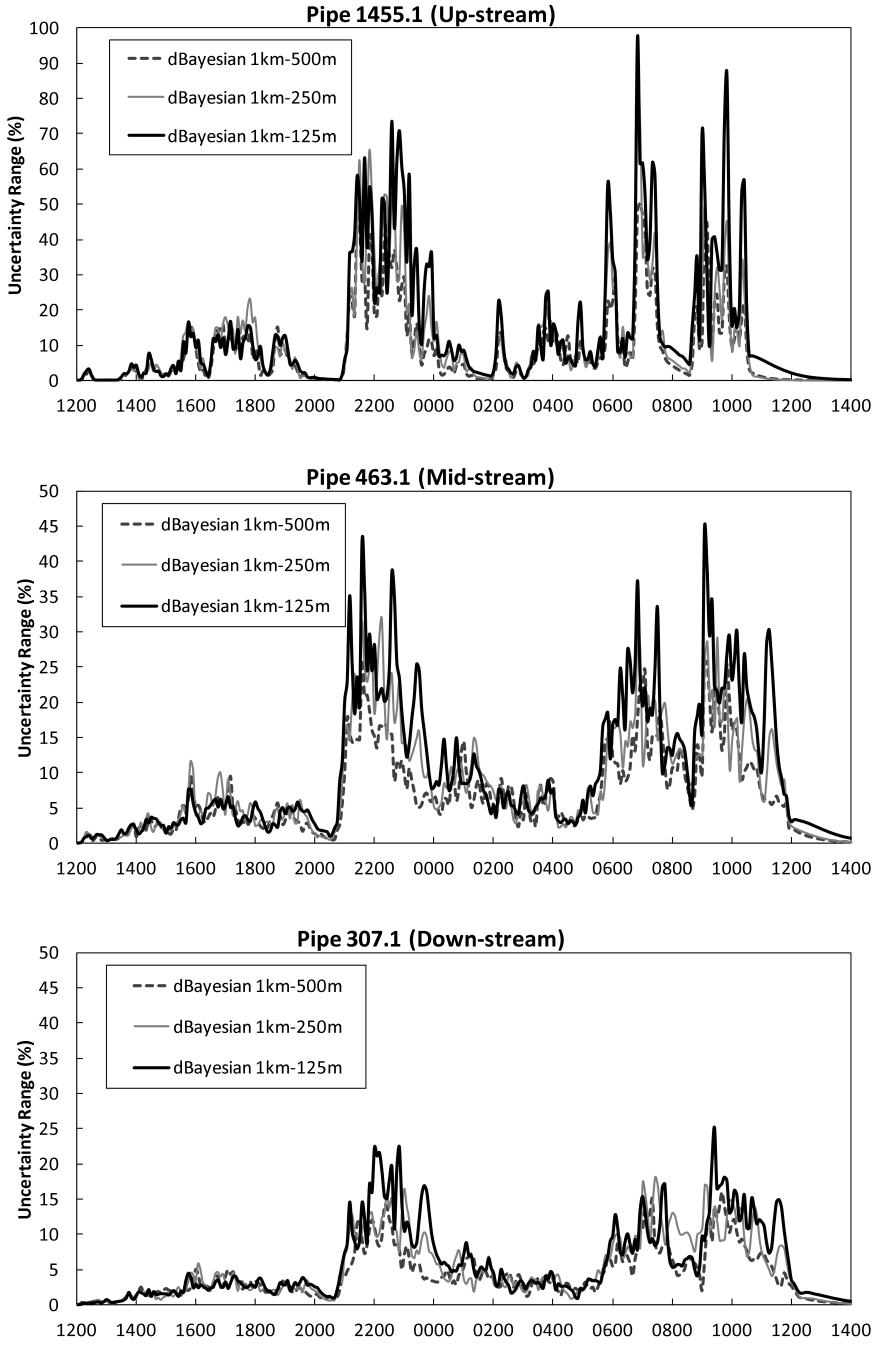


Figure 5.23: Variation of uncertainty range profiles at three selected pipes (from upper to lower figures: 1455.1 up-stream; 463.1 mid-stream; 307.1 down-stream) in the Cranbrook catchment for the event 05-06/06/2011. The estimated ranges were obtained by using the rainfall estimates, downscaled from the **adjusted** 1 km radar rainfall to 500 (gray dashed lines), 250 (gray solid lines) and 125 (dark solid lines) m, as inputs

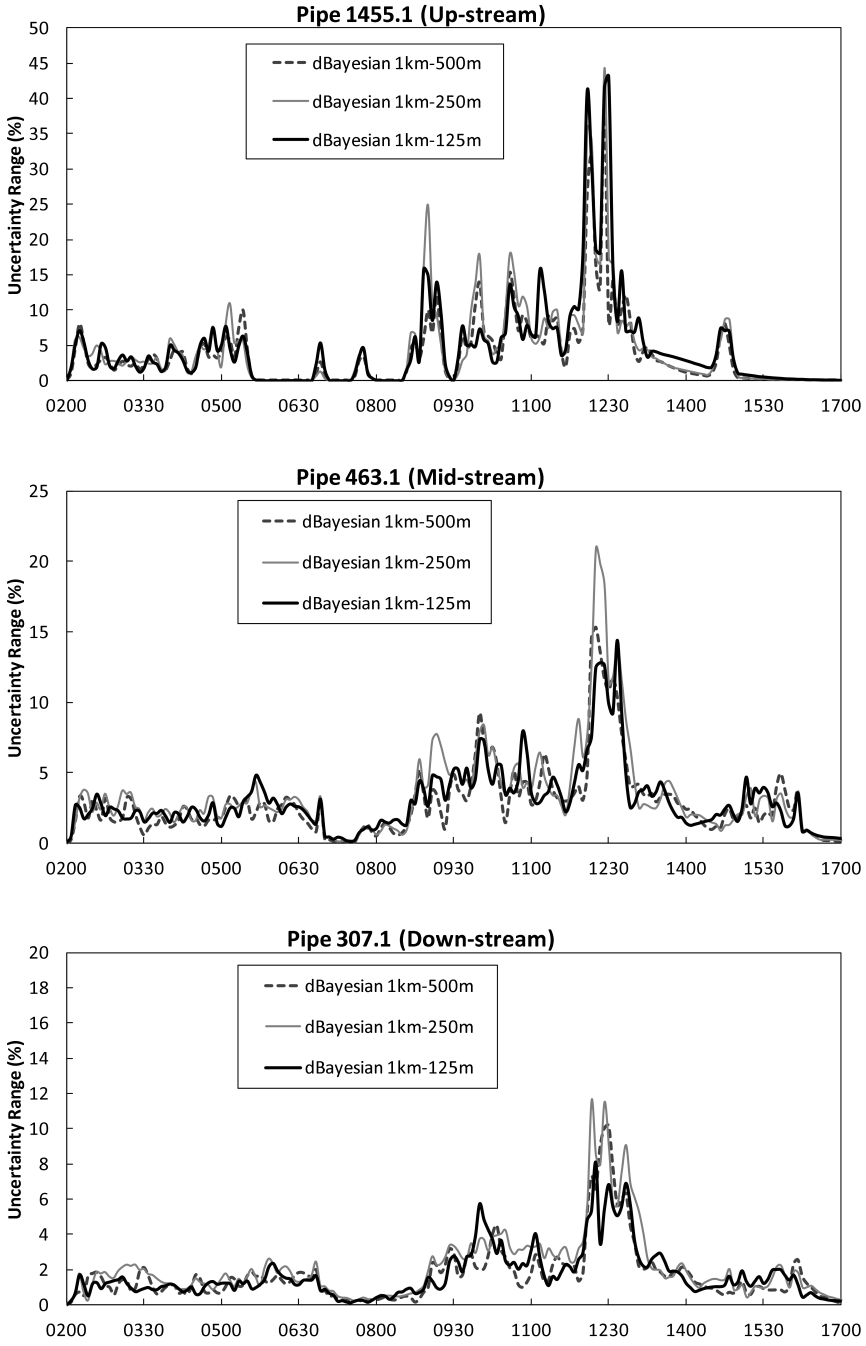


Figure 5.24: Variation of uncertainty range profiles at three selected pipes (from upper to lower figures: 1455.1 up-stream; 463.1 mid-stream; 307.1 down-stream) in the Cranbrook catchment for the event 03/01/2012. The estimated ranges were obtained by using the rainfall estimates, downscaled from the **adjusted** 1 km radar rainfall to 500 (gray dashed lines), 250 (gray solid lines) and 125 (dark solid lines) m, as inputs

Chapter 6

Conclusions and Perspectives for further Research

In this thesis, a brief review of the current development of urban pluvial flood modelling and forecasting, particularly in the UK, was firstly given to provide the background of this research and to identify the shortcomings of the operational short-term rainfall forecast system for urban hydrological uses.

This work, instead of developing the rainfall processing techniques at the country level, provides a different view on rainfall processing from the angle of urban hydrology. The focus of the research is on exploring techniques to improve the suitability (i.e. accuracy and resolution) of rainfall data particularly for urban hydrological and hydraulic applications (such as urban pluvial flood modelling). Based upon the review of state-of-the-art developments, the Bayesian-based adjustment technique was employed in this work to enhance the accuracy of operational radar data by merging them with the coincidental raingauge observations; and new downscaling technique, based upon the theory of Multifractals and the multiplicative cascade method, were developed to produce high spatial- and temporal-resolution rainfall estimates. These developments were tested with real rainfall events recorded in London and show promising results.

However, because of the functional differences, the adjustment and downscaling techniques make different "contributions" to the uncertainty of the rainfall estimates and the subsequent hydraulic outputs. The former is to reduce the uncertainty mainly caused by the rainfall volume bias, whilst the latter, due to the stochastic nature, inevitably introduces uncertainty into the subsequent hydrological or hydraulic modelling during the process of generating rainfall estimates of higher resolution (and variability).

In general, the rainfall volume bias is reckoned as the major uncertainty source and can be largely reduced through adjustment, and the uncertainty caused by the downscaling process (in order to higher-resolution representativeness of rainfall structures) is relatively minor and is sometimes ignored. However, for urban hydrological applications, because the size and the scale of the catchment and the weather system are relatively small, their local and nonlinear features are less averaged and therefore the uncertainty caused by downscaling process are less smoothed and cannot be ignored. For example, the results in Chapter 5 demonstrate that the rainfall downscaling process may dominate the uncertainty when the drainage area is very small.

In addition, a combination of these two techniques was tested in this work, aiming to generate high-resolution and accurate rainfall estimates. This combination however introduces additional uncertainty to the hydrological and hydraulic modelling. This is mainly because the adjustment process somewhat alters the structure of rainfall and this minor change is magnified in the (nonlinear) downscaling process. Nonetheless, this combination still confirms the potential to link adjustment and downscaling techniques together.

Based upon the work done in this research, the contributions of this thesis can be summarised as follows:

1. The latest developments in tackling urban pluvial floods in the UK were reviewed, and shortcomings and possible improvements were identified and proposed.

2. The state-of-the-art gauge-based radar rainfall adjustment techniques, most of which had been developed for larger scale applications, were reviewed. A new way to categorise these techniques into two groups was proposed (different from the literatures where each mathematical model represents one group, such as Todini (2001b) and Ehret et al. (2008)). Based upon the methodologies used to characterise the error fields (which are the matrices composed of the differences between radar and co-located raingauge estimates), existing techniques are grouped into the mean-bias adjustment and error variance minimisation methods in this work. Their applicability to urban hydrology was further tested and assessed with real rainfall events.

3. Existing cascade-based downscaling models were intensely reviewed in this work; based upon this, a general framework for applying cascade models to rainfall (or other hydrological processes) was newly proposed in this work, which enables the accessibility of multifractals or cascade theories for hydrologists.

4. New downscaling techniques were developed, based upon the theory of Multifractals and random cascade models, to produce high spatial and temporal rainfall estimates. There are in total two cascade-based downscaling models that were developed in this work: Semi-deterministic cascade model (SD model) and Fully empirical cascade model (FE model). The former is established based upon the theory of Left-sided Multifractals (Mandelbrot, 1990) together with the heuristic searching algorithm. It improves the applicability of the left-sided multifractals to hydrological processes (Mandelbrot, 1990; Mandelbrot et al., 1990). In addition, it does not require the fitting of any specific probability distribution and provides a more general form to characterise the patterns of high nonlinearity than existing cascade models, such as the log-Poisson model (Deidda et al., 1999), log-Normal model (Over and Gupta, 1994) and log-Levy model (Schertzer et al., 1997). The other model (FE model) proposed in this work is an extension of Olsson (1998)'s disaggregation model for hourly/sub-hourly rainfall time series downscaling. The FE model successfully strengthened the auto-correlation feature that is widely observed in high-resolution rainfall series in order to improve the applicability of discrete-in-scale cascade models to urban hydrology.

5. A combined application of adjustment and downscaling techniques was tested to demonstrate the potential of this combination to produce accurate and high-resolution rainfall estimates through processing the operational rainfall data.

6. The associated uncertainty of downscaling and its combination with adjustment was conducted to study the impact of downscaling process (compared to the adjustment process) upon urban hydrological applications.

According to the results of this work, some conclusions and perspectives for further research are given as follows:

1. This work suggests that the mean bias adjustment, which is widely used in national weather service, is insufficient for urban hydrological applications. A more complex adjustment, based upon the minimisation of the difference (or errors) between radar and interpolated raingauge rainfall fields, is suggested.

2. Cascade-based downscaling techniques are useful tools to synthesise street-scale rainfall estimates and to project their behaviour and their impacts on the corresponding

hydrological and hydraulic modelling, particularly for areas where advanced rainfall sensors (such as X-band radar) or very dense raingauge networks are not available.

3. The proposed SD model is currently more suitable for spatial downscaling because its cascading process is probabilistically symmetric. This means that the SD model currently cannot satisfactorily tackle the asymmetric behaviour (i.e. causality) of temporal downscaling. Future research is recommended which will focus upon adding external forcing to the cascading process to improve SD model's ability to reproduce specific physical phenomena that are widely observed in rainfall process, such as causality and spatial dependence.

4. This work demonstrates the importance of the spatial variability of rainfall (as compared to the rainfall volume bias) in urban hydrological applications; however, a more systematic way of quantifying the relationship between the spatial/temporal variability of rainfall, the rainfall volume bias, and the size of the urban catchment would be a very useful topic of further research.

5. The importance of spatial variability of rainfall may have been underestimated in this work due to the way spatial rainfall estimates are applied to the overland (surface) network of the study catchment and to the conversion between rainfall and runoff. The method used in this work to apply rainfall estimates to hydraulic models, is to input rainfall to the manhole of each subcatchment first and if water exceeds the capacity of sewer system, it surcharges over the ground surface. This may not be able to reflect realistically in time the impact of the spatial distribution of rainfall. In addition, the runoff coefficient of each subcatchment is obtained through an averaging process. This may also smooth the impact of the spatial variability of rainfall. It is therefore suggested that different hydraulic models, particularly with more detailed surface properties (e.g. the fully-distributed models), should be tested to assess the impact of spatial variability of rainfall.

6. In order to tackle the additional uncertainty introduced by the combination of two proposed techniques, a study of the variation of scaling features of adjusted and unadjusted rainfall estimates could usefully be conducted to understand the impact of the adjustment process upon downscaled rainfall estimates.

Bibliography

Allitt, R., Blanksby, J., Djordjevic, S., Maksimovic, C., Stewart, D., 2009. Investigations into 1d/1d and 1d/2d urban flood modelling. In: WaPUG Autumn Conference. Blackpool, UK.

Anagnostou, E. N., Krajewski, W. F., 1999. Rea-time radar rainfall estimation. part i: algorithm formulation. Journal of Atmospheric and oceanic technology 16, 189–197.

Bellone, E., 2004. Review of some multifractal models for rainfall. Tech. rep., Department of Civil and Environmental Engineering Imperial College and Department of Statistical Science University College London.

Berne, A., Delrieu, G., Creutin, J.-D., Obled, C., 2004. Temporal and spatial resolution of rainfall measurements required for urban hydrology. Journal of Hydrology 299 (3-4), 166–179.

Bowler, N. E., Pierce, C. E., Seed, A. W., 2006. Steps: A probabilistic precipitation forecasting scheme which merges an extrapolation nowcast with downscaled nwp. Quarterly Journal of the Royal Meteorological Society 132 (620), 2127–2155.

Bowler, N. E. H., Pierce, C. E., Seed, A., 2004. Development of a precipitation nowcasting algorithm based upon optical flow techniques. Journal of Hydrology 288 (1-2), 74–91.

Bringi, V. N., Chandrasekar, V., 2001. Polarimetric Doppler Weather Radar: Principles and Applications, 1st Edition. Cambridge University Press, Cambridge.

Butler, D., Davies, J. W., 2011. Urban Drainage, 3rd Edition. Spon, London.

Cârsteanu, A., Foufoula-Georgiou, E., 1996. Assessing dependence among weights in a multiplicative cascade model of temporal rainfall. Journal of Geophysical Research 101 (D21), 26363–26370.

Chandler, R. E., Wheater, H. S., 2002. Analysis of rainfall variability using generalised linear models: a case study from the west of Ireland. Water Resources Research 38 (10), 1192–1201.

Cole, S. J., Moore, R. J., 2008. Hydrological modelling using raingauge- and radar-based estimators of areal rainfall. Journal of Hydrology 358, 159–181.

Collier, C. G., 1996. Applications of Weather Radar Systems, 2nd Edition. Wiley, Chichester, England.

Collier, C. G., 2009. On the propagation of uncertainty in weather radar estimates of rainfall through hydrological models. Meteorological Applications 16 (1), 35–40.

Cressie, N., 1993. Statistics for Spatial Data. Wiley, New York.

Deidda, R., 2000. Rainfall downscaling in a space-time multifractal framework. Water Resources Research 36 (7), 1779–1794.

Deidda, R., Benzi, R., Siccardi, F., 1999. Multifractal modeling of anomalous scaling laws in rainfall. Water Resources Research 35 (6), 1853–1867.

Djordjević, S., Prodanović, D., Maksimović, C., Ivetić, M., Savić, D., 2005. SIPSON - Simulation of Interaction between Pipe flow and Surface Overland flow in Networks. Water Science and Technology 52 (5), 275–283.

EA, 2006. River Roding flood risk management strategy, strategic environmental assessment, environmental report, non technical summary. Tech. rep., Environment Agency.

EA, 2007. Review of 2007 summer floods. Tech. rep., Environment Agency.

EA, 2009. Flooding in England: A national assessment of flood risk. Tech. rep., Environment Agency.

Ehret, U., Gotzinger, J., Bardossy, A., Pegram, G. G. S., 2008. Radar based flood forecasting in small catchments, exemplified by the Goldersbach catchment, Germany. International Journal of River Basin Management 6 (4), 323–329.

Einfalt, T., Arnbjerg-Nielsen, K., Golz, C., Jensen, N.-E., Quirmbach, M., Vaes, G., Vieux, B., 2004. Towards a roadmap for use of radar rainfall data in urban drainage. Journal of Hydrology 299 (3-4), 186–202.

Einfalt, T., Jessen, M., Mehlig, B., 2005. Comparison of radar and raingauge measurements during heavy rainfall. Water Science and Technology 51 (2), 195–201.

Evertsz, C. J. G., Mandelbrot, B. B., 1992. Multifractal measures. In: Peitgen, H.-O., Jurgens, H., Saupe, D. (Eds.), Chaos and Fractals. Springer, New York, pp. 922–953.

Fabry, F., Bellon, A., Duncan, M. R., Austin, G. L., 1994. High resolution rainfall measurements by radar for very small basins: the sampling problem reexamined. Journal of Hydrology 161, 415–428.

Falconer, K., 2003. Fractal Geometry: mathematical foundations and applications, 2nd Edition. John Wiley & Sons Ltd., West Sussex, UK.

FFC, 2010. Extreme Rainfall Alert (ERA) Service User Guide. Tech. rep., Flood Forecast Centre.

Fulton, R. A., Breidenbach, J. P., Dong-Jun, S., Miller, D. A., 1998. The WSR-88D rainfall algorithm. Weather and Forecasting 13 (2), 377–377–395.

Germann, U., Galli, G., Boscacci, M., Bolliger, M., 2006. Radar precipitation measurement in a mountainous region. Quarterly Journal of the Royal Meteorological Society 132, 1669–1692.

Gerstner, E.-M., Heinemann, G., 2008. Real-time areal precipitation determination from radar by means of statistical objective analysis. Journal of Hydrology 352, 296–308.

Golding, B. W., 1998. Nimrod: a system for generating automated very short range forecasts. Meteorological Applications 5 (1), 1–16.

Golding, B. W., 2009a. Long lead time flood warnings: reality or fantasy? Meteorological Applications 16 (1), 3–12.

Golding, B. W., 2009b. Uncertainty propagation in a london flood simulation. Journal of Flood Risk Management 2 (1), 2–15.

Golz, C., Einfalt, T., Gabella, M., Germann, U., 2005. Quality control algorithms for rainfall measurements. Atmospheric Research 77 (1-4), 247–255.

Gupta, V. K., Waymire, E. C., 1993. A statistical analysis of mesoscale rainfall as a random cascade. Journal of Applied Meteorology 32 (2), 251–267.

Halsey, T. C., Jensen, M. H., Kadanoff, L. P., Procaccia, I., Shiraiman, B. I., 1986. Fractal measures and their singularities: the characterization of strange sets. Physical Review A 33 (2), 1141–1151.

Harrison, D. L., Driscoll, S. J., Kitchen, M., 2000. Improving precipitation estimates from weather radar using quality control and correction techniques. Meteorological Applications 7 (2), 135–144.

Harrison, D. L., Scovell, R. W., Kitchen, M., 2009. High-resolution precipitation estimates for hydrological uses. Proceedings of the Institution of Civil Engineers: Water Management 162 (2), 125–135.

Harte, D., 2001. Multifractals: theory and applications. Chapman & Hall/CRC, Boca Raton.

Hentschel, H. G. E., Procaccia, I., 1983. The infinite number of generalized dimensions of fractals and strange attractors. Physica D: Nonlinear Phenomena 8 (3), 435–444.

Houston, D., Werritty, A., Bassett, D., Geddes, A., Hoolachan, A., McMillian, M., 2011. Pluvial (rain-related) flooding in urban areas: the invisible hazard. Tech. rep., Joseph Rowntree Foundation.

Imgarten, J., Vieux, B., 2012. On the scale-dependent propagation of hydrologic uncertainty using high-resolution X-band radar rainfall estimates. Atmospheric Research 103, 96–105.

Jessen, M., Einfalt, T., Stoffer, A., Mehlig, B., 2005. Analysis of heavy rainfall events in North Rhine-Westphalia with radar and raingauge data. Atmospheric Research 77 (1-4), 337–346.

Kalman, R. E., 1960. A new approach to linear filtering and prediction problems. Transactions of the ASME–Journal of Basic Engineering 82 (Series D), 35–45.

Kang, B., Ramírez, J. A., 2010. A coupled stochastic space-time intermittent random cascade model for rainfall downscaling. Water Resources Research 46 (10), W10534.

Koutsoyiannis, D., 2003. Rainfall disaggregation methods: Theory and applications. In: Workshop on Statistical and Mathematical Methods for Hydrological Analysis. Rome.

Koutsoyiannis, D., Onof, C., 2001. Rainfall disaggregation using adjusting procedures on a Poisson cluster model. Journal of Hydrology 246, 109–122.

Krajewski, W. F., 1987. Cokriging radar-rainfall and rain gage data. Journal of Geophysical Research 92 (D8), 9571–9580.

Krämer, S., Fuchs, L., Verworn, H., 2007. Aspects of radar rainfall forecasts and their effectiveness for real time control-the example of the sewer system of the city of Vienna. Water Practice & Technology 2 (2), 0042–0049.

Lean, H. W., Bornemann, J., Tang, Y., Mittermaier, M., Roberts, N., Trueman, M., 2011. Experiences with a 1.5 km version of the Met Office Unified Model for short range forecasting. In: 91st American Meteorological Society Annual Meeting. Seattle, USA.

Leitão, J. P., Simões, N. E., Maksimović, C., Ferreira, F., Prodanović, D., Matos, J. S., Sá Marques, A., 2010. Real-time forecasting urban drainage models: full or simplified networks? Water Science and Technology 62 (9), 2106–2114.

Liguori, S., Rico-Ramirez, M. A., Schellart, A. N. A., Saul, A. J., 2011. Using probabilistic radar rainfall nowcasts and NWP forecasts for flow prediction in urban catchments. Atmospheric Research 103, 80–95.

Looper, J. P., Vieux, B. E., 2011. An assessment of distributed flash flood forecasting accuracy using radar and rain gauge input for a physics-based distributed hydrologic model. Journal of Hydrology 412-413, 114–132.

Lovejoy, S., 2010. Why the bare/dressed cascade distinction matters: Interactive comment on "reconstruction of sub-daily rainfall sequences using multinomial multiplicative cascades" by L. Wang et al. Hydrology and Earth System Sciences Discussion 7, C1–C4.

Lovejoy, S., Mandelbrot, B. B., 1985. Fractal properties of rain, and a fractal model. Tellus 37A, 209–232.

Lovejoy, S., Schertzer, D., 1990. Multifractals, universality classes and satellite and radar measurements of cloud and rain fields. Journal of Geophysical Research 95.

Lovejoy, S., Schertzer, D., 2010a. On the simulation of continuous in scale universal multifractals, Part I: Spatially continuous processes. Computers & Geosciences 36 (11), 1393–1403.

Lovejoy, S., Schertzer, D., 2010b. On the simulation of continuous in scale universal multifractals, Part II: Space-time processes and finite size corrections. Computers & Geosciences 36 (11), 1404–1413.

Maksimović, C., Prodanović, D., Boonya-Aroonnet, S., Leitão, J. P., Djordjević, S., Allitt, R., 2009. Overland flow and pathway analysis for modelling of urban pluvial flooding. Journal of Hydraulic Research 47 (4), 512–523.

Mandelbrot, B. B., 1983. The Fractal Geometry of Nature. W. H. Freeman and Company, New York.

Mandelbrot, B. B., 1989. Multifractal measures, especially for the geophysicist. Pure and Applied Geophysics 131 (1), 5–42.

Mandelbrot, B. B., 1990. New "anomalous" multiplicative multifractals: Left sided f(alpha) and the modelling of DLA. Physica A: Statistical Mechanics and its Applications 168 (1), 95–111.

Mandelbrot, B. B., Evertsz, C. J. G., Hayakawa, Y., 1990. Exactly self-similar left-sided multifractal measures. Physical Review A 42 (8), 4528.

Marsan, D., Schertzer, D., Lovejoy, S., 1996. Causal space-time multifractal processes: Predictability and forecasting of rain fields. Journal of Geophysical Research 101.

Mazzetti, C., 2004. Report on performance of the new methodology. Deliverable 7.4, MUSIC Project (Multiple Sensor Precipitation Measurements, Integration, Calibration and Flood Forecasting). Tech. rep., European Commission.

McIntyre, N., Wheater, H., Lees, M., 2002. Estimation and propagation of parametric uncertainty in environmental models. Journal of Hydroinformatics 4, 177–198.

Molnar, P., Burlando, P., 2005. Preservation of rainfall properties in stochastic disaggregation by a simple random cascade model. Atmospheric Research 77 (1-4), 137–151.

Moore, R., Watson, B., Jones, D., Black, K., 1989. London weather radar local calibration study: Final report. contract report prepared for the national rivers authority thames region. Tech. rep., NERC/Institute of Hydrology, Wallingford, UK.

Ochoa, S., Simões, N. E., Wang, L., Dinkneh, A., Cortés, J., Almoradie, A., 2011a. Guidelines for informatics support to awareness raising and resilience enhancement activities.

Deliverable 5.1, DIANE-CM Project (Decentralised Integrated Analysis and Enhancement of Awareness through Collaborative Modelling and Management of Flood Risk). Tech. rep., Era-Net CRUE Funding Initiative on Flood Resilience.

Ochoa, S., Simões, N. E., Wang, L., Dinkneh, A., Cortés, J., Almoradie, A., 2011b. Guidelines for novel risk quantification and communication. Deliverable 5.1, DIANE-CM Project (Decentralised Integrated Analysis and Enhancement of Awareness through Collaborative Modelling and Management of Flood Risk). Tech. rep., Era-Net CRUE Funding Initiative on Flood Resilience.

Olsson, J., 1995. Limits and characteristics of the multifractal behaviour of a high-resolution rainfall time series. Nonlinear Process in Geophysics 2, 23–29.

Olsson, J., 1998. Evaluation of a scaling cascade model for temporal rainfall disaggregation. Hydrology and Earth System Sciences 2 (1), 19–30.

Olsson, J., Niemczynowicz, J., Berndtsson, R., 1993. Fractal analysis of high-resolution rainfall time series. Journal of Geophysical Research 98.

Olsson, J., Niemczynowicz, J., Berndtsson, R., Larson, M., 1992. An analysis of the rainfall time structure by box counting–some practical implications. Journal of Hydrology 137 (1-4), 261–277.

Onof, C., Arnbjerg-Nielsen, K., 2009. Quantification of anticipated future changes in high resolution design rainfall for urban areas. Atmospheric Research 92, 350–363.

Onof, C., Chandler, R. E., Kakou, A., Northrop, P., Wheater, H. S., Isham, V., 2000. Rainfall modelling using Poisson-cluster processes: a review of developments. Stochastic Environmental Research and Risk Assessment 14 (6), 384–411.

Onof, C., Townend, J., Kee, R., 2005. Comparison of two hourly to 5-min rainfall disaggregators. Atmospheric Research 77, 176–187.

Onof, C., Wheater, H. S., 1993. Modelling of British rainfall using a random parameter Bartlett-Lewis rectangular pulse model. Journal of Hydrology 149, 67–95.

Onof, C., Wheater, H. S., 1994. Improvements to the modelling of British rainfall using a modified random parameter Bartlett-Lewis rectangular pulse model. Journal of Hydrology 157, 177–195.

Over, T. M., Gupta, V. K., 1994. Statistical analysis of mesoscale rainfall: Dependence of a random cascade generator on large-scale forcing. Journal of Applied Meteorology 33 (12), 1526–1542.

Over, T. M., Gupta, V. K., 1996. A space-time theory of mesoscale rainfall using random cascades. Journal of Geophysical Research 101 (D21), 26319–26331.

Parker, D. J., Priest, S. J., McCarthy, S. S., 2011. Surface water flood warnings requirements and potential in England and Wales. Applied Geography 31 (3), 891–900.

Pathirana, A., Herath, S., 2002. Multifractal modelling and simulation of rain fields exhibiting spatial heterogeneity. Hydrology and Earth System Sciences 6 (4), 695–708.

Pathirana, A., Herath, S., Yamada, T., 2003. Estimating rainfall distributions at high temporal resolutions using a multifractal model. Hydrology and Earth System Sciences 7 (5), 668–679.

Pierce, C. E., 2009. The short term ensemble prediction system: a guide to model design and performance for the wet bench. Tech. rep., Met Office Joint Center for Hydro-Meteorological Research.

Pitt, M., 2008. The Pitt Review: Learning lessons from the 2007 floods. Tech. rep., Cabinet Office, UK.

Rico-Ramirez, M. A., Schellart, A. N. A., Liguori, S., Saul, A. J., 2009. Quantitative precipitation forecasting for a small urban area: Use of high-resoultion numerical weather prediction model. In: Molnar, P., Burlando, P., Einfalt, T. (Eds.), 8th Internation Workshop on Precipitation in Urban Areas. St. Moritz, Switzerland, pp. 47–51.

Riedi, R., 1995. An improved multifractal formalism and self-similar measures. Journal of Mathematical Analysis and Applications 189 (2), 462–490.

Riedi, R. H., Mandelbrot, B. B., 1995. Multifractal formalism for infinite multinomial measures. Advances in Applied Mathematics 16 (2), 132–150.

Rinehart, R. E., 2010. Radar for Meteorologists. Rinehart Publications, Grand Forks.

Ryzhkov, A. V., Giangrande, S. E., Melnikov, V. M., Schuur, T. J., 2005. Calibration issues of dual-polarization radar measurements. Journal of Atmospheric and Oceanic Technology 22 (8), 1138–1155.

Schertzer, D., Lovejoy, S., 1987. Physical modeling and analysis of rain and clouds by anisotropic scaling multiplicative processes. Journal of Geophysical Research 92.

Schertzer, D., Lovejoy, S., Gupta, V. K., Waymire, E. C., 1997. Universal multifractals do exist!: Comments on a statistical analysis of mesoscale rainfall as a random cascade. Journal of Applied Meteorology 36 (9), 1296–1304.

Sebastianelli, S., Russo, F., Napolitano, F., Baldini, L., 2010. Comparison between radar and rain gauges data at different distances from radar and correlation existing between the rainfall values in the adjacent pixels. Hydrology and Earth System Sciences Discussion 7 (4), 5171–5212.

Seed, A. W., 2003. A dynamic and spatial scaling approach to advection forecasting. Journal of Applied Meteorology 42 (3), 381–388.

Segond, M.-L., Onof, C., Wheater, H. S., 2006. Spatial-temporal disaggregation of daily rainfall from a generalized linear model. Journal of Hydrology 331, 647–689.

Seo, D.-J., Breidenbach, J. P., Johnson, E. R., 1999. Real-time estimation of mean field bias in radar rainfall data. Journal of Hydrology 223, 131–147.

Shrestha, R., Tachikawa, Y., Takara, K., 2004. Downscaling spatial rainfall field from global scale to local scale using improved multiplicative random cascade method. Annuals of Disas. Prev. Res. Inst. 47B.

Simões, N. E., Leitão, J. P., Maksimović, C., Sá Marques, A., Pina, R., 2010. Sensitivity analysis of surface runoff generation in urban flood forecasting. Water Science and Technology 61 (10), 2595–2601.

Simões, N. E., Ochoa, S., Leitão, J. P., Pina, R., Sá Marques, A., Maksimović, C., 2011a. Urban drainage models for flood forecasting: 1d/1d, 1d/2d and hybrid models. In: 12th International Conference on Urban Drainage. Porto Alegre, Brazil.

Simões, N. E., Wang, L., Ochoa, S., Leitão, J. P., Pina, R., Onof, C., Sá Marques, A., Maksimović, C., David, M., Davíd, L., 2011b. A methodology for urban flood forecast based on a network of raingauges. In: 12th International Conference on Urban Drainage. Porto Alegre, Brazil.

Singh, V. P., 1997. Effect of spatial and temporal variability in rainfall and watershed characteristics on stream flow hydrograph. Hydrological Processes 11 (12), 1649–1669.

Smith, J. A., Baeck, M. L., Meierdiercks, K. L., Miller, A. J., Krajewski, W. F., 2007. Radar rainfall estimation for flash flood forecasting in small urban watersheds. Advances in Water Resources 30 (10), 2087–2097.

Sokol, Z., Pešice, P., 2009. Evaluation of precipitation nowcasting by sam model. In: Molnar, P., Burlando, P., Einfalt, T. (Eds.), Proceedings of the 8th International Workshop on Precipitation in Urban Areas. St. Moritz, Switzerland, pp. 235–239.

Stern, R. D., Coe, R., 1984. A model fitting analysis of daily rainfall data. Journal of Royal Statistical Society 147 (1), 1–34.

Syed, K. H., Goodrich, D. C., Myers, D. E., Sorooshian, S., 2003. Spatial characteristics of thunderstorm rainfall fields and their relation to runoff. Journal of Hydrology 271 (1-4), 1–21.

Tabios, G. Q., Salas, J. D., 1985. A comparative analysis of techniques for spatial interpolation of precipitation1. JAWRA Journal of the American Water Resources Association 21 (3), 365–380.

Tessier, Y., Lovejoy, S., Schertzer, D., 1993. Universal multifractals: Theory and observations for rain and clouds. Journal of Applied Meteorology 32 (2), 223–250.

Todini, E., 2001a. Influence of parameter estimation uncertainty in kriging: Part 1 - theoretical development. Hydrol. Earth Syst. Sci. 5 (2), 215–223.

Todini, E., 2001b. A Bayesian technique for conditioning radar precipitation estimates to rain-gauge measurements. Hydrol. Earth Syst. Sci. 5 (2), 187–199.

Vieux, B. E., Bedient, P. B., 2004. Assessing urban hydrologic prediction accuracy through event reconstruction. Journal of Hydrology 299 (3-4), 217–236.

Vischel, T., Quantin, G., Lebel, T., Viarre, J., Gosset, M., Cazenave, F., Panthou, G., 2011. Generation of high resolution rainfields in West Africa: evaluation of dynamical interpolation methods. Journal of Hydrometeorology 12, 1465–1482.

Wang, L., 2005. Applications of multifractals to rainfall forecast. Master's thesis, National Taiwan University.

Wang, L., Maksimović, C., Onof, C., 2009a. An improved multifractal model for short-term rainfall forecast. In: Computing and Control in the Water Industry 2009. University of Sheffield, UK.

Wang, L., Maksimović, C., Onof, C., 2009b. A semi-deterministic multiplicative cascade method for sub-daily rainfall forecast. In: Molnar, P., Burlando, P., Einfalt, T. (Eds.), Proceedings of the 8th International Workshop on Precipitation in Urban Areas. St. Moritz, Switzerland.

Wang, L., Onof, C., Maksimović, C., 2010. Analysis of high-resolution spatiotemporal structures of mesoscale rainfields based upon the theory of left-sided multifractals. In: American Geophysics Union (AGU) Fall Meeting 2010. San Francisco, CA, USA.

Wang, L., Simões, N. E., Rico-Ramirez, M., Ochoa, S., Maksimović, C., 2011. Radar-based pluvial flood forecasting over urban areas: Redbridge case study. In: International Symposium on Weather Radar and Hydrology (WRaH). Exeter, UK.

Wheater, H., Chandler, R., Onof, C., Isham, V., Bellone, E., Yang, C., Lekkas, D., Lourmas, G., Segond, M. L., 2005. Spatial-temporal rainfall modelling for flood risk estimation. Stochastic Environmental research and risk assessment 19 (6), 403–416.

Wood, S. J., Jones, D. A., Moore, R. J., 2000. Static and dynamic calibration of radar data for hydrological use. Hydrology and Earth System Sciences 4 (4), 545–554. URL `http://www.hydrol-earth-syst-sci.net/4/545/2000/`

Yang, C., Chandler, R. E., Isham, V. S., Wheater, H. S., 2005. Spatial-temporal rainfall simulation using generalised linear models. Water Resources Research 41, 1–13.

Appendix A

Urban Flood Forecasting in the Cranbrook Catchment

Radar-based pluvial flood forecasting over urban areas: Redbridge case study

LI-PEN WANG[1], NUNO SIMÕES[1, 2], MIGUEL RICO-RAMIREZ[3], SUSANA OCHOA[1], JOAO LEITÃO[4] & ČEDO MAKSIMOVIĆ[1]

1 *Department of Civil and Environmental Engineering, Imperial College London, Skempton Building, South Kensington Campus, London, SW7 2AZ, UK*
li-pen.wang08@imperial.ac.uk

2 *Department of Civil Engineering, University of Coimbra, Coimbra, Rua Luís Reis Santos, 3030-788 Coimbra, Portugal*

3 *Department of Civil Engineering, University of Bristol, UK*

4 *Laboratório Nacional de Engenharia Civil, Av. do Brasil 101, 1700-066 Lisboa, Portugal*

Abstract A nowcasting model coupled with an urban drainage model is used in this study to assess the forecasting of pluvial floods in urban areas. The deterministic nowcasting model used in this paper is part of the Met Office STEPS (Short-Term Ensemble Prediction System) system, and the hydraulic model is run based up the 1D/1D dual drainage simulation scheme. A highly-urbanised catchment, Cranbrook (located in the London Borough of Redbridge), is employed for this case study to analyse the associated uncertainties. The aim of this work is to assess the impact of using rainfall forecasts with different spatial and temporal resolutions to forecast pluvial flooding over urban areas. Results show that promising performance in hydraulic forecasting is in general observed by using higher spatial and temporal resolution nowcasts as inputs; this implies the necessity of using advanced radar-based nowcasting techniques to improve the state-of-the-art pluvial flood forecasting over urban areas.

Key words nowcasting; flood forecasting; radar; rainfall; urban drainage

INTRODUCTION

In the last decades, urban pluvial (surface) flooding has caused enormous economic losses all over the world, and has affected thousands of people. For this reason, it has been pointed out as an important issue that urgently needs to be appropriately tackled (Pitt, 2008). In order to accurately predict floods over urban areas, high-resolution rainfall measurements and forecasts, as well as efficient hydraulic models, are required.

Many studies have thus been conducted on the use of weather radar in urban hydrology (Einfalt *et al.*, 2004), as these devices are able to provide rainfall measurements with high spatial and temporal resolutions. Furthermore, the use of radar to produce a rainfall forecast and its subsequent combination with runoff models has been recently studied (Krämer *et al*. 2007, Liguori *et al*. 2012) and constitutes the focus of several current studies, like the one presented here.

Regarding the runoff models used for urban pluvial flood forecasting, the dual-drainage concept, which entails integrating the overland and sewer networks, has been widely accepted as a feasible physically-based representation of pluvial flooding (Leitão *et al*., 2009; Maksimović *et al*., 2009; Simões *et al*., 2010).

A radar-based nowcasting model coupled with an urban drainage model is therefore employed in this study to simulate urban (pluvial) floods. The main aim of this work is to assess the impact of using rainfall nowcasts with different spatial and temporal resolutions to forecast pluvial flooding over urban areas.

EXPERIMENTAL SITE AND DATASET

Cranbrook catchment

The case study used for testing our pluvial flood forecasting methodology is the Cranbrook catchment, which is located within the London Borough of Redbridge (situated in the northeast part of Greater London) and is drained by the River Roding (Fig. 1(a)). According to the Environment Agency (2006), the River Roding has a rapid response to rainfall, which is typical of

Copyright © 2012 IAHS Press

densely-urbanised catchments overlying London Clay. Flood events have been recorded in the Roding catchment since 1926, with the most recent events being in 2000 and 2009, when several properties were flooded. These events are relatively well documented and can be used in the development of advanced flood prediction methodologies.

The drainage area of the Cranbrook catchment is approximately 910 ha; the main water course is about 5.75 km long, of which 5.69 km are piped or culverted.

Radar data

The Cranbrook catchment is in the coverage of two radars: Chenies and Thurnham (Fig. 1(c)). The radar data are provided by the Met Office through the British Atmospheric Data Centre (BADC) with spatial and temporal resolutions of 1 km and 5 min, respectively. This dataset has been averaged to obtain a spatial resolution of 2 km. The radar data have been quality-controlled by the Met Office following the correction techniques proposed by Harrison *et al.* (2000) to account for all the errors inherent to radar rainfall measurements (see Rico-Ramirez *et al.*, 2007).

Monitoring system

A real-time accessible monitoring system is installed in this catchment (Fig. 1(d)), including three tipping-bucket raingauges, one pressure sensor for Roding River level monitoring, two sensors for water depth measurement in sewers, and one sensor for water depth measurement in open channels. The collected measurements however are not used to verify the forecasting results but for the calibration of the hydraulic model because the focus of this study lies in assessing the forecast errors rather than the forecast plus hydraulic errors.

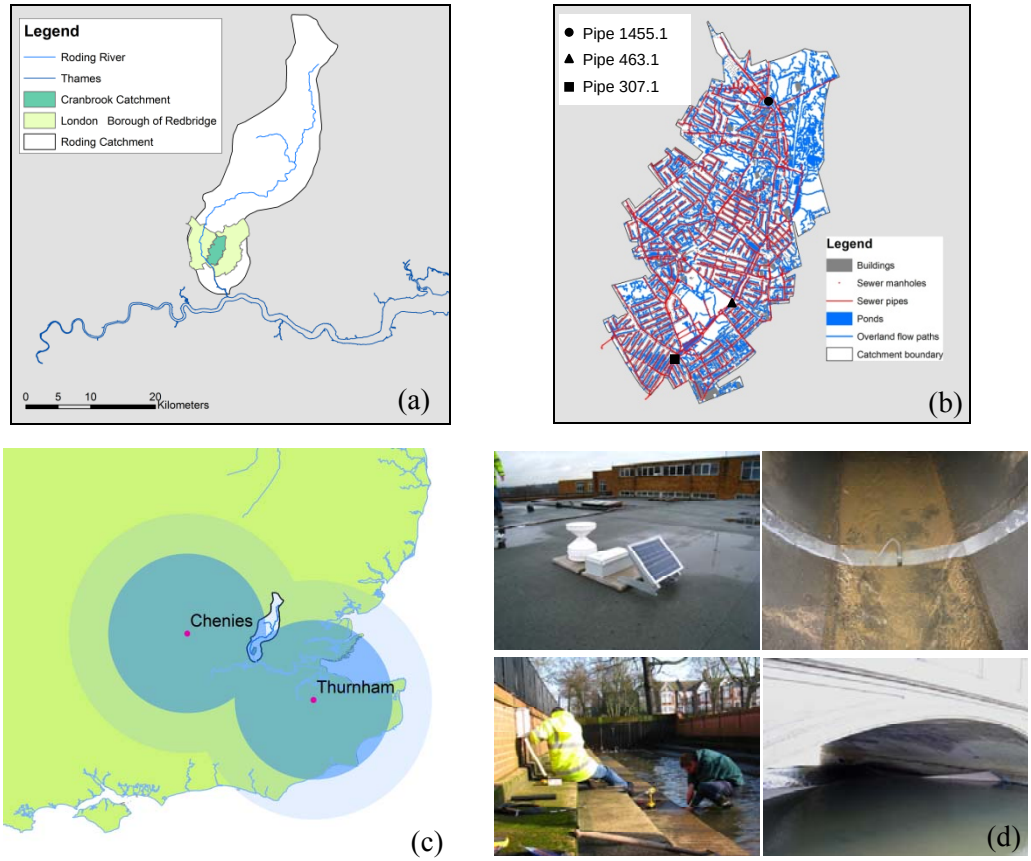


Fig. 1 Cranbrook catchment: (a) location of Cranbrook catchment in relation to the Roding River catchment; (b) dual drainage networks of the Cranbrook catchment; (c) radars which cover the study area; (d) monitoring system installed in the study area.

NOWCASTING MODEL

The deterministic nowcasting system employed in this study is the Short-Term Ensemble Prediction System (STEPS) developed by the Met Office and the Australian Bureau of Meteorology. The deterministic nowcasting system in STEPS is based on the spectral decomposition proposed by Seed (2003) with the incorporation of the optical flow equation proposed by Bowler *et al*. (2004). The deterministic nowcasts produced in this study are purely based on radar.

The nowcasting model has been setup to run at 1 km and 2 km spatial resolutions and 5 min, 10 min and 15 min temporal resolutions. At both spatial resolutions, the domain size was fixed to 500 km × 500 km covering the window with lower left coordinates of 200 km (easting), –100 km (northing) and top right coordinates of 700 km (easting) and 400 km (northing). The radar data have been pre-processed to cover this domain size and also to remove any spurious echoes. The nowcasting model has been setup to produce 3 h forecasts initialised every 10 min for all the events.

HYDRAULIC MODEL

Based upon the dual-drainage concept, the hydraulic model of the Cranbrook catchment was implemented in InfoWorks CS by coupling the overland network generated by the AOFD (Automatic Overland Flow Delineation) (Maksimovic *et al.*, 2009) and the sewer system. The overland network model is implemented using a LiDAR (Light Detection And Ranging) DEM (Digital Elevation Model) with 1 m resolution and vertical accuracy of approximately 0.15 m. The sewer network model was obtained from the water utility of the study area. The original simulation parameters were unchanged for all simulations.

The AOFD, an in-house tool developed by the Urban Water Research Group (UWRG) at Imperial College London, was employed in this study to generate the overland network. This tool automatically creates the overland flow network to enable its interaction with the sewer drainage system. The AOFD analyses several GIS layers such as DEM, buildings, manhole location, etc. to generate a 1-dimensional (1D) overland flow network model consisting of ponds and flow pathways. The resulting model can be further coupled with the sewer network model in order to simulate and forecast pluvial flooding (Leitão, 2009; Maksimovic *et al.*, 2009). The advantage of having a 1D model of the overland network (instead of a 2D model) is its short computational time, which makes it suitable for real-time forecasting of pluvial urban flooding. Analyses conducted by Leitão *et al*. (2010) justify the fact that a 1D model produces reasonable results when compared to 2D models, while requiring significantly less computational time.

CASE STUDY

Three events occurring since August 2010 (22–23 August 2010, 1 October 2010 and 17–18 January 2011) are selected in this analysis. The event 22–23 August 2010 was associated with a warm front and the rainfall falling within the Redbridge catchment was approximately 30 mm in around 18 h, with more than 20 mm falling in a period of 5 h. The event 1 October 2010 produced around 35 mm of rain in approximately 72 h. The event 17–18 January 2011 was associated with an occluded front passing over southeast England, producing heavy rain in the Redbridge catchment with total accumulations of around 30 mm in 24 h.

RESULTS

Precipitation forecasting

Figure 2 shows the performance of the radar-based forecasts versus lead time at different spatial and temporal scales for the event on 22–23 August 2010. Figure 2(a)–(c) show the results of the simulations performed at 1 km spatial resolution and 5 min, 10 min and 15 min temporal resolutions.

In the same figures, the performances of the forecasts are also shown when averaging the rainfall forecasts at 1 km to produce larger spatial scales (e.g. 2 km, 5 km and 10 km). As shown in these figures (Fig. 2(a)–(c)), the performance of the rainfall forecasts is very similar for the different temporal resolutions (i.e. 5 min, 10 min and 15 min). On the other hand, Fig. 2(d)–(e) show the results of the simulations performed at 2 km spatial resolution and different temporal resolutions. These results indicate that the performance of the forecasts shown in Fig. 2(d)–(e) is slightly higher than the performance of the forecasts shown in Fig. 2(a)–(c) for the same spatial scale of 2 km. Similar results are obtained for the other two events (not shown in this paper). These results have important implications for urban flood forecasting, where forecasts with small spatial scales are required. The results shown in Fig. 2 also indicate that the performance of the precipitation forecast depends on the spatial scale, with lower performance obtained at small scales but higher performance at larger scales, which is consistent with the results shown by Liguori *et al*. (2011).

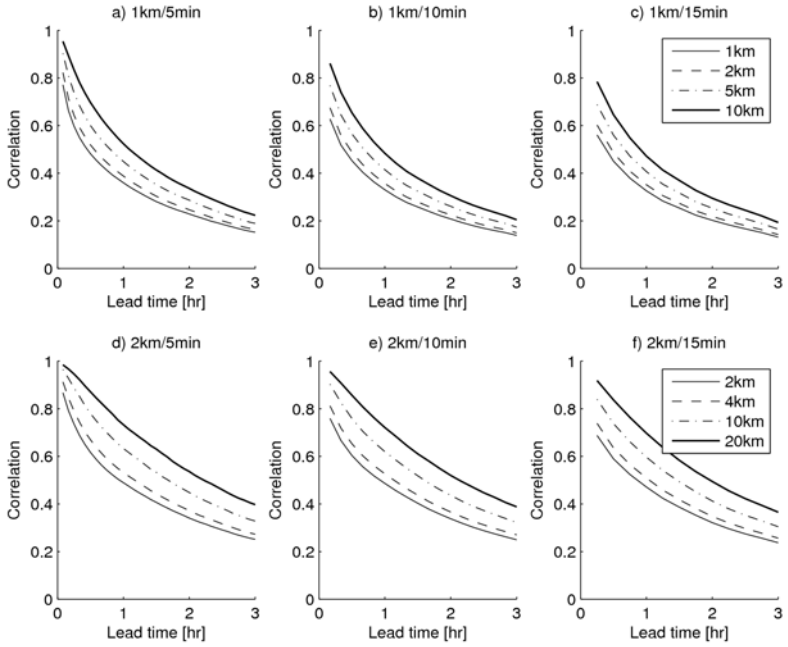


Fig. 2 Performance of the radar-based forecasts versus lead time at different spatial and temporal scales for event 22–23 August 2010.

Hydraulic modelling

Three pipes with significantly different drainage area (located in the upper, mid and lower part of the Cranbrook catchment) have been selected to demonstrate the impact of the spatial and temporal resolution of rainfall forecasts on the forecast of pluvial flooding over the Cranbrook catchment. The location of these pipes is shown in Fig. 1(b).

Figure 3 shows the performance of different flood forecasts for the event on 22–23 August 2010 against lead time for each pipe considered in the analysis. The different flood forecasts are obtained by feeding rainfall forecasts with different spatial and temporal resolution into the hydraulic model. The benchmark results are the hydraulic model results obtained using the real Nimrod data with 1 km and 5 min resolution. In the figure "*1-Relative Error*" is used as a surrogate measure of performance. The *Relative Error* (*RE*) is defined by:

$$1 - Relative\ Error = 1 - \left\langle \frac{\left| Y_{Nowcast} - Y_{Nimrod} \right|}{Y_{Nimrod}} \right\rangle \tag{1}$$

where <·> means the average, and the Y_{Nimrod} and $Y_{Nowcast}$ represent the flow depths in a specific pipe estimated, respectively, using the Nimrod data and Nowcasting results. When

"*1-Relative Error*" is equal to unity, it represents a perfect forecast. It is expected that this quantity will decrease with increasing forecasting lead-time. Furthermore, Fig. 4 shows the rain-rate profiles over the Cranbrook catchment on 23 August 2010 (00:00 h - 08:00 h), as well as the water levels estimated in pipe 1455.1 with Nimrod data and with nowcasting results at different spatial and temporal resolutions.

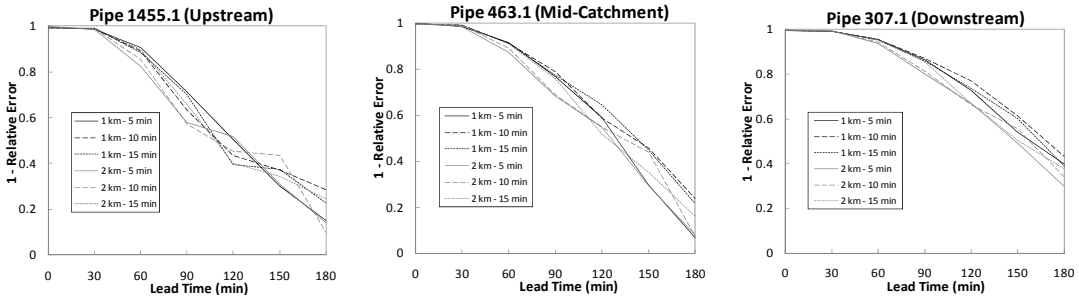


Fig. 3 Three pipes (1455.1, 463.1 and 307.1 located at the upstream, mid-catchment and downstream areas of the Cranbrook catchment, respectively) are used here to show the uncertainties in using rainfall nowcasts over different spatial and temporal scales for event 22–23 August 2010.

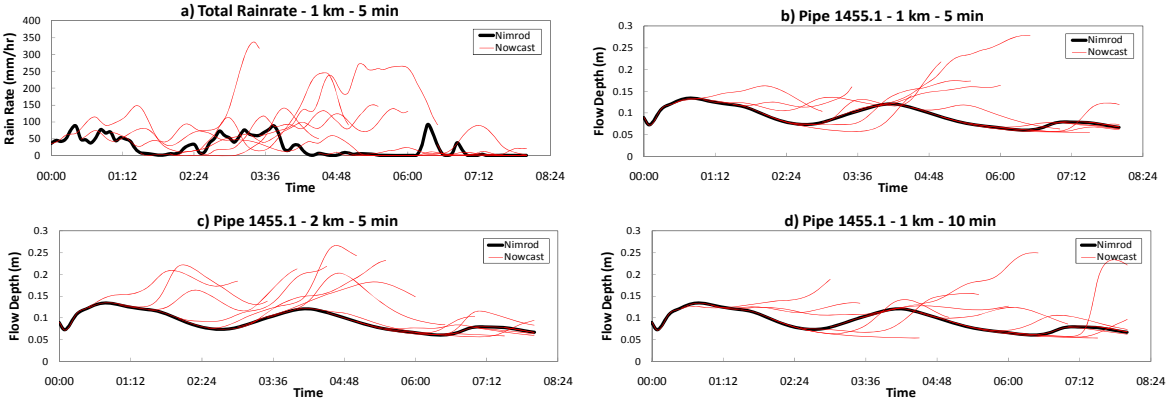


Fig. 4 Profiles of (a) the total rain-rate over the Cranbrook catchment on 23 August 2010 (00:00 h – 08:00 h) and the associated water levels of pipe 1455.1: (b) 1 km – 5 min, (c) 2 km – 5 min, and (d) 1 km – 10 min scales generated from Nimrod rainfall (dark lines) data and 3 h nowcasting results, respectively (red lines).

The results show that both the spatial and temporal resolutions of the rainfall forecast have an impact on the flood forecast. Regarding the spatial resolution, it can be seen that, in general, the flood forecasts obtained with 1 km resolution rainfall forecast are better than those obtained with the 2 km resolution rainfall forecast. However, for lead-times longer than 120 min the difference in the flood forecast obtained for the two spatial resolutions decreases, and in some cases better performance is achieved with the 2 km rainfall forecasts as input. This indicates that although 2 km nowcasts have higher correlation with Nimrod data, in this case the 1 km nowcasts, which exhibit higher spatial variability, are better inputs for the hydraulic model with lead-times up to 120 min.

In terms of temporal resolution, the results show that for lead-times up to 90 minutes the rainfall forecast at 5 min resolution generates the best flood forecast. After 90 minutes lead-time the performance of the 5 min resolution rainfall forecast decreases significantly and better flood forecasts are achieved with 10 min and 15 min rainfall forecasts.

In addition, it can be noticed that the magnitude of the impact of the spatial and temporal resolution of the rainfall forecast on the flood forecast also depends on the drainage area of the pipe or

conduit that is being analysed. As shown in Fig. 3, the impact of the temporal and spatial resolution decreases as the area drained by the pipe increases. This can be explained by the fact that in a greater drainage area the differences in the spatial and temporal distribution of the rainfall are smoothed.

CONCLUSIONS

In this study, a radar-based nowcasting model coupled with an advanced 1D/1D hydraulic model is used to simulate flood forecasting over urban areas. The Cranbrook catchment in London is employed for this case study to demonstrate the feasibility of using high-resolution radar rainfall data as inputs to forecast floods. An uncertainty study has been carried out by applying various spatial (1 and 2 km) and temporal (5, 10 and 15 min) rainfall nowcasts to a hydraulic model. The results show that better performance in flood simulation is in general obtained using higher spatial resolution rainfall nowcasts as inputs. This implies that the reliability of operational urban flood models may be improved by employing finer resolution rainfall information which has a better ability to reproduce the high spatial and temporal variability of urban rainfall. The perspective research will be focused on generating street-scale rainfall nowcasts using radar-based nowcasting techniques in synergy with statistically-based downscaling methods and studying the associated uncertainties.

Acknowledgement The research was conducted as part of the Flood Risk Management Research Consortium (FRMRC2, SWP3). The first author acknowledges the full financial support of the Ministry of Education of Taiwan for the postgraduate research programme. The second author acknowledges the financial support from the Fundação para a Ciência e Tecnologia – Ministério para a Ciência, Tecnologia e Ensino Superior, Portugal [SFRH/BD/37797/2007]. The third author acknowledges the support of the Engineering and Physical Sciences Research Council (EPSRC) grant EP/I012222/1. The authors thank the Met Office for providing the radar data and the STEPS model, thank the British Atmospheric Data Centre (BADC) for providing some of the datasets, thank MWH Soft for providing the InfoWorks CS software and thank Thames Water for providing the information of the sewer network over the Cranbrook catchment.

REFERENCES

Bowler, N. E. H., Pierce, C. E. & Seed, A. W. (2004) Development of a precipitation nowcasting algorithm based upon optical flow techniques. *J. Hydrol.* 288(1–2), 74–91.

Bowler, N. E. H., Pierce, C. E. & Seed, A. W. (2006) STEPS: A probabilistic precipitation forecasting scheme which merges an extrapolation nowcast with downscaled NWP. *Quart. J. Roy. Met. Soc.* 132(620), 2127–2155.

Einfalt, T., Arnbjerg-Nielsen, K., Golz, C., Jensen, N.-E., Quirmbach, M., Vaes, G. & Vieux, B. (2004) Towards a roadmap for use of radar rainfall data in urban drainage. *J. Hydrol.* 299(3–4), 186–202.

Environment Agency (2006) River Roding flood risk management strategy. *Strategic Environmental Assessment Environmental Report, Non technical summary*.

Harrison, D. L., Driscoll, S. J. & Kitchen, M. (2000). Improving precipitation estimates from weather radar using quality control and correction techniques. *Meteorol. Appl.* 7(2), 135–144.

Krämer, S., Fuchs, L., Verworn, H. (2007) Aspects of radar rainfall forecasts and their effectiveness for real time control – the example of the sewer system of the city of Vienna. *Water Practice & Technology* 2(2), 0042-0049.

Leitão, J. P., Simões, N. E., Ferreira, F., Prodanović, D., Maksimović, Č., Matos, J. & Sá Marques A. (2010) Real-time forecasting urban drainage models: full or simplified networks? *Water Sci. Technol.* 62(9), 2106–2114.

Leitao, J. P., (2009) Enhancement of digital elevation models and overland flow path deliniation methods for advanced urban flood modelling. PhD thesis, Imperial College London, London, UK.

Liguori, S., Rico-Ramirez, M. A., Schellart, A. N. A. & Saul, A.J. (2012) Using probabilistic radar rainfall nowcasts and NWP forecasts for flow prediction in urban catchments. *Atmos. Res.* 103, 80-95. DOI: 10.1016/j.atmosres.2011.05.004.

Maksimović, Č., Prodanović, D., Boonya-aroonnet, S., Leitão, J. P., Djordjević, S. & Allitt, R. (2009) Overland flow and pathway analysis for modelling of urban pluvial flooding. *J. Hydraul. Res.* 47(4), 512–523.

Pitt, M. (2008) The Pitt review: learning lessons from the 2007 floods. *Technical Report*, UK Cabinet Office, London, UK.

Rico-Ramirez, M. A., Cluckie, I. D., Shepherd, G. & Pallot, A. (2007) A high-resolution radar experiment on the island of Jersey. *Meteorol. Appl.* 14(2), 117–129.

Seed, A. W. (2003) A dynamic and spatial scaling approach to advection forecasting. *J. Appl. Met.* 42(3), 381–388.

Simões, N. E., Leitão, J. P., Maksimović, Č., Sá Marques, A. & Pina, R. (2010) Sensitivity analysis of surface runoff generation in urban floods forecasting. *Water Sci. Technol*. 61(10), 2595–2601.

Appendix B

Estimation of Empirical $\tau(q)$ Curves

There are in general two methods for empirically estimating $\tau(q)$ (or the multifractal spectrum $f(\alpha)$) curves from measurements; they are the histogram method and the method of moment (Evertsz and Mandelbrot, 1992). The prior follows the definition of α and $f(\alpha)$ (Eqs. (4.4) and (4.5)) to numerically estimate first the multifractal spectrum and then the associated $\tau(q)$ curves through introducing the Legendre Transform (Eq. (4.17)); whilst the latter directly estimates $\tau(q)$ curves (and if necessary, the associated $f(\alpha)$ curves can still be obtained through applying Legendre transform, Eq. (4.17)). In this work, the latter, the method of moment, developed based upon Eq. (4.14), was employed because first, the empirical $\tau(q)$ curves can be directly obtained through this method to minimise the loss of accuracy during numerical computing, and second, this method provides a mechanism for implicitly justifying whether the data used really behaves in a multifractal way so that the reliability of the following estimation based upon the empirical $\tau(q)$ curves is assured.

The steps to implement the method of moment are summarised as follows (Evertsz and Mandelbrot, 1992):

(a) Determine the box-measures $\mu_i(B_i(\epsilon))$ of the data of interest, where $B_i(\epsilon)$ is the box of size (i.e. spatial or temporal scales) ϵ and $i = 1, 2, \ldots, N(\epsilon)$. For time series (1-D) data (e.g. raingauge observations), $B_i(\epsilon) = \epsilon$; for spatial (2-D) data (e.g. radar rainfall measurements), $B_i(\epsilon) = \epsilon^2$.

(b) Compute the partition function $\chi(q, \epsilon)$ in Eq.(4.14) of a given order q for various values of (temporal or spatial) scales ϵ.

(c) Plot the logarithm of $\chi(q, \epsilon)$ against $\log \epsilon$, and check whether these plots follow a straight line. If it does, $\tau(q)$ is the slope of the line corresponding to the given q.

(d) Repeat the previous two steps with various values of q, where $q \geq 0$ and usually q is not larger than 5 (Olsson, 1998); an empirical $\tau(q)$ curve can be therefore obtained.

(e) (If necessary) The associated multifractal spectrum $f(\alpha)$ can be estimated by applying the Legendre transform in Eq. (4.17) to the obtained $\tau(q)$ curve.

Note that, in step (c) the straight-line relationship of $\log \chi(q, \epsilon)$-$\log \epsilon$ shall be strictly justified to confirm the existence of scale-invariance of the date used rather than directly applying linear regression to $\log \chi(q, \epsilon)$-$\log \epsilon$.

Appendix C

Discrete-in-Scale Random Cascade Models

C.1 Random Cascade processes and $\tau(q)$ curve

In the application of a binomial cascade to rainfall downscaling, a specific rainfall volume at a given cascade level (e.g. V_{21} at the level $n = 2$ in Figure 4.3) can be obtained by multiplying the rainfall volume at the prior cascade level by certain fragmentation ratios (e.g. $V_{21} = V w_2^1 w_1^2$ where V is the rainfall volume at level $n = 0$). A "measure" is then introduced herein to normalise this rainfall volume, i.e., $\mu_{21} = V_{21}/V = w_2^1 w_1^2$, the quantity of which is related to the position and the size of the scale of this measure (which can be obtained from the cascade level of the target measure), so μ_{21} can be further expressed as $\mu_j((1/2)^2)$, where j is the position index of the measure and $1/2$ is the contracting ratio for the size of the scales between two successive levels in a binomial cascade process. Now if the case of a binomial cascade is extended to a multinomial cascade with the branching number equal to b, the measure at a certain level n can be expressed as,

$$\mu_j(\epsilon) = w_{i_1}^1 w_{i_2}^2 \cdots w_{i_n}^n = \prod_{L=1}^{n} w_{i_L}^L, \tag{C.1}$$

where $\epsilon = b^{-n}$ and $i_L \in \mathbb{Z}$, $1 \leq i_L \leq b$. In order to (statistically or macrocanonically) preserve the total mass of measures, the constraint $\sum_{j=1}^{N(\epsilon)} \mu_j(\epsilon) = 1$ can be applied, where $N(\epsilon) = b^n$, representing the total number of measures at the level n (or the timescale ϵ). However, in most conventional discrete-in-scale cascade models, rather than using this

summation relation, a further derived constraint, i.e.,

$$\begin{aligned} E[\mu_j(\epsilon)] &= E[\mu(\epsilon)] = 1/N(\epsilon) = b^{-n} \\ &= \epsilon, \end{aligned} \tag{C.2}$$

is applied, where $E[\mu(\epsilon)]$ is the expectation of each measure.

The q-th moment of the measure can be therefore expressed as

$$E[\mu^q(\epsilon)] = E[(\prod_{L=1}^{n} w_{i_L}^L)^q] = E[\prod_{L=1}^{n} (w_{i_L}^L)^q]. \tag{C.3}$$

To simplify the derivation, $w_{i_L}^L$ is further assumed to be an independently- and identically-distributed (i.i.d.) random variable (i.e. $w_{i_L}^L$ is a sampling of $\mathbf{W}$, which is i.i.d.), so Eq. (C.3) can be further termed

$$\begin{aligned} E[\mu^q(\epsilon)] &= E[\prod_{L=1}^{n} (w_{i_L}^L)^q] = E[\prod_{L=1}^{n} \mathbf{W}^q] \\ &= E[\mathbf{W}^q]^n. \end{aligned} \tag{C.4}$$

Rearranging $\epsilon = b^{-n}$, we can obtain $n = -\log_b \epsilon$ and, by substituting this expression of n into Eq. (C.4), a further relation can be derived, i.e.,

$$\begin{aligned} E[\mu^q(\epsilon)] &= E[\mathbf{W}^q]^n = E[\mathbf{W}^q]^{-\log_b \epsilon} \\ &= \epsilon^{-\log_b E[\mathbf{W}^q]}. \end{aligned} \tag{C.5}$$

Based upon the relation expressed in Eq. (4.14), i.e., $\sum_j \mu_j^q(\epsilon) \sim \epsilon^{\tau(q)}$, we define

$$\sum_{j}^{N(\epsilon)} \mu_j^q(\epsilon) = \epsilon^{\tau(q)}, \tag{C.6}$$

and a further derivation can be carried out as follows:

$$
\begin{aligned}
\sum_{j}^{N(\epsilon)} \mu_j^q(\epsilon) &= \sum_{j}^{N(\epsilon)} E[\mu_j^q(\epsilon)] \\
&= \sum^{N(\epsilon)} E[\mu^q(\epsilon)] \\
&= N(\epsilon) \cdot E[\mu^q(\epsilon)] \\
&= b^n \cdot E[\mu^q(\epsilon)] \\
&= \epsilon^{-1} \cdot E[\mu^q(\epsilon)]. \qquad \text{(C.7)}
\end{aligned}
$$

Substituting Eq. (C.6) into Eq. (C.7), we can obtain

$$
\begin{aligned}
\sum_{j}^{N(\epsilon)} \mu_j^q(\epsilon) &= \epsilon^{-1} \cdot E[\mu^q(\epsilon)] \\
&= \epsilon^{\tau(q)} \\
\Rightarrow E[\mu^q(\epsilon)] &= \epsilon^{\tau(q)+1} \qquad \text{(C.8)}
\end{aligned}
$$

Comparing Eqs. (C.8) and (C.5), we can obtain $\tau(q) = -\log_b E[\mathbf{W}^q] - 1$. This expression of $\tau(q)$ and Eq. (C.8) play very important roles in the derivation of theoretical $\tau(q)$ curve and its link to the cascade model.

C.2 Relation of $\tau(q)$ and $K(q)$ curves

However, in most random cascade models, the structure function $K(q)$, which is derived from the codimension function rather than from the multifractal spectrum (See Section 4.2.4), is more widely-used to characterise the cascade process. The relation of $\tau(q)$ and $K(q)$ therefore needs to be clarified here.

The cascade models shown in this work (e.g. Figure 4.3 or 4.8), in the jargon of the field of multifractals, are usually called "additive" cascade models. That means that the sum of subdivided measures is equal to the associated parent measure, i.e., $\sum_{j=1}^{N(\epsilon)} \mu_j(\epsilon) = 1$ (or $E[\mu(\epsilon)] = b^{-n}$). This expression of mass conservation however can be formed in another way if we consider the density, rather than the mass, of measures. Substituting the expression of the density of a measure (i.e. $I(\epsilon) = \mu(\epsilon)/\epsilon$) and $\epsilon = b^{-n}$, we can obtain

$$
\begin{aligned}
E[I(\epsilon)] &= E[\mu(\epsilon)/\epsilon] = E[\mu(\epsilon)/b^{-n}] \\
&= b^n E[\mu(\epsilon)] = (b^n)(b^{-n}) \\
&= 1, \qquad \text{(C.9)}
\end{aligned}
$$

where $I(\epsilon)$, in a physical sense, can be explained as the (normalised) rainfall intensity. By introducing Eq. (C.8), the $q-$moment of this expression, i.e., $E[I^q(\epsilon)]$, can be further derived, i.e.,

$$
\begin{aligned}
E[I^q(\epsilon)] &= b^{nq} E[\mu^q(\epsilon)] = (b^{-n})^{-q} \epsilon^{\tau(q)+1} = \epsilon^{-q} \epsilon^{\tau(q)+1} \\
&= \epsilon^{\tau(q)-q+1}. \qquad \text{(C.10)}
\end{aligned}
$$

Because of the convention of using λ (i.e. resolution) rather than ϵ (i.e. scale) in random cascade models, the inverse relation of ϵ and λ, i.e., $\lambda = 1/\epsilon$, is substituted into Eq. C.10, we can obtain

$$
\begin{aligned}
E[I^q(\epsilon)] &= \epsilon^{\tau(q)-q+1} = \lambda^{q-\tau(q)-1} \\
&= \lambda^{K(q)}, \qquad \text{(C.11)}
\end{aligned}
$$

where the relation of $\tau(q)$ and $K(q)$ can be identified and termed $K(q) = q - \tau(q) - 1$.

C.3 β Model

In the β model, a simple expression of "with/without" rainfall dichotomy is assumed as follows:

$$
\begin{aligned}
&P(\mu(\epsilon)/\epsilon = I(\epsilon) = \lambda^{\beta}) = \lambda^{-\beta} \\
&P(\mu(\epsilon)/\epsilon = I(\epsilon) = 0) \quad = 1 - \lambda^{-\beta}.
\end{aligned} \qquad \text{(C.12)}
$$

Based upon this expression, the expectation of the mass of a measure can be expressed as

$$\begin{aligned} E[\mu(\epsilon)] &= \epsilon \cdot E[I(\epsilon)] = \epsilon \cdot (\lambda^{\beta})(\lambda^{-\beta}) \\ &= b^{-n}, \end{aligned} \tag{C.13}$$

where $\lambda = 1/\epsilon$ and $\epsilon = b^{-n}$. This shows that the total mass of measures can be (statistically or macrocanonically) conserved based upon this simple dichotomy assumption. The q-th moment $E[\mu(\epsilon)]$ can be therefore expressed as

$$\begin{aligned} E[\mu^q(\epsilon)] &= \epsilon^q E[I^q(\epsilon)] = \epsilon^q(\lambda^{\beta q}\lambda^{-\beta}) \\ &= \epsilon^{q(1-\beta)+\beta}. \end{aligned} \tag{C.14}$$

Comparing Eqs (C.14) and (C.8), we can derive that

$$\tau(q) = q(1-\beta) + \beta - 1, \tag{C.15}$$

or furthermore, $K(q) = \beta(q-1)$.

C.4 α Model

In the α model, a more realistic (also complex) alternative, rather than only the "with-/without" rainfall dichotomy, is assumed as follows:

$$\begin{aligned} &P(\mu(\epsilon)/\epsilon = I(\epsilon) = \lambda^{\gamma_+}) = \lambda^{-\beta} \\ &P(\mu(\epsilon)/\epsilon = I(\epsilon) = \lambda^{\gamma_-}) = 1 - \lambda^{-\beta}, \end{aligned} \tag{C.16}$$

where $\gamma_+ = \beta/\alpha$ and $\gamma_- = -\beta/\alpha^{'}$. This considers a more realistic α-instability (hence the name α-model) allowing a "more intense/less intense" rainfall dichotomy.

Based upon Eq. (C.16), the expectation of the mass of a measure can be expressed as

$$\begin{aligned} E[\mu(\epsilon)] &= \epsilon \cdot E[I(\epsilon)] \\ &= \epsilon \cdot [\lambda^{\gamma_+}\lambda^{-\beta} + \lambda^{\gamma_-}(1-\lambda^{-\beta})]. \end{aligned} \tag{C.17}$$

In order to preserve the total mass of measures, $E[\mu(\epsilon)] = b^{-n} = \epsilon$ is applied, and Eq. (C.17) can be further derived to obtain the expression

$$\lambda^{\gamma_-} = \frac{1-\lambda^{\gamma_+-\beta}}{1-\lambda^{-\beta}}. \tag{C.18}$$

The $q-$th moment of $E[\mu(\epsilon)]$ can be therefore stated as

$$\begin{aligned} E[\mu^q(\epsilon)] &= \epsilon^q E[I^q(\epsilon)] \\ &= \epsilon^q(\lambda^{\gamma+q}\lambda^{-\beta} + \lambda^{\gamma-q}(1-\lambda^{-\beta})) \\ &= \epsilon^{q(1-\gamma_+)+\beta} + \epsilon^{q(1-\gamma_-)}(1-\epsilon^{\beta}). \end{aligned} \tag{C.19}$$

Substituting Eq. (C.18) and comparing Eqs (C.19) and (C.8), we can derive that

$$\tau(q) = q - \frac{\log(b^{\gamma_+-c} + \frac{(1-b^{\gamma_+-c})^q}{(1-b^{-c})^{q-1}})}{\log b} - 1. \tag{C.20}$$

Considering the case of $\gamma_+ = \beta$, we can obtain that $\tau(q) = q(1-\beta) + \beta - 1$; the α-model therefore can be regarded as a more general form of the β-model.

C.5 Log-Poisson Model

In the log-Poisson model, each fragmentation ratio W (or called the cascade generator) is assumed to be a log-Poisson distributed random variable and is termed

$$W = A\beta^N, \tag{C.21}$$

where A and β are to be identified parameters and N is a random variable sampled from

the Poisson distribution,

$$P(N = m) = \frac{c^m e^{-c}}{m!}, \tag{C.22}$$

where c is also a to be identified parameter. The expectation of the cascade generator can be therefore expressed as

$$\begin{aligned} E[W] &= \sum_{m=0}^{\infty} A\beta^m P(W = A\beta^m) = \sum_{m=0}^{\infty} A\beta^m P(N = m) \\ &= \sum_{m=0}^{\infty} A\beta^m \frac{c^m e^{-c}}{m!}, \end{aligned} \tag{C.23}$$

and q-th moment can be consequently derived, i.e.,

$$E[W^q] = \sum_{m=0}^{\infty} A^q \beta^{mq} \frac{c^m e^{-c}}{m!} = A^q e^{-c} \sum_{m=0}^{\infty} \frac{c^m \beta^{mq}}{m!}. \tag{C.24}$$

By introducing the Taylor expression of $c\beta^q$, Eq. (C.24) can be further expressed as $E[W^q] = A^q e^{c(\beta^q - 1)}$ and consequently $E[\mu^q(\epsilon)] = E[W^q]^n = A^{qn} e^{nc(\beta^q - 1)}$. Apply the conservation of total mass (i.e. $E[\mu(\epsilon)] = b^{-n}$), and then we can obtain $A = b^{-1} e^{c(\beta - 1)}$. The expression of A can be substituted into $E[W^q] = A^q e^{c(\beta^q - 1)}$ to obtain

$$E[W^q] = b^{-q} e^{c(q(1-\beta) + \beta^q - 1)}, \tag{C.25}$$

and consequently,

$$\begin{aligned} E[\mu^q(\epsilon)] &= E[W^q]^n \\ &= b^{-nq} e^{nc(q(1-\beta) + \beta^q - 1)} \\ &= (b^{-n})^q b^{n \log_b e^{c(q(1-\beta) + \beta^q - 1)}} \\ &= (b^{-n})^q (b^{-n})^{-\log_b e^{c(q(1-\beta) + \beta^q - 1)}} \\ &= \epsilon^{q - \log_b e^{c(q(1-\beta) + \beta^q - 1)}}. \end{aligned} \tag{C.26}$$

Comparing Eqs (C.26) and (C.8), we can obtain

$$\begin{aligned} \tau(q) &= q - \log_b e^{c(q(1-\beta)+\beta^q-1)} - 1 \\ &= q - c\frac{q(1-\beta)+\beta^q-1}{\ln b} - 1, \end{aligned} \tag{C.27}$$

and therefore,

$$K(q) = c\frac{q(1-\beta)+\beta^q-1}{\ln b}. \tag{C.28}$$

Appendix D

Statistical Moments of a Semi-Deterministic Cascade Process

Based upon the theory of "Left-sided multifractals," this work proposed a new cascade model which produces random processes with deterministic fragmentation ratios. Although the processes generated by the proposed model are random, the associated statistics are however deterministic (hence named the semi-deterministic cascade model) due to the use of deterministic fragmentation ratios. In this section, the derivation of the first two statistical moments, i.e., mean (μ_{mean}) and variance (σ^2), from the definition of the semi-deterministic model is detailed.

Assume that there is a multinomial cascade with constant fragmentation ratios (denote $\mathbf{W}^n = (w_{i_1}^n, w_{i_1}^n, \cdots, w_{i_b}^n)$ at the level n) over a range of levels (shown as Figure 4.8). This means, within this range of levels, the fragmentation ratios from different cascade levels are the same (i.e. $\mathbf{W}^n = \mathbf{W}^m$, where $m \neq n$), so the fragmentation ratios can be denoted $\mathbf{W} = (w_{i_1}, w_{i_1}, \cdots, w_{i_b})$.

Based upon this, the mean of a multinomial cascade with branching number equal to b can be derived. At level $n = 0$, the mean $\mu_{mean}(0)$ is 1; and at $n = 1$,

$$
\begin{aligned}
\mu_{mean}(1) &= (w_{i_1}^1 + w_{i_2}^1 + \cdots + w_{i_b}^1)/b \\
&= b^{-1} \sum_{k=1}^{b} w_{i_k}^1 \\
&= b^{-1} \sum_{k=1}^{b} w_{i_k} \\
&= b^{-1}, \qquad \text{(D.1)}
\end{aligned}
$$

where $\mu_{mean}(1)$ denotes the mean at the level $n = 1$, and $\sum_{k=1}^{b} w_{i_k} = 1$. The value of mean at the level $n = 2$ can be derived as,

$$
\begin{aligned}
\mu_{mean}(2) &= (1/b^2)(w_{i_1}^1 w_{i_1}^2 + w_{i_1}^1 w_{i_2}^2 + \cdots + w_{i_1}^1 w_{i_b}^2 \\
&\quad + w_{i_2}^1 w_{i_1}^2 + w_{i_2}^1 w_{i_2}^2 + \cdots + w_{i_2}^1 w_{i_b}^2 \\
&\quad + \cdots \\
&\quad + w_{i_b}^1 w_{i_1}^2 + w_{i_b}^1 w_{i_2}^2 + \cdots + w_{i_b}^1 w_{i_b}^2) \\
&= b^{-2}(w_{i_1}^1 \sum_{k=1}^{b} w_{i_k}^2 + w_{i_2}^1 \sum_{k=1}^{b} w_{i_k}^2 + \cdots + w_{i_b}^1 \sum_{k=1}^{b} w_{i_k}^2) \\
&= b^{-2}(\sum_{k=1}^{b} w_{i_k}^1)(\sum_{k=1}^{b} w_{i_k}^2) \\
&= b^{-2}(\sum_{k=1}^{b} w_{i_k})^2 \\
&= b^{-2},
\end{aligned}
$$

The value of mean at the level n can be therefore derived as,

$$
\begin{aligned}
\mu_{mean}(n) &= b^{-n}(\sum_{k=1}^{b} w_{i_k})^n \\
&= b^{-n}. \qquad \text{(D.2)}
\end{aligned}
$$

The derivation process of mean shows that in the semi-deterministic cascade model the

total mass of measures is conserved at each branching; which means that this model belongs to the microcanonical cascade models.

The variance at each cascade level can be derived as follows. At level $n = 0$, $\sigma^2(0) = 0$; at level $n = 1$,

$$\begin{aligned}
\sigma^2(1) &= [(w_{i_1}^1 - b^{-1})^2 + (w_{i_2}^1 - b^{-1})^2 + \cdots + (w_{i_b}^1 - b^{-1})^2]/b \\
&= b^{-1}[\sum_{k=1}^{b}(w_{i_k}^1)^2 + (b/b^2) - 2(1/b)(\sum_{k=1}^{b} w_{i_k})] \\
&= b^{-1}[\sum_{k=1}^{b}(w_{i_k}^1)^2 + (1/b) - 2(1/b)] \\
&= b^{-1}[\sum_{k=1}^{b}(w_{i_k})^2 - b^{-1}], \qquad \text{(D.3)}
\end{aligned}$$

where $\sigma^2(1)$ denotes the value of variance at level $n = 1$ in a multinomial cascade process. he value of mean at the level $n = 2$ can be derived as,

$$\begin{aligned}
\sigma^2(2) &= (1/b^2)[(w_{i_1}^1 w_{i_1}^2 - b^{-2})^2 + (w_{i_1}^1 w_{i_2}^2 - b^{-2})^2 + \cdots + (w_{i_1}^1 w_{i_b}^2 - b^{-2})^2 \\
&\quad +(w_{i_2}^1 w_{i_1}^2 - b^{-2})^2 + (w_{i_2}^1 w_{i_2}^2 - b^{-2})^2 + \cdots + (w_{i_2}^1 w_{i_b}^2 - b^{-2})^2 \\
&\quad +\cdots \\
&\quad +(w_{i_b}^1 w_{i_1}^2 - b^{-2})^2 + (w_{i_b}^1 w_{i_2}^2 - b^{-2})^2 + \cdots + (w_{i_b}^1 w_{i_b}^2 - b^{-2})^2] \\
&= b^{-2}[(w_{i_1}^1)^2 \sum_{k=1}^{b}(w_{i_k}^2)^2 + (w_{i_2}^1)^2 \sum_{k=1}^{b}(w_{i_k}^2)^2 + \cdots + (w_{i_b}^1)^2 \sum_{k=1}^{b}(w_{i_k}^2)^2 - (1/b^2)] \\
&= b^{-2}[(\sum_{k=1}^{b}(w_{i_k}^1)^2)(\sum_{k=1}^{b}(w_{i_k}^2)^2) - (1/b^2)] \\
&= b^{-2}[(\sum_{k=1}^{b}(w_{i_k})^2)(\sum_{k=1}^{b}(w_{i_k})^2) - (1/b^2)] \\
&= b^{-2}[(\sum_{k=1}^{b}(w_{i_k})^2)^2 - b^{-2}].
\end{aligned}$$

The value of variance at the level n can be therefore deduced as,

$$\sigma^2(n) = b^{-n}[(\sum_{k=1}^{b}(w_{i_k})^2)^n - (1/b^n)]. \tag{D.4}$$

The derivation process shows that the value of variance at a given cascade level (i.e. at a given scale) will be determined once the associated fragmentation ratios are obtained. Eq. (D.4) can be further linked to the $\tau(q)$ curve by introducing Eq. (4.20). Rearranging Eq. (4.20) to $\sum_{i=1}^{b} w_i^q = b^{-\tau(q)}$ and substituting it into Eq. (D.4), we can obtain (let $q = 2$)

$$\begin{aligned}
\sigma^2(n) &= b^{-n}[(\sum_{k=1}^{b}(w_{i_k})^2)^n - (1/b^n)] \\
&= b^{-n}[(b^{-\tau(2)})^n - (1/b^n)] \\
&= b^{-n}(b^{-n\tau(2)} - b^{-n}).
\end{aligned} \tag{D.5}$$

This equation not only demonstrates the relation of $\tau(2)$ value and the variance, but also verifies that $\tau(q)$ curves could be a useful tool to characterise the structure (i.e. statistical features) of random processes.

Appendix E

Results: Adjusted Radar Rainfall and Hydraulic Outputs

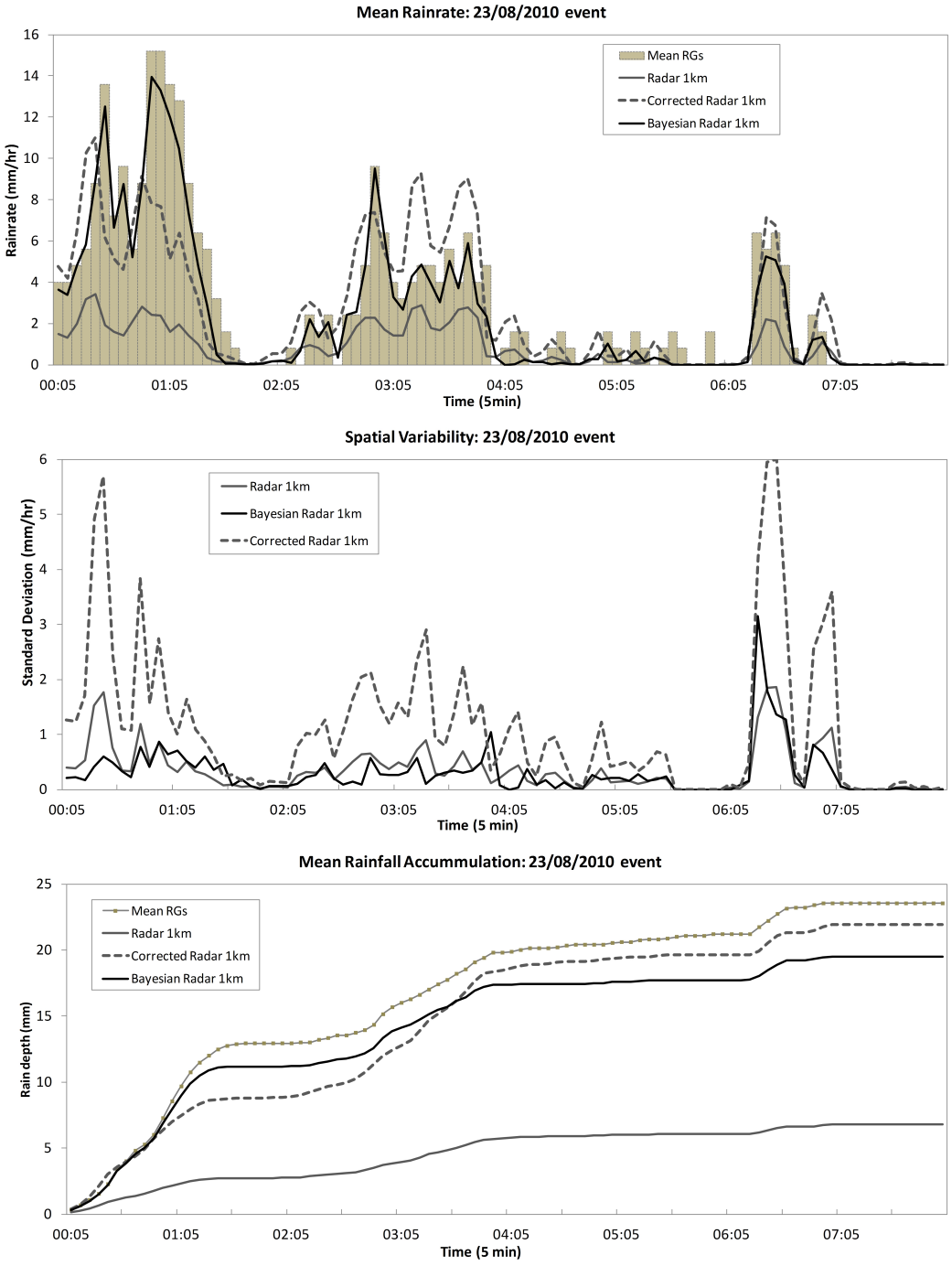


Figure E.1: The comparison of mean raingauge observations (the brown bars or markers) and the coincidental radar estimates (the gray solid line: the original radar rainfall; the gray dashed line: the mean-field adjusted radar rainfall; the dark line: the Bayesian adjusted radar rainfall) for the 23/08/2010 event crossing the Cranbrook catchment (from upper to bottom): variations of rainfall rates, standard deviations and accumulations

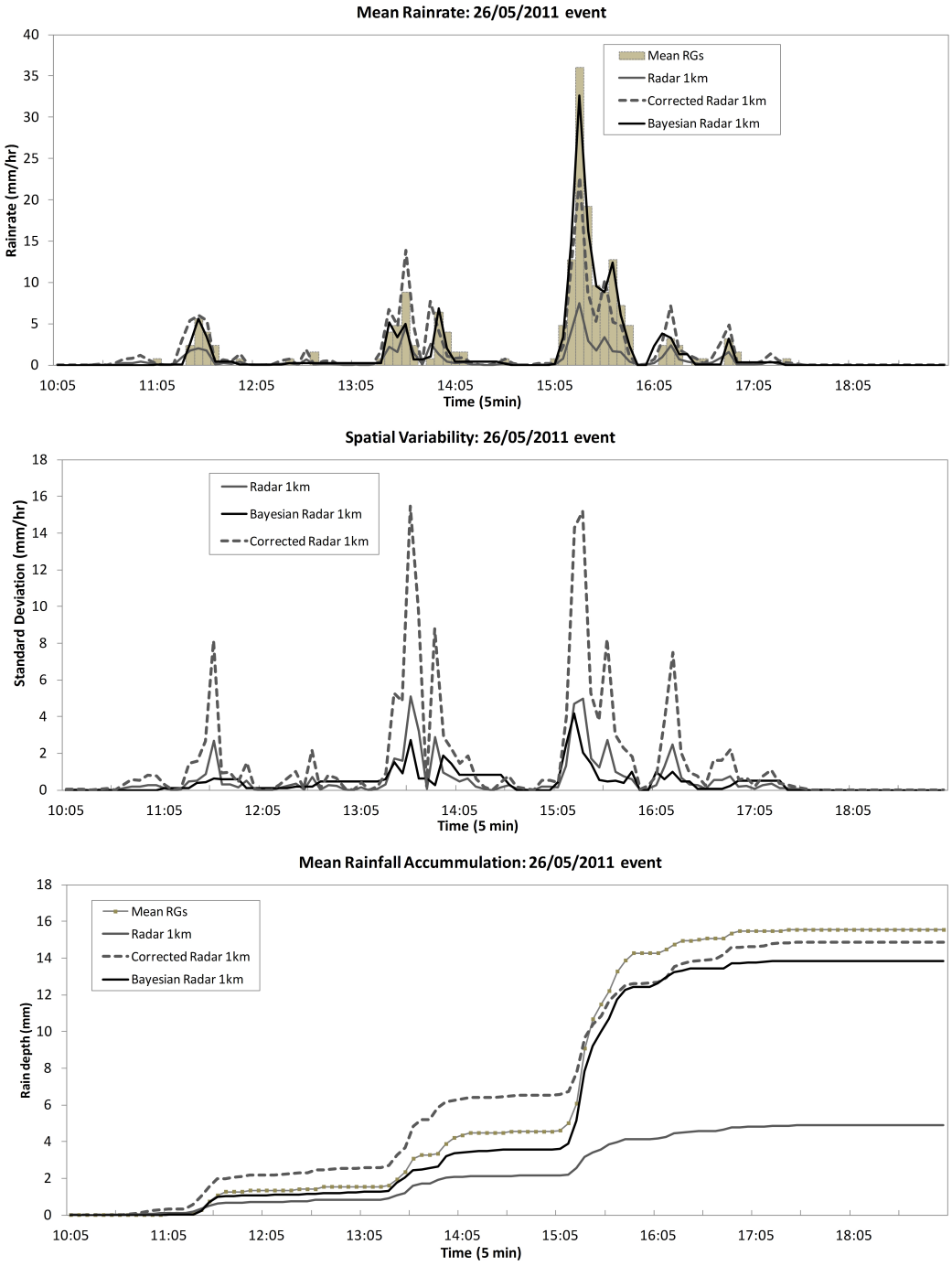


Figure E.2: The comparison of mean raingauge observations (the brown bars or markers) and the coincidental radar estimates (the gray solid line: the original radar rainfall; the gray dashed line: the mean-field adjusted radar rainfall; the dark line: the Bayesian adjusted radar rainfall) for the 26/05/2011 event crossing the Cranbrook catchment (from upper to bottom): variations of rainfall rates, standard deviations and accumulations

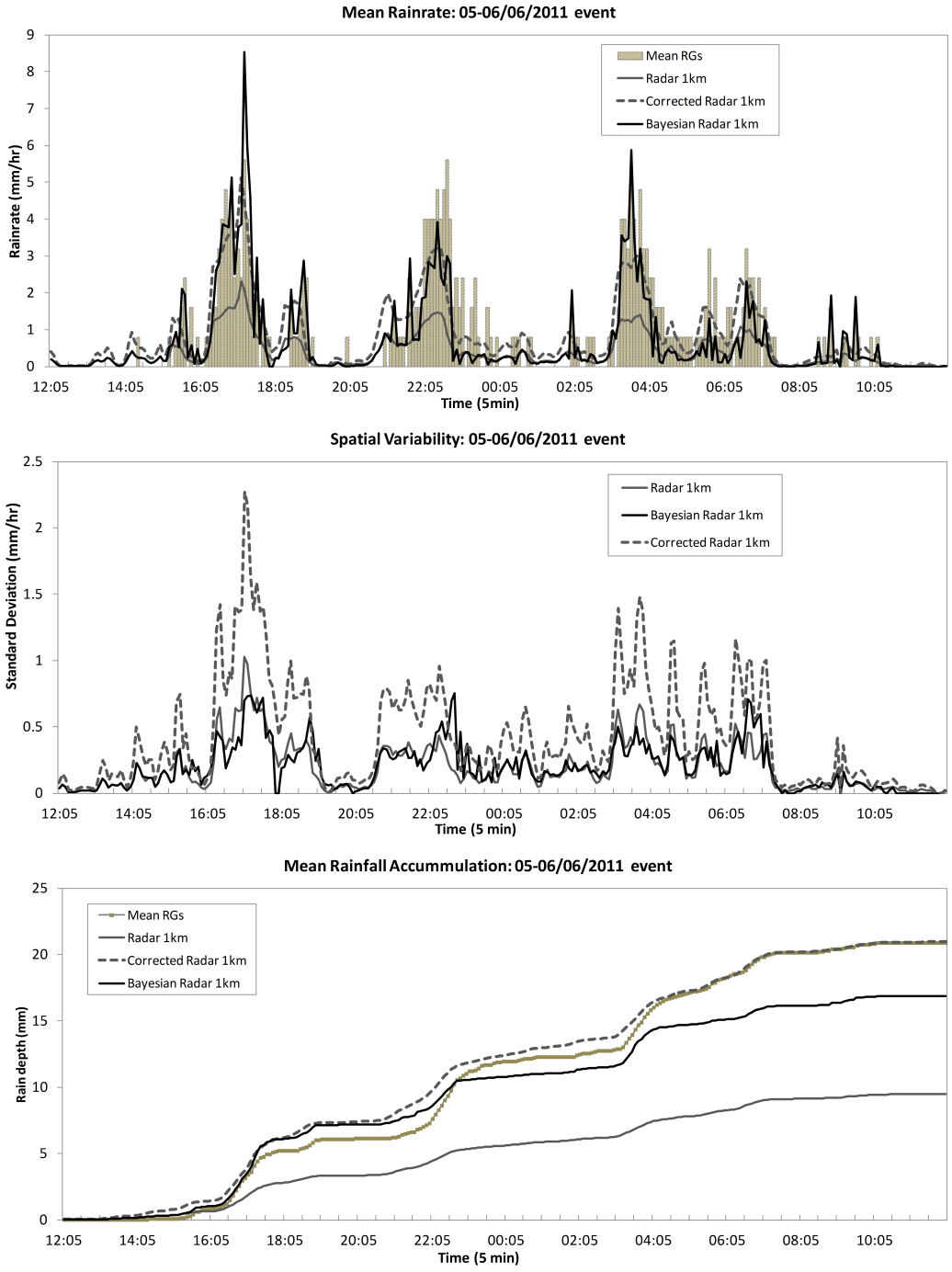


Figure E.3: The comparison of mean raingauge observations (the brown bars or markers) and the coincidental radar estimates (the gray solid line: the original radar rainfall; the gray dashed line: the mean-field adjusted radar rainfall; the dark line: the Bayesian adjusted radar rainfall) for the 05-06/06/2011 event crossing the Cranbrook catchment (from upper to bottom): variations of rainfall rates, standard deviations and accumulations

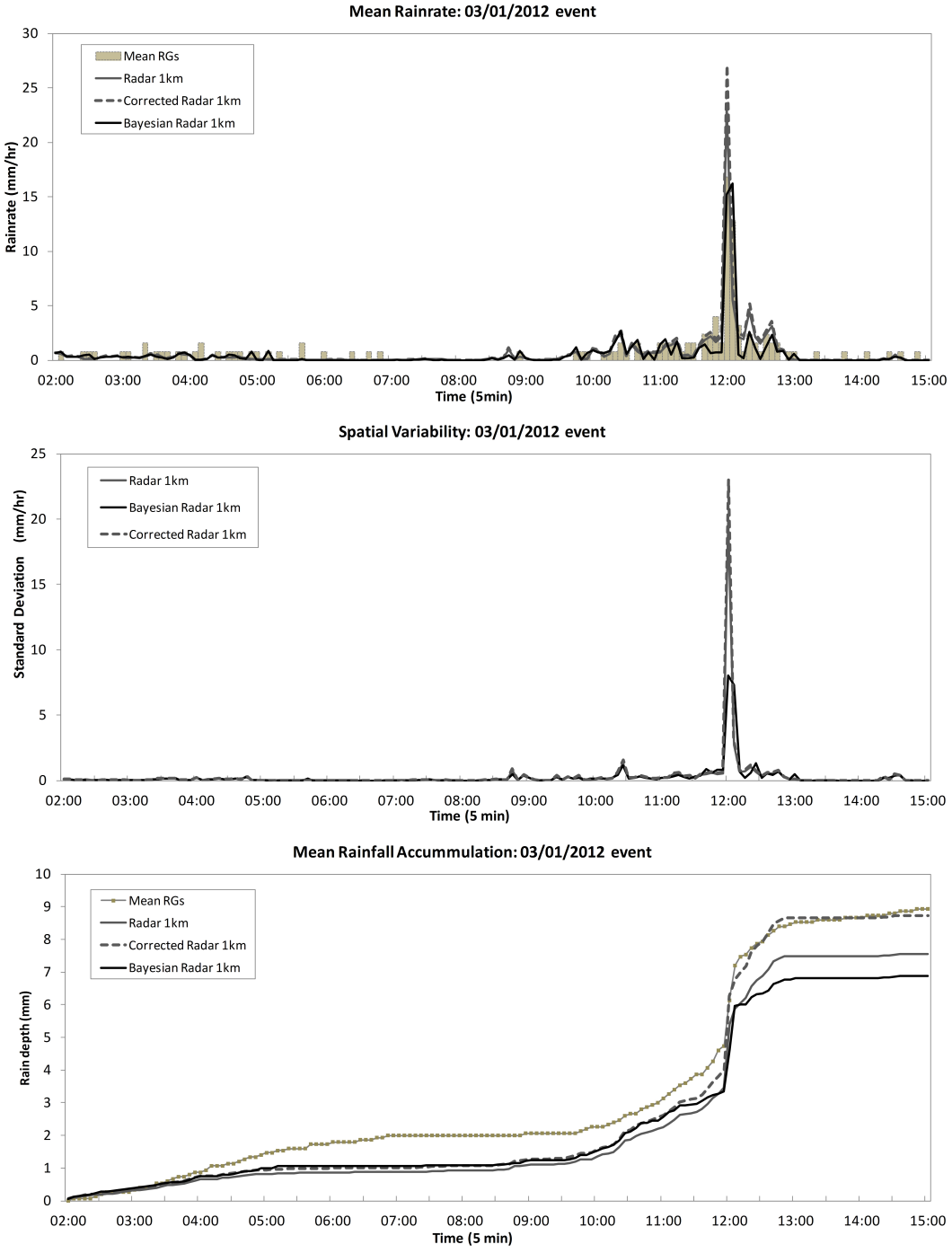


Figure E.4: The comparison of mean raingauge observations (the brown bars or markers) and the coincidental radar estimates (the gray solid line: the original radar rainfall; the gray dashed line: the mean-field adjusted radar rainfall; the dark line: the Bayesian adjusted radar rainfall) for the 03/01/2012 event crossing the Cranbrook catchment (from upper to bottom): variations of rainfall rates, standard deviations and accumulations

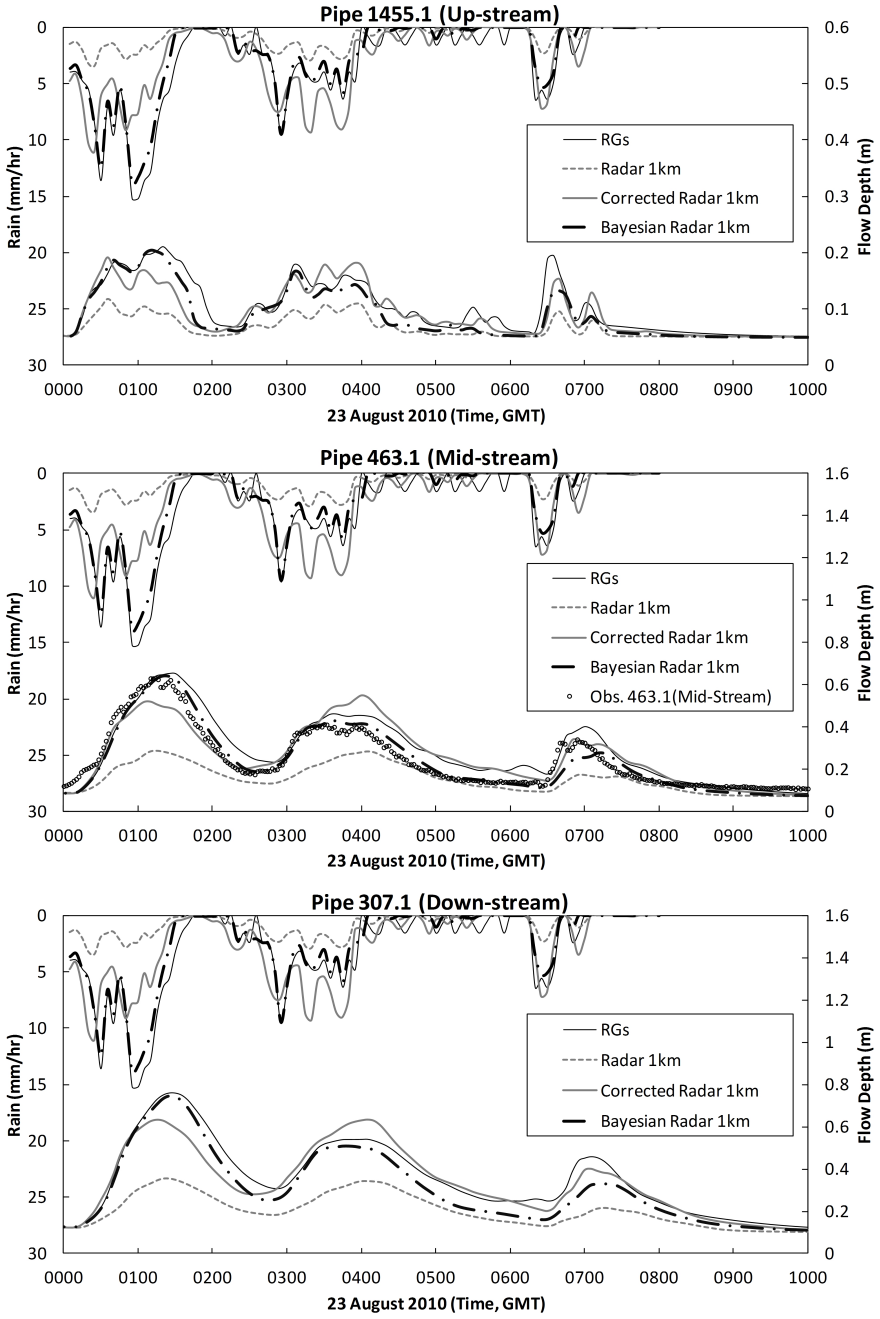


Figure E.5: The comparison of the observed (the round markers) with the estimated flow depths at three selected pipes (1455.1: up-stream; 463.1: mid-stream; 307.1: down-stream) in the Cranbrook catchment for the event 23/08/2010. The estimated flow depths were obtained by using mean raingauge observations (the dark solid line) and the coincidental radar estimates (the gray dashed line: the original radar rainfall; the gray solid line: the mean-field adjusted radar rainfall; the dashed-dotted line: the Bayesian adjusted radar rainfall) as inputs

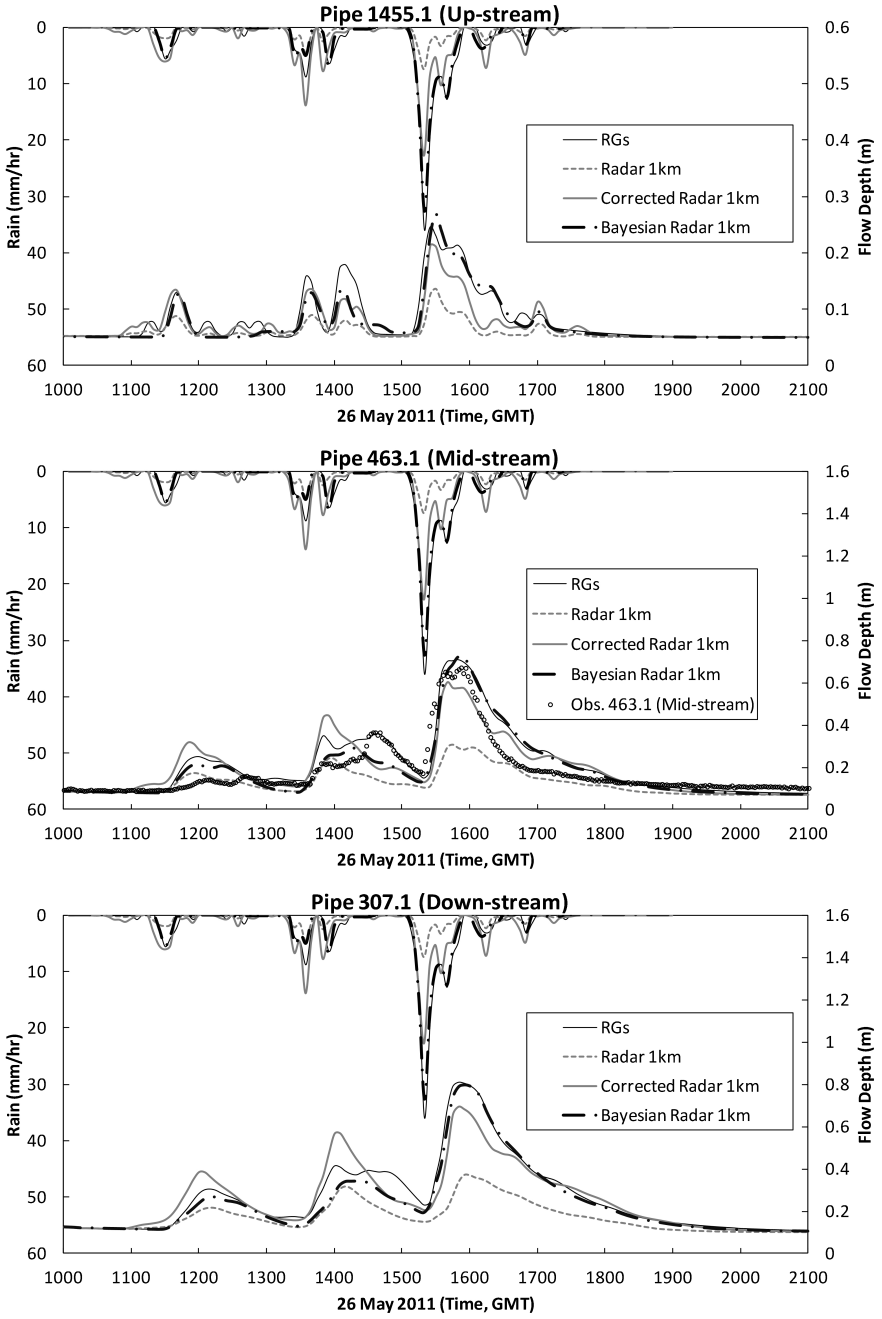


Figure E.6: The comparison of the observed (the round markers) with the estimated flow depths at three selected pipes (1455.1: up-stream; 463.1: mid-stream; 307.1: down-stream) in the Cranbrook catchment for the event 26/05/2011. The estimated flow depths were obtained by using mean raingauge observations (the dark solid line) and the coincidental radar estimates (the gray dashed line: the original radar rainfall; the gray solid line: the mean-field adjusted radar rainfall; the dashed-dotted line: the Bayesian adjusted radar rainfall) as inputs

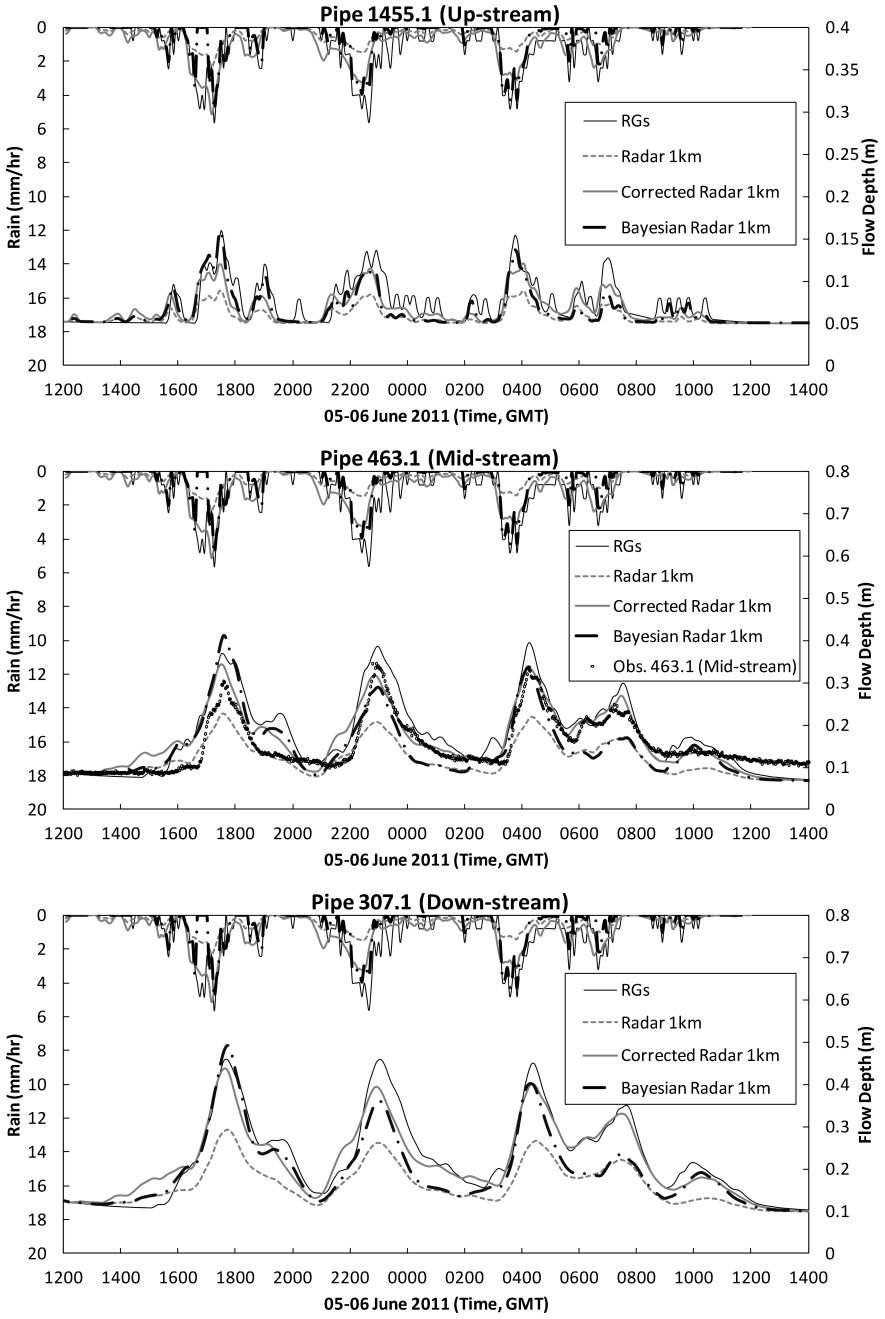


Figure E.7: The comparison of the observed (the round markers) with the estimated flow depths at three selected pipes (1455.1: up-stream; 463.1: mid-stream; 307.1: down-stream) in the Cranbrook catchment for the event 05-06/06/2011. The estimated flow depths were obtained by using mean raingauge observations (the dark solid line) and the coincidental radar estimates (the gray dashed line: the original radar rainfall; the gray solid line: the mean-field adjusted radar rainfall; the dashed-dotted line: the Bayesian adjusted radar rainfall) as inputs

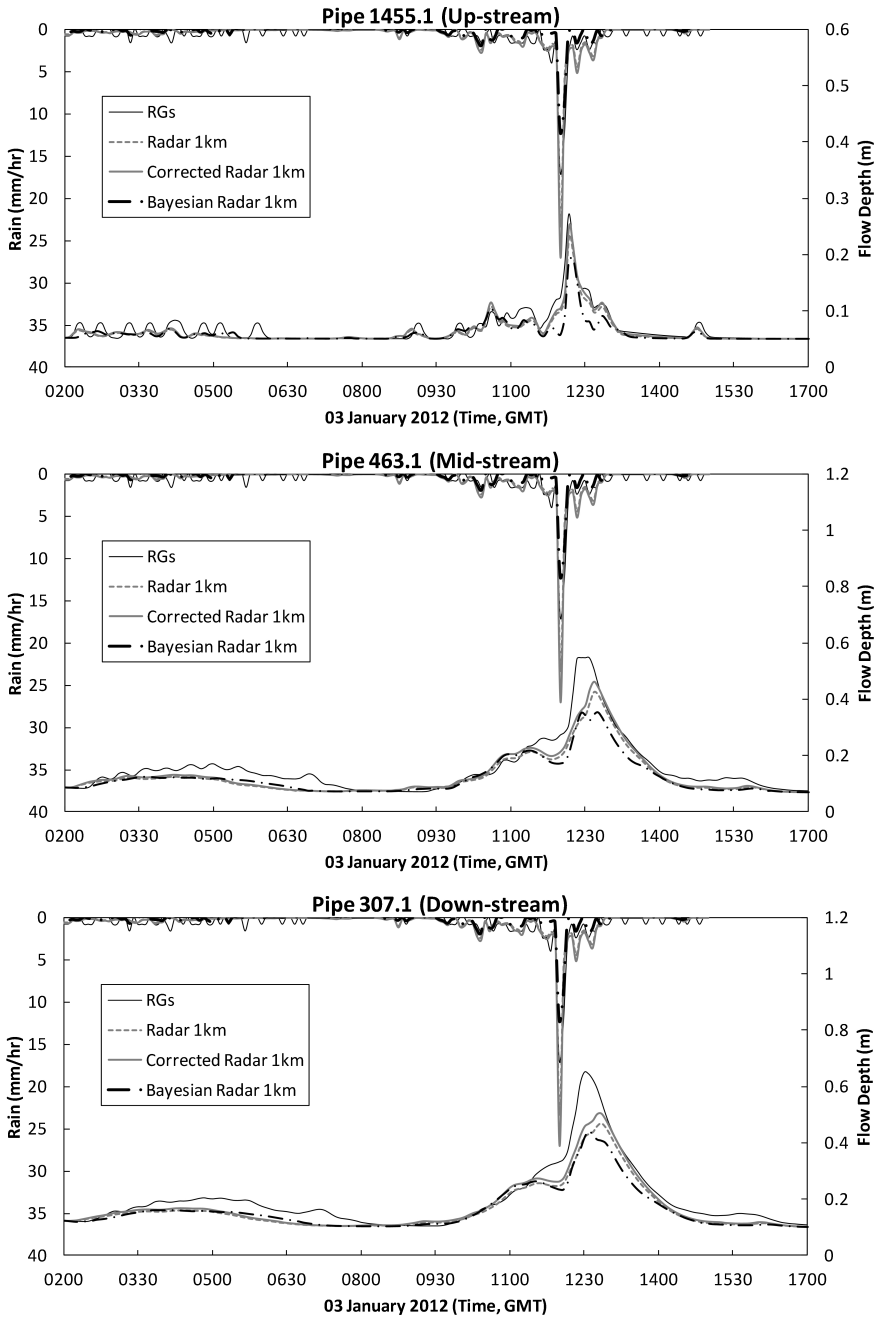


Figure E.8: The comparison of the flow depths obtained by using mean raingauge observations (the dark solid line) and the coincidental radar estimates (the gray dashed line: the original radar rainfall; the gray solid line: the mean-field adjusted radar rainfall; the dashed-dotted line: the Bayesian adjusted radar rainfall) as inputs at three selected pipes (1455.1: up-stream; 463.1: mid-stream; 307.1: down-stream) in the Cranbrook catchment for the event 03/01/2012